von Karman Institute for Fluid Dynamics
Environmental and Applied Fluid Dynamics Department

Université catholique de Louvain
Institute of Mechanics, Materials and Civil Engineering

Prandtl number effects in abruptly separated flows: LES and experiments on an unconfined backward facing step flow

PhD Dissertation

Sophia Buckingham

Thesis Committee:

Prof. Yann Bartosiewicz, Université catholique de Louvain (Advisor)
Prof. Grégoire Winckelmans, Université catholique de Louvain (Advisor)
Prof. Hervé Jeanmart, Université catholique de Louvain
Dr. Lilla Koloszar, von Karman Institute for Fluid Dynamics
Dr. Afaque Shams, Nuclear Research and Consultancy Group NRG
Prof. Jeroen van Beeck, von Karman Institute for Fluid Dynamics
Prof. Laurent Delannay, Université catholique de Louvain (President)

"L'avenir n'est pas ce qui va arriver, mais ce que nous allons en faire."
Henri Bergson

Abstract

Liquid metal cooled reactors have been relying on Computational Fluid Dynamics (CFD) analyzes for their design and safety evaluation. However, the major challenge is the modeling of the turbulent heat transfer in the low Prandtl number coolant ($Pr \simeq 0.001 - 0.01$). More advanced models require to be tested, calibrated and validated on a wide variety of flows to make them applicable to Liquid Metal Reactors. In this thesis, Prandtl number effects on the turbulent heat transfer are investigated by carrying out Large-Eddy Simulations (LES) and experiments in abruptly separated flows. To represent simply the detached flow areas and wall interactions that dominate the upper plenum, an unconfined Backward-Facing Step (BFS) is chosen as benchmark test-case.

An essential contribution of this work has been to propose an efficient and flexible approach to generate inflow turbulence for LES. The use of the temperature perturbation method (TPM), up to now restricted to large scale atmospheric flows, has been extended to all types of wall-bounded flows. The key modification relies on artificially increasing buoyancy effects up to levels that are strong enough to generate turbulence, via a suitable perturbation function that will avoid any stratification effects from increasing the flow recovery distance. The optimized TPM enables to minimize this distance needed to obtain "realistic" turbulence, without the need to impose second order statistics.

To evaluate the accuracy of the LES, tests are performed in a He-Xe gas mixture ($Pr \simeq 0.2$), that is close to the lowest achievable value for a transparent medium, thus enabling to measure turbulent quantities while providing an insight into moderate Prandtl number effects. PIV measurements are carried out in air to validate the LES velocity field. A double sensor probe, consisting of a hot-wire and a thermocouple, is used to correlate velocity and temperature fluctuations in order to characterize the transport of heat due to turbulence. This work has demonstrated the importance of integrating the probe's limitations while processing the LES data, resulting in a meaningful and satisfactory comparison between LES and experiment.

Based on the LES results obtained at $Pr = 0.025, 0.2$ and 0.71, Prandtl number effects are investigated. As opposed to heat transport in moderate Prandtl number fluids that is strongly dominated by turbulence effects, in low Prandtl number fluids, the heat is transported much further away due to a strong molecular contribution that is comparable to the turbulent part. More generally, this work confirms the necessity of resorting to anisotropic turbulent heat transfer models for RANS, that can now be assessed by comparison to this newly generated validation data.

Acknowledgements

I would like to thank in particular my promotors from UCL, Prof. Grégoire Winckelmans and Yann Bartosiewicz for following me from the start to the end. Thank you for always being available to discuss and for providing me the scientific guidance I needed to carry out this research. Thank you for your interest in my work, your meticulous readings, corrections and numerous improvements. You have taught me a lot about LES and CFD in general, I consider myself extremely lucky to have benefited from your expertise, your advice and your criticism, which have made me I think a better researcher.

I would like to thank all the members of my jury, starting with Dr. A. Shams from NRG, Prof. H. Jeanmart and Prof. L. Delannay from UCL. You have provided me a very precious outside view on my work. Your critical feedback and your suggestions have greatly helped me to improve this thesis. Thank you to my colleagues and VKI supervisors Dr. L. Koloszar and Prof. J. van Beeck. Thank you Jeroen for always radiating your passion for fluid dynamics. I am very grateful for your endless support, from the time I was your DC student almost ten years ago, to when I "changed" my mind about wanting to do a Ph.D., and until this day. Lilla, I have appreciated working with you since the very first day I started at VKI as a Research Engineer. I have learnt so much from you, thank you for all your advice during this Ph.D. You gave me a lot of strength by always believing in me and my work.

I would like to thank all the people without whom this work would not have been possible. Thank you Philippe for all your support. I remember us agreeing when you hired me that a Ph.D would probably be out of the picture. Well, thank you for reconsidering, and for writing together the part of the MYRTE proposal that would become my financial support. You gave me the freedom I needed and I am very grateful to you. You also handled the design and construction of the MYRTE wind tunnel, together with the design office, the workshop and the EA technical team. Special thanks to Mathieu Delsipee, Michel Quinet, Michel Bavier and Laurent Neubourg for their hard work and ingenious ideas on how to make the facility trully sealed, even to Helium. I would also like to aknowledge the students and colleagues that have greatly contributed to the project. Thank you Chiara for sharing with me your expertise in PIV. You helped me acquire high quality data that constituted an essential milestone, and to you Agustin for always being available to help me with the coding and compiling in OpenFOAM. I have also had the chance to work with Katrien van Tichelen and Steven Keijers from SCK•CEN. During our many DEMOCRITOS meetings, you have shared with us your extended knowledge about thermal-hydraulics and liquid metals, and made our work on MYRRHA even more meaningful. It has been a pleasure to work with you and

I hope our collaboration will continue for many years.

To my Dear Friends, some of you have been part of my life since childhood, the ESTACA band, les Pucistes, you may have the impression I have been talking about this Ph.D. since ages, it actually took me some time to get started.. thank you for all your encouragements. Ariane, I am very lucky to have shared this journey with you, first discussed during our car-pooling rides to Cenaero until the last week-ends of writing, while the super daddys were in action. And of course, to the Pairi-Daiza friends: Fabri, Ale, Marina, Bernd, Ale, Chiara, JB, Anabel, Işıl, Clara and Jorge, thank you for all the good times and for taking care of us in bright and harder times. It is thanks to you all that we enjoy our life in Brussels so much, which we now consider our second home.

Finally, I want to thank my family for all their love and support. I owe everything to my parents, Richard and Margaret, for giving me the freedom to choose and to live my life. Although your dinner time discussions about developmental biology did seem rather obscure to me at the time, maybe they did inspire me in doing research... Thank you mum for your endless support, it is while you were taking care of Timo that I wrote a good part of this thesis. Last but not least, thank you canım, for supporting me all the way, for cheering me up when I was down and convincing me I would eventually get there. I will always remember you setting off with our two little ones for hours at the week-ends, so that I could progress on the thesis. I would have never managed without you, and I am very proud of what we have accomplished together. To my little sunshines, Timoté and Déniz, who would always remind me of what reaaaally matters.

Contents

Nomenclature

Roman Symbols

AR Aspect Ratio
C_f Skin friction coefficient
C_s Smagorinsky coefficient
C_p specific scalar capacity $[J/(kg.K)]$
d displacement of the PIV particle tracers $[m]$
d_c diagonal of the perturbation cell $[m]$
E voltage $[V]$ OR energy spectra $[a^2]$
ER Expansion Ratio
f frequency $[Hz]$
f_μ damping function
F_i forcing term of the momentum equation $[m/s^2]$
g_i gravity vector $[m/s^2]$
G wake function
H domain height OR Hill slope
H_{12} boundary layer shape factor
h step height $[m]$
h_c convective heat transfer coefficient $[W/(m^2.K]$
I_{ij} integral length scale tensor
k turbulent kinetic energy $[m^2/s^2]$
L length $[m]$
M magnification factor of the PIV image $[mm/px]$
n_c number of grid cells per perturbation cell side
$n_{x,y,z}$ unit vectors in the x, y and z directions
N number of mesh points OR number of independent samples
Nu Nusselt number
p pressure $[Pa]$
P kinematic pressure $[m^2/s^2]$
q heat flux $[W/m^2]$
$\tilde{P}$ modified kinematic pressure $[m^2/s^2]$
Pe Peclet number
Pr molecular Prandtl number
Re Reynolds number
Ri Richardson number
S surface area $[m^2]$ OR sensitivity coefficient
S_{ij} strain rate tensor
St Strouhal number OR Stanton number
t time $[s]$
T temperature $[K]$

T_{obs} observation time $[s]$
T_u characteristic time of the flow $[s]$
TF transfer function
TI local turbulence level [%]
U velocity magnitude $[m/s]$
V vertical velocity $[m/s]$
u instantaneous streamwise velocity $[m/s]$
u_i instantaneous velocity components $[m/s]$
u_τ friction velocity $[m/s]$
v instantaneous vertical velocity $[m/s]$
w yaw angle coefficient
x, y, z cartesian coordinates in the streamwise, wall-normal and spanwise directions $[m]$
z_{i0} temperature inversion height $[m]$

Greek Symbols

α thermal diffusivity $[m^2/s]$
β thermal expansion coefficient $[K^{-1}]$
δ channel half width [m] OR boundary layer thickness $[m]$
δ^* boundary layer displacement thickness $[m]$
δ_{ij} Kronecker symbol
δ_{SL} shear layer thickness
Δ quantity difference OR cube root of the cell volume $[m]$
ϵ turbulent dissipation $[m^3/s^2]$ OR error
η Kolmogorov scale $[m]$
η_T Corrsin scale $[m]$
Γ dimensionless perturbation time scale
κ von Karman constant
λ thermal conductivity $[W/(m.K)]$
μ dynamic viscosity $[Pa.s]$
ν kinematic viscosity $[m^2/s]$
ω vorticity $[s^{-1}]$
ϕ scalar quantity
ψ stream function
ρ density $[kg/m^3]$
σ_{ij} stress tensor $[Pa]$
τ_{ij} shear stress $[Pa]$
θ boundary layer momentum thickness $[m]$

Subscripts

$*$ unscaled quantity
a fully active region property OR related to artificial buoyancy effects
amb ambient conditions

b	bulk quantity OR bi-normal component
c	cut-off
d	parameter at a downstream location
$diff$	differential parameter
eff	effective part
F	filtered quantity
f	fluid property
h	step related parameter
hw	hot-wire related parameter
i	initial parameter
in	inlet parameter
k	kinematic quantity
L	Lagrangian quantity
m	molecular part
mm	quantity in mm
max	maximum value
min	minimum value
N	resulting component
n	normal component
noF	non-filtered quantity
noS	quantity without probe spacing
p	characteristic of the perturbation region or method
px	quantity in $pixel$
r	parameter at the location of flow reattachment
$rand$	random quantity
ref	reference parameter
res	resolved part of the turbulent stresses
rms	root mean square
S	parameter including probe spacing
s	characteristic of the seeding zone OR sampling characteristic
sgs	subgrid-scale part
$step$	parameter at the step location
sys	systematic quantity
t	turbulent part
T	tangential component
tot	total quantity
tr	characteristic of the transition region
u	parameter at an upstream location
w	wall property
0	reference part
x, y, z	streamwise, wall-normal and spanwise components

Superscripts

$\bar{}$	filtered quantity OR

$\bar{}$	quantity averaged over time and the homogeneous direction
$'$	fluctuating part
$+$	dimensionless quantities normalized using $\overline{u}_\tau, \nu, \overline{T}_\tau$
$*$	non-dimensional form
d	deviatoric part
sgs	subgrid-scale part

Acronyms

ADS	Accelerator Driven Systems
BFS	Backward-Facing Step
BL	Boundary Layer
BTBL	Buoyant Turbulent Boundary Layer
CFD	Computational Fluid Dynamics
DNS	Direct Numerical Simulation
E-SCAPE	European SCaled Pool Experiment
ESNII	European Sustainable Nuclear Industry Initiative
FNR	Fast Neutron Reactor
FPJ	Forced Plane Jet
HLM	Heavy Liquid Metal
HWA	Hot-Wire Anemometry
IR	InfraRed
KTH	Royal Institute of Technology
LBE	Lead-Bismuth Eutectic
LDA	Laser Doppler Anemometry
LDV	Laser Doppler Velocimetry
LES	Large Eddy Simulation
LFR	Lead-cooled Fast Reactor
MYRRHA	Multi-purpose hYbrid Research Reactor for High-tech Applications
MYRRHABelle	MYRRHA Basic sEt-up for Liquid fLow Experiments
MYRTE	MYRRHA Research and Transmutation Endeavour
OpenFOAM	Open Field Operation and Manipulation
PBC	Periodic Boundary Conditions
PISO	Pressure Implicit with Split Operator
PIV	Particle Image Velocimetry
POD	Proper Orthogonal Decomposition
PTV	Particle-Tracking Velocimetry
RANS	Reynolds Averaged Navier-Stokes
RFG	Random Flow Generator
RMSE	Root Mean Square Error
SCK·CEN	StudieCentrum voor Kernenergie
SGS	Sub-Grid Scale
SEM	Synthetic Eddy Method
SFR	Sodium-cooled Fast Reactor
SGDH	Simple Gradient Diffusion Hypothesis

STH	System Thermal-Hydraulic
TBL	Turbulent Boundary Layer
TC	Thermocouple
THINS	Thermal-hydraulics of Innovative Nuclear Systems
TPM	Temperature Perturbation Method
VKI	von Karman Institute for Fluid Dynamics
XC	Xie and Castro
XCMC	Xie and Castro with Mass Correction
ZPG	Zero Pressure-Gradient

Chapter 1

Introduction

1.1 Liquid metal cooled reactors

Today, nuclear energy represents 30 % of the electric power produced in the European Union and 16 % worldwide. As denoted in the projections of the World Energy Outlook 2017 [55], it is expected to continue playing an important role to fulfill the future energy needs. With the growing rate of energy demand, the question of uranium resources becomes increasingly relevant, since the amount known at present could only cover a period of 100 to 300 years of worldwide electricity production with the existing park based on light water technology. Moreover, the environmental impact of nuclear power remains a major concern because the required time scale for the geological disposal of nuclear waste exceeds the time span of profound historical knowledge.
To meet these future energy challenges, the European Commission presented the Vision Report of the Sustainable Nuclear Energy Technology Platform (Euratom 2007) [42]. In particular, the role of nuclear fission energy in the European transition towards a low-carbon energy mix by 2050 is adressed. Within the Vision Report, a large role is attributed to the development of Fast Neutron Reactors (FNR), and the European Sustainable Nuclear Industry Initiative (ESNII) largely relies on the industrial application of this technology for a sustainable nuclear energy production [41]. In Europe, the preferred innovative concept is the Sodium-cooled Fast Reactor (SFR) with the Lead-cooled Fast Reactor (LFR) as one of the two back-ups. This clearly shows the importance of liquid metals in the development of future nuclear energy technologies.

Fast reactors are firstly very promising because of their ability to efficiently use uranium. By relying on fast neutrons to cause fission, the energy output is multiplied by a factor of 50 to 100, compared to current light water reactors. They have therefore the potential to provide energy for the next thousands of years with the already known uranium resources. Moreover, this can be combined with the objective of reducing the volume and lifetime of nuclear waste. Indeed, the Partitioning and Transmutation (P&T) concept has been identified numerous times and more recently in the framework of the Gen-IV initiative as the strategy that can help reduce this lifespan down to technological and manageable time scales.
For these reasons, Generation IV reactor designs are largely FNRs, and international collaboration on FNR designs is proceeding with high priority. In Europe, four demonstration projects are currently undergoing, see Fig. 1.1.

The ASTRID industrial prototype has the objective to demonstrate the relevance and performance of innovations for the development of SFR technology, for the fuel cycle and for waste management [31]. The ALFRED project aims at constructing a LFR demonstrator in Romania and is being developed through the ESNII [8]. MYRRHA is a multi-purpose flexible irradiation facility proposed to operate as a European large research infrastructure [22]. It is currently being developed by SCK•CEN, the Belgian Nuclear Research Centre, and would replace the BR2 reactor (Mol, Belgium), which is part of a limited set of three large research reactors together with HFR (Petten, The Netherlands) and OSIRIS (Saclay, France), that supplies about 60 % of the world's needs for medical radioisotopes. It answers the need for a demonstration of the Accelerator Driven Systems (ADS) concept for waste transmutation, while serving as an experimental pilot plant for the lead technology. Finally, SEALER is a small lead-cooled reactor currently under development by the Swedish company LeadCold. Its main objective is to be deployed in Canadian arctic communities that remain disconnected from national power grids and road networks. All of these are pool type reactors, as all primary components are installed inside the reactor vessel. The main advantage of this concept over loop type reactors is that it benefits from a higher thermal inertia. This implies that, in the case of an accidental scenario leading to a loss of flow, the temperature rise will be slower due to higher heat capacity.

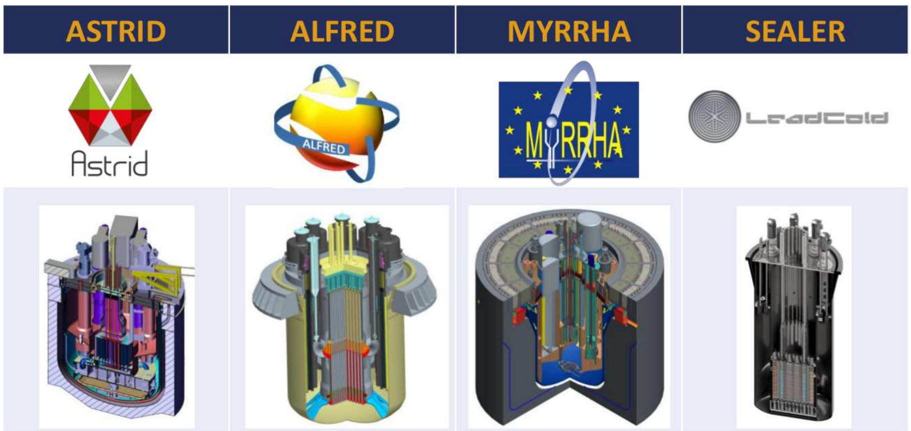

Figure 1.1: *European liquid metal cooled reactor demonstration projects [129].*

The investigation of reactor performance in operational conditions and during accidental conditions has always been one of the main concerns of nuclear safety. From a thermal-hydraulic point of view, innovative reactors are mainly characterized by their different coolants (gas, water, liquid metals and molten salt). Liquid metals represent a promising technology to be used as coolant fluids for Generation IV nuclear power plants because of their high thermal conductivity, large thermal inertia and their good neutronic properties. However these low Prandtl number fluids ($Pr \simeq 0.001 - 0.01$) exhibit a rather different convective heat transfer behavior compared to typical fluids such as water or gas. As proposed in [128], the thermal hydraulic challenges related to LFR can be regrouped in different reactor subsystems, represented schematically in Fig. 1.2, namely: the nuclear core (1), the reactor pool (2), the heat transfer systems (3), such as the heat exchangers and steam generators, and finally the challenges related to the heat transport systems (4).

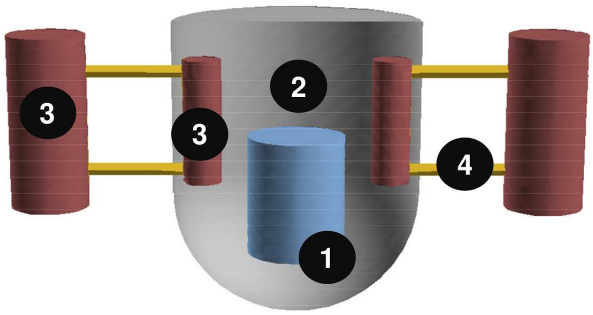

Figure 1.2: *Reactor subsystems as considered in [128].*

The core is where the fuel assemblies, composed of a large number of fuel pins, are located and from which the heat produced by nuclear fission is transported into the coolant. The main challenges in this area of the reactor rely on the correct prediction of heat transport under nominal, transient and accidental conditions. Moreover, these evaluations are needed at various levels of detail, ranging from the complete core for pressure drop calculations, down to a sub-channel for the localization of hot spots. Extensive work has been performed on fuel pins that are separated by wire wrap spacers since these represent the vast majority of cases. An inclusive overview of these studies can be found in Roelofs et al. [129], to which we may add the recently published quasi-DNS data of Shams et al. [149], for an infinite wire-wrapped fuel assembly including heat transport. On the contrary, there is no data available for now in the open litterature on bare rod-bundles.

As far as the reactor pool is concerned, many thermal hydraulic challenges are regrouped in this part of the reactor. Papers dedicated to this problematic [162, 167] highlight how many of these are concentrated in the upper plenum of the reactor. A few of these issues are represented in Fig. 1.3 [128] and all require an accurate prediction of the temperature field. Consequently, heat transfer plays a crucial role as it will directly impact the structural integrity of the reactor components and the chemical phenomena taking place such as oxidation.
Although only a few components are represented, many others (i.e. in-vessel fuel handling machines, pumps and tubes) are inserted in the upper plenum. As the flow exits from the above core structure into the upper plenum through a number of barrel holes, jets are produced leading to strong shear as they expand into this lower velocity region. As a result, important wall interactions are induced by the flow impacting the inserted components, thus leading also

to large separation areas in some places.

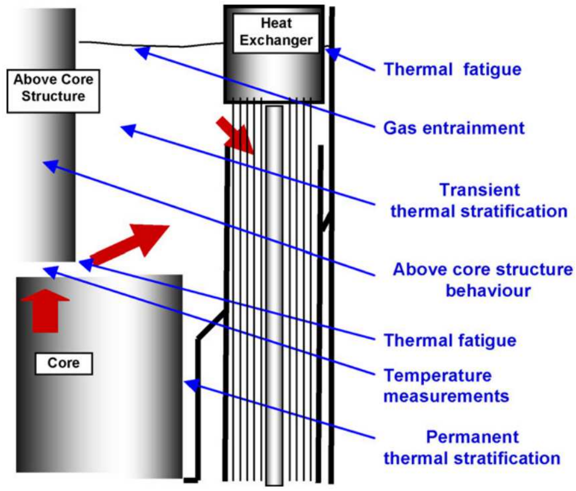

Figure 1.3: *Upper plenum thermal-hydraulic challenges as represented in [128].*

This problematic has been the subject of a number of European collaborative programs, and most recently the European FP7 THINS (Thermal-hydraulics of Innovative Nuclear Systems) project. As an outcome, the main challenges that have been identified for future development of liquid metal cooled reactors [126] have served as a starting point for defining the work description of the Horizon 2020 MYRTE (MYRRHA Research and Transmutation Endeavour) project. This PhD work is carried out within the framework of the MYRTE project, and aims at addressing issues related to liquid-metal pool thermal hydraulics by numerical simulation and experimental validation. It is certainly worth mentioning the Horizon 2020 SESAME (thermal-hydraulics Simulations and Experiments for the Safety Assessment of MEtal cooled reactors) project that is very complementary to the thermal-hydraulic work package of the MYRTE proposal and has therefore led to strong interactions between both projects. While the MYRTE project is dedicated to the specific challenges of MYRRHA, the SESAME project aims at the generic development and validation of a methodology that can be applied to any kind of liquid metal fast reactor design. Further explanation of the motivation of this work and the objectives of the thesis first requires understanding in more detail the challenges related to pool thermal hydraulics and liquid metal heat transfer.

1.2 Pool thermal-hydraulics

The understanding of the thermal hydraulic phenomena occuring in the reactor pool is one of the key problematics in the design and safety assessment of these reactors. Pool thermal hydraulics regroups many challenges that can be subdi-

vided into upper plenum and lower plenum thermal-hydraulics. As pointed out by Tenchine [162], these are mostly concentrated in the upper plenum, often considered as one of the noblest parts of fast reactor thermal hydraulics. In general, a good knowledge of convection patterns, flow mixing and stratification in operational and accidental conditions is absolutely necessary.
Following the Fukushima accident, effort has been put on developing enhanced passive safety systems for decay heat removal. This is for instance one of the guiding principles of the MYRRHA reactor and it is therefore indispensable to demonstrate that the natural circulation is able to achieve this purpose. Among other challenges that have been identified [162, 167], thermal fluctuations caused by changes in coolant level, jets at the core outlet or thermal stratification play a key role. These lead to thermal fluctuations and potentially thermal fatigue, which must be properly estimated during the design process, so that the structural integrity of the reactor components can be insured.

In the past, experiments have been the main source of information available to obtain a clear understanding of the flow in a reactor pool. For several decades, water model experiments have been very useful in providing a global idea of the thermal hydraulic behavior. Such studies have been performed for the development of SFR in France, Japan, Germany and India [47, 68, 162]. For LFR in Belgium, the von Karman Institute (VKI) operates, in collaboration with SCK•CEN, a 1/5 scale mock-up of the MYRRHA flow in the reactor: MYRRHABelle, [155] shown in Fig. 1.4. By respecting similarity parameters and applying proper scaling laws, many thermal-hydraulic challenges of HLM reactors can be addressed. Thanks to the transparent coolant, measurement techniques such as Particle Image Velocimetry (PIV) that require optical access can be applied to measure velocity, and help identify the presence of stagnant flow regions for example.
It is also constitutes a very useful tool to investigate transient scenarios such as loss of flow or single component failures [119]. Nevertheless, the low thermal conductivity of water might lead to differences in the case of specific phenomena such as thermal stratification [47]. For this reason, liquid metal experiments remain very valuable. The E-SCAPE facility in Belgium [163], is a thermal-hydraulic 1/6 scale model of the primary system of MYRRHA. This Lead-Bismuth Eutectic (LBE) facility aims at providing further insight into natural and forced circulation flow patterns. However, detailed measurements in liquid metals are very challenging [159], especially from a fundamental research point of view when it comes to gathering data for detailed physical modeling. Moreover, this experimental feedback is very expensive and remains design specific.

To address these issues, a number of modelling approaches are used by nuclear engineers, ranging from the application of analytical and empirical correlations to the use of numerical tools of various complexity. Among these, system thermal-hydraulic (STH) codes are widely used to evaluate safety aspects, and are particularly useful when a fast-running tool is needed to assess plant transients. Even though they can apply 3D modelling, they do not allow

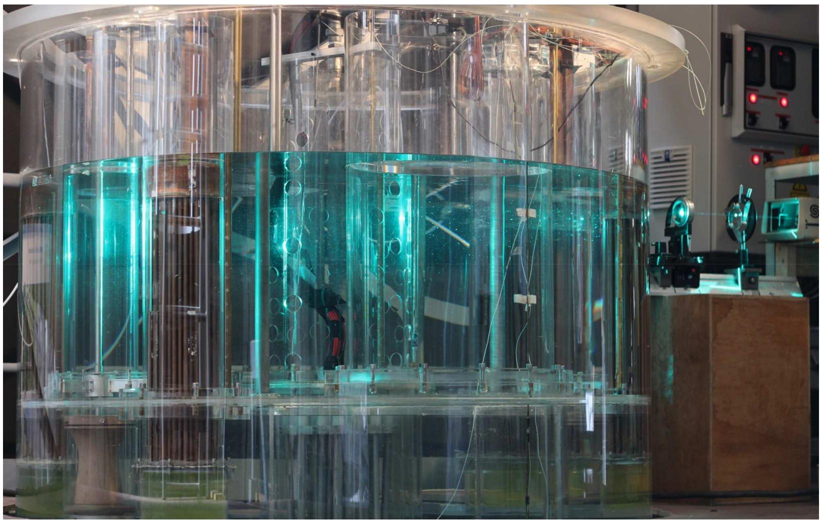

Figure 1.4: *PIV measurements in the MYRRHABelle facility [119].*

to include effects taking place at smaller scales, which becomes problematic in the reactor pool since local three-dimensional effects play a crucial role. Consequently, the complex nature of the flow phenomena that occur in pool type reactors requires the three-dimensional capabilities of Computational Fluid Dynamics (CFD). With the increase in computational power, CFD now becomes an affordable approach even at the scale of a whole reactor pool. A previous benchmark related to the prediction of natural circulation in the French Phenix SFR end-of-life tests [54], demonstrated that CFD could predict the development of pool stratifications, which provided a clear added value over system codes. Nevertheless, a considerable challenge for CFD codes is to properly predict the turbulent heat transfer in liquid metal flows.

1.3 Heat transfer modeling in liquid metals

At reactor scale, CFD users apply Reynolds-averaged Navier Stokes (RANS) methods for flow predictions as a direct computation of all the turbulent scales remains unaffordable at this level. The RANS approach aims at providing a statistical time-averaged description of the flow. However, the averaging time is much larger than any of the turbulent fluctuations and, as a result, the equations that are resolved only describe the evolution of the mean flow quantities. The momentum and thermal turbulent fluctuations are incorporated into the Reynolds stress tensor and turbulent heat fluxes. These require to be modeled appropriately depending on the type of liquid and flow.

Liquid metals are characterized by a very low Prandtl number, Pr, typically ranging from 0.001 to 0.01. This parameter gives the ratio between the molecular momentum diffusivity and the thermal molecular diffusivity, such that

$Pr = \nu/\alpha$. At such low values, the turbulent mixing only becomes larger than the molecular contribution at high Reynolds number, e.g. $Re > 60000$ for $Pr = 0.025$ [49]. This difference in behavior, compared to air with Pr of order unity, can be shown by Direct Numerical Simulation (DNS) of the flow along a channel heated at top and bottom, see Fig. 1.5.

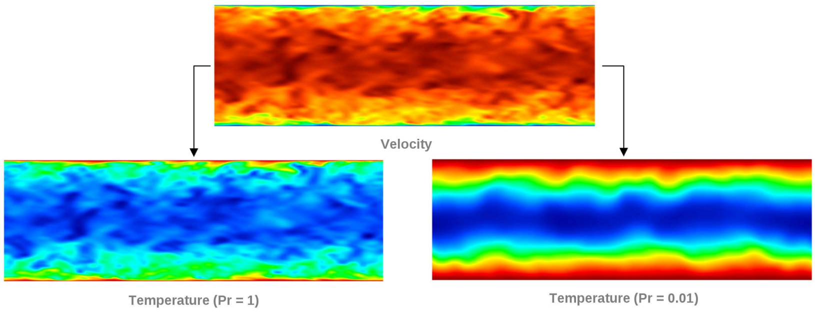

Figure 1.5: *Velocity and temperature field along a heated channel flow [127] for a fluid like air ($Pr \simeq 1$) and a typical liquid metal ($Pr \simeq 0.01$).*

With Prandtl numbers close to unity, the velocity and temperature fields are very similar: wall layers have about the same thickness and their fluctuations are of the same order. Consequently, model developers have mostly assumed that the turbulent heat transfer can be predicted from the knowledge of the turbulent momentum transfer. A proportionality factor, defined as the turbulent Prandtl number, $Pr_t = \nu_t/\alpha_t$, relating turbulent viscosity (ν_t) and turbulent diffusivity (α_t) is introduced. The common approach consists in applying a gradient assumption, thus assuming that the turbulent shear stress is aligned with the vertical gradient of velocity:

$$-\overline{u'v'} = \nu_t \frac{\partial \overline{u}}{\partial y} \, , \tag{1.1}$$

and similarly for the turbulent heat flux:

$$-\overline{T'v'} = \alpha_t \frac{\partial \overline{T}}{\partial y} \, . \tag{1.2}$$

The turbulent Prandtl number is then defined by the turbulent shear stress and turbulent heat flux, and by the gradient of velocity and temperature in the vertical direction:

$$Pr_t = \frac{(-\overline{u'v'})}{\partial \overline{u}/\partial y} \cdot \frac{\partial \overline{T}/\partial y}{(-\overline{T'v'})} \, . \tag{1.3}$$

This implies that, strictly speaking, Pr_t can only be defined in regions where there is a free shear flow or a boundary layer flow (which corresponds to a shear flow with a wall). Indeed, the concept has no physical meaning outside of these areas since ν_t and/or α_t cannot be defined. Moreover, reactor flows involve anisotropic turbulent fluxes and strong buoyancy influences. Consequently, the use of isotropic scalars for ν_t and α_t remains very questionable. Nevertheless, in most codes, Pr_t is simply set to a constant value (e.g. of 0.85). This approach provides reasonable predictions of global parameters such as Nusselt numbers and mean temperature distributions [14] at Prandtl unity. However, this concept, known as the Reynolds analogy, is no longer valid at low Prandtl numbers. Due to the large thermal conductivity, the conductive sub-layer thickens and the conductive heat flux near the walls becomes increasingly important. Thus, there is no similarity between the time-averaged velocity and temperature fields. Moreover, the two fluctuation fields exhibit differences in spatial scales, as illustrated by the energy spectra shown in Fig. 1.6. At Pr around unity, the two spectra have the same distribution and dependance on the Reynolds number, Re; whereas the temperature spectra at low Pr is limited to larger scales, and with reduced energy content due to the increasing thermal diffusivity [51].

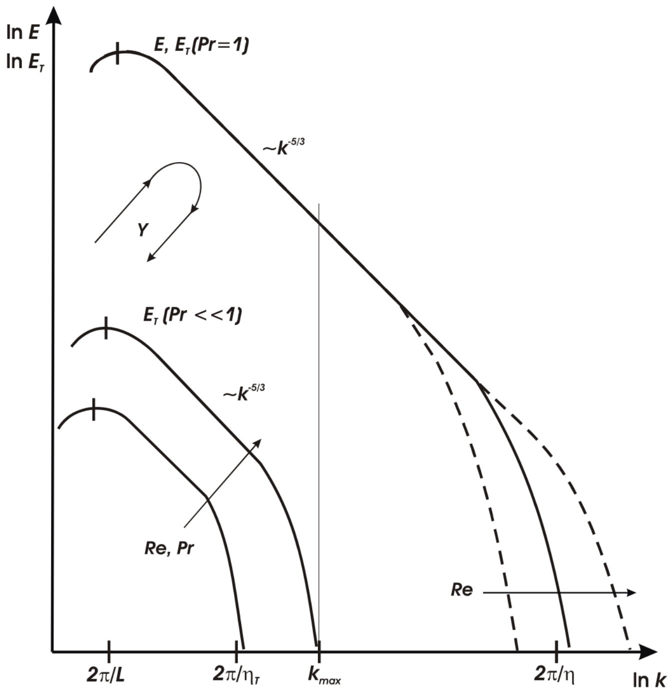

Figure 1.6: *From [48] - Energy spectra for velocity and temperature fluctuations, $E(k)$ and $E_T(k)$ respectively.*

The review of Grötzbach [48] provides a good overview of the issues related to the numerical simulation of turbulent heat transfer in liquid metal flows. Channel flow simulations using DNS [2, 61], and more recently wall-resolved Large Eddy Simulation (LES) results up to $Re_\tau = 2000$ [37] clearly demonstrate that Pr_t has a complex dependence on Re_τ, Pr and the dimensionless wall distance, y^+ (see Fig. 1.7). To represent better the complex behavior of Pr_t, several correlations [29, 62, 170] have been proposed for channel flows, which can greatly improve predictions. One can therefore expect them to be acceptable for flows with a boundary layer character; but in buoyancy influenced cases such as large pools, it is not surprising that the Pr_t concept fails to predict the temperature field and wall heat fluxes [104].

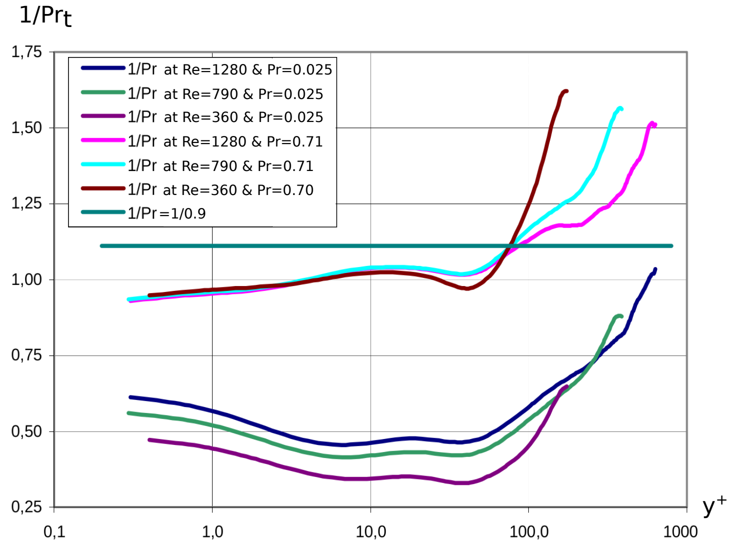

Figure 1.7: *From [48] - Profiles of* $1/Pr_t$ *from channel flow DNS of [2, 61] for* $Re_\tau = 360$, *790*, *1280 and* $Pr = 0.025$ *and 0.71.*

To conclude, it is now well understood that standard conductivity models, which form the base of the Pr_t concept, are inadequate for extended pools where the flow is widely three-dimensional and shows strongly anisotropic heat fluxes. Better suited models for low Prandtl fluids have been proposed by increasing the level of sophistication on the thermal side. As a counter part to the $k - \epsilon$ model for momentum, transport equations are added for the temperature variance, $\overline{T'^2}$, and for its dissipation, ϵ_θ [85]. Such 4-equation models are expected to be suitable at low Pr thanks to the introduction of separate time scales for the velocity and temperature fields. Satisfactory results are obtained in forced flows along cylindrical and square bundle geometries. To account for anisotropic features, a tensorial form is also proposed [33].
Particularly suited to strongly buoyant flows in which the mean flow gradients are near zero or in which counter-gradient fluxes appear, the Algebraic Heat Flux Model (AHFM) gets rid of the gradient assumptions by using an algebraic formulation for the turbulent heat flux itself [64]. A separate transport equation is solved for $\overline{T'^2}$, while the model is adapted so that ϵ_θ is evaluated from a variable time scale ratio to allow for variable Prandtl number [148].

For these more advanced RANS-models to become applicable to HLM reactors, further testing, calibration and validation is necessary on a wide variety of flows. As pointed out already, HLM experiments are unable to determine modeling terms due to insufficient resolution in time and in space. Therefore, DNS simulations or wall-resolved LES, are needed to provide reference data concerning these high order closure terms. Part of those simulations should be performed on somewhat more realistic geometries. Up to now, studies for liquid metal heat transfer (e.g. in FP7 THINS) have mainly relied on developed flow in channels or closed cavities to validate models. The general conclusion from the THINS project highlights the necessity to focus on further validation of the existing models in more complex configurations [148]. Thus, there exists a strong need for reference data in a non-confined environment, that would be more representative of turbulent thermal behaviour of pool flows.

1.4 Objectives and structure of the thesis

The main goal of this PhD thesis is to generate and further analyze high-fidelity data representative of the behaviour of low Prandtl fluids in pool type reactors. By doing so, a key contribution of this work is to improve our physical understanding of the low Prandtl number effects to expect in liquid metal reactors, and retrieve crucial information concerning the way heat is transported across the low Prandtl number coolant.
The outcome of this work is twofold. Firstly, the reference data can be used to assess the performance of existing RANS turbulent heat transfer models. Moreover, by providing further insight into the physical behavior of low Prandtl number flows in pool type configurations, this study can help to further improve these models, which is an essential step towards the ultimate goal that is to propose a model providing reasonable results in all flow regimes present in reactor flows.

The upper plenum of the reactor pool is dominated by the presence of jets that are exiting the core and impacting on the various reactor components (e.g. heat exchangers, in vessel fuel handling machines). These induce regions of strong shear and detached flow, together with important wall interactions. The most meaningful geometry to represent these combined effects is the backward facing step (BFS). Not only does it reproduce the essential flow mechanisms of interest, but it also remains simple and therefore computationally affordable. The sudden expansion forces the flow to separate abruptly, thus forming a free-shear layer which, by entrainment and reattachment at the wall, creates a low velocity recirculation region. Buoyancy effects are generated by heating the step area, which reproduces mixed flow conditions that are very similar to pool flows.

At low Prandtl number, the smallest scales associated to the temperature field are much larger than those related to the velocity field. Thus, a wall-resolved LES approach is chosen for these simulations, since it will be able to fully resolve the temperature fluctuations without requiring a subgrid scale heat flux model. In order to reach the final objective of this thesis, a series of steps have to be accomplished:

- Setting-up of an efficient and flexible inflow turbulence generation method for the LES simulations: further development of the temperature perturbation method (TPM) and validation on a channel flow.

- Carrying-out experiments over a BFS to validate the LES simulations: tests with a transparent gas mixture ($Pr = 0.2$), to obtain velocity statistics by PIV and simultaneous measurements of velocity and temperature.

- Further testing of the optimised TPM on a developing turbulent boundary layer (TBL) in order to properly match the inflow conditions obtained experimentally upstream of the BFS.

- Comparison of the LES simulations and experimental results over the BFS, with particular care on matching quantities between numerics and experiments.

- In depth analysis of the LES results obtained with air, the gas-mixture and LBE: investigation of low Prandtl number effects on the heat transfer in abruptly separated flows.

The present work is divided according to these steps. Chapter 1 introduces the general context and objectives of the thesis. Chapter 2 is dedicated to the development of the optimized TPM. Chapter 3 describes the experimental set-up, i.e. the newly designed MYRTE wind tunnel, the measurement techniques and design of experiments. The dependency of the results on free-stream velocity and also heating effects are investigated. Chapter 4 focuses on applying the optimized TPM to a TBL, representative of non-confined flows. Special care is required to ensure that experimental conditions upstream of the BFS are reproduced in the LES simulations, for a meaningful comparison of the results in Chapter 5. In Chapter 6, the LES data obtained at different Prandtl numbers corresponding to $Pr = 0.71, 0.2$ and 0.025 are analyzed, to provide a better understanding of the role played by the different transport mechanisms at low Prandtl number. Finally, Chapter 7 presents conclusions and perspectives.

Chapter 2

An optimized Temperature Perturbation Method for generating inflow turbulence in LES

2.1 Introduction

The proper specification of turbulent inflow conditions for both LES and DNS remains a considerable challenge. For developing flows, the most straightforward approach is to impose a laminar profile with small perturbations and to compute the transition to turbulence. However, simulating the transition process itself is very costly, and coupling this with a simulation of the downstream turbulent flow would be extremely expensive. The most common approach is to impose an already turbulent flow at the inlet. This too is a difficult task since turbulent flows are coherent in both space and time. Thus, imposing inflow conditions that are physically "almost correct" remains a considerable challenge. The flow needs to adjust until an equilibrium is reached where the governing equations are satisfied. The key requirement for a turbulent inflow technique is to be as "efficient as possible" in order to minimize this recovery length and thus reduce the computational cost.
With the aim of setting-up an efficient LES simulation of the flow over the BFS, this published chapter [25] is dedicated to the problematic related to the generation of realistic inflow turbulence for LES/DNS simulations. All simulations are run using the Open source CFD code OpenFOAM [105] (version 3.0.1). This finite volume code uses a collocated arrangement of the flow variables together with second order accurate spatial and temporal discretisation schemes [69]. It offers a great flexibility to the user that is free to implement or modify any of the two categories of applications: solvers, each designed to solve a specific problem in continuum mechanics; and utilities, that are designed to perform tasks that involve data manipulation. This framework has been chosen by the VKI for its CFD related activities and more specifically in the context of this work, for the development of solvers and models able to handle the complex physics involved in the simulation of liquid metal flows.

The methodology proposed to select the best suited inflow generation technique is described, and based on these conclusions, the temperature perturbation method (TPM) clearly stands out. This alternative technique perturbates the temperature instead of the velocity. It benefits from a much greater flexibility since only first-order statistics are required as input. This makes the TPM particularly convenient since it can be applied without prior knowledge of second order moments or integral length scales. Moreover, the approach is very simple: it consists in seeding the flow with random temperature perturbations which, through a buoyancy triggered mechanism, will induce the creation of turbulent structures. Naturally, this implies that the physical buoyancy effects need to be sufficiently strong. Consequently, the TPM in its current formulation is only applicable to atmospheric flows.

The considerable added value of this work is therefore to fundamentally modify the TPM so that it is no longer restricted to flows that are naturally buoyant. In this novel approach, a perturbation zone is defined at the entrance of the domain, along which an artificial local Richardson number is applied so that buoyancy effects are sufficiently strong to create turbulence. In addition, these effects are modulated appropriately in order to help pre-mix the flow and avoid stratification effects from slowing down the flow recovery. Thanks to this new approach, the optimized TPM can be applied to a wide variety of applications, thus including flows that involve much smaller length scales than in the atmosphere. Moreover, it remains efficient with a flow recovery that is comparable to competing methods, but with the great advantage of only requiring as input the mean inlet velocity profile [25].

Testing of the optimized TPM is carried out in several steps. Firstly, a periodic channel flow is run at a friction velocity Re_τ of 395. The main purpose of this preliminary test case is to obtain the fully developed turbulent state that will serve as reference while testing the inflow technique. Moreover, since no inflow specifications are required, it allows to concentrate on the numerical LES set-up, with the aim of best approaching reference DNS results. Modifications in the wall damping function are proposed so that a physical behavior is retrieved near the wall. As an outcome, guidelines are formulated in terms of numerical settings and suitable level of mesh refinement. Secondly, the TPM is tested on a plane channel flow with inlet/outlet boundary conditions, where the periodic results serve as basis to optimize the TPM according to key governing parameters. Several perturbation functions are applied to modulate these artificial effects, in order to identify the function that most efficiently pre-mixes the flow, thus enabling faster recovery. Comparison of the optimized TPM with competing methods is essential to conclude on its overall performance, in terms of the recovery distances of both the wall shear stress and the Reynolds stresses. This last comparison with respect to the synthetic turbulence generator method of Xie and Castro [174] provides a representative assessment of how efficiently the optimized TPM performes, before applying it later on to a developing Turbulent Boundary Layer (TBL), representative of the inflow conditions arriving at the BFS.

2.2 Turbulent inflow generation techniques

The existing techniques to generate inflow turbulence can be grouped into two main categories: precursor simulation methods and synthetic methods. Among the precursor simulation methods, two variants exist where the first consists in running an auxiliary calculation on a separate domain with periodic inlet-outlet boundary conditions, used for instance in [79] and [118]. The velocity in a section is stored at each time step; it is then fed at the inlet of the main domain that simulates the flow of interest. An important limitation, in addition to the need for an extensive database so that different flow regimes can be simulated, is that this approach is restricted to fully developed flows that rarely occur in reality. Moreover, the auxiliary simulation introduces "spurious" periodicity into the inflow as observed by Spille-Kohoff and Kaltenbach [157].
Cyclic or recycling methods are the second variant; these eliminate the necessity of generating a pre-computed library by placing a cyclic plane in the inflow region of the actual computational domain. In the case of developing boundary layers, Lund et al. [84] proposed a procedure to rescale the velocity profile according to similarity laws before re-introducing it at the inlet. The computational effort of this second approach is reduced but, as precursor methods, the solution is affected by contamination due to periodicity [150]. Attempts to remove these effects have been made by superimposing random perturbations, but the results remain dependent on the characteristics of these random fluctuations.

Synthetic turbulence methods generate a pseudo-random coherent field of fluctuating velocities that tries to reproduce certain aspects of a turbulent flow. This requires the velocity field to be correlated both in time and space, with given first and second order moments, an assigned spectra, and the appropriate phase information between modes. While the moments and the spectra can be closely matched thanks to stochastic methods, the phase information strongly depends on the type of flow and location in the flow. It is therefore more difficult to specify but nevertheless crucial since the structure and shape of the turbulent eddies depend on it.
Different techniques exist to generate these random perturbations, such as proper orthogonal decomposition analysis (POD), Fourier decomposition, digital filter methods or Synthetic Eddy Method (SEM). POD techniques take as input instantaneous realizations of the flow acquired experimentally and extract basis functions that are optimal to represent the data and reconstruct turbulence. Perret et al. [115] used this method based on stereoscopic PIV measurements to provide inlet conditions for the LES of a mixing layer.
The Fourier or spectral methods use a decomposition of the signal into Fourier modes. Based on the work of Kraichnan [73], Smirnov et al. [153] proposed the random flow generation (RFG) technique that is implemented in Fluent as the Spectral Synthesizer [9]. It is able to generate an inhomogeneous and anisotropic turbulent flow, provided that an anisotropic velocity correlation tensor is specified. Modifications of the RFG method have been proposed by Keating et al. [63], adding a forcing term to amplify/damp velocity fluctua-

tions in the wall-normal direction. Although the establishment length of the Reynolds stresses could be reduced by two along the channel down to about 10 halfchannel heights (δ), the turbulent kinetic energy needed a longer distance to reach its fully-developed value.
Another option is to use digital filtering. Xie and Castro [174] developed a digital filter that uses exponential functions in time and space for spatially developing boundary layers. LES of a plane channel provided satisfactory validation of the technique. In order to reduce the artificial pressure fluctuations introduced by the original turbulent inflow, Kim et al. [67] developed a divergence free version. This modification resulted in significantly reduced pressure fluctuations; however the recovery length (x_r) for the skin friction coefficient for the channel simulation was increased to $16\,\delta$ instead of 10 with the original method of Xie and Castro [174].
Jarrin [58] proposed a synthetic eddy method (SEM) which creates velocity fluctuations by superposing eddies with random position and intensity. The author concluded that 15 δ were needed for the flow to recover equilibrium along a plane channel. Poletto et al. [121] derived a divergence free SEM (DFSEM) by modifying the shape function in the velocity computation. As a result, pressure fluctuations were almost eliminated while the recovery length along the channel was reduced by 33 % compared to the original method of Jarrin [58]. This latest reference also proposes a comprehensive review of several other methods to generate inflow turbulence, such as mixed methods that combine Fourier decomposition and digital filtering, forcing techniques or immersed boundary methods.

The important characteristics to consider while assessing turbulent inflow methods are the following:

1. What are the inlet inputs required by the method ?
2. Is the method divergence free, thus avoiding additional artificial pressure fluctuations ?
3. What is the skin friction recovery length needed to reach equilibrium ?

These questions are addressed in Table 2.1 for the main numerical methods and authors cited previously. The different inlet parameters are denoted as $\overline{U}$ for the mean velocity, $\overline{u_i'u_j'}$ for the Reynolds stresses, I_{ij} for the integral length scales and $\overline{k}$ for the turbulent kinetic energy.

To conclude, although flow recovery may be reduced to about $10\,\delta$ while satisfying divergence-free conditions, all of these turbulent inflow methods require *a priori* detailed information about the flow (i.e., length scales, anisotropy or turbulence levels); something that is unknown in a majority of cases. The purpose of the TPM introduced in the following section is to propose a simpler approach that only requires first order statistics, thus making it easily applicable to a variety of flows.

Method	Author	Inputs	Div. free	x_r
Digital Filter	Xie and Castro [174]	$\overline{U}$, $\overline{u_i' u_j'}$, I_{ij}	no	$10\,\delta$
	Kim et al. [67]		yes	$16\,\delta$
Synthetic Eddy	Jarrin [58]	$\overline{U}$, $\overline{u_i' u_j'}$, I_{ij}, $\overline{k}$	no	$15\,\delta$
	Poletto et al. [121]		yes	$10\,\delta$
Fourier	Smirnov et al. [153]	$\overline{U}$, $\overline{u_i' u_j'}$	yes	$20\,\delta$
(+forcing)	Keating et al. [63]		yes	$10\,\delta$

Table 2.1: *Overview of turbulent inflow methods.*

2.3 Numerical methodology

2.3.1 The temperature perturbation method

The shortcomings of the existing turbulent inflow methods highlighted in Section 2.2 have motivated the development of alternative approaches that would be less complex and more flexible. In the frame of atmospheric boundary simulations, a new method was introduced [94] that is based on the inclusion of random temperature perturbations. This technique relies on the principle that the seeded perturbations help to speed up turbulence generation by inducing local buoyancy effects. These vertical accelerations induce the creation of three-dimensional motions that eventually form turbulent structures. This method presents major advantages over the classical velocity perturbations. Instead of trying to impose realistic turbulence as boundary condition, turbulence is triggered through buoyancy, hence making the process naturally divergence-free. Moreover, it requires very limited information regarding the inlet flow specifications.
The temperature perturbations of Mirocha et al. [86] were sinusoidal in space and varied in size as a function of the model grid spacing. To limit their correlated aspect, the sign of the perturbations were reversed at specified frequencies. This approach was tested on a developing atmospheric boundary layer over a flat terrain. While encouraging results were obtained, exhibiting an accelerated development of turbulence compared to natural transition, further testing of the concept was required.

Thorough testing of the technique was carried out by Muñoz-Esparza [94] summarized in [95]. Four new approaches based on the temperature perturbation concept were proposed: spectral inertial subrange perturbations, spectral low wavelengths perturbations, point perturbations and cell perturbations. These were tested on a convective developing boundary layer and applied to the first three rows of cells located along the inlet boundary. The first two approaches perturbate the spectral distribution of temperature, while the last two impose spatial distributions; the spectral inertial subrange approach consists in perturbating essentially three modes that are located in the inertial subrange, in order to develop faster the energy-containing eddies. Similarly to a synthetic method,

the spectral low wavelengths approach perturbates randomly the spectra obtained from a periodic simulation. The point and cell perturbation approaches consist in randomly perturbating the temperature in each cell, or group of cells, respectively.
These four propositions were assessed by comparing their spectral behavior compared to a reference fully-developed periodic simulation. Results highlighted a spiky velocity spectrum in the case of the point perturbation method, suggesting that changing the random perturbations from one grid cell to another tends to excite the harmonics of the fundamental wavelength. The spectral inertial subrange method provided an enhanced energy content for the wavenumbers contained within the interval delimited by the three perturbated modes. These first two methods were clearly outperformed by the spectral low wavelengths and cell perturbation methods. Although larger levels appeared at intermediate wavelengths, their spectra were found to be already close to the periodic inlet/outlet simulation after only 15 x/z_{i0}, z_{i0} being the temperature inversion height that limits the boundary layer height. Very similar energy distributions were obtained at 30 x/z_{i0}. The cell perturbation was preferred over the spectral low wavelengths as it requires less parallel communications, thus limiting the computational cost. It is therefore chosen in this study to investigate the generation of turbulent inflow conditions for LES simulations.

2.3.2 Application to wall bounded flows

2.3.2.1 Governing equations

Up to now, the temperature perturbation method has been applied to atmospheric boundary layer flows using the Weather Research and Forecasting (WRF) LES model [152]. The objective of this study is to apply the concept to incompressible wall bounded flows. The solver of OpenFOAM *buoyantBoussinesqFoam* is chosen to accommodate this technique as it models the buoyancy effects that will provoke the formation of turbulent structures by converting the seeded temperature gradients into velocity perturbations. The equations used by the solver are described hereafter. The constant-density filtered (LES) continuity equation is

$$\frac{\partial \overline{u}_j}{\partial x_j} = 0 \,. \tag{2.1}$$

The constant-density (except in the gravity term) filtered momentum equation is

$$\frac{\partial \overline{u}_i}{\partial t} + \frac{\partial}{\partial x_j}(\overline{\overline{u}_i \overline{u}_j}) = -\frac{\partial}{\partial x_i}\left(\frac{\overline{p}}{\rho_0}\right) + \frac{\partial}{\partial x_j}(\overline{\tau}_{ij} + \overline{\sigma}_{ij}^{sgs}) + \frac{\overline{\rho}}{\rho_0} g_i \,, \tag{2.2}$$

where $g_i = [0, g, 0]$ is the gravity vector and $\overline{\tau}_{ij}$ is the shear stress tensor due to molecular viscosity

$$\overline{\tau}_{ij} = \nu_0 \left(\frac{\partial \overline{u}_i}{\partial x_j} + \frac{\partial \overline{u}_j}{\partial x_i} - \frac{2}{3}\frac{\partial \overline{u}_k}{\partial x_k}\delta_{ij} \right) \,, \tag{2.3}$$

where ν_0 is the molecular kinematic viscosity. The LES sub-grid scale stress tensor is given by:

$$\overline{\sigma}_{ij}^{sgs} = \overline{\overline{u}_i \overline{u}_j} - \overline{u_i u_j}. \tag{2.4}$$

It can be divided into a deviatoric part, R_{ij}^d, and an isotropic part, where $\overline{k}^{sgs} = -\frac{1}{2}\overline{\sigma}_{kk}^{sgs}$ is the LES sub-grid scale kinetic energy:

$$\overline{\sigma}_{ij}^{sgs} = R_{ij}^d + \frac{2}{3}\,\overline{k}^{sgs}\,\delta_{ij}\,. \tag{2.5}$$

Note that, in OpenFOAM, the pressure is always normalized by the density for the incompressible solvers, denoted as $\overline{P} \triangleq \frac{\overline{p}}{\rho_0}$ in $[m^2/s^2]$, while the isotropic part of $\overline{\sigma}_{ij}^{sgs}$ is also placed in the pressure term. Similarly, a so-called kinematic density is defined as $\overline{\rho}_k = \frac{\overline{\rho}}{\rho_0}$. Eq. (2.2) can be rewritten as follows:

$$\begin{aligned} \frac{\partial \overline{u}_i}{\partial t} + \frac{\partial}{\partial x_j}(\overline{\overline{u}_i \overline{u}_j}) = & - \frac{\partial}{\partial x_i}\left(\overline{P} + \frac{2}{3}\,\overline{k}^{sgs}\,\delta_{ij}\right) \\ & + \frac{\partial}{\partial x_j}\left[\nu_0\left(\frac{\partial \overline{u}_i}{\partial x_j} + \frac{\partial \overline{u}_j}{\partial x_i} - \frac{2}{3}\frac{\partial \overline{u}_k}{\partial x_k}\,\delta_{ij}\right) + R_{ij}^d\right] \\ & + g_i\,\overline{\rho}_k\,. \end{aligned} \tag{2.6}$$

The deviatoric part of the subgrid-scale stress tensor is modeled as

$$R_{ij}^d = \nu_{sgs}\left(\frac{\partial \overline{u}_i}{\partial x_j} + \frac{\partial \overline{u}_j}{\partial x_i} - \frac{2}{3}\frac{\partial \overline{u}_k}{\partial x_k}\,\delta_{ij}\right)\,, \tag{2.7}$$

where ν_{sgs} is the effective sub-grid scale kinematic viscosity. Substituting these different terms into Eq. (2.6) yields

$$\begin{aligned} \frac{\partial \overline{u}_i}{\partial t} + \frac{\partial}{\partial x_j}(\overline{\overline{u}_i \overline{u}_j}) & - \frac{\partial}{\partial x_j}\left[\nu_{eff}\left(\frac{\partial \overline{u}_i}{\partial x_j} + \frac{\partial \overline{u}_j}{\partial x_i} - \frac{2}{3}\frac{\partial \overline{u}_k}{\partial x_k}\right)\right] \\ = & - \frac{\partial}{\partial x_i}\left(\overline{P} + \frac{2}{3}\overline{k}^{sgs}\,\delta_{ij}\right) + g_i\,\overline{\rho}_k\,, \end{aligned} \tag{2.8}$$

where $\nu_{eff} = \nu_0 + \nu_{sgs}$ is the effective kinematic viscosity. After manipulating the right-hand side of Eq. (2.8), a kinematic pressure, $\overline{P}_k$, defined as $\overline{P}_k = \overline{P} - \overline{\rho_k}\,g_i\,x_i$ is introduced. For simplicity, let us define a so-called modified kinematic pressure, $\tilde{P} = \overline{P}_k + \frac{2}{3}\,\overline{k}^{sgs}\delta_{ij}$. Assuming that $\beta\left(\overline{T} - T_0\right) << 1$, the the Boussinesq approximation is applied, yielding

$$\overline{\rho}_k = 1 + \frac{(\overline{\rho} - \rho_0)}{\rho_0} = 1 - \beta\left(\overline{T} - T_0\right)\,, \tag{2.9}$$

where β is the thermal expansion coefficient in $[K^{-1}]$, T is the temperature in $[K]$ and T_0 is a reference temperature in $[K]$. The equation that is finally resolved by the solver is

$$\begin{aligned}\frac{\partial \overline{u}_i}{\partial t} + \frac{\partial}{\partial x_j}(\overline{\overline{u}_i \overline{u}_j}) &- \frac{\partial}{\partial x_j}\left[\nu_{eff}\left(\frac{\partial \overline{u}_i}{\partial x_j} + \frac{\partial \overline{u}_j}{\partial x_i} - \frac{2}{3}\frac{\partial \overline{u}_k}{\partial x_k}\right)\right] \\ &= -\frac{\partial \tilde{P}}{\partial x_i} + g_i\, x_i\, \beta\, \frac{\partial\left(\overline{T} - T_0\right)}{\partial x_j} \; . \end{aligned} \tag{2.10}$$

It should be noted that the last term of Eq. (2.10) will induce buoyancy effects in the presence of temperature variations, that would result in thermal stratification if sufficiently strong. In the case of a channel, this could therefore introduce asymmetry between the upper and lower parts.

The filtered temperature equation can be written as

$$\frac{\partial \overline{T}}{\partial t} + \frac{\partial}{\partial x_j}(\overline{\overline{T}\overline{u}_j}) = \frac{\partial}{\partial x_j}\left[\frac{k_0}{\rho_0\, c_p}\frac{\partial \overline{T}}{\partial x_j}\right] + \frac{\partial}{\partial x_j}\left(\frac{k_{sgs}}{\rho_0\, c_p}\frac{\partial \overline{T}}{\partial x_j}\right) \; . \tag{2.11}$$

The right-hand side can be rearranged by recalling that $Pr = c_p\, \mu_0/\lambda_0$ and by defining that $Pr_{sgs} = c_p\, \mu_{sgs}/\lambda_{sgs}$, such that Eq. (2.11) becomes

$$\frac{\partial \overline{T}}{\partial t} + \frac{\partial}{\partial x_j}(\overline{\overline{T}\overline{u}_j}) = \frac{\partial}{\partial x_j}\left[\left(\frac{\nu_0}{Pr} + \frac{\nu_{sgs}}{Pr_{sgs}}\right)\frac{\partial \overline{T}}{\partial x_j}\right] \; . \tag{2.12}$$

The turbulent and molecular contributions to the heat transfer diffusivity are combined as

$$\alpha_{eff} = \frac{\nu_{sgs}}{Pr_{sgs}} + \frac{\nu_0}{Pr} \; , \tag{2.13}$$

with α denoting the thermal diffusivity. As is usually the case in LES, one assumes that Pr_{sgs} is constant. It is here taken as $Pr_{sgs} = 1$.

2.3.2.2 Similarity parameters

The non-dimensional form of these governing equations can be obtained by scaling the variables as follows:

$$\begin{aligned}\overline{u}_i^* = \overline{u}_i/U_0;\; x_i^* = x_i/L_0;\; t^* = t\, U_0/L_0;\; \tilde{P}^* = \tilde{P}/U_0^2; \\ (\Delta\overline{T})^* = (\overline{T} - T_0)/(\Delta T)_0;\; g_i^* = g_i/g_0 \; , \end{aligned} \tag{2.14}$$

with U_0, L_0, $(\Delta T)_0$ and g_0 that are reference quantities defining the problem.

This results in the dimensionless form of Eq. (2.10) for the momentum equation:

$$
\begin{aligned}
\frac{\partial \overline{u}_i^*}{\partial t^*} + \frac{\partial}{\partial x_j^*}(\overline{\overline{u}_i^* \overline{u}_j^*}) &= \frac{1}{Re}\frac{\partial}{\partial x_j^*}\left[\left(1+\frac{\nu_{sgs}}{\nu_0}\right)\left(\frac{\partial \overline{u}_i^*}{\partial x_j^*}+\frac{\partial \overline{u}_j^*}{\partial x_i^*}-\frac{2}{3}\frac{\partial \overline{u}_k^*}{\partial x_k^*}\right)\right] \\
&\quad -\frac{\partial \tilde{P}^*}{\partial x_i^*} + Ri\frac{\partial\left(\Delta\overline{T}\right)^*}{\partial x_j^*} g_i^*\, x_i^* \,, \qquad (2.15)
\end{aligned}
$$

where the Reynolds number, Re, gives the ratio between advective and viscous forces:

$$
Re = \frac{U_0\, L_0}{\nu_0} \,, \qquad (2.16)
$$

and the Richardson number, Ri, gives the ratio between inertial and convective forces:

$$
Ri = \frac{g_0\, \beta(\Delta T)_0\, L_0}{U_0^2} \,. \qquad (2.17)
$$

Similarly for the temperature equation, one obtains its dimensionless form as

$$
\frac{\partial \overline{T}^*}{\partial t^*} + \frac{\partial}{\partial x_j^*}\left(\overline{\overline{T}^* \overline{u}_j^*}\right) = \frac{1}{Pe}\frac{\partial}{\partial x_j^*}\left[\left(1+\frac{\alpha_{sgs}}{\alpha_0}\right)\frac{\partial \overline{T}^*}{\partial x_j^*}\right] \,, \qquad (2.18)
$$

where the Peclet number, Pe, is defined as

$$
Pe = Re\, Pr = \frac{U_0\, L_0}{\alpha_0} \,, \qquad (2.19)
$$

with the Prandtl number, Pr, giving the ratio between the momentum diffusivity and the thermal diffusivity, previously defined.

Referring to the momentum equation Eq. (2.15), one understands how the inclusion of temperature gradients can generate a buoyancy force that will induce the development of turbulent structures. The importance of these buoyancy effects are governed by the Richardson number, identified as a key parameter of the cell perturbation method.

One may note that the overline notation, used to denote filtered quantities in the above equations, will be used hereafter for averaged quantities.

2.3.3 Computational settings

The cell perturbation method proposed by Muñoz-Esparza [95] imposes random temperature perturbations along square bidimensional groups of cells. Through buoyancy effects, these have shown to induce the formation of three-dimensional turbulent structures. This research was extended by the same author [96] with the objective of identifying and optimizing the governing parameters in order to reduce the recovery length. These recommendations serve as main guidelines in this work, in order to help define the key parameters of the TPM.

2.3.3.1 Optimum perturbation time scale

The perturbation time scale defines the frequency at which the perturbation values are changed. Thus, a dimensionless perturbation time scale (Γ) is proposed by Muñoz-Esparza [96], based on the perturbation time step Δt_p:

$$\Gamma = \frac{\Delta t_p \, U_1}{d_c} \, . \tag{2.20}$$

This parameter represents the time taken by the flow to be advected across a perturbation cell in the most adverse flow conditions. This is considering that the flow direction is along the diagonal of the perturbation cell, $d_c = \sqrt{2}\, n_c \, \Delta x$, with n_c the number of grid cells per perturbation cell side and Δx the cell size in the streamwise direction, for a velocity U_1 taken at the first vertical grid point.
The influence of this parameter on the results was investigated in [96], revealing that the performance of the method can be optimized by leaving sufficient time for the flow to assimilate the perturbations before imposing the next perturbations, such that $\Gamma \simeq 1$. Indeed, for insufficient times ($\Gamma << 1$) the triggered instabilities were amplified, resulting in too much energy in the production range and longer distances to redistribute this energy content. If, on the contrary, $\Gamma >> 1$, the flow showed signs of loosing memory from one perturbation to the next, inducing alternating laminar and turbulent patches. Consequently, a value of $\Gamma = 1$ will here be taken to calculate the perturbation frequency.

2.3.3.2 Spatial distribution of the perturbations

The temperature perturbations are distributed over a so-called "seeding zone" that starts from the inflow boundary. A uniform value is randomly attributed to tridimensional perturbation cells of $8\,\Delta x$ in the streamwise (x) direction and $8\,\Delta z$ in the wall-normal (y) and spanwise (z) directions. The seeding zone of length L_s, shown in Fig. 2.1, extends three perturbation cells parallel to the inflow boundary, thus covering 24 grid cells in the streamwise direction.

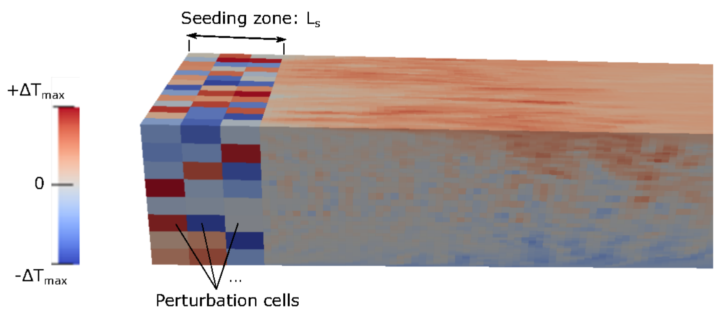

Figure 2.1: *3D contours of temperature, cell average values obtained with $\beta\,(x) = +linX$.*

The perturbation cell size is chosen based on the study of Muñoz-Esparza [96] that recommends choosing a minimum size of $8\,\Delta x$ to avoid the energy from rapidly dissipating when applied to higher wavelengths. Higher sizes were also tested to study the impact of the perturbation cell size on the performance of the method. Although energy is placed into different scales, similar turbulent structures were observed in the flow, resulting in comparable recovery lengths. Therefore, the perturbation cell size is not considered as critical and will be kept constant throughout this study.

A major difference compared to the previous application concerns the length scales involved. In atmospheric flows, even at a microscale level these may range from an order of magnitude of 10^{-1} to 10^{2} m, such that buoyancy effects are naturally present in these types of flows, with a typical Richardson number of $Ri = 0.3$. Wall bounded flows though involve smaller length scales ($< 10^{-1}$ m) and typically for air and limited gradients ($\Delta T < 1\,K$), a plane channel flow simulation at $Re_\tau = 395$ is characterized by $Ri << 1$ and hence negligible buoyancy effects. Let us recall how the buoyancy force of Eq. (2.10) is defined in the current framework:

$$-\,\beta\left(\overline{T} - T_0\right) g_i \;\Leftrightarrow\; -Ri\left(\Delta\overline{T}\right)^{*} g_i^{*}\;. \tag{2.21}$$

Since the purpose of the temperature method is to generate inflow turbulence without affecting the downstream flow in a significant way, some modifications of the temperature perturbation method are needed to fulfill both of these criteria. In particular, the buoyancy force needs to play an active role only close to the inflow region. To fulfill this requirement, the solution is to manipulate the local thermal expansion ratio (β field), or equivalently the local Richardson number (Ri field), by artificially increasing its value within a so-called perturbation zone near the inflow. This will enable the seeded perturbations to induce vertical accelerations that are sufficient to trigger the onset of three-dimensional motions and eventually accelerate the formation of turbulent structures. By setting Ri back to zero outside of the perturbation zone, these effects will be rendered inactive downstream. The maximum local artificial Richardson number that is applied within the fully active zone is defined according to guidelines formulated in [96]. Although it will be varied later, a value of 0.2 is used here initially, representative of a mixed convection regime.

2.4 Fully developed turbulent channel flow

2.4.1 Initial set-up and reference results

A LES simulation of a periodic inlet/outlet channel flow, referred to as "case PBC", is first run as preliminary test case. The Reynolds number is set to $Re_\tau = 395$ based on the channel half height, δ, and the friction velocity, u_τ. The problem domain consists of two infinite parallel plates that lead to the development of an equilibrium turbulent flow. It is approximated by a finite sub-domain to which periodic boundary conditions are applied in the streamwise and spanwise directions. For this simplification to remain acceptable, these boundaries should be sufficiently far apart to be able to contain the largest turbulent eddy structures. Considering a channel half height δ, a classical domain size of $L_x \times L_y \times L_z = 2\pi\delta \times 2\delta \times \pi\delta$ is taken (ref. Fig. 2.2).

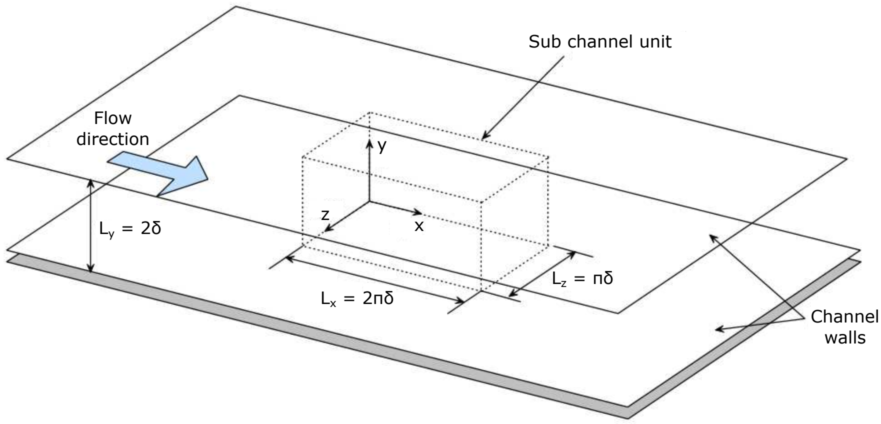

Figure 2.2: *Problem domain for the channel flow test case.*

The main purpose of this preliminary simulation is to obtain a fully developed turbulent solution that provides a straightforward validation while testing the TPM. The flow is driven by a stream-wise pressure gradient term, F_i, that is added to the streamwise momentum equation. To allow control of the friction Reynolds number, $Re_\tau = \frac{u_\tau\,\delta}{\nu}$, the value of the term $F_i = -\frac{dP_f}{dx}\,n_x$ is fixed to a constant. Consequently, the mass flux is adapting at every time step in order to keep the pressure gradient constant. By applying a global force balance on the channel, one obtains:

$$2\,\delta\,L_z\,(\rho\,F_1\,L_x) = 2\,(L_z\,L_x)\,\overline{\tau}_w \;\Leftrightarrow\; \rho\,F_1\,\delta = \overline{\tau}_w\;, \tag{2.22}$$

where $\overline{\tau}_w$ is the wall shear stress. It can be related to the frictional velocity by $\overline{\tau}_w = \rho\,\overline{u_\tau}^2$, which yields:

$$F_1 = \frac{\overline{u_\tau}^2}{\delta}\;. \tag{2.23}$$

The number of grid points for the LES is $N_x \times N_y \times N_z = 62 \times 80 \times 70$. The mesh is uniform in the streamwise and spanwise directions with resolutions of $\Delta x^+ = 39.5$ and $\Delta z^+ = 19.8$ respectively. A vertical stretching is required in the wall-normal direction in order to fully resolve the viscous effects at the wall while limiting the mesh size. As shown in Appendix A.2, the use of a stretching law in order to limit the maximum mesh size has no added value compared to simply applying a constant expansion ratio. A value of 1.1 is used, resulting in a first cell center at $y^+ = 0.9$. All quantities denoted by the superscript

$^+$ are non-dimensionalized appropriately using the friction velocity u_τ, as for instance the wall distance:

$$y^+ = \frac{y\, u_\tau}{\nu} \, . \tag{2.24}$$

The Smagorinsky sub-grid scale model is applied with a coefficient $C_s = 0.065$ [87] combined with a van Driest near wall damping (ref. Section 2.4.2). It is worth noting that the WALE model [98] was tested at the beginning of the project (2015), based on the version v2.3 released by OpenFOAM. However, the results were far from the reference, thus suggesting that the model was not correctly implemented at the time. Although it would perform better in a laminar shear flow, for turbulent flows, the WALE model would not have any added value compared to the Smagorinsky model with proper wall damping (model coefficient to be adjusted in both cases). Consequently, the Smagorinsky model was conserved throughout this work.
A second order implicit scheme is used for the time discretization and the time step is adjusted to ensure that the CFL number remains less than unity. A second order central discretization scheme is used for space discretization. The flow is solved using the buoyant incompressible solver of OpenFOAM, that is later modified to accomodate the TPM. Naturally, no buoyancy effects are present since the flow remains isothermal. The Poisson equation is solved so as to satisfy the continuity equation. It applies the PISO algorithm for pressure-velocity coupling, with two pressure corrector steps in this case.

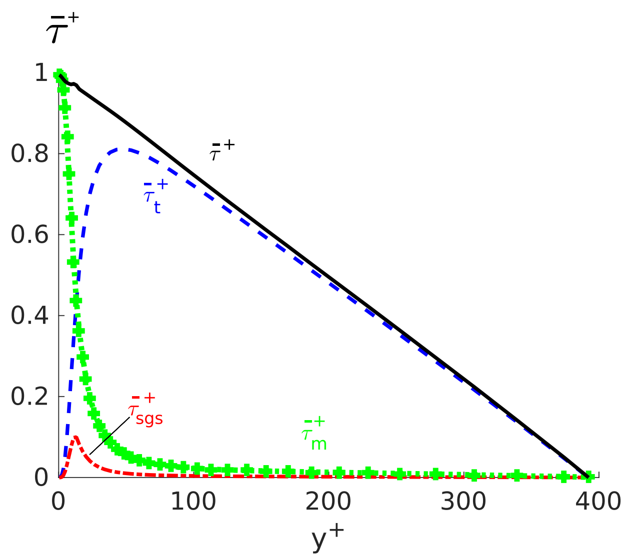

Figure 2.3: *Mean stress profiles obtained by LES for the periodic channel flow at $Re_\tau = 395$.*

The statistical convergence of the data can be assessed by looking at the shear stress decomposition shown in Fig. 2.3, where all shear stresses are non-dimensionalized by the wall shear stress $\overline{\tau}_w$. The mean viscous stress is given by $\overline{\tau}_m^+ = d\overline{u}^+/dy^+$, while the mean turbulent shear stress is expressed as $\overline{\tau}_t^+ = -\overline{u'v'}^+$ and $\overline{\tau}_{sgs}^+$ represents the mean SGS stress. The total shear stress, $\overline{\tau}^+ = \overline{\tau}_m^+ + \overline{\tau}_t^+ + \overline{\tau}_{sgs}^+$, should indeed decrease linearly across the channel, from a maximum value at the wall to zero at the centre. As the flow is turbulent, the main contribution across the channel comes from the mean turbulent shear stress, while the mean viscous stress is mostly negligible. The mean stress due to the SGS model acts very slightly on the large scales in the near-wall region, where it is seen to participate in the mean momentum exchange.

Results obtained from "case PBC" for the mean velocity and Reynolds stress profiles are compared with reference DNS data [92] in Fig. 2.4. As commonly observed in LES simulations with similar grid resolution [67], the mean velocity is slightly over-predicted in the center of the channel, while $\overline{u'u'}^+$ is over-predicted near the wall. On the contrary $\overline{v'v'}^+$ is under-predicted in the near wall region [172].

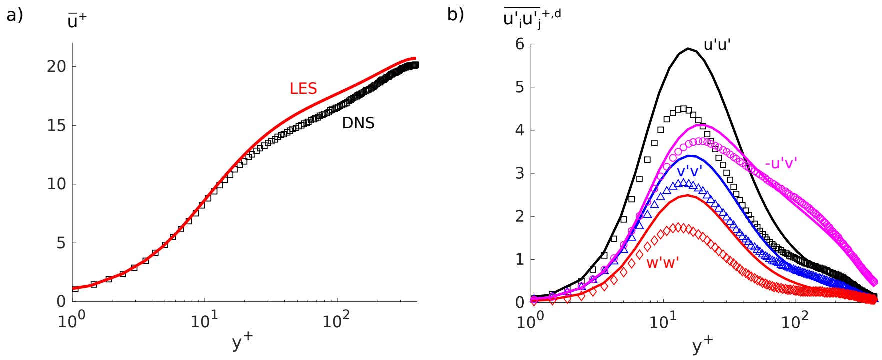

Figure 2.4: *Profiles obtained from "case PBC" a) mean velocity b) Reynolds stresses. Here, deviatoric part for the diagonal elements: i.e.* $\overline{u'u'}^d = \overline{u'u'} - \frac{1}{3}(\overline{u'u'} + \overline{v'v'} + \overline{w'w'})$*, etc. LES results (lines) and DNS data [92] (symbols).*

However, the quality of the LES results remains satisfactory and, despite these differences, the primary aim is to test the TPM at a reasonable cost. Most importantly, "case PBC" remains the reference for the present turbulent inflow channel, the essential point being to conserve identical numerical settings. The results obtained with this initial set-up are therefore taken as reference while testing the TPM; the Reynolds stresses of Fig. 2.4 b) will be the target while assessing the streamwise evolution of the second moment statistics obtained with the TPM.

Nevertheless, the periodic channel flow is the ideal test case to investigate the sensitivity of the LES with respect to key aspects such as the SGS parameters or the mesh resolution (see Appendix D). This will later serve as guidelines while setting-up the LES of the experimental BFS.

2.4.2 Near-wall behavior of eddy-viscosity LES models

The high-resolution LES that is performed here ensures that the energy carrying eddies are fully-resolved up to the wall. The smallest scales require a subgrid scale stress model, and the Smagorinsky model with constant coefficient is used for this purpose. The unknown residual stress tensor is related to the strain rate tensor, S_{ij}, through an eddy viscosity that is given by:

$$\nu_{sgs} = (C_s \Delta)^2 |\overline{S}| \,, \tag{2.25}$$

where the filter width is the cube-root of the cell volume: $\Delta = \sqrt[3]{\Delta x \, \Delta y \, \Delta z}$ and the norm of the strain rate tensor is given by $|\overline{S}| = \sqrt{2 S_{ij} \, S_{ij}}$. Although relatively successful, the Smagorinsky model is not without problems and several modifications are required to simulate wall-bounded flows. One of the serious shortcomings of the model is that the coefficient C_s is not universal, and requires to be changed depending on the type of flow and mesh resolution [145]. Furthermore, the standard model is nonzero at the wall, which is contrary to the notion that the eddy viscosity should be zero where there is no turbulence. Thus, it must be supplemented at the wall by an empirical wall function. The turbulent viscosity can be damped using a combination of a mixing length minimum function, and a viscosity damping function:

$$\nu_{sgs} = min(l_{mix}, f_\mu \, C_s \, \Delta)^2 |\overline{S}| \,, \tag{2.26}$$

By default, the damping function f_μ is 1 in OpenFOAM, and the mixing length is related to the mesh size Δ. A damping function can be specified by the user. A function that has been widely used to reduce the near wall eddy viscosity is the Van Driest damping [166], defined as:

$$f_\mu = 1 - e^{-y^+/A^+} \,, \tag{2.27}$$

where A^+ is a coefficient usually set to 25. Nevertheless, the correct asymptotic behavior is not retrieved since the subgrid viscosity should scale as $(y^+)^3$ in the near-wall region. Therefore, Piomelli [117] proposed an alternate form:

$$f_\mu = \sqrt{1 - e^{(-y^+/A^+)^3}} \,. \tag{2.28}$$

The influence of these different approaches on the near-wall behavior of the eddy viscosity is investigated in Fig. 2.5, where the default case without any damping appears as *noDamp*. It is worth noting that, in OpenFOAM, the van Driest damping is implemented differently, and the variable Δ of Eq. (2.25) is replaced by the wall distance, y. This naturally results in a different near wall behavior, denoted as $vanD_{OF}$, compared to the original formulation, referred to as $vanD_{orig}$. This latest implementation behaves as expected, with ν_{sgs} that decreases as $(y^+)^2$. The Piomelli damping, *piom*, is also added to the code and results in the proper behavior with a slope of $(y^+)^3$.
Let us now examine the influence of the damping function compared to the LES results obtained previously with $vanD_{OF}$. The near-wall behavior has a limited effect on the mean velocity profiles that are plotted in Fig. 2.6. However, there is a noticeable impact on the Reynolds stresses shown in Fig. 2.7.

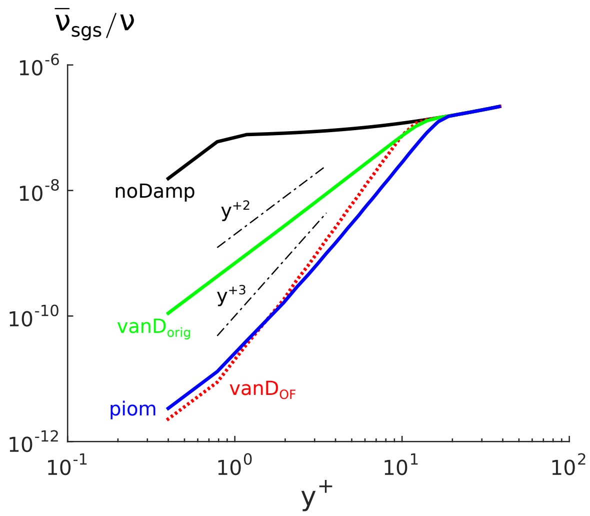

Figure 2.5: *Effect of the near-wall damping on the eddy viscosity.*

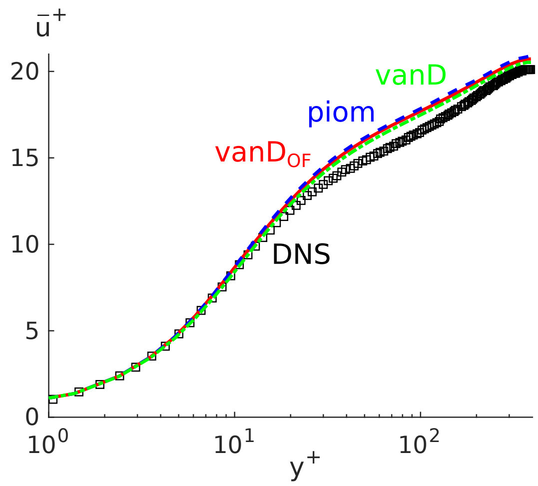

Figure 2.6: *Influence of the near-wall damping on the mean velocity profile.*

Although the differences observed between the OF version of van Driest and the Piomelli damping in Fig. 2.5 are limited to the region where $y^+ \simeq 5-20$, this greatly improves the prediction of all three normal stresses. The improvement on the shear stress is less obvious; the LES now under-estimates this quantity but the overall shape of the profile is better captured. To conclude, it is clearly beneficial to use the newly implemented Piomelli damping function for the LES simulations that will be carried out in this work. By reproducing the correct behavior in the near-wall region, the Reynolds stresses are better predicted and a good agreement is reached compared to the reference DNS.

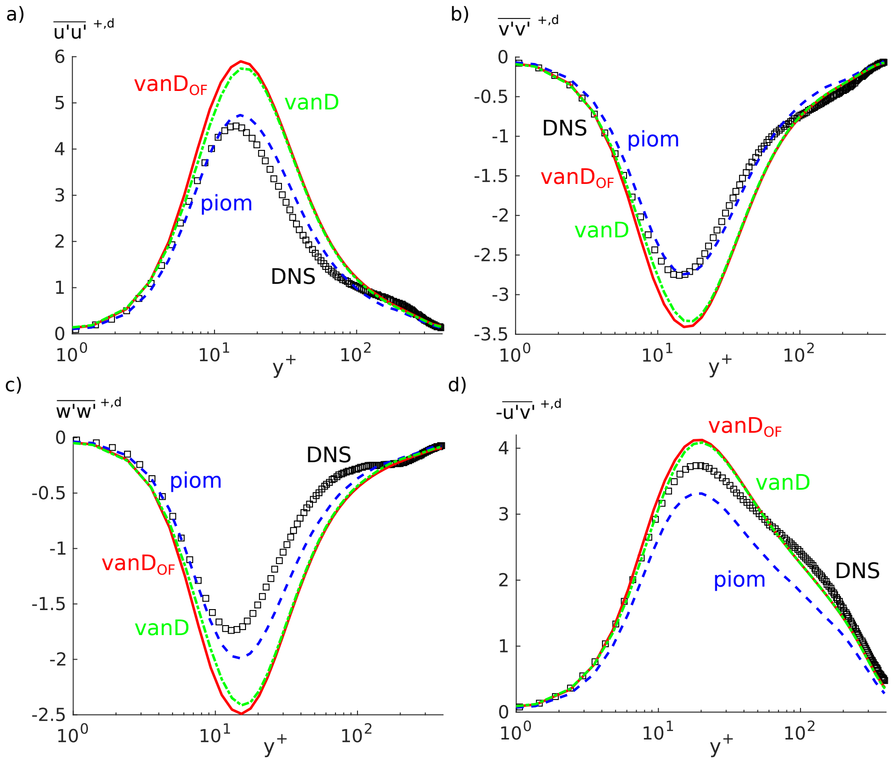

Figure 2.7: *Influence of the near-wall damping on the Reynolds stresses.*

2.5 Validation on a plane channel flow

2.5.1 Numerical description

A plane channel flow is simulated with a domain size of $30\,\delta \times 2\,\delta \times 3.5\,\delta$, for the selected $Re_\tau = 395$. The influence of mesh refinement is investigated in Appendix A.2, and as explained the baseline mesh ($\Delta x^+ = 39.5$, $\Delta z^+ = 17.7$ and $y^+_{min} = 0.9$) is selected for the continuation of this work. It is made of 1.68 Million cells, with a number of grid points of $300 \times 80 \times 70$ in the streamwise, vertical and spanwise directions respectively.
The solver is modified to include the temperature perturbation method, such that pseudo-random temperature perturbations are seeded every perturbation time step Δt_p, applying uniform values to the predefined perturbation cells. The Prandtl number is fixed to a value of 0.71 throughout the study.
No-slip wall boundary conditions are applied to the top and bottom walls while periodic boundary conditions are applied in the spanwise direction. The mean velocity profile extracted from the periodic inlet/outlet channel simulation described in Section 2.4.1 is applied at the inlet. A zero velocity gradient is imposed at the outlet.

A uniform inlet temperature T_0 is inserted at the inlet while a zero temperature gradient is applied to the outlet. The top and bottom walls of the channel are adiabatic. An aspect of the temperature perturbation method is to verify that, when introducing the perturbations, no net heat is added into the solution. This is checked by integrating the random values imposed over the perturbation cells. Summarizing the guidelines formulated in Section 2.3.3 and followed in this study, the perturbation time is given by $\Gamma = 1$ and the strongest local buoyancy force is initially set for $Ri = 0.2$. This maximum value, denoted as Ri_a, is reached in the fully active zone, while it is brought back to zero outside of the perturbation zone. Within the seeding zone, a random uniformly distributed set of perturbations is imposed within a $\pm Ri_a$ interval. In accordance with the theoretical standard deviation value of $1/\sqrt{3}\, Ri_a$, a mean value of $0.59\, Ri_a$ is obtained over 100 time samples, for a seeding zone composed of 336 perturbation cells. The influence of the strength of the buoyancy force and the extent of the transition zone on the recovery distance is investigated hereafter.

2.5.2 Optimization of the perturbation method for faster turbulence development

2.5.2.1 Effect of the perturbation function

A preliminary study [24] was performed where special emphasis was brought on the specifications of the perturbation zone. We recall that the purpose of this zone is to trigger turbulence by manipulating the thermal expansion coefficient. By doing so, the buoyancy force becomes sufficiently strong to perturbate the flow, while keeping the temperature gradients negligible. The results of [24] highlighted the necessity of introducing a transition region of length L_{tr} between the fully active region of length L_a , where Ri_a was applied from the inlet, to the rest of the domain that is characterized by zero buoyancy ($Ri = 0$). Therefore, the perturbation zone has a total length of $L_p = L_a + L_{tr}$.
Several parametric studies had been carried out to try and provide guidelines on how to best define the perturbation zone. The main conclusions that could be drawn from this preliminary work can be summarized as follows; firstly, the use of a simple linear function within the transition region was found to be most beneficial. Secondly, the different lengths defining the perturbation zone were varied and the shortest recovery length was obtained for a total length L_p of $13\,\delta$, along which the fully active region covered $5\,\delta$, followed by a transition region of $8\,\delta$. Fig. 2.8 represents the Ri field along with these different regions and associated lengths. This previous optimized set-up, referred to as $Ri\,(X) = linX$, is represented in Fig. 2.8 a), where the coordinates X and Y are set depending on the characteristic lengths of the perturbation zone.

In addition, by examining more the details of the turbulent flow solution, the normal stresses in the spanwise direction, $\overline{w'w'}^+$, and particularly in the wall normal direction, $\overline{v'v'}^+$, suggested that a minimum length of $20\,\delta$ was required for the stratification effects to fully dissipate. These are created by the last forcing term of Eq. (2.10), on which the TPM relies to artificially generate

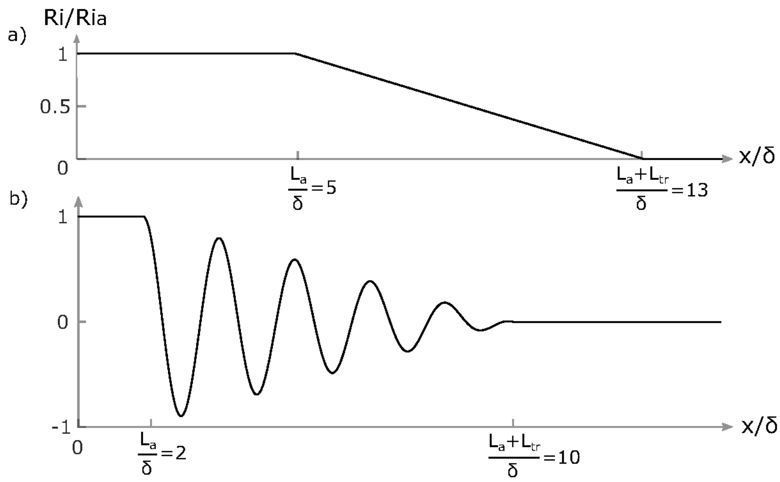

Figure 2.8: *Streamwise variation of the local artificial Richardson number - fully active region of length L_a and transition region of length L_{tr} a) $Ri\,(X) = linX$ b) $Ri\,(X) = linX \cdot cosX$.*

turbulence. These vertical flow motions are caused by a perturbation function, $Ri\,(X) = linX$, that remains linearly positive along the streamwise direction, and uniform in the vertical direction. As a consequence, the fluid stratifies, as could already be observed in Fig. 2.1.

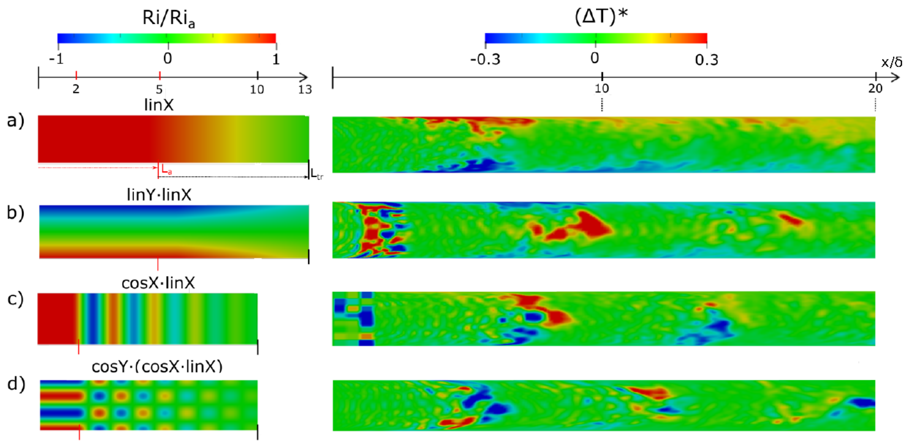

Figure 2.9: *2D contour fields in a vertical plane, obtained with different perturbation functions: artificial Richardson number on the left and temperature on the right.*

To reduce stratification effects and therefore further minimize the flow recovery length, several alternative perturbation functions have been tested. Based on the previous conclusions, all of them retain a linear decrease of Ri along the

streamwise direction. However, to enhance the flow mixing, different functions are added to this linear variation.
The first approach consists in superposing a linear function in the wall normal direction, as presented in Fig. 2.9 b). This function, denoted as $Ri\,(X,Y) = linY \cdot linX$, goes within the fully active region from $\pm Ri_a$ from one vertical wall to the other, while conserving the initial lengths L_a and L_{tr} of $5\,\delta$ and $8\,\delta$ respectively. The initial purpose was to prevent the flow from stratifying. However, some layering effects remain since the hot fluid still rises from the bottom wall, since $Ri = Ri_a$, until the middle of the channel. Similarly, the warmer fluid is pushed down from the upper wall, where $Ri = -Ri_a$. As a result, hot pockets of fluid agglomerate in the center, at every perturbation step. These first results suggest that a more complex perturbation function is needed to destroy the stratification effects more efficiently.
In the following trials, the fully active region is kept equal to the seeding zone ($L_a = L_s$) for simplicity, which roughly measures $2\,\delta$. After this, the transition region extends until $10\,\delta$. The third function is shown in Fig. 2.9 c) and it superposes a cosine function in the streamwise direction, referred to as $Ri\,(X) = cosX \cdot linX$, with five periods within the transition region of length L_{tr}. It successfully insures further mixing of the thermal field, with hot and cold areas that are less localized compared to cases a) and b). The last function represented in Fig. 2.9 d) includes, on top of case c), a cosine variation in the vertical direction, with $Ri\,(X,Y) = cosY \cdot (cosX \cdot linX)$. There again, better mixing of the thermal field is achieved.

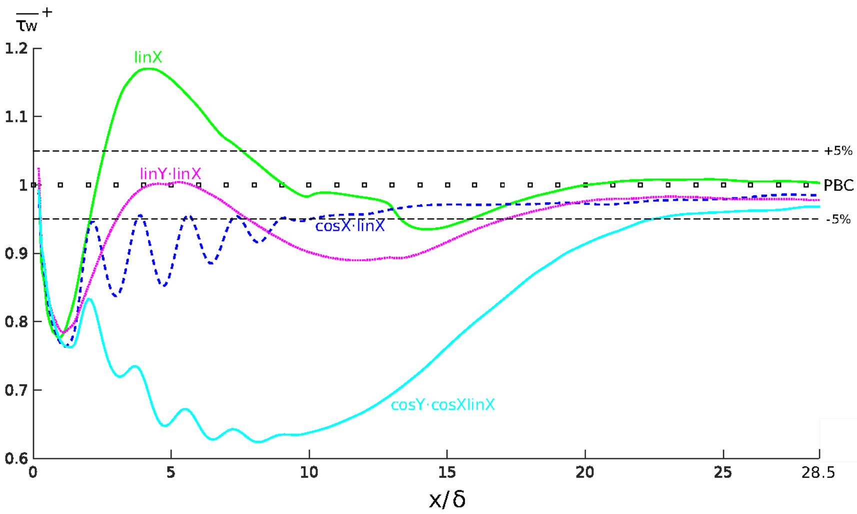

Figure 2.10: *Effect of the perturbation function on the wall shear stress recovery.*

The contour plots give a first indication of how efficient each of these perturbation functions may be in preventing the establishment of stratification. However, they may affect the flow behavior in various ways. For a quantitative

measure of their performance, we should refer to how quickly the flow recovers from this perturbation. For this, the recovery length is assessed based on the dimensionless wall shear stress, $\overline{\tau}_w^+ = \overline{\tau}_w/(u_\tau^2)$. An error criteria of 5 % around the reference value of 1 is added to the graphs. This parameter is plotted in Fig. 2.10 for each of the different perturbation functions.
As suspected, in the case where a linear damping ($linX$) is applied, the presence of stratification effects results in a longer fetch of about $20\,\delta$ for the flow to reach equilibrium. We recall that the influence of the temperature field on the flow is limited to the perturbation zone, after which the coupling between the two becomes negligible, as $Ri = 0$. However, in this initial case the flow still requires a certain fetch downstream to mix thanks to turbulence and de-stratify. Similarly, the perturbation function ($linY \cdot linX$) that exhibited pockets of hot fluid in the center of the channel, requires a comparable distance before reaching a stable state.
Already temperature contours had suggested that superposing a cosine variation streamwise could help promote mixing of the thermal field. Indeed, the function ($cosX \cdot linX$) appears to be much more efficient. In addition to a shorter development length, the perturbation felt by the wall shear stress is reduced in amplitude. This enables the flow to converge faster along the channel towards a stabilized solution, reducing the flow recovery to roughly $10\,\delta$ based on an error criteria of 5 %. On the contrary, the addition of a cosine function in the wall normal direction ($cosY \cdot (cosX \cdot linX)$) is counter effective as it induces an excessive perturbation of the flow that requires a fetch longer than $20\,\delta$ to recover.
We may conclude from this first study that the perturbation function must provide sufficient mixing to eliminate stratification effects, but without perturbing the flow excessively. The use of a cosine variation coupled with a linear transition in the streamwise direction appears to constitute a most efficient way of manipulating the artificial local Richardson number Ri inside the transition region of the perturbation zone.

2.5.2.2 Variation of the transition length

The transition length of the perturbation zone, L_{tr} (ref. Fig. 2.8), is varied with the aim of finding an optimum value that will minimize the development distance. The initial value of $8\,\delta$ is compared to various lengths ranging from 4 to $10\,\delta$, while the length of the fully active region placed at the entrance and characterized by Ri_a remains equal to about $2\,\delta$ ($L_a = L_s$). The optimum perturbation function ($cosX \cdot linX$) is adjusted to keep five periods of the cosine function within the transition region. The effect on the development of the wall shear stress is reported in Fig. 2.11 along with the associated recovery lengths.
The results indicate that a transition length of $8\,\delta$ provides the fastest development distance. Based on an error criteria of 5 %, a minimum recovery length of $10\,\delta$ is reached. This is considerably less than with shorter distances of 6 and $4\,\delta$, for which a fetch of $16\,\delta$ is needed. This suggests that the flow requires a minimum time to be sufficiently perturbed. On the contrary, a longer region

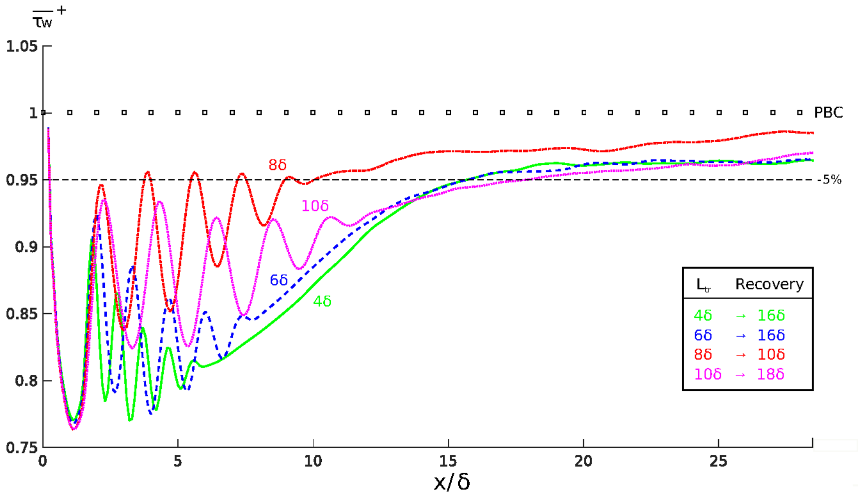

Figure 2.11: *Effect of the transition length on the wall shear stress recovery with* $Ri\,(X) = cosX \cdot linX$.

of $10\,\delta$ is excessive since the flow then takes almost twice longer to recover compared to the optimum set-up.

2.5.2.3 Strength of the buoyancy effects

The Richardson number was identified in Section 2.3.2.2 as the key parameter governing the strength of the buoyancy effects.

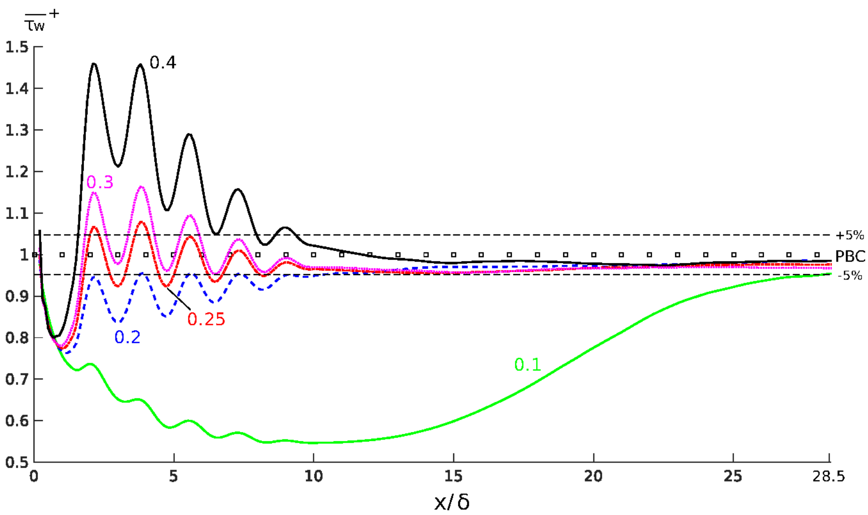

Figure 2.12: *Effect of the Richardson number on the wall shear stress recovery with* $Ri\,(X) = cosX \cdot linX$.

Its influence on the results is investigated in Fig. 2.12. Various values are tested around the initial value of 0.2, keeping Ri within the range $[0.1-0.4]$. The variations observed by the wall shear stress are directly related to the Richardson number. For $Ri = 0.1$, the imposed perturbations are not sufficiently strong and the buoyancy triggering mechanism is less effective. A much greater fetch of roughly $30\,\delta$ is needed for turbulence to fully develop. The initial value of $Ri = 0.2$ is within an optimal perturbation range that goes up to $Ri = 0.3$. Within this interval, the buoyancy effects are just enough to insure a rapid development of turbulence with a minimum recovery length of approximately $10\,\delta$. Stronger perturbations, represented by the case where $Ri = 0.4$, will induce a further distortion of the velocity field near the inlet, characterized by a perturbation of stronger amplitude in the wall shear stress. This additional energy will take longer to dissipate, thus requiring a longer fetch for the flow to stabilize. In conclusion, an optimum Richardson number of 0.25 has been identified, for which the flow distortion is the least and the recovery length is reduced down to $10\,\delta$.

2.5.2.4 Frequency of perturbation

The frequency of the perturbation function $(cosX \cdot linX)$ obtained from the parametric study performed in Section 2.5.2.1 has been adjusted up to now so that five periods $(5\,T)$ would appear throughout the transition region. The aim is to further optimize this modulation by changing the cosine frequency and analyzing its effect on the results. The transition length and the Richardson number are kept equal to $8\,\delta$ and 0.2 respectively.

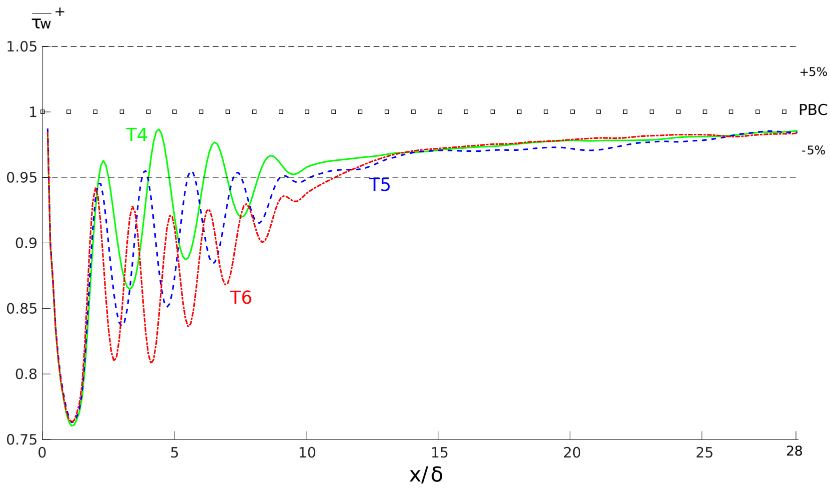

Figure 2.13: *Effect of the perturbation frequency on the wall shear stress.*

Two additional configurations are tested, where the number of periods is reduced to four $(4\,T)$ and increased to six $(6\,T)$. Above this limit, a mesh refinement would be required in the streamwise direction to correctly capture the cosine variation. A slight influence is observed on the evolution of the wall shear stress plotted in Fig. 2.13. On the one-hand, the recovery length reduces with the number of periods if one considers an error criteria of 5 %. On the other-hand, the distance to reach a more stable behavior appears similar. Consequently, to truly evaluate the frequency effect, the mean velocity profiles are compared in Fig. 2.14. Although the profile at $5\,\delta$ along the channel is the closest to the reference "case PBC" with $4\,T$, this position is clearly too close to the perturbation if one refers to the vertical stress plotted in Fig. 2.15. Furthermore, considering the streamwise and shear stresses shown in Fig. 2.16 and Fig.2.17 respectively, the streamwise position at $10\,\delta$ is more representative since close to the flow recovery and indicates that the differences obtained with $4\,T$ and $5\,T$ are negligible, while the peak values are slightly over-estimated with $6\,T$. To conclude, adjusting the frequency of perturbation to five periods within the transition region appears to be appropriate.

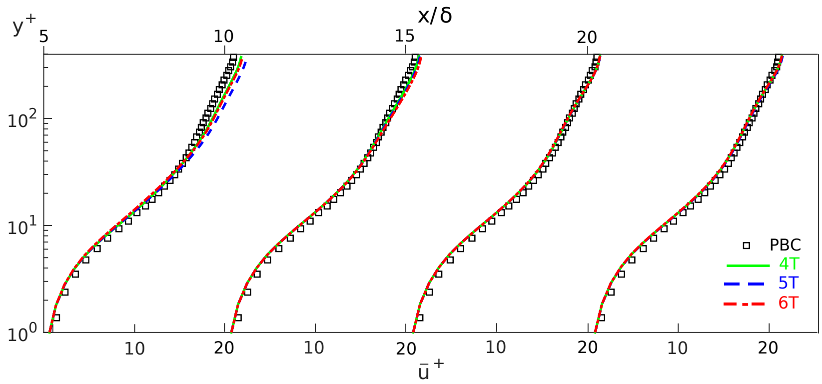

Figure 2.14: *Effect of the perturbation frequency on the mean velocity profile.*

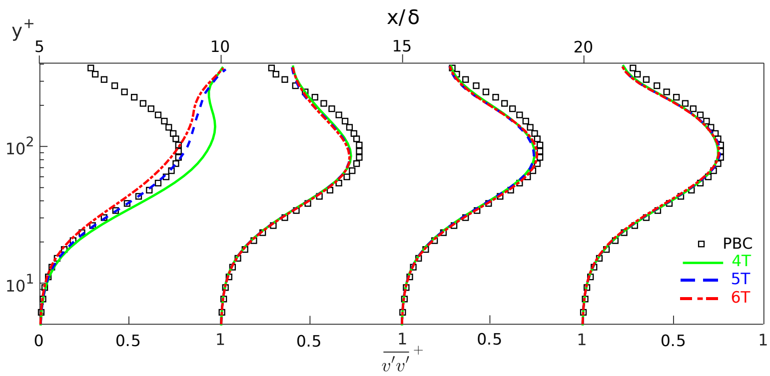

Figure 2.15: *Effect of the perturbation frequency on the Reynolds vertical stress profile.*

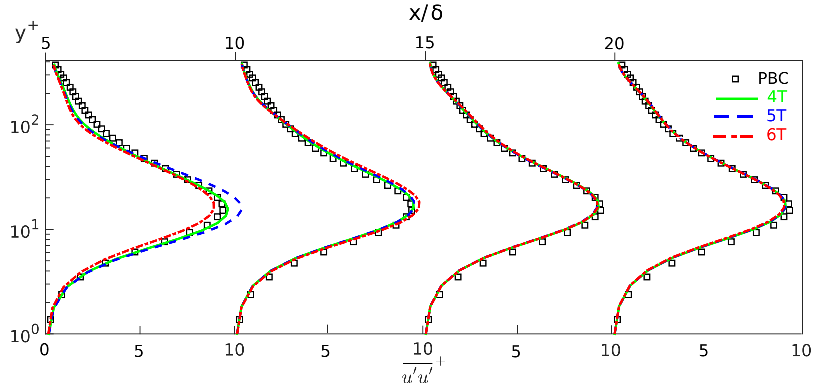

Figure 2.16: *Effect of the perturbation frequency on the Reynolds streamwise stress profile.*

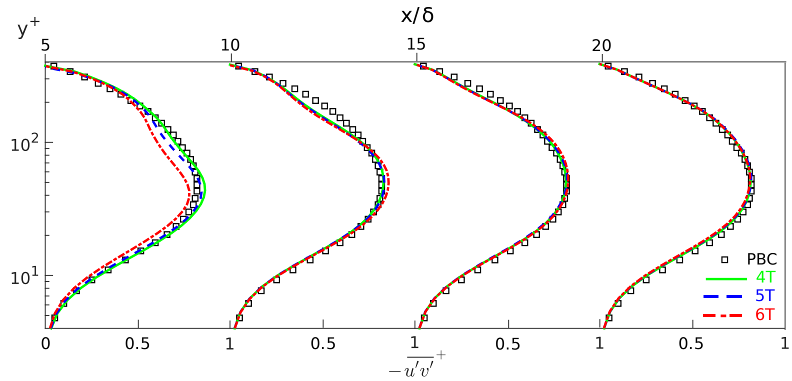

Figure 2.17: *Effect of the perturbation frequency on the Reynolds shear stress profile.*

2.5.3 Turbulent flow solution

The turbulent flow that is generated by the TPM is of primary interest. A first assessment of the flow development has been performed based on the recovery length of the wall shear stress. A thorough investigation is now proposed by analyzing the turbulent statistics obtained in the optimum case, where a perturbation function $Ri\,(X) = cosX \cdot linX$ is applied, with $L_a = 2\,\delta$, $L_{tr} = 8\,\delta$ and $Ri = 0.25$. Fig. 2.18 provides the Reynolds shear stress along the channel, while the vertical profiles of velocity and Reynolds normal stresses are provided in Fig. 2.19, at different streamwise locations. All dimensionless quantities are time and spanwise averaged.

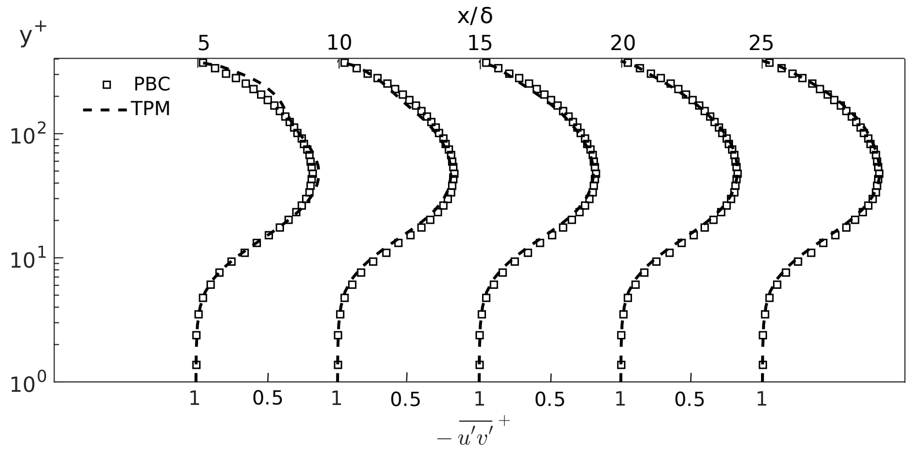

Figure 2.18: *Vertical profiles of Reynolds shear stress* $-\overline{u'v'}^+$ *along the channel.*

We recall that the first moment statistics are imposed at the inlet in the form of the mean velocity profile obtained from "case PBC". As observed in Fig. 2.19 a), the turbulent inflow method has very little influence on this quantity. Naturally, the second moment statistics, plotted in Fig. 2.19 b) to d), take longer to reach equilibrium since the turbulent structures require a certain length to develop. In accordance with the behavior observed by the wall shear stress (ref. Fig. 2.12), a good agreement with the reference is obtained already at $10\,\delta$. Stratification effects previously obtained in [24] with the use of a purely linear function ($linX$) are negligible when examining the Reynolds stress normal to the wall $\overline{v'v'}^+$. This confirms that the enhanced mixing achieved thanks to the added cosine variation has fulfilled its purpose by eliminating most of the discrepancies that were appearing in the center of the channel. As to the profiles of Reynolds shear stress shown in Fig. 2.18, an excellent agreement with the reference is obtained all along the channel. From these observations, we may conclude that a satisfactory recovery of the flow is reached in terms of the wall shear stress and the Reynolds stresses by $10\,\delta$. At this location, all profiles show satisfactory agreement with the "case PBC" representative of a fully developed turbulent state.

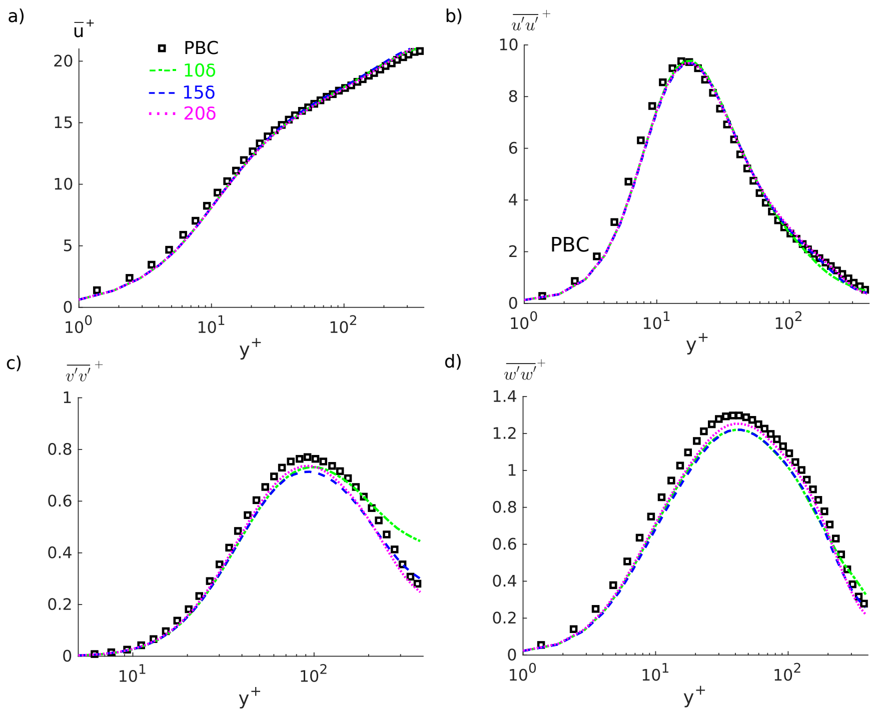

Figure 2.19: *Turbulent statistics at different streamwise locations a) Velocity b)-d) Normal Reynolds stresses.*

2.5.4 Spectral analysis and influence of the perturbation time scale

A spectral analysis is carried out in order to investigate the quality of the generated turbulence. The development of the streamwise velocity spectrum is shown in Fig. 2.20 for the initial case ($\Gamma = 1$). The signal is acquired in the center of the channel at streamwise positions $x = 5\,\delta$, $10\,\delta$, $15\,\delta$ and $20\,\delta$. It is sampled at a frequency corresponding to the simulation time step over a time window of $200\,\Delta t_p$. All spectra are then spanwise averaged. They are compared to the periodic reference "case PBC" that is additionally averaged over the streamwise direction.

The spectrum obtained at $x = 5\,\delta$ is located within the perturbation zone. The footprint of the seeded perturbation is clearly visible, with a main peak located at the frequency of perturbation, $f_p = 1/\Delta t_p$, along with several harmonics. The spectrum exhibits an over-production of turbulence near the integral length, that is reflected throughout the energy cascade. However, this energy is progressively dissipated at downstream distances, as the solution approaches the reference quasi-equilibrium state. Nevertheless, the fundamental frequency related to the TPM remains present in the flow.

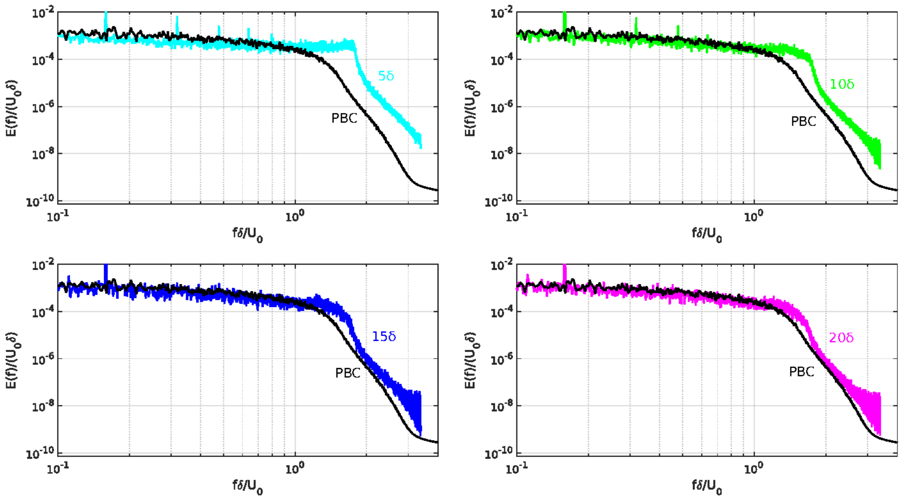

Figure 2.20: *Evolution of the streamwise velocity spectrum at the streamwise position* 5 δ, 10 δ, 15 δ *and* 20 δ. *Initial case obtained at* $\Gamma = 1$ *is compared to reference "case PBC".*

The influence of the perturbation time scale on the results and the energy content was also investigated. This parameter is changed to $\Gamma = 0.5$ and its effect on the frequency content can be observed in Fig. 2.21.

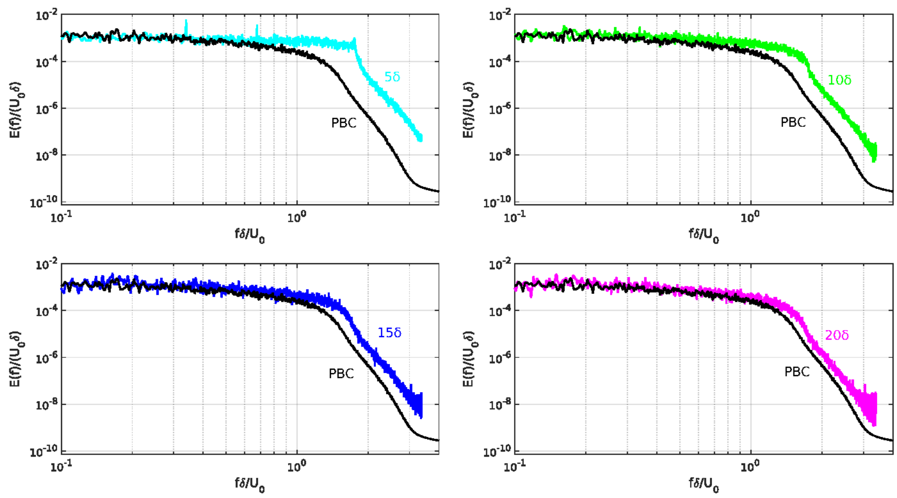

Figure 2.21: *Evolution of the streamwise velocity spectrum at the streamwise position* 5 δ, 10 δ, 15 δ *and* 20 δ. *Results obtained at* $\Gamma = 0.5$ *are compared to reference "case PBC".*

By increasing the frequency of perturbation, the step-changes in temperature are introduced sufficiently close to each other for them to interact. As a result, the footprint that appears at $5\,\delta$ is no longer visible at $10\,\delta$.

As already pointed out in the work of Muñoz-Esparza [96], it is also important to leave sufficient time for the flow to assimilate the perturbations before introducing a new step-change. The reduced Γ value of 0.5 may therefore have impacted the turbulent flow solution. This is indeed the case if one examines in particular the vertical Reynolds stresses and shear stresses plotted in Fig. 2.22. Comparison with the initial case (see Fig. 2.19) shows that the flow takes slightly longer to recover, with a similar result obtained at $15\,\delta$ instead of $10\,\delta$.

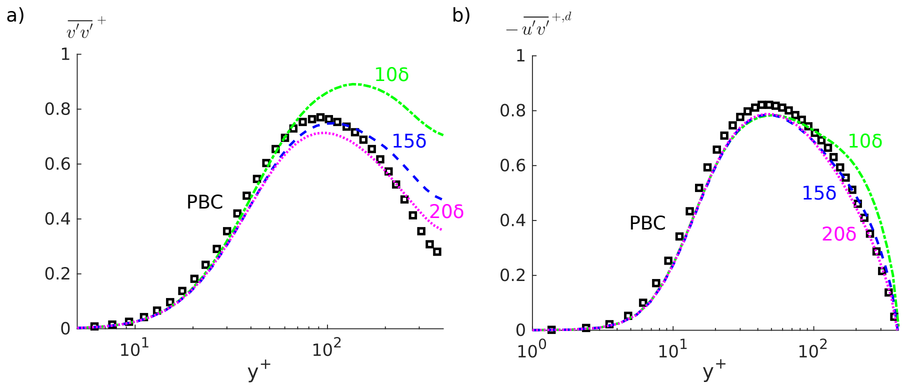

Figure 2.22: *Turbulent statistics at different streamwise positions obtained at $\Gamma = 0.5$ and compared to reference "case PBC" a) Wall-normal Reynolds stresses b)-d) Shear stresses.*

Although not shown here, the spectra and turbulent flow solution obtained for an intermediate case, characterized by $\Gamma = 0.7$, were found to be almost identical to the initial case. Finally, the effect of this parameter on the wall shear stress is represented in Fig. 2.23. As already suggested by the turbulent flow solution, on one-hand introducing step-changes that are close enough to interact (e.g. $\Gamma = 0.5$), amplifies the triggered instabilities. On the other-hand, the energy content gets closer to the reference equilibrium which also translates into a reduced deviation in wall shear stress.

To conclude, this last parametric study has provided a better understanding of the complex role played by the perturbation time scale. While the flow certainly requires a minimum time to assimilate the perturbations, it appears beneficial to impose a new step-change soon enough for the perturbation packages to interact. Despite a slightly longer flow recovery of about $15\,\delta$, a value of $\Gamma = 0.5$ avoids leaving a distinct footprint in the energy spectra and therefore insures to have a good quality energy content in close agreement with the reference equilibrium state. This last configuration can be considered as the optimized

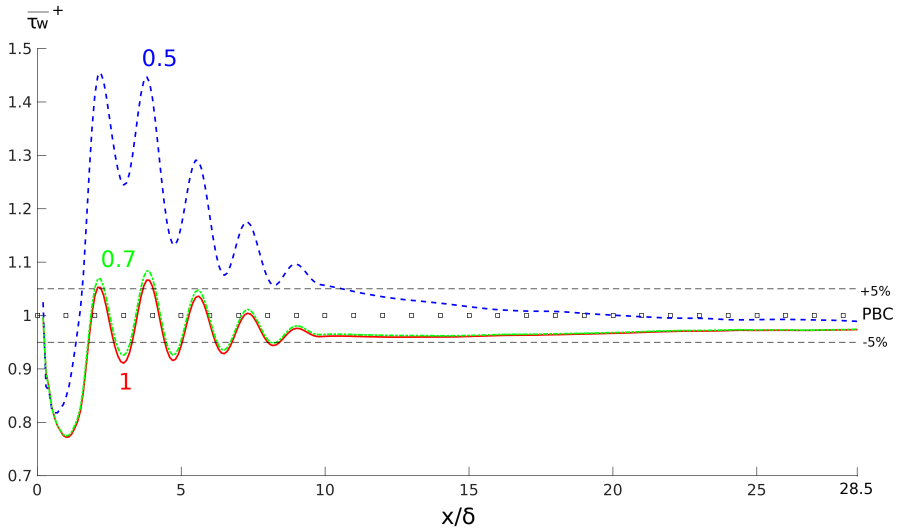

Figure 2.23: *Effect of the perturbation time scale on the wall shear stress recovery.*

TPM set-up, that will provide the most efficient use of the technique. It is summarized in Table 2.2 hereafter:

Ri_a	Γ	L_a	L_t
0.25	0.5	$2\,\delta$	$8\,\delta$

Table 2.2: *Reference parametrization of the optimized TPM.*

2.6 Comparison to results obtained with a synthetic turbulence generator

2.6.1 Results and discussion

The results presented in the previous section have demonstrated that the optimized TPM is able to generate realistic turbulence shortly after the inlet boundary. However, to further evaluate the efficiency of the method, a comparison with results obtained using a synthetic turbulence generator method is performed on the plane channel flow test case.

The approach proposed by Xie and Castro [174], introduces velocity perturbations by adding fluctuations to the average velocity profile obtained from the reference “case PBC”. This fluctuating field is constructed based on the assumption that in most turbulent shear flows, turbulent velocity correlations can be approximated by an exponential function both in time and in space [90]. It requires, as inlet inputs, the Reynolds stresses and the integral length scales. Kim et al. [67] proposed a modification to insure constant mass flux at the inlet, denoted as "XCMC", for "Xie and Castro with Mass Correction". The original implementation was kindly provided by the authors [174], such that a true comparison of the two methods could be performed within the OpenFOAM environment using the same numerical set-ups (see Section 2.5.1).

The results obtained using the XCMC approach and the TPM approach, are compared to each other and to the reference "case PBC".

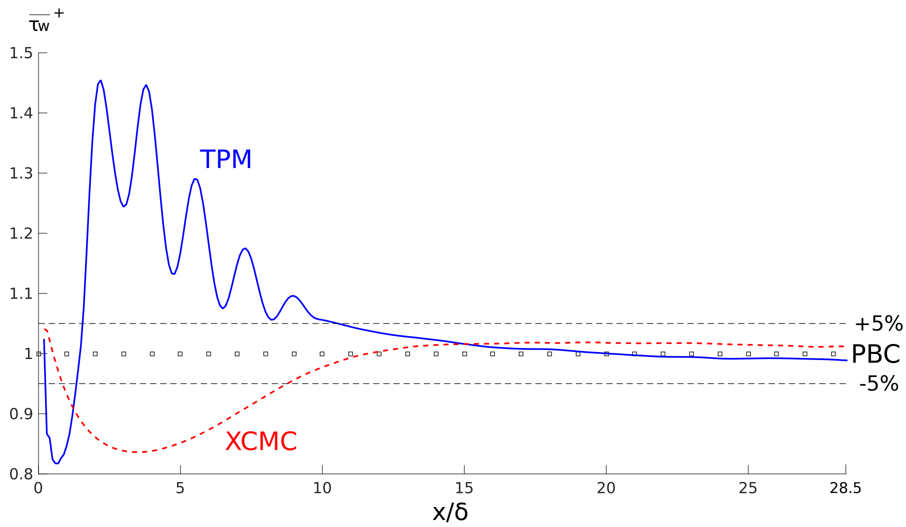

Figure 2.24: *Dimensionless wall shear stress obtained with the TPM (full line) and XCMC (dash-dot line), compared to the reference "case PBC" (square symbol).*

First, the dimensionless wall shear stress is plotted along the channel in Fig. 2.24. The development distance of the two methods are similar and appear to be approximately $15\,\delta$. Around this location, the error on the wall shear stress is within $5\,\%$, and both curves are stabilizing around the reference equilibrium.

A more detailed comparison is proposed in Fig. 2.25 to 2.27, where the Reynolds stresses are plotted at 10, 15 and $20\,\delta$ along the channel. At the first location, the flow still shows signs of being slightly affected by the inlet perturbation, particularly the wall normal stress $\overline{v'v'}^{+}$. However, in agreement with the previous statement based on the wall shear stress, a streamwise length of $15\,\delta$, is sufficient for the turbulent structures to develop and approach an equilibrium state. Indeed, both the XCMC approach and the optimized TPM exhibit a very good agreement with the reference "case PBC". An excellent agreement is reached by the time the flow reaches $20\,\delta$. In terms of CPU time, around

5-6 flow throughs were sufficient for the optimized TPM to reach statistical convergence. To conclude, if one considers the recovery length based on both wall shear stress and Reynolds stresses, the optimized TPM and the XCMC perform similarly. However, the XCMC requires non-trivial input data such as second moment statistics and integral length scales, whereas the optimized TPM only requires the mean velocity profile at the inlet.

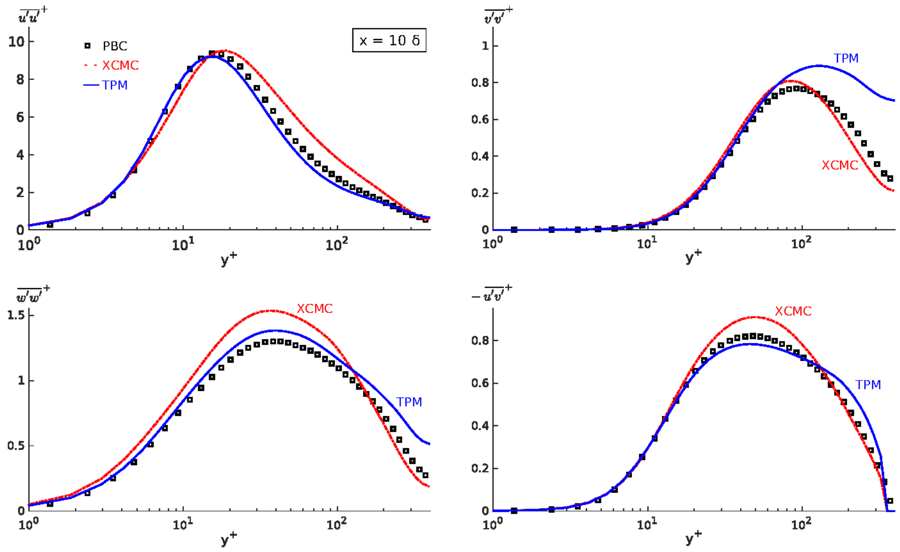

Figure 2.25: *Reynolds stresses obtained at $x = 10\,\delta$ with the TPM (full line) and XCMC (dash-dot line), compared to the reference "case PBC" (square symbol).*

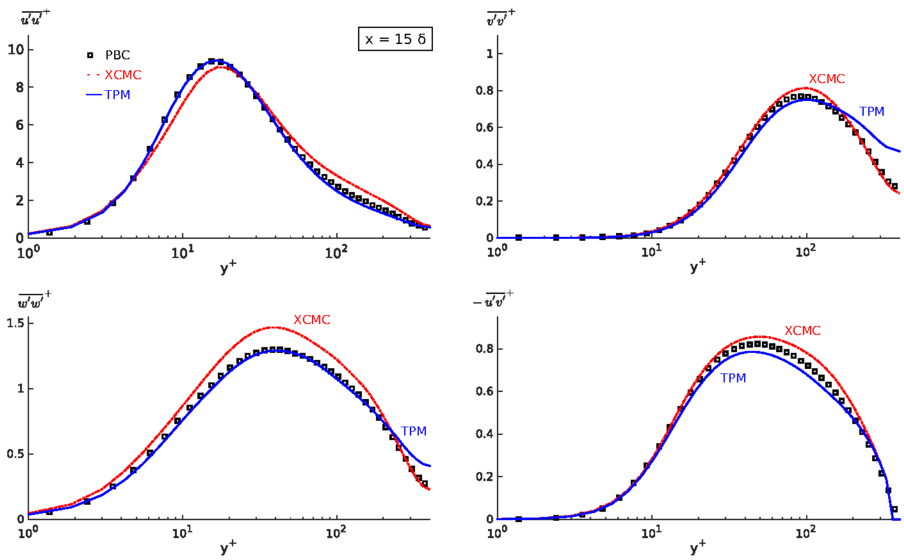

Figure 2.26: *Reynolds stresses obtained at $x = 15\,\delta$ with the TPM (full line) and XCMC (dash-dot line), compared to the reference "case PBC" (square symbol).*

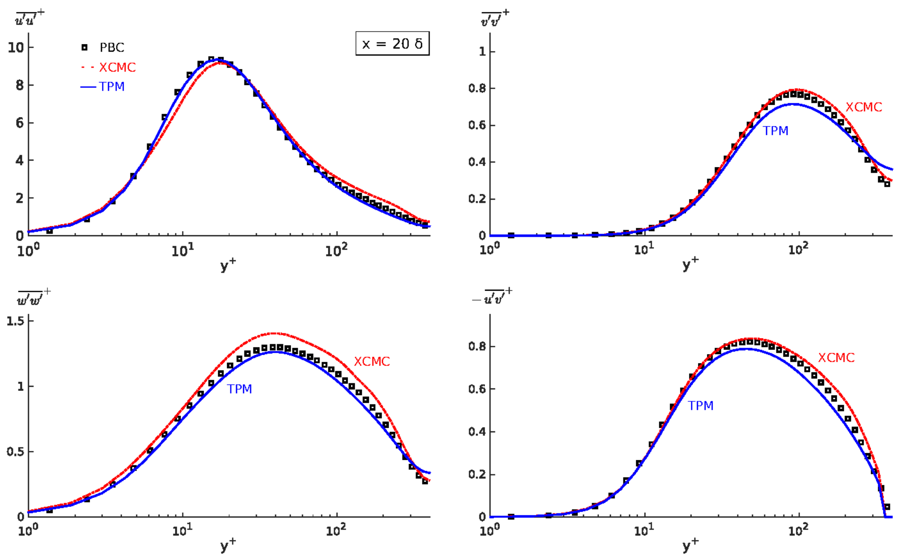

Figure 2.27: *Reynolds stresses obtained at $x = 20\,\delta$ with the TPM (full line) and XCMC (dash-dot line), compared to the reference "case PBC" (square symbol).*

2.7 Conclusions

The temperature perturbation method has been optimized to efficiently generate inflow turbulence for LES (or DNS) simulations of a variety of wall-bounded flows. As previously developed for atmospheric flows, the flow is seeded with random temperature perturbations applied to groups of mesh cells placed at the inlet of the domain. The principle relies on the creation of turbulent structures via physical buoyancy effects. However, in the case of typical wall-bounded flows, that exhibit much smaller length scales than in the atmosphere, these effects are negligible and have to be artificially increased for turbulence to be generated. Further optimization of this modified approach is necessary for the method to minimize the flow recovery length. In this context, the incompressible solver of OpenFOAM v3.0.1 with the Boussinesq approximation is used to account for buoyancy. A plane channel flow is chosen as test case to validate this new approach, as it provides straightforward validation data by using periodic inlet/outlet boundary conditions, thus generating fully developed turbulence which serves as reference. LES simulations of the plane channel flow, applying the optimized TPM at the inlet, are run to further improve the method and minimize the flow recovery to this equilibrium state. An interesting question remains whether another competing method could be developed following the same principle but based on an arbitrary body force rather than physical effects such as buoyancy. It is also important to stress that, by the time the flow reaches equilibrium, the remaining artificial thermal effects are negligible and will not influence any physical thermal effects present within the region of interest. Nevertheless, the velocity could be perturbated via an artificial buoyancy force associated to another scalar ϕ. Similarly, the optimized TPM would be applied to ϕ instead of the temperature. This would enable to simulate other fluids characterized by different Prandtl numbers, while still associating a Prandtl number of 0.71 to the perturbation scalar ϕ, value at which the TPM was optimized in this study.

The key modification that is proposed consists in creating a perturbation zone at the entrance of the domain. A local artificial Richardson number is applied within the perturbation zone, so as to enhance buoyancy. This zone is divided into a fully active region, where buoyancy effects reach a maximum, and a transition region that is essential to insure a smooth progression of the Richardson number back to zero. A preliminary study [24] demonstrated that using a linear variation as transition is able to efficiently limit the flow distortion compared to an abrupt change. However, the stratification effects that are created by a simple linear transition proved to be detrimental in terms of flow recovery length, which remained equal to $20\,\delta$ despite the optimization of the characteristic lengths of the perturbation zone and the strength of the buoyancy effects within this area.
Consequently, the focus of this work has been to adapt the approach and propose an appropriate modulation to be applied to the local artificial Richardson number. The purpose of this perturbation function is to trigger the formation of turbulent structures while, at the same time, pre-mixing the flow and avoiding

stratification effects from slowing down the flow recovery length. Among the different functions that were tested, the most efficient one consists in adding a cosine variation of five periods to the linear decrease of the artificial local Richardson number within the transition region. The optimum transition length was found to be equal to $8\,\delta$, preceeded by a fully active region of $2\,\delta$, where a maximum artificial local Richardson number of 0.25 insured the shortest recovery length. An additional aspect to consider is the spectral content resulting from the TPM. The perturbation time scale has proven to play an important role in the quality of the generated turbulence. Despite a slightly longer recovery that is caused by interacting packages, a value of 0.5 avoids contaminating the flow with a distinct footprint characteristic of the perturbation frequency. Shortly after the perturbation zone, a satisfactory flow recovery is reached around $15\,\delta$, in terms of the wall shear stress, the Reynolds stresses and the energy spectrum. A comparison of the results obtained using the optimized TPM with those obtained using the synthetic turbulence generator method of Xie and Castro with mass correction [67], shows that the TPM is as efficient. Even though similar performance is achieved, the major advantage of the optimized TPM over existing turbulent inflow methods is that, it does not require any second order moments or integral length scales as input, other than the mean velocity profile at the inlet. Therefore, in addition to it simplicity, it appears to be very flexible and potentially applicable to a wide variety of flows. The next step will consist in applying the method to developing flows that include physical temperature effects after the region of physical establishment, such as the flow over a heated backward-facing step. Indeed, the temperature variations inserted by the optimized TPM do not influence the flow downstream of the perturbation region, making it applicable to such cases.

Chapter 3

Backward Facing Step experiment

3.1 Introduction

The separation and subsequent reattachment of turbulent flows occur not only in nuclear reactors, but also in many practical engineering applications. These are commonly observed in turbomachinery systems, heat exchangers, combustors or urban flows. In the presence of heat transfer, the problem becomes all the more challenging for heat transfer engineers since large variations in the local heat transfer coefficient are observed. These lead to significant increases in heat transfer rates [168] which require a clear understanding of the phenomena to properly predict the thermal loads caused by the reattachment. This problematic is well represented by a generic BFS geometry, and has therefore been the most common benchmark for assessing turbulence and heat transfer models in abruptly separated flows [17].
Nevertheless, most studies have focused on the flow field and do not include thermal effects. The BFS flow is therefore much less documented from a heat transfer point of view. Refering to previous reviews on experimental heat transfer studies [12], the work of Vogel and Eaton [168] remains the most comprehensive, characterized by $Re_h = 28000$ and $ER = 1.25$. A thermal-hydraulic study was performed combining laser-Doppler anemometry (LDA) and thermocouples, revealing that the maximum heat transfer near reattachment was closely related to fluctuations of the skin friction coefficient. LES performed by Keating et al. [63] showed close agreement with the experiment, providing further insight into these underlying flow mechanisms. Also the LES of Avancha and Pletcher [13], including property variations, provided results comparable to the particle-tracking velocimetry (PTV) measurements of Kasaga and Matsunaga [60], conducted at $Re_h = 5540$ and $ER = 1.5$. Similarly, the peak in heat transfer coefficient appeared just before the flow reattachment.

Coming back to pool reactor flows, the confined nature of these experiments limits their interest for this particular type of application. Although thermal effects are not included, the DNS of Le et al. [75] features a relatively unconfined BFS flow with $ER = 1.2$, at moderate $Re_h = 5100$, reproducing very well the corresponding experiment of Jovic and Driver [59]. A developing TBL is found upstream of the step, it is therefore quite similar to the configuration tested in the MYRTE experiment.
This configuration has been studied numerous times in isothermal conditions, while experiments including heat transfer have only been conducted in air or

water. Only recently, DNS of turbulent heat transfer behind a BFS has been performed for liquid sodium ($Pr = 0.0088$) by Niemann and Fröhlich [99]. This is supposedly the only study done at low Prandtl number but, there again, the inlet is a developed channel flow profile. Consequently, the MYRTE experiment conducted at $Re_h = 8930$ and $ER = 1.09$ with a He-Xe gas-mixture ($Pr = 0.2$) provides unique data in the case of an unconfined BFS flow at moderate Prandtl number.

3.2 Description of the work

As described in Chapter 1, the Prandtl number effects present in the flow over a heated Backward Facing Step (BFS) will be investigated via LES. Although the accuracy of this approach is well established, it remains essential to demonstrate that the data generated in this particular work can be used with sufficient confidence for the validation of RANS turbulent heat transfer models. To assess its validity, experiments featuring a non-confined BFS flow are carried out. Unfortunately, testing of liquid metals such as LBE would require building a complex facility where the use of laser optical techniques or conventional probes would not be possible. Applying methods adapted to HLM experiments [141] would result in insufficient information regarding turbulence and temperature fluctuations, essential for the development of suitable turbulent heat transfer models.
Instead, a transparent gas mixture composed of Helium and Xenon is used in order to reach Prandtl number values lower than air [81]. As already tested in a convection cell, a mixture made of 30 % Xenon and 70 % Helium enables to reach a value as low as 0.2 [52]. Previous investigations of He-Xe mixtures include testing along a heated circular tube [161], to study the heat transfer performance of low Prandtl number fluids. Although this remains an order of magnitude higher than HLM, DNS of the flow over a wavy channel [40] have shown that $Pr = 0.2$ is sufficiently low to have a measurable influence on the heat transfer performance compared to air. Moreover, this value enables to maintain a higher Peclet number ($Pe = Re\,Pr$), which is of particular interest for RANS modelers since the higher the Pe, the more likely it is to have turbulence dominated heat transfer. Consequently, the Re is kept lower (implying a smaller mesh size), while the flow conditions are closer to industrially relevant conditions. Therefore, in similar conditions where flow separation occurs, this gaseous mixture is expected to give a first insight into low Prandtl number effects, and it represents a valuable experiment towards the validation of more affordable RANS simulations for low Prandtl number fluids. Indeed, a satisfactory comparison at $Pr = 0.2$ would prove that the LES can provide trustable results, also at low Prandtl number, representative of HLM.

In this Chapter, the experimental set-up that was implemented to accomodate the BFS experiment is described, starting with the newly designed MYRTE wind tunnel. The test section requirements needed to ensure that the flow remains unconfined over the BFS are described. The measurement techniques are then introduced, along with the design of experiments. These are carefully planned so that all the inputs needed to set up an LES with corresponding boundary conditions are measured. An error analysis associated to each measurement technique is provided, so that, when the results are compared in Chapter 5, an estimate of the measurement uncertainty can also be considered. Experiments with air are firstly conducted, in order to measure the velocity field with PIV. Now that the facility is constructed, this campaign also constitutes an opportunity to conduct some comparative studies much faster than by LES. For instance, the dependency of the flow field with respect to the Reynolds number is investigated, which helps clearly define the flow regime. Thermal effects are also studied by PIV, which helps quantify the importance of buoyancy effects in the simulated flow conditions. These are complemented by micro-thermocouple measurements, which clearly highlight the different convection regimes.

3.3 Experimental set-up

3.3.1 MYRTE wind tunnel

3.3.1.1 Description of the facility

A new facility was designed at the VKI in 2015, to carry out the experiments planned in the frame of the MYRTE project.

Figure 3.1: *MYRTE wind tunnel.*

To be able to perform tests with a gaseous mixture made of Helium and Xenon, the MYRTE wind tunnel has the particularity of being a closed-loop sealed facility. A high vacuum level is first reached before the tunnel is filled with the gas mixture. The He-Xe is supplied by the company SOL Group that through a certified industrial process, pre-mixes these two gases. The wind tunnel operates at a slight over-pressure in order to avoid any air contamination, while providing a way of monitoring air tightness. The axial fan is driven by a 1.1 kW variable-speed motor and it provides a maximum flow velocity of 30 m/s. To avoid leakages, a sealing system has been designed [154], based on O-ring type seals placed between each wind tunnel component. A vacuum pump then extracts the air between the double seals to ensure air tightness.
A picture of the wind tunnel is shown in Fig. 3.1. Its vertical orientation was motivated by the interest of also being able to reproduce a Buoyant Turbulent Boundary Layer (BTBL) and a Forced Plane Jet (FPJ), thus avoiding gravity effects. The wind tunnel is expected to reproduce two additional experiments: a Turbulent Boundary Layer (TBL) and a Backward-Facing Step (BFS). Due to space constraints, its overall height was limited to 3.75 m, resulting in a test section of 1 m long. Another challenge was to design a wind tunnel with a good flow quality and test sections of adequate dimensions with a low global volume, to limit the cost of using the noble gas. The total volume of the facility is equal to 2.4 m^3. This work focuses on the BFS test case for which a more detailed description of the test section is proposed hereafter.

3.3.1.2 Calibration of the wind tunnel

The calibration of the free stream wind tunnel velocity is performed by placing a pitot tube in the center of the test section. It is connected to a pressure transducer, which is a type 5812 piezoresistive measuring cell, calibrated with a water manometer in the pressure range of interest.

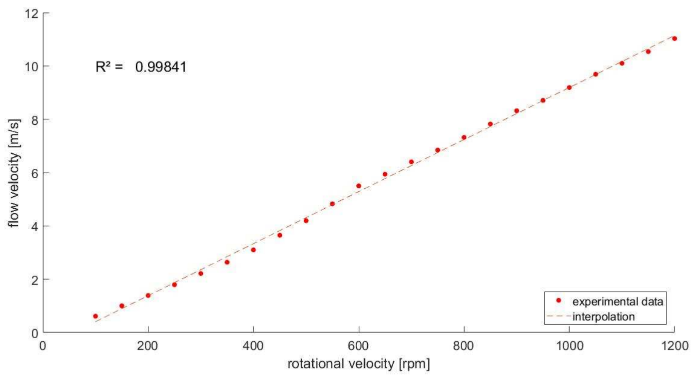

Figure 3.2: *Free-stream velocity Versus RPM.*

The velocity measured by the Pitot tube is deduced based on this linear calibration curve. The wind tunnel calibration curve shown in Fig. 3.2 is determined by varying the fan's rotational speed up to a velocity of 12 m/s. This characteristic curve exhibits a linear behavior and provides the free-stream velocity according to the wind tunnel's rpm setting.

3.3.2 Characterization of the BFS test section

3.3.2.1 BFS configuration

As its name suggests, the BFS presents a step in the floor of the test section, thus creating a sudden expansion in the flow. First considerations while designing this wind tunnel component focused on dimension requirements, represented in Fig. 3.3. The step height, h, is initially fixed to 2 cm, in order to ensure good measurement resolution in this nominal case. The primary objective while dimensioning the test section is to limit the flow confinement. Moreover, the spanwise effects should be minimized so that, in the simulations, the flow can be assumed to be homogeneous in that direction. Previous reviews [38] highlight how dependent the results can be with respect to these geometrical aspects.

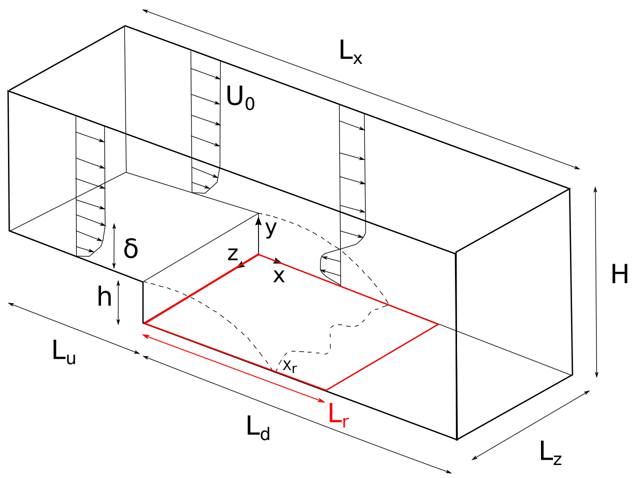

Figure 3.3: *Dimensions of BFS test section.*

The aspect ratio, AR, defined as the ratio between the channel width, L_z, and the step height, is shown to have an influence on the separation area. To limit these three-dimensional effects caused by corner flows and side wall boundary layers, the test section should be wide enough. Previous studies [34] demonstrate that, for aspect ratios smaller than 10, the reattachment length decreases if the boundary layer at separation is turbulent. This constraint is therefore taken into account to ensure two-dimensionality of the flow in the mid-plane. For a step height of 2 cm, the test section should be at least 20 cm wide.

The expansion ratio, ER, is defined as the ratio between downstream and upstream channel height. This change in area partly controls the streamwise

pressure gradient in the reattachment zone. This effect was investigated by [112], covering a large range of expansion ratios. It was found that larger expansion ratios lead to higher turbulence intensities inside the separation area. This increase in turbulent diffusion induces a faster shear layer growth and consequently shorter reattachment lengths of at most 4.5 %. To keep confinement effects negligible, the area change must be kept very small ($ER \leq 1.1$).
The Final dimensions are fixed so that the section remains square to facilitate the connection with the circular section of the fan. For $h = 2\,cm$, the BFS test case is therefore characterized by a test section that is $1\,m$ long, $0.25\,m$ wide ($L_z = 12.5\,h$) and $0.23\,m$ high ($H = 12.5\,h$) prior to the expansion, which results in $ER = 1.09$ and $AR = 12.5$. The step itself is placed at $0.4\,m$ ($L_u = 20\,h$) from the start of the section, leaving a length of $0.6\,m$ ($L_d = 30\,h$) after the step in order to limit the effect of the downstream diffuser.

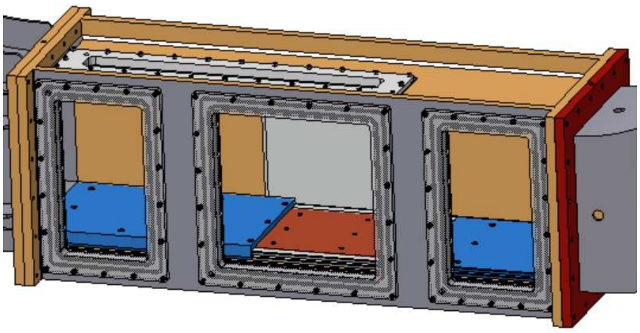

Figure 3.4: *CAD of the BFS test section.*

The CAD design of the BFS test section is illustrated in Fig. 3.4. For the use of optical measurement techniques, visual access is made possible by positioning three glass windows. This solution was chosen over a single glass piece tunnel in order to reduce mechanical constraints [154]. A glass slit is placed on top so that a laser sheet can pass and illuminate the mid-plane. Only the portion of wall after the step is heated up *(brown)*. A resistance is placed under an aluminium plate over a length of $0.294\,m$ ($L_r = 14.7\,h$), while the upsteam and downstream plates are insulated *(blue)* to avoid heat conduction through the walls.
A tripping device is needed upstream of the test section, in order to insure that the inflow boundary layer is fully turbulent. Indeed, simply relying on natural transition would require a too long fetch before obtaining a thick enough boundary layer. For this purpose, a sandpaper strip of $14.5\,cm$ long and $P60$ roughness grade is placed at the end of the convergent along the bottom wall, just upstream of the test section.

3.3.2.2 Thermal characterization

The heated step is characterized from a thermal point of view in order to verify that it has been properly insulated. A picture of the heated plate is taken by InfraRed (IR) Thermography. The IR camera is positioned at the level of the top slit as shown in Fig. 3.5. The principle of this measurement technique relies on the detection of thermal energy that is radiated from the plate in one of the IR bands of the electromagnetic spectrum, that is then converted into a video signal and represented as a surface temperature map. The appropriate temperature boundary condition to apply in the simulations can then be deduced. Three contact thermocouples are placed on the heated plate to measure the wall temperature, T_w, at $x = 1\,h$, $3\,h$ and $5\,h$ after the step. These are used to monitor the time variations as the flow gradually warms up inside the wind tunnel. The inlet free-stream temperature, T_{in}, is measured by a TC-100 sensor.

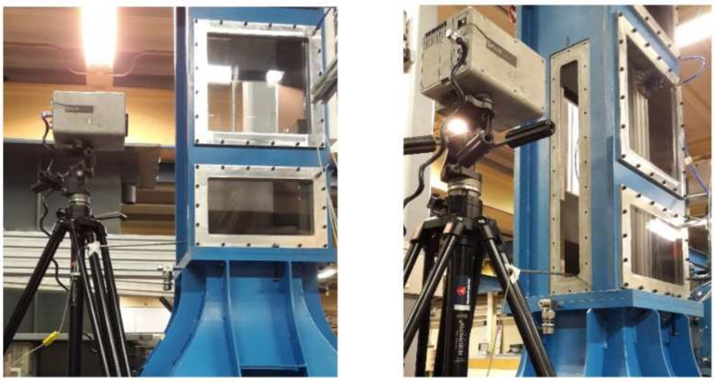

Figure 3.5: *Infra-red camera measurements.*

3.3.3 Design of PIV experiments

As shown by Scarano and Riethmuller [134], the turbulent flow over a BFS can be successfully measured by means of the PIV technique. Indeed, a good agreement with the DNS data of Le et al. [75] had been obtained. The same approach has been selected here to characterize the velocity field. These sets of measurements were carefully planned to fulfill the following two objectives:

1. The boundary conditions should be well known to provide the necessary input to the simulations.
2. The separation area should be properly captured as well as the developing shear layer after flow expansion.

The first one ensures that the experiments and computations are performed under the same conditions, for a true comparison. The second one provides detailed validation data within the area of interest in view of validating the

CFD. PIV has been mostly applied for the aeraulic characterization of the flow. Unlike probes for instance, it is a non-intrusive velocity measurement which does not disturb the flow within the separation area. A schematics of the set-up is provided in Fig. 3.6.

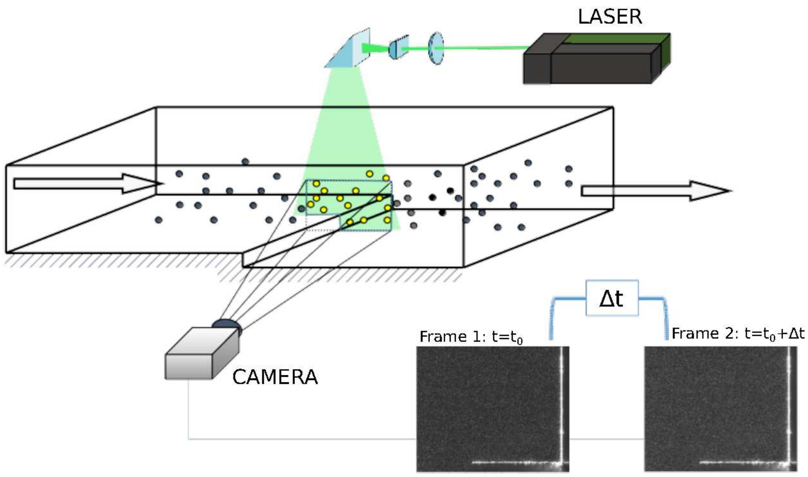

Figure 3.6: *Schematics of the PIV set-up.*

The basic principle of this technique relies on measuring the displacement of particles injected into the flow. A smoke generator has been used to seed the flow with condensed oil droplets of about $1\,\mu m$. They are then illuminated twice by a thin laser sheet directed towards the region of interest. An optical setup composed of three different lenses is implemented: a spherical lens focuses the laser beam, a cylindrical lens broadens it in order to produce a sheet while a prism lens deflects the laser sheet towards the measurement region. In synchronisation with these two short illuminations and the scattering of light from the particles, two images are taken by a digital imaging device (CCD camera). To perform a statistical analysis of the flow, a time series of 2000 images is acquired at a frequency of $4\,Hz$. An error analysis is also conducted in Appendix B.1.

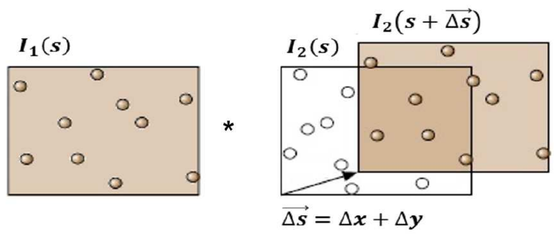

Figure 3.7: *Processing of PIV images: building of the predictor.*

These images are then processed with the software *DaVis 8*. The information relative to the displacement of the particles is extracted by cross-correlating the pairs of pictures taken during the experiment. The separation time between the two images is adjusted to limit the particle displacement to 8 pixels [4]. An adaptive multi-pass method is applied during post-processing that combines a window displacement and a grid refinement process. Firstly, the displacement is estimated based on an initial interrogation window that is applied to pre-shift smaller windows. This so-called "predictor" step (see Fig. 3.7) has the advantage of limiting the out of window motion.
Secondly, this displacement procedure is coupled with a grid refinement so that the resolution is improved by four at each iterative step. In this work, the initial interrogation window is set to 128 by 128 pixels and two iterative step is applied, resulting in a final window size of 32 by 32 pixels. A 50 % overlap (see Fig. 3.8) is used between two adjacent interrogation windows in order to reach a higher spatial resolution of 22 pixels.

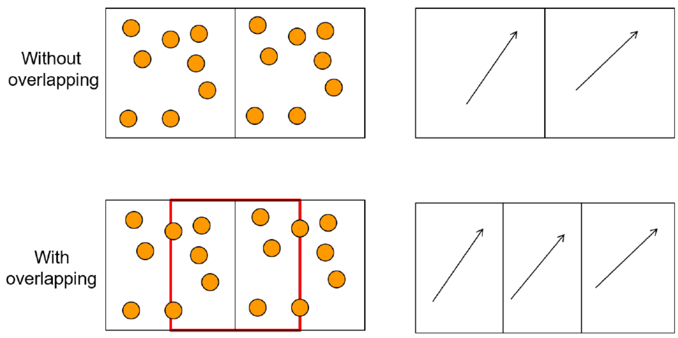

Figure 3.8: *Processing of PIV images: over-lapping.*

Considering that the camera sensor covers 1376 by 1040 pixels, the spatial resolution can be deduced from the magnification factor. The resolutions corresponding to the windows related to the boundary layer development, the top boundary condition and the separated area are the following, respectively: 0.33 mm, 3.1 mm and 0.49 mm.
After processing of the PIV images, 2D contours of the instantaneous velocities (u', v') are obtained for each pair of images. The statistical tool of *DaVis 8* is then used to calculate the average velocity field $(\overline{u}, \overline{v})$ and the Reynolds stresses $(\overline{u'u'}, \overline{v'v'}, \overline{u'v'})$.

The sketch presented in Fig. 3.9 summarizes the different PIV windows that were acquired. The CFD domain is represented as well since the inlet and the top boundary conditions need to be extracted from the PIV measurements. For this purpose, an objective of 28 mm focal length is used for the large measurement windows *(blue: 1-3)* from which the vertical velocities are extracted along the top boundary *(CFD top)*. To reach a higher resolution for the inlet boundary layer, an objective of 105 mm focal length is used. The boundary layer development along the upstream fetch is assessed by measuring the flow at the inlet, at an intermediate location and just before the step *(red: 1-3)*. The velocity profile along the inlet boundary *(CFD inlet)* is obtained by combining the two measurement windows *(red, blue: 1)*, needed as input for the CFD simulations. Finally, the separated flow region is covered by 8 measurement windows *(green: 1-8)* using this same objective. Stitching of these images insures a complete view of the recirculation area until reattachment, expected to measure approximately $6\,h$ [75].

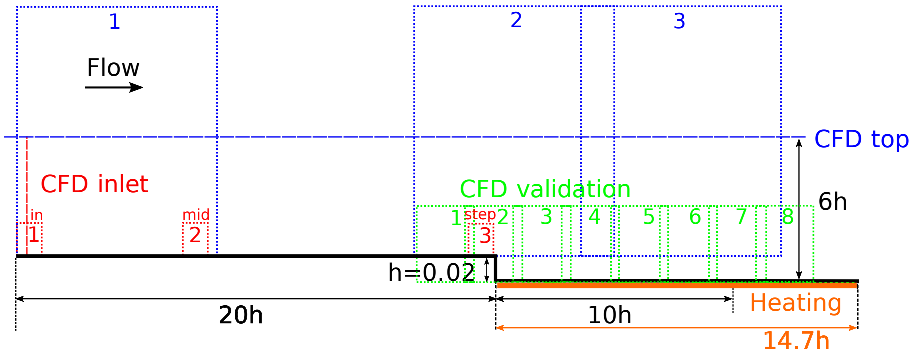

Figure 3.9: *PIV measurement windows.*

3.3.4 Simultaneous measurements of velocity and temperature

In the RANS approach, Reynolds averaging of the conservation equations results in additional flux terms. The extra terms that arise from the momentum equation take the form

$$\overline{\sigma}_{ij}^t = -\rho\,\overline{u_i^{'}u_j^{'}}\,, \tag{3.1}$$

which are referred to as the Reynolds stresses, also expressed as:

$$\overline{\sigma}_{ij}^t = -\frac{2}{3}\rho\overline{k}\delta_{ij} + \overline{\tau}_{ij}^t\,, \tag{3.2}$$

where k is the turbulent kinetic energy. The extra terms that arise from the energy equation are given by

$$\overline{q}_j^t = -\rho Cp\,\overline{T^{'}u_j^{'}}\,, \tag{3.3}$$

which is known as the turbulent heat flux. These additional flux terms represent the influence of the fluctuations over the averaging time period. Although additional terms have appeared, no new equations have been obtained to account for these new unknowns. By modeling the fluxes of Eq. (3.2) and (3.3), turbulence models provide closure to the RANS equations, by either using simplifications or providing additional equations.

One of the objectives of this work is to provide data concerning the turbulent heat fluxes, so that turbulent heat transfer models better suited for low Prandtl fluids can be further developed. Experimentally, this requires to measure simultaneously the velocity and temperature at high frequency allowing to resolve all the turbulence fluctuations that are modeled by RANS.
Several techniques have been already developed to experimentally characterize highly turbulent flows over a BFS. For instance, Abu-Mulaweh and Armaly [3] investigated turbulent mixed convection over a vertical BFS with Laser Doppler Velocimetry (LDV) and cold wire anemometry, used to measure the velocity and temperature fluctuations respectively. However, seeding the flow as required by the LDV technique appears to be particularly challenging in a sealed facility. Moreover, this would likely alter the gas mixture properties. As an alternative technique, a new probe combining a Hot-Wire Anemometer (HWA) and a Thermocouple (TC) has been designed. Further details about this new HWA-TC probe are provided hereafter.

3.3.4.1 Design of a HWA-TC probe

In order to measure simultaneously the velocity and temperature, a double probe (ref. Fig. 3.10) combining a HWA and a TC has been designed and constructed by the VKI-Instrumentation team. The wire is platinum-coated tungsten and has a diameter of 9 μm. It has an active length of 0.6 mm and a total length of 1.5 mm. A type-K micro-TC is used, made of two 12 μm diameter wires welded together at one end. The spacing between the center of the hot-wire and the micro-TC junction is 1.5 mm.
The two probes are each fed through a ceramic tube of 1.5 mm diameter and put together inside a metal tube of 3 mm diameter, that constitutes the main probe support. A traverse system has also been designed to move the probe along the mid-plane of the test section. As shown in Fig. 3.11, it is made of two electric motors that are used to translate the probe in the streamwise and wall-normal directions. The system is then enclosed inside a sealed casing. Both probe and motor cables come out through leak proof connectors placed at the extremity of the casing.

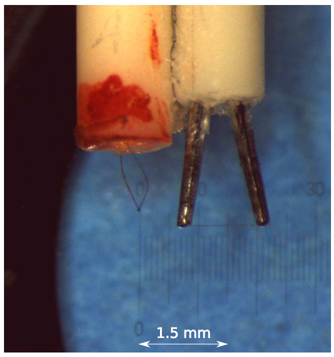

Figure 3.10: *HWA-TC probe.*

3.3.4.2 Characterization of the micro-TC

The micro-TC consists of two dissimilar metals that are connected together at the measuring junction. The voltage generated by the TC depends on the local temperature, and it is measured by a voltmeter connected to the other end. The calibration curve is directly inserted in the LabView program used for acquiring the data.

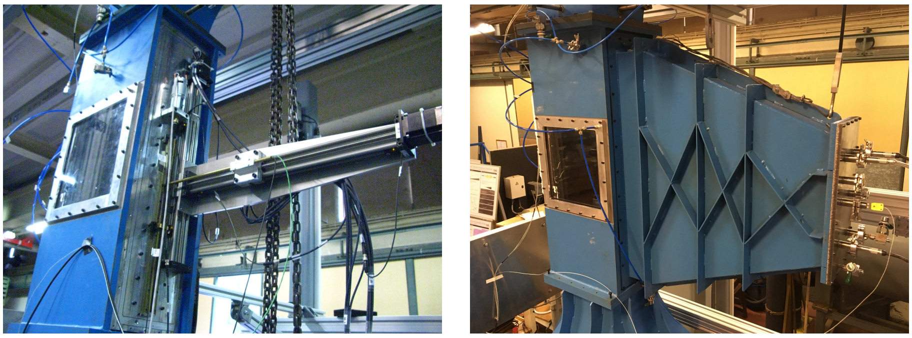

Figure 3.11: *Traverse system used for probe measurements and sealed casing.*

The response time of the TC is a very important characteristic since it defines up to what extent it is able to measure the different turbulent scales. A TC is limited by its thermal inertia; the smaller it is, the faster it responds. For this purpose, thin wires of 12 μm diameter are used. The probe's response is then determined by applying a step change. The test setup consists of a shutter which suddenly opens (¡1 ms), thus exposing the micro-TC to a hot laser at T_{max}. The probe is initially at T_i and is exposed to a step change of $\Delta T = T_{max} - T_i$. The transient response is recorded and plotted in Fig. 3.12 a).

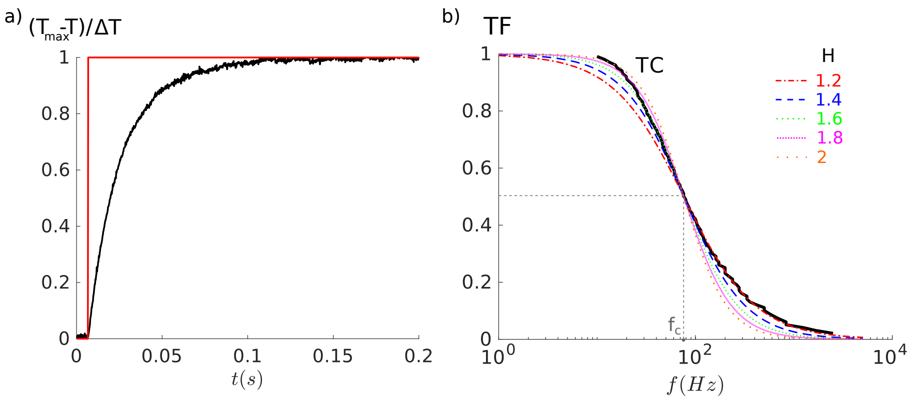

Figure 3.12: *Dynamic response of the micro-TC probe a) Step response b) Approximation of the TC transfer function with the Hill equation for different values of the Hill slope (H).*

The probe's transfer function (TF) is plotted in Fig. 3.12 b), corresponding to its response in the frequency domain. It follows a sigmoidal shape that can be approximated by the so-called Hill equation, expressed as:

$$G_{Hill}(f) = (1 - G_0) + \frac{(G_\infty - G_0)}{1 + (Gf_{50}/f)^H}\ , \tag{3.4}$$

where G_0 and G_∞ are the minimum and maximum asymptotes of the transfer function, Gf_{50} is the frequency at which the gain has reduced by half and H is the Hill slope. Three of these parameters are known since the gain reduces from 1 to 0 and Gf_{50} corresponds to the cut-off frequency $f_c = 75Hz$. Eq. (3.4) then becomes:

$$G_{Hill}(f) = 1 + \frac{1}{1 + (75/f)^H}\ . \tag{3.5}$$

The experimental curve is fitted with several Hill slope values, ranging from 1.2 to 2. Unfortunately, the sampling frequency f_s is limited to 75 Hz by the acquisition card NI 9213 (high speed mode). Indeed, it would have been preferable to acquire data at a higher sampling frequency $f_s > 2\,f_c$, in order to avoid any aliasing phenomenon that could alter the signal's frequency content. Nevertheless, this issue does not affect the time signal, which is of primary interest in this work. Taking into account that all frequency content above f_c will be lost, $H = 1.8$ appears to be the most suitable value to approximate the probe's dynamic response across the range [0-75] Hz.

3.3.4.3 Calibration of the hot-wire

As mentioned before, the velocity is measured by means of a HWA. The principle of this technique relies on the convective heat transfer between the wire and the surrounding flow. The hot wire is placed in a Wheatstone bridge that regulates the current feeding the wire in order to keep the wire temperature constant. This technique benefits from a high frequency response and is ideal for the characterization of turbulent flows.

For future comparison with the LES results, it is essential to clearly understand what the hot-wire is actually measuring. This is done prior to running the simulations, so that this quantity can be averaged during run-time, for a meaningfull comparison with the measurements.
The hot-wire is cooled down by the flow coming from all directions, without any sense of flow orientation or direction. Consequently, the hot-wire output can be interpreted in terms of an Effective Cooling Velocity, U_{hw}, defined as:

$$U_{hw} = \sqrt{U_N^2 + w^2.U_T^2} \tag{3.6}$$

with U_N the resulting velocity composed of the normal and bi-normal velocity components, U_n and U_b respectively, such that $U_N = \sqrt{U_n^2 + U_b^2}$, U_T, the velocity component aligned with the wire and w, the yaw angle coefficient that is usually around 0.1. This longitudinal cooling effect was first recognized by Newman and Leary [97] and later expressed by Champagne et al. [27] in this form.

The calibration of the HWA is performed in two steps. Firstly, its frequency response is optimized by adjusting the bridge components when exposed to a square wave test. A cut-off frequency of 7.5 kHz is obtained and defined as the sampling frequency. The acquisition time is set to 60 s during the measurements and only 20 s during the calibration since only the mean value needs to be converged. A detailed error analysis is proposed in Appendix B.2.
Secondly, the HWA is calibrated based on the wind tunnel calibration curve (ref. Fig. 3.2), for a set of velocities covering the range expected during the BFS experiment $[0-8\,m/s]$. This procedure was chosen as it remains repeatable regardless of the fluid tested, air or gas mixture. Moreover, it is necessary to apply a temperature correction whenever differences of more than $0.5°C$ are expected, since this will affect the bridge resistance. This correction is essential in this application considering that $\Delta T \simeq 20°C$ is expected in the step area. The temperature correction formula [78] provided hereafter is applied:

$$E_1^2 = E_2^2 \, \frac{T_w - T_{f,1}}{T_w - T_{f,2}} \, . \tag{3.7}$$

where T_w is the wire temperature, $T_{f,1}$ is the fluid temperature for a velocity U_{hw} and $T_{f,2}$ is a different fluid temperature for the same velocity. E_1 and E_2 are the voltages corresponding to the two respective temperatures. As illustrated in Fig. 3.13 a), this procedure is applied during calibration, and the wire temperature is deduced from Eq. (3.7). Using this same formula, all hot-wire voltages are brought back to a given reference temperature, T_{ref}. As observed, the two fourth order polynomial fits collapse to a given calibration curve that is used to convert all corrected voltages measured during the experiment.

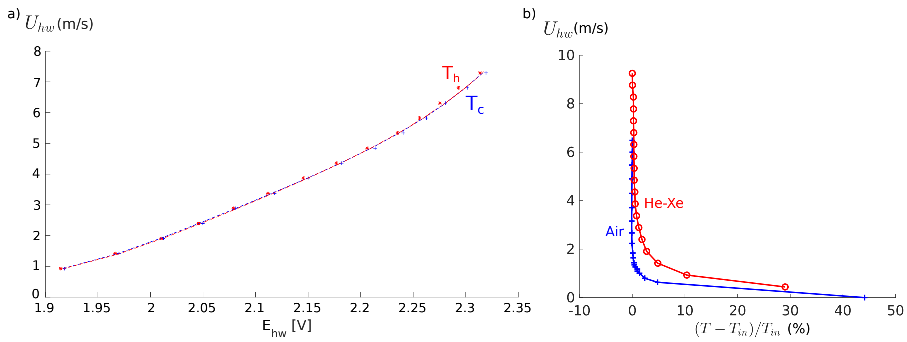

Figure 3.13: *a) HWA calibration curve with temperature correction b) micro-TC measured temperature during the HWA static calibration.*

An important observation made during the calibration concerns the micro-TC behaviour. As shown in Fig. 3.13 b), at low velocities the probe is heated up by the presence of the HWA due to radiation effects. This is an important limitation of the HWA-TC probe. On one-hand, the spacing between the HWA and the micro-TC was reduced so that velocity and temperature would be acquired as close as possible. On the other-hand, interactions between the two measurement devices become inevitable. In the case of air, this effect becomes noticeable ($> 1\%$) below $1\ m/s$. However, while testing in the gas mixture, it is felt already at $3\ m/s$ since the thermal diffusivity is higher. While it may have a limited influence on the thermal fluctuations, so on the so-called turbulent heat flux $\overline{u'_{hw}T'}$, it will certainly affect the mean temperatures. For this reason, temperature measurements will be carried-out using the double sensor HWA-TC probe but also with a single micro-TC probe.

3.4 Presentation of the results in air

The aim of this section is to focus on fully characterizing the thermal-hydraulic field in air, in order to extract all the necessary LES inputs, a well as investigate the influence of the free-stream velocity and the heating effects. Consequently, only the PIV and single micro-TC measurements are presented here. All the probe measurements acquired in the He-Xe gas mixture can be found in Chapter 5, that concentrates on the LES and experimental comparison at moderate Prandtl numbers.

3.4.1 Thermal measurements of the heated step

In order to characterize the experiment from a thermal point of view, the temperature distribution along the heated flat-plate is measured by IR Thermography. In addition, the efficiency of the insulated plates that are meant to minimize conduction effects before and after the step is assessed. IR images are taken from the bottom and the top of the test section. The resulting temperature maps are shown in Fig. 3.14 a) and b) respectively. This second image characterizes the surfaces that are in contact with the fluid, needed to properly set the thermal boundary condition used in the simulations.

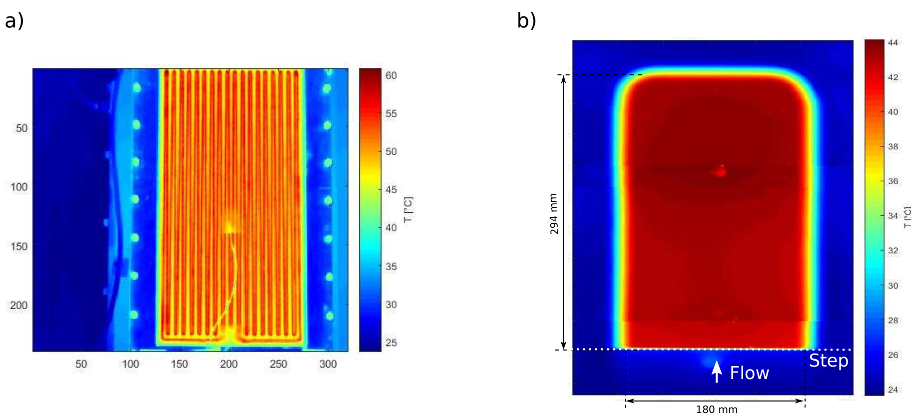

Figure 3.14: *IR measurements of the plate temperature in air at 7 m/s a) Outside wall of the test section b) Inside wall of the test section.*

Although the heating resistance is not perfectly uniform (see Fig. 3.14 a)), the conductive plate under which it is fixed has a high thermal diffusivity. This results in a temperature distribution that is practically uniform inside the test section (see Fig. 3.14 b)). One can notice two colder spots along the center line of the test section, which can be attributed to the presence of screws, but these effects remain negligible. Furthermore, this latest image also demonstrates that the heated plate is well insulated on either sides, and conjugate heat transfer effects can thus be neglected in the simulations. Consequently, it seems reasonable to impose in the LES a constant temperature T_w along the heated plate and adiabatic walls elsewhere. The power supplied to the thermal resistance is adjusted during the experiment in order to keep the temperature gradient between the heated plate and the flow approximately constant ($\Delta T = T_w - T_{in} \simeq 22\,°C$). This gradient serves as reference in the LES with air and the gas mixture.

In thermal problems, the importance of natural convection can be represented by the Richardson number. In the case of a BFS, it is defined as follows:

$$Ri = \frac{g\,\beta\,\Delta T\,h}{U_{in}^2}\,. \tag{3.8}$$

In this case, it is equal to roughly 3×10^{-4}, which clearly corresponds to a forced convection regime. However, this value is based on the free-stream velocity, while much lower velocities are found within the separated flow area. Nevertheless, buoyancy effects may still have a non-negligible influence in this zone.

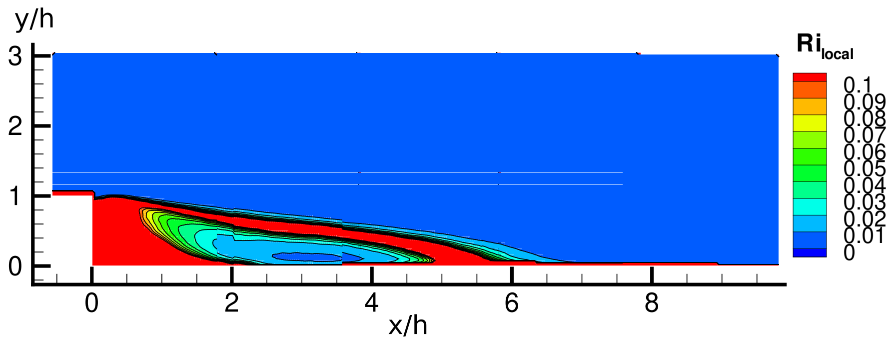

Figure 3.15: *Contours of local Richardson number obtained in air by PIV, for the heated BFS at 7 m/s.*

To help quantify these effects, a local Richardson number can be defined based on the local velocity magnitude as measured by PIV. These contours, shown in Fig. 3.15, are saturated above 0.1 in order to exclude much higher values that go towards infinity because of very low velocities. This way of representation also highlights the areas where buoyancy may start playing a more dominant role (saturated levels, $Ri > 0.1$). The influence of heating effects will be further investigated in Section 3.4.2.3, where PIV results obtained with and without heating will be compared.

3.4.2 Thermal-hydraulic characterization

3.4.2.1 Boundary conditions for the LES

As explained previously, one of the objectives of the PIV campaign is to clearly define the inputs required by the LES. By measuring the TBL development along the upstream fetch, the inlet velocity profile and the reference state at one step height before the step ($x = -1\,h$) are obtained. The first is needed as input by the optimized TPM to generate inflow turbulence. Profiles of streamwise and wall-normal velocity all along the inlet boundary are extracted from the the PIV. The second needs to be approached by the LES, if one wants the flow conditions to be comparable to the experiment. Because this particular aspect of this work is fundamental, it is the focus of Chapter 4, where more details can be found about the adjustments needed in the LES to reach this objective.
The streamwise component of velocity measured at the three locations shown in Fig. 3.9 are represented in Fig. 3.16 hereafter. Considering the importance of the step profile, it is also measured with a HWA and both measurement techniques appear to be in good agreement.

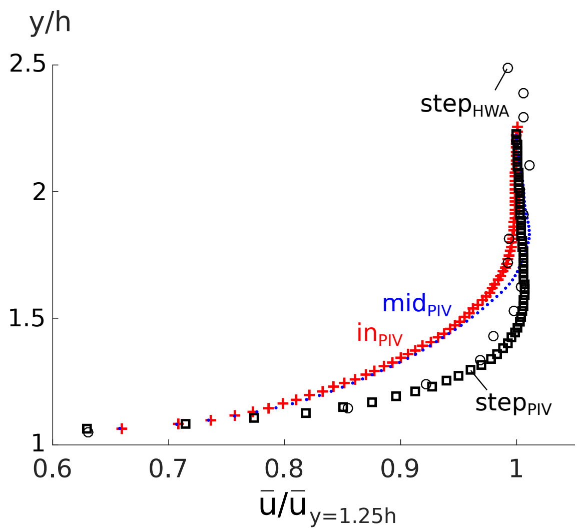

Figure 3.16: *Streamwise velocities measured in air by PIV and HWA upstream of the step.*

The variation in boundary layer thickness along the fetch is of particular interest for the LES. The following values are obtained experimentally: $\delta_{in} = 1.3\,cm$ and $\delta_{step} = 0.85\,cm$. Instead of growing, the boundary layer shrinks by 35 %, which can be related to the very short distance available downstream of the sand strip. As a consequence, some modifications in the inlet velocity profile will be needed in order to match the targeted ratio $\delta/h = 0.425$ that is obtained experimentally.

3.4.2.2 Top boundary conditions

While setting-up the LES, a boundary condition for velocity and pressure has to be specified along the top boundary of the domain.

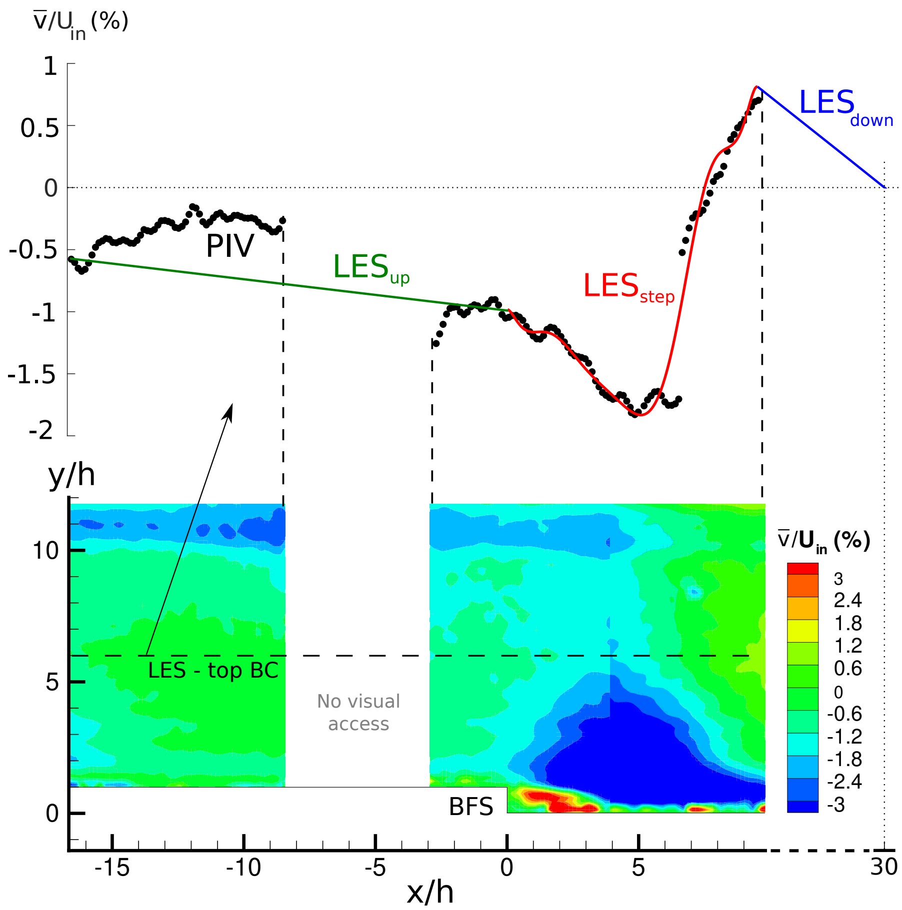

Figure 3.17: *Contours of vertical velocity (saturated) obtained in air by PIV, for the non-heated BFS at 7 m/s.*

Different approaches are investigated in Appendix C, and the most realistic results are obtained by imposing zero vorticity along the upper boundary together with the normal velocity. Consequently, measuring this distribution is one of the objective of the PIV campaign, which is done by covering the part of the domain that can be visually accessed (see Fig. 3.9). Contour levels measured through the wind tunnel windows are represented in Fig. 3.17. These serve as reference while adjusting the height of the top boundary in order to limit its influence in the region of interest. While the separation area has a noticeable impact on the flow near the step, this influence reduces from a vertical distance of 6 h and above. Above this map, variations along this top LES boundary are plotted and serve as basis while imposing the normal velocity distribution in the LES. The measurements are fitted in the step area and a linear variation is applied elsewhere.

3.4.2.3 Separated flow area

General flow description

PIV contours of the streamwise and vertical velocity are shown in Fig. 3.18 and Fig. 3.19 that typically illustrate the common features observed in a BFS flow.

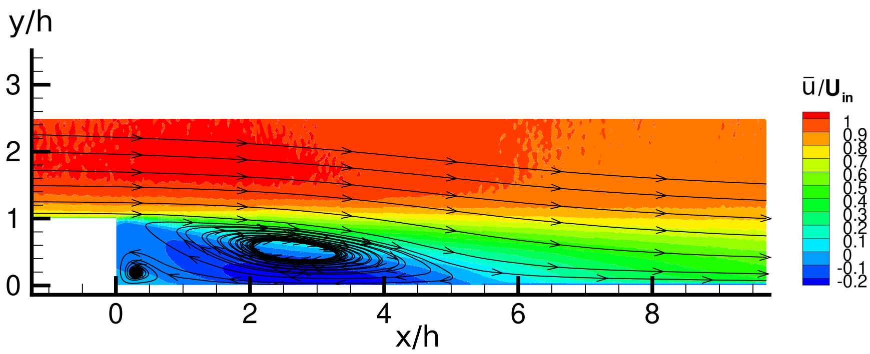

Figure 3.18: *PIV contours of the time averaged streamwise velocity for the heated BFS, in air at 7 m/s ($Re_h = 8930$).*

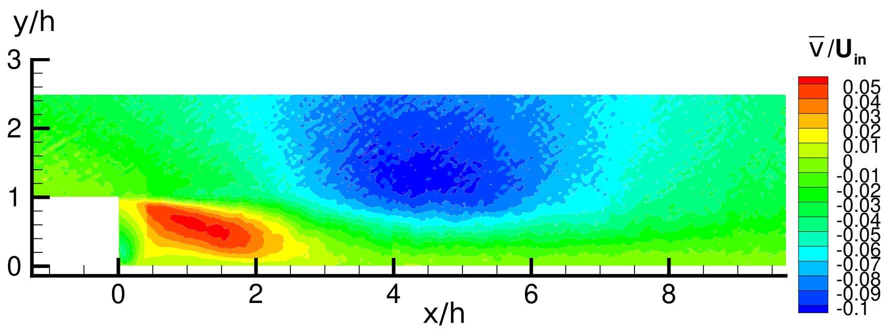

Figure 3.19: *PIV contours of the time averaged wall-normal velocity for the heated BFS, in air at 7 m/s. Streamlines are also shown (solid line with arrows).*

Its general characteristics are initiated by an upstream boundary layer that separates at the step corner, due to the sudden expansion. The turbulent structures contained within the growing shear layer region entrain the outside flow, thus creating a low velocity recirculation region in between the layer and the step wall. Examining the reconstructed PIV data that is obtained by stitching the height measurement windows presented in Section 3.3.3, the continuity between levels appears to be very good.
The turbulence intensity contours are represented in Fig. 3.20. More generally, a free shear layer originates at the separation point. It is created due to the difference in velocities between the free-stream and the low momentum fluid in the wake of the step. In the shear layer, the exchange of momentum is related to a vortex pairing mechanism [21]. It is characterized by the rolling and amalgamation of vortices that play an important role in the growth of the turbulent shear layer. Fluid entrainement also participates in this expansion and the shear layer curves down towards the wall and impinges at the reattachment point.

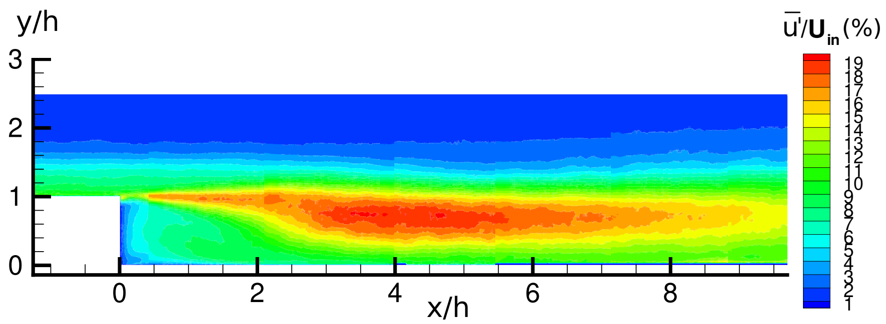

Figure 3.20: *PIV contours of the streamwise turbulent intensity for the heated BFS, in air at 7 m/s.*

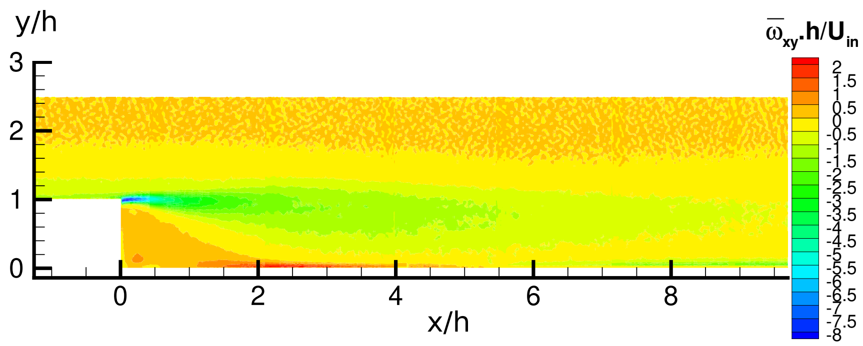

Figure 3.21: *PIV contours of the time averaged vorticity for the heated BFS, in air at 7 m/s.*

As suggested by the results of Bradshaw and Wong [19], the shear layer continues to spread after reattachment into a new shear layer with a sub-boundary layer underneath. This explains why high turbulence levels are still observed downstream of the recirculation area. Contours of vorticity are shown in Fig. 3.21. High vorticity is observed in regions of strong velocity gradient that appear within the shear layer and near the wall. These also confirm that considering zero vorticity along the top boundary in the LES constitutes a very good assumption.

Reynolds number independency

During this campaign, measurements have been performed at two different free-stream velocities of 7 m/s (700 rpm) and 10.3 m/s (1000 rpm). The corresponding Reynolds numbers based on the step height are $Re_h = 8930$ and $Re_h = 13200$ respectively.

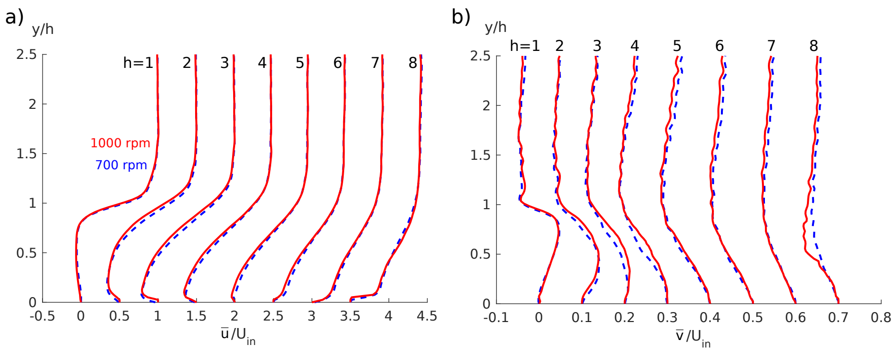

Figure 3.22: *Influence of the free-stream velocity on the velocity profiles, PIV measurements in air for the heated BFS.*

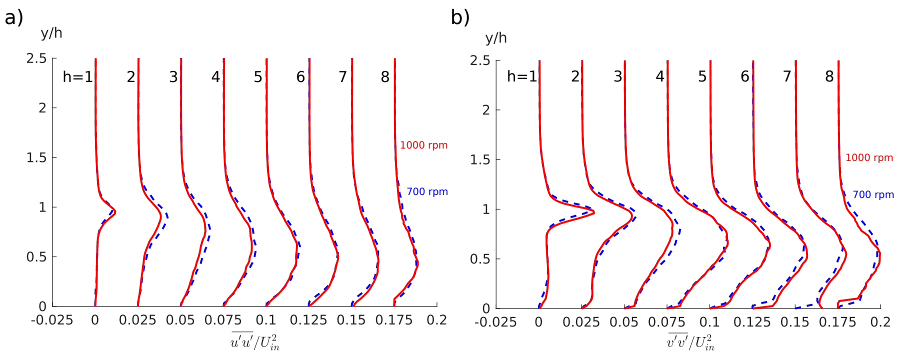

Figure 3.23: *Influence of the free-stream velocity on the streamwise and wall-normal Reynolds stresses, PIV measurements in air for the heated BFS.*

Armaly et al. [11] studied in detail the effect of Reynolds number on the reattachment length. Their results indicate that, once in the turbulent flow regime ($Re_h > 6600$), the size of the separated flow area remains relatively constant. In agreement with these previous observations, the streamwise and vertical velocity profiles, extracted every h after the step and presented in Fig. 3.22, show negligible differences. The streamwise and wall normal Reynolds stresses are also extracted from the PIV results in Fig. 3.23 and, there again, the change in free stream velocity has very little influence.

Thermal effects

As computed previously, the Richardson number is equal to about 3×10^{-4} which is representative of a forced convection case. Thus, the buoyancy effects, even in the recirculation area, should remain negligible. These effects are investigated by comparing two sets of PIV results obtained with and without heating. The recirculation area remains roughly the same size, with a reattachment length of $5.2\,h$ without heating and $5.3\,h$ with heating, which represents less than $2\,\%$ variation. The profiles of velocity and Reynolds stresses are compared in Fig. 3.24 and 3.25. As expected, the natural buoyancy effects are very limited as heating effects have a negligible influence on the flow within the separation area.

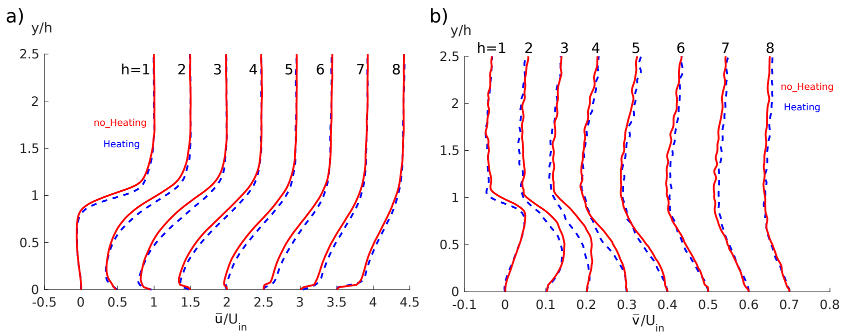

Figure 3.24: *Thermal effects on the velocity field, PIV measurements in air at 7 m/s ($Re_h = 8930$).*

This investigation is complemented by micro-TC measurements of the flow temperature across the separated flow area at the streamwise locations of $0.15\,h$, $2.15\,h$, $4.15\,h$ and $8.15\,h$ after the step [28]. The free-stream velocity is changed to cover regimes from forced to natural convection. The mean temperature profiles obtained at rest and low velocity ($U_{in} \simeq 2\,m/s$) are shown in Fig. 3.27. The profiles acquired at higher velocities ($U_{in} > 5\,m/s$) are presented in Fig. 3.26. The forced convection dominates at these higher speeds and the thermal-hydraulic field remains unchanged. The highest temperatures (i.e. lowest $T_w - T$) appear in the step corner region where a secondary recirculation forms. In the case of mixed convection ($U_{in} \simeq 2$ m/s) however, the

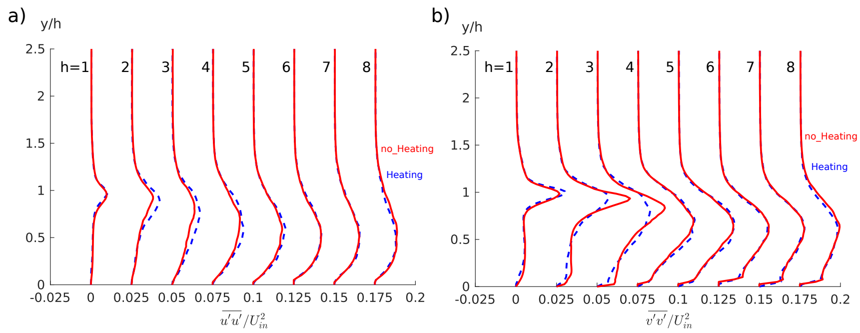

Figure 3.25: *Thermal effects on the streamwise and wall-normal Reynolds stresses, PIV measurements in air at 7 m/s ($Re_h = 8930$).*

increasing buoyancy effects start to affect the average flow. The primary recirculation is reduced as the buoyancy accelerates the flow near the heated wall, and counteracts the clockwise rotating vortex [101]. At rest, the natural convection effects alone are sufficient to create a small bubble in the step corner while a thicker boundary layer appears further downstream.

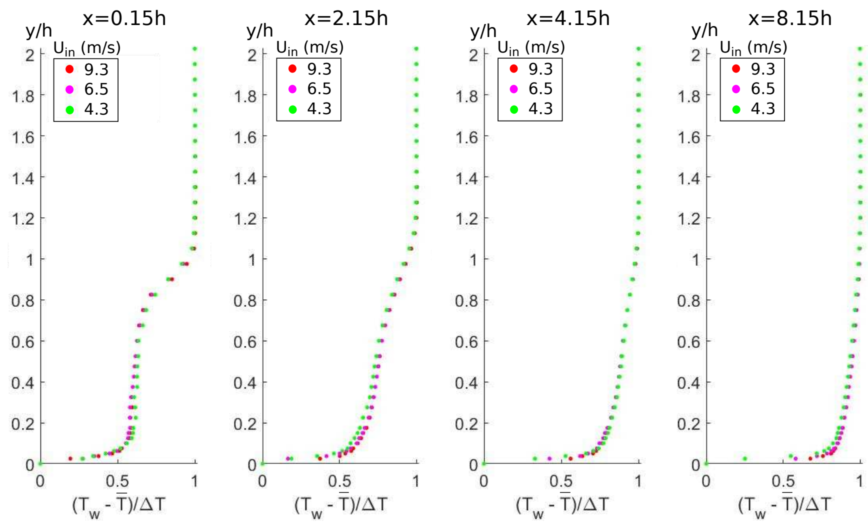

Figure 3.26: *Micro-TC measurements in air, forced convection regime (4-10 m/s).*

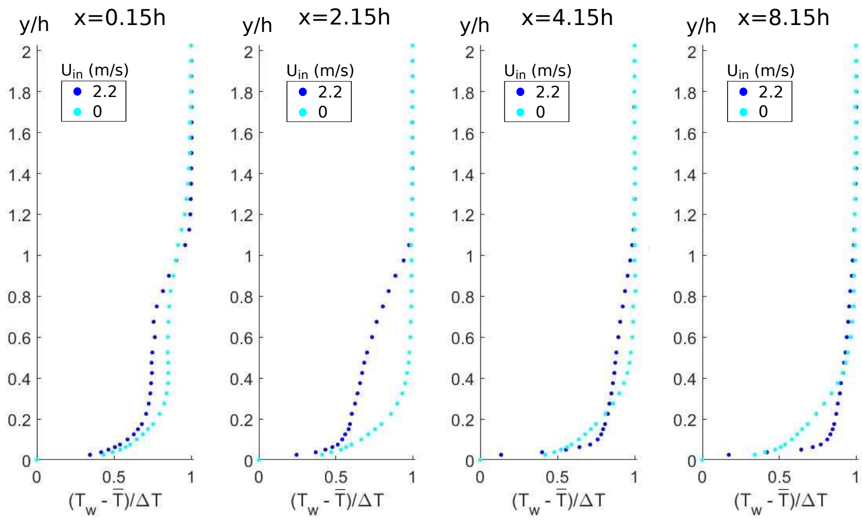

Figure 3.27: *Micro-TC measurements in air, at rest and in mixed convection regime ($U_{in} \simeq 2\,m/s$).*

3.5 Conclusions

This Chapter summarizes the experimental set-up used for the BFS experiment. After a brief introduction to the MYRTE wind tunnel, the dimensions of the test section are defined so that the flow remains unconfined. It is further characterized by carrying out surface temperature measurements at the level of the heated step. IR images highlight a quasi-uniform distribution which serves as a basis for later assuming a constant temperature T_w in the LES.
Experimental results obtained with air are presented. The flow is characterized from a hydraulic point of view by PIV. A very accurate description of the average flow field is obtained by acquiring a large number of samples and by covering the separated area with height windows that are then stitched together. This reduces considerably the random error, even on the turbulence quantities ($< 4.3\,\%$), while a high spatial resolution of about $0.5mm$ is reached. A long recirculation, typical of the BFS flow in forced convection, is found. The shear layer is bent down by the low pressure region caused by the expansion and reattaches at approximately 5.3 step heights downstream of the step. This data will serve as reference in Chapter 5 when comparing with the average flow field obtained by LES. There also probe measurements done in the gas mixture that will be compared to the LES. For this, the new probe designed to measure simultaneously the velocity and temperature, by combining a HWA and a micro-TC, is introduced. Limitations due to spatial constraints and frequency response are highlighted. These will be further investigated by LES before comparing the data with the simulations run at moderate Prandtl numbers.
For the LES to be trully comparable to the experiment, it is crutial for the

incoming flow just before the step to be similar. The TBL development along the upstream fetch is measured by PIV and will serve as reference in Chapter 4, where special attention is given to this particular aspect. Finally, the normal velocity distribution along the top boundary of the computational domain is measured so that all inputs required by the LES are known.
These measurements in air also provide the opportunity to study how sensitive the flow is to changes in free-stream velocity. As expected in a turbulent flow regime, the results are Reynolds number independent at $Re_h = 8930$ since negligible differences are observed compared to the PIV results obtained at $Re_h = 13200$. In this forced convection regime ($Ri \simeq 3 \times 10^{-4}$), hardly any variations are observed between the average flow fields obtained with and without heating the step wall. This tendency is confirmed by micro-TC measurements done at different free-stream velocities. However, buoyancy forces play an important role at lower velocity by attenuating substancially the primary recirculation. Natural convection effects alone are sufficient to drive a flow and create a small recirculation in the step corner.

Chapter 4

Temperature Perturbation Method applied to a turbulent boundary layer

4.1 Introduction

Previously in Chapter 2, the TPM has been further improved to be able to generate turbulence in the case of typical wall-bounded flows. This new approach consists in creating a perturbation zone at the entrance of the computational domain, through which the Richardson number that controls buoyancy effects is modified. Appropriate modulation of this artificial quantity has proved to efficiently create turbulence along a channel flow. Up to now, the optimized TPM has only been applied to a confined flow, whereas the final objective is to simulate a non-confined flow over a BFS. Consequently, the next step is to test the approach in representative flow conditions, meaning that the flow should be free to develop in the absence of confinement, similarly to the MYRTE experiment upstream of the step.

The focus of this Chapter is therefore to simulate a zero-pressure gradient (ZPG) TBL developing along a flat plate. Firstly, the DNS database of the Royal Institute of Technology (KTH) [80] serves as reference, while the MYRTE experiment was under preparation. This preliminary database is very useful to get acquainted with this new flow configuration and to point out specificities such as top boundary conditions that have to be carefully handled in order to avoid disrupting the flow development. The parametrization of the method is reviewed and key modelling parameters are adjusted in order to reduce discrepencies.
Secondly, the MYRTE upstream section before the step is simulated by LES. The measurements carried out along the section and presented in Chapter 3 provide the necessary information for the TPM, with the mean velocity profile needed as input and information regarding the TBL development. The aim is to adjust the numerical inflow to best approach the BL state measured just before the step, for the LES and the experiment to be comparable over the BFS.

4.2 Background on turbulent boundary layers

4.2.1 Progress in simulations of TBL

The study of wall bounded turbulence certainly constitutes one of the most important subjects of research in turbulence. A large part of the frictional drag produced by moving bodies immersed in a fluid originates from fluid motion close to the wall. The prospect of reducing drag thanks to a better understanding of wall turbulence is very interesting for air transportation for instance. Although practical cases usually feature complex geometries with curved surfaces that induce pressure gradients, or bluff bodies promoting separation, the canonical case with ZPG has always remained an important flow for theoretical, experimental and numerical studies, for which a large amount of literature data exists.
Experiments have been used in fundamental research for decades, and although computational power is increasing fast, the Reynolds numbers reached numerically remain limited because of the long averaging times induced by the loss of streamwise homogeneity compared to periodic flows in pipes or channels. On the one-hand, experimental measurements have the great advantage of dealing with the "real" flows, as these will always remain physically correct. On the other-hand, the main drawback of experiments is that their accuracy often deteriorates close to the wall. Nevertheless, the rapid improvement of visualization-based techniques such as PIV, allows great insight into the vortical structure of the flow [5]. Also more traditional techniques, such as hot-wires, are constantly being improved to deal with issues related to spatial resolution [107] or correct determination of the wall position [108]. As far as low Reynolds number TBL measurements are concerned, in depth analysis of existing data [106] has shown that direct skin-friction measurements are often missing and ZPG equilibrium conditions are not properly controlled. Moreover, inflow and upstream conditions are not usually well documented, which prevents any serious cross-validation between experiments and simulations below the limit of $Re_\theta \simeq 2000$ [137]. Considering the limited range of $Re_\theta < 1000$ that will be reproduced in the MYRTE experiment, the availability of more trust-worthy numerical simulations is investigated.

For validation, direct numerical simulations (DNS) provide the most accurate answer to the governing equations and provides detailed information about the flow field. The Navier-Stokes equations are solved without any assumptions for the physics. The absence of turbulence modelling limits the source of errors to numerical approximations and domain truncation, provided this "numerical experiment" is subject to the same scrutiny than laboratory experiments. As highlighted by a recent assessment of available DNS data carried out by Schlatter and Örlü [136], the flow is particularly sensitive to inflow boundary conditions and computational box dimensions. Unlike turbulent channel flows, the number of DNS database is small at medium to high Reynolds numbers ($Re_\theta > 650$). This latest Reynolds number is commonly used to describe boundary layers, and is based on the momentum thickness θ, the velocity U_∞

above the boundary layer and the viscosity ν, such that $Re_\theta = \theta U_\infty/\nu$.

Authors	$Re_{\theta,max}$	Method
Spalart (1988) [156]	1410	Spectral Spatio-temporal
Komminaho et al. (2002) [70]	716	Spectral Tripping at $Re_\theta \simeq 200$
Khujadze et al. (2004, 2007) [65, 66]	2807	Spectral Tripping close to inflow
Ferrante et al. (2005) [44]	2900	Finite differences Rescaling and recycling
Simens et al. (2009) [150]	1968	Finite difference/spectral Rescaling and recycling
Schlatter et al. (2009) [138]	4271	Spectral Tripping at $Re_\theta = 180$
Wu and Moin (2009) [173]	900	Finite differences Free-stream disturbances

Table 4.1: *List of considered DNS databases in the assessment performed by Schlatter and Örlü [136].*

Among the DNS databases listed in Table 4.1, most have been compared and validated with experimental results (e.g. [39, 106, 109]). The DNS of Spalart [156] has been extensively used for the last decades. However, the multi-scale procedure used to insure turbulent flow by retaining periodic streamwise conditions did not allow for a natural development of the boundary layer. To simulate a truly spatially developing TBL, turbulence has to be somehow generated at the inflow. Laminar-turbulent transition can be induced by tripping the boundary layer [70], for instance using a random volume force near the wall [65, 66]. Wu and Moin [173] trigger transition via free-stream disturbances, which allows the structures to evolve naturally from the wall layer. However, a long streamwise domain is required to simulate the transition process. Recycling and rescaling of downstream turbulence [84] is often used [44], and although spurious periodicity may be introduced by these methods, excellent agreement on both the mean and other statistics was observed by Simens et al. [150]. It was noted however that a developing distance of at least 300 initial momentum thicknesses was necessary for the artificial inflow to be "forgotten" by the flow.

The DNS of Schlatter et al. [138] is selected to validate the wall-resolved LES performed in this study. This recent simulation has been carried out at KTH, Stockholm, using an in-house spectral code SIMSON. A laminar Blasius velocity profile is inserted at $Re_\theta = 180$ and the flow is tripped by a random volume force shortly after. The domain extends all the way up to $Re_\theta = 4300$, after which the outflowing fluid is forced back to the laminar inflow within a so-called fringe region, to accomodate for the streamwise boundary conditions enforced by the Fourier discretization. The mesh resolution is given by $\Delta x^+ \simeq 9$ and $\Delta z^+ \simeq 4$, which is comparable to high Reynolds channel flow simulations (e.g. [53]). This DNS was performed in close collaboration with an experimental investigation by means of hot-wire and oil-film interferometry. An exceptional agreement was found between the two sets of results in the skin-friction coefficient, integral quantities, mean and also root-mean square profiles. It therefore constitutes an excellent reference for validation. A detailed database is available online [135], containing integral quantities and velocity profiles at a number of selected streamwise positions.

4.2.2 Theoretical description

4.2.2.1 Integral quantities

As opposed to fully-developed channel flows, the flow over a flat-plate evolves spatially in the streamwise direction. The development can be assessed by determining the variations of boundary layer parameters.
As a global parameter, the boundary layer thickness is defined as the distance from the wall to a point where the mean steamwise velocity $\overline{u}$ has reached 99 % of the free-stream velocity, U_∞, such that:

$$\overline{u}(\delta) = 0.99\, U_\infty\ . \tag{4.1}$$

Integral quantities include the displacement thickness, δ^*, and the momentum thickness, θ. These correspond to the distance by which a surface would be displaced away from the wall to give the same flow rate and the same total momentum respectively, in an inviscid fluid. These are calculated as follows:

$$\delta^* = \int_0^\delta \left(1 - \frac{\overline{u}}{U_\infty}\right) dy\ , \tag{4.2}$$

$$\theta = \int_0^\delta \frac{\overline{u}}{U_\infty}\left(1 - \frac{\overline{u}}{U_\infty}\right) dy\ . \tag{4.3}$$

For the case with constant velocity above the boundary layer, $\rho U_\infty^2(\theta_{x_2} - \theta_{x_1})$ is the drag force exerted on the fluid by the plate between x_1 and x_2 [1].

The shape factor, H_{12}, defined as the ratio between these two distances:

$$H_{12} = \frac{\delta^*}{\theta}\ , \tag{4.4}$$

is used to determine the nature of the flow, and is therefore very useful to characterize the state of development of the boundary layer. It also gives a direct quantitative assessment of the mean streamwise velocity profile independently from the skin friction (i.e. wall-normal derivatives).
A self-consistent description of such parameters could be obtained from the

[1] This is no longer the case with varying velocity: see von Karman integral equation.

work of Monkewitz et al. [89] on the asymptotic behavior of integral parameters. Some other physical parameters of interest are the Rotta-Clauser length scale $\Delta = U_e^+ \delta^*$ where U_e^+ is the outer velocity normalized by the friction velocity. The *Monkewitz* correlation is obtained by combining the exact result

$$H_{12} = \frac{1}{1-(C'/U_e^+)}\,, \quad C' = \int_0^\infty \left(U_e^+ - u^+(y)\right)^2 d(\frac{y}{\Delta}) \tag{4.5}$$

with the empirical approximation $C' = 7.135 + (1/Re_\theta)$.

4.2.2.2 Boundary layer equations

For statistically steady two-dimensional boundary layers, the governing equations for the mean flow can be obtained by averaging the Navier-Stokes equations and assuming boundary layer approximations [140]

$$Re \to \infty,\ \overline{v} << \overline{U}_\infty,\ \partial/\partial x << \partial/\partial y\,, \tag{4.6}$$

such that constant-density averaged continuity and momentum equations become:

$$\frac{\partial \overline{u}}{\partial x} + \frac{\partial \overline{v}}{\partial y} = 0\,, \tag{4.7}$$

$$\overline{u}\,\frac{\partial \overline{u}}{\partial x} + \overline{v}\,\frac{\partial \overline{u}}{\partial y} = -\frac{d\overline{p}_\infty}{dx} + \frac{\partial}{\partial y}\left(\frac{1}{Re}\frac{\partial \overline{u}}{\partial y} - \overline{u'v'}\right) - \frac{\partial}{\partial x}\left(\overline{u'u'} - \overline{u'v'}\right)\,. \tag{4.8}$$

According to Bernouilli's equation, the free-stream pressure p_∞ can be replaced by $U_\infty \frac{dU_\infty}{dx}$. Schlatter et al. [139] show that the contribution coming from the last term of Eq. (4.8), namely the "Townsend term" $\frac{\partial}{\partial x}\left(\overline{u'u'} - \overline{u'v'}\right)$, is one order of magnitude smaller than the other leading terms. The so-called von Karman integral momentum equation is obtained by integrating Eq. (4.8) from the wall to the free-stream:

$$\frac{\overline{\tau}_w}{\rho} = \frac{d}{dx}\left[U_\infty^2 \int_0^\infty \frac{\overline{u}}{U_\infty}\left(1-\frac{\overline{u}}{U_\infty}\right)dy\right] + U_\infty\frac{dU_\infty}{dx}\int_0^\infty \left(1-\frac{\overline{u}}{U_\infty}\right)dy\,, \tag{4.9}$$

where τ_w is the total shear stress. Introducing the skin friction coefficient C_f, and using the definitions given by Eq. (4.2) and (4.3), Eq. (4.9) can be rewritten as

$$C_f = \frac{\overline{\tau}_w}{\frac{1}{2}\rho U_\infty^2} = 2\,\frac{d\theta}{dx} + \frac{4\,\theta + 2\,\delta^*}{U_\infty}\frac{dU_\infty}{dx}\,. \tag{4.10}$$

In ZPG conditions, the second term of Eq. (4.10) is identical to zero. From experiments, the skin friction can be calculated according to Eq. (4.10), however this requires a very well resolved mean velocity profile and as noted by Örlü [106], a direct measurement via oil-film interferometry is the most accurate way of determining the skin friction. Correlations have been derived that express the skin-friction coefficient as a function of Re_θ, for instance by Kays and Crawford [62]):

$$C_f = 0.024\, Re_\theta^{-1/4}\,, \tag{4.11}$$

and by Österlund [109]:

$$C_f = 2\left[(1/0.38)\log Re_\theta + 4.08\right]^{-2}\,. \tag{4.12}$$

In turbulent boundary layers, the entire flow field is divided into the outer irrotational flow, and the boundary layer that is turbulent. Within this turbulent boundary layer and for the case of a hydraulically smooth wall, two layers can be distinguished; the inner layer which is the region close to the wall ($y/\delta \leq 0.15 - 0.2$) and the outer layer which is the rest ($0.15 - 0.2 \leq y/\delta \leq 1$). Within the inner layer, an overlap layer is found, where turbulence dominates.

4.2.2.3 The turbulent boundary layer

In the very near-wall region, the viscous dissipation increases and, as a result, the velocity fluctuations decrease as the wall is approached. The Reynolds shear-stress becomes negligible compared to the growing contribution of viscosity. The boundary layer equation simplify to the following:

$$0 = \nu\frac{\partial^2\overline{u}}{\partial y^2} - \frac{\partial\overline{u'v'}}{\partial y} = \frac{1}{\rho}\frac{\partial\overline{\tau}_{tot}}{\partial y}\,. \tag{4.13}$$

As for the channel flow, the mean friction velocity u_τ is defined as

$$\overline{u}_\tau \equiv \sqrt{\frac{\overline{\tau}_w}{\rho}} = \sqrt{\mu\frac{\partial\overline{u}}{\partial y}\Big|_{y=0}}\,. \tag{4.14}$$

Viscous scaling is applied to all variables, based on u_τ and ν. These are denoted by the superscript $^+$. Within the inner layer, the so-called "law of the wall" governs the fluid and states that the flow only depends on the distance from the wall y, the wall shear stress τ_w and the fluid properties, i.e. $\overline{u}^+ = f(y^+)$. Eq. (4.13) becomes

$$\frac{d\overline{u}^+}{dy^+} - \overline{u'v'}^+ = 1\,. \tag{4.15}$$

and expresses the conformity of the total shear stress, consisting in a sum of viscous shear stress and Reynolds shear stress. At the wall, the Reynolds shear stress becomes zero and $\overline{\tau}_w = \rho\, u_\tau^2$. The Reynolds shear stress remains negligible within the so-called viscous sublayer, i.e. $y^+ \leq 5$, and a linear relation is obtained:

$$\overline{u}^+ = y^+\,. \tag{4.16}$$

Leaving the viscous sublayer, the effect of viscosity becomes negligible beyond the buffer layer ($y^+ \geq 70 - 90$, or more precisely $y^+ \geq 2.8\sqrt{\delta^+}$) and turbulence dominates. Under ZPG conditions, Eq. (4.8) becomes

$$\overline{u}\,\frac{\partial \overline{u}}{\partial x} + \overline{v}\,\frac{\partial \overline{u}}{\partial y} = -\frac{\partial \overline{u'v'}}{\partial y}\,. \tag{4.17}$$

The mean velocity profile follows a logarithmic law [169], given by

$$\overline{u}^{+} = \frac{1}{\kappa}\ln\left(y^{+}\right) + A\,, \tag{4.18}$$

where κ is the von Kármán constant and $A \simeq 5$ according to Schlichting [140]. Spalart [156] has shown that for κ, a value of 0.41 gives a good agreement with experimental data for lower Reynolds numbers. Despite the fact that a remarkable scatter in these experimentally deduced constants has been observed until the late 1990 [175], these values have generally been assumed to be universal. Recent DNS [139] and experiments [110] have shown that values of $\kappa \simeq 0.385$ and $A \simeq 4.1 - 4.2$ are better suited for ZPG TBL flows at high-Reynolds numbers.

In the outer layer, the turbulence dominates but the "law of the wall" no longer holds. The velocity profile can be expressed using a composite form

$$\overline{u}^{+} = \frac{1}{\kappa}\ln\left(y^{+}\right) + A + G\left(\frac{y}{\delta}\right)\,, \tag{4.19}$$

following codes where $G\left(\frac{y}{\delta}\right)$ is the complement function (the so-called "wake function"). This function is therefore negligible in the near wall region, and it becomes significant, and thus required, beyond $y/\delta \simeq 0.15 - 0.2$.

For the entire "turbulence dominated" part of the boundary layer ($y^{+} \geq 2.8\sqrt{\delta^{+}}$) one can then also write

$$\begin{aligned}
\overline{u}^{+}(\delta) - \overline{u}^{+}(y) &= \frac{1}{\kappa}\left(\ln\left(\delta^{+}\right) - \ln\left(y^{+}\right)\right) + \left(G(1) - G\left(\frac{y}{\delta}\right)\right) \\
&= -\frac{1}{\kappa}\ln\left(\frac{y}{\delta}\right) + \left(G(1) - G\left(\frac{y}{\delta}\right)\right) \\
&\equiv F\left(\frac{y}{\delta}\right)\,,
\end{aligned} \tag{4.20}$$

which is the "defect law". In the logarithmic part, $y^{+} \geq 2.8\sqrt{\delta^{+}}$ and $y/\delta \leq 0.15 - 0.2$, one thus has both

$$\overline{u}^{+}(y) = \frac{1}{\kappa}\ln\left(y^{+}\right) + A\,, \tag{4.21}$$

and

$$\overline{u}^{+}(\delta) - \overline{u}^{+}(y) = -\frac{1}{\kappa}\ln\left(\frac{y}{\delta}\right) + G(1)\,. \tag{4.22}$$

This is why this region is called the overlap region.

4.2.2.4 Determination of skin friction from experimental data

In the MYRTE experiment over the BFS, the upstream TBL profile obtained by LES will be compared with the measured one just before the step. As commonly done for TBL cases, this comparison will be done in wall units which requires extracting from the measurements the skin friction coefficient C_f. As the closest measurement point to the wall is out of the viscous sublayer, this estimation is made based on the logarithmic law.

A common approach is the so-called Clauser chart method [30]. However, it requires selecting the range of points that are believed to fall within the log-region by visual inspection. This is of course source of uncertainty and estimations were reported to have an error between 8 and 20 % [123].
Instead, the Bradshaw method is chosen as it can easily be automated and is no longer subject to user subjectivity (yet, the law of the wall evaluated at $y^+ = 100$ must not yet be contaminated by the law of the wake, and thus $y/\delta \geq 0.15$ must be satisfied). The value of the dimensionless velocity at $y^+ = 100$ is "known" to be $\overline{u}^+ \simeq 16.2$. Consequently, at this location

$$\frac{\overline{U}_{hw}}{U_\infty} = \frac{\overline{U}^+_{hw} u_\tau}{U_\infty} = \frac{16.2\, y^+ \nu}{yU_\infty} = \frac{1620\, \nu}{yU_\infty} \,. \tag{4.23}$$

The experimental profile is plotted as $\frac{\overline{U}_{hw}}{U_\infty}$ versus $\frac{y\, U_\infty}{\nu}$, together with the hyperbola given by the right-hand side of Eq. (4.23). It results that these two curves intersect at $y^+ = 100$ (and $u^+ = 16.2$). Noting $\overline{U}^*_{hw}$ the velocity at this point, it comes that $\overline{u}_\tau = \overline{U}^*_{hw}/16.2$, and hence

$$C_f = 2\left[\frac{1}{16.2}\left(\frac{\overline{U}^*_{hw}}{U_\infty}\right)\right]^2 \,. \tag{4.24}$$

Thus, the friction velocity needed to plot the mean velocity profile and Reynolds stresses in wall units is directly deduced.

4.3 LES of a zero-pressure gradient turbulent boundary layer

4.3.1 Numerical methodology

The LES that is set-up to reproduce the test case of KTH [138] is described hereafter. The computational domain is $x_L \times y_L \times z_L = 110\, \delta_{in} \times 10\, \delta_{in} \times 2\pi\, \delta_{in}$. The height is chosen to be at least three times the largest boundary layer thickness $\delta_{0.99}$ obtained at the outlet. The inflow is located further downstream compared to the reference, such that laminar-turbulent transition is not part of the set-up. The turbulent mean velocity profile obtained by DNS at $Re_\theta = 670$, is inserted at the inlet. Inflow turbulence is generated using the optimized TPM described in Chapter 2. It is applied for the first time to a TBL, therefore a few adjustments are required compared to a channel flow. As shown in Fig. 4.1

a), the perturbation cells are limited to the inlet boundary layer height where turbulence is the strongest.

The guidelines summarized in Table 2.2 are used to parametrize the technique. As previously, three rows of cells are generated at the inlet. Instead of measuring $8\,\Delta x \times 8\,\Delta z \times 8\,\Delta z$, these are reduced down to $5\,\Delta x \times 5\,\Delta z \times 5\,\Delta z$, in order to fit four perturbation cells across the boundary layer height. A local artificial Richardson number of 0.25 is initially applied along a perturbation zone of $10\,\delta_{in}$. As illustrated in Fig. 4.1 b), this parameter follows a cosine variation of five periods, and is linearly damped from $2\,\delta_{in}$ onwards. The perturbation time scale is set to 0.5.

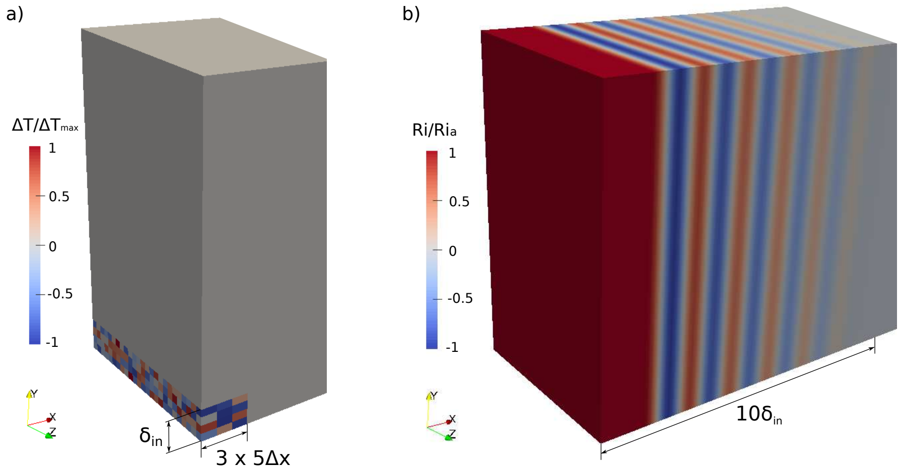

Figure 4.1: *TPM applied to a developing TBL a) Random temperature values assigned to the perturbation cells b) Contours of artificial Richardson number within the perturbation zone.*

A fine resolution grid has been chosen in order to obtain accurate simulations. The mesh is wall resolved ($y^+_{min} < 1$) and the maximum grid spacing in wall units is $\Delta x^+ \times \Delta y^+_{max} \times \Delta z^+ = 30 \times 30.5 \times 15$, based on the friction velocity at $Re_\theta = 800$. An expansion ratio of 1.1 is used in the wall-normal direction up to δ_{in}, with at least 20 points within the region $y^+ < 10$. It is reduced to 1.03 above δ_{in} in order to limit cell growth as the TBL grows. The total mesh size is 10.2 millions cells.
The Smagorinsky sub-grid scale model is used in combination with a Piomelli near wall damping (ref. Section 2.4.2). The model coefficient C_s is initially set to 0.065. The solver settings and numerical schemes are the same as for the LES of a channel flow (ref. Section 2.4.1).

Specifying an appropriate boundary condition along the top of the computational box is not a trivial issue. This point is further discussed in Appendix C, where different boundary conditions are compared in the case of a laminar boundary layer. Conclusions drawn from this study highlighted that a zero vorticity boundary condition allows proper boundary layer growth. The TBL approximate correlation $\frac{\delta^*}{x} \simeq 1.721/\sqrt{Re_x}$ is used in Eq. (C.10) to estimate the wall normal velocity distribution. Zero vorticity is applied to the two other velocity components together with zero pressure gradient.

The TPM appears to successfully triggered the onset of turbulence. Statistics collected on-the-fly over $\Delta t^+ \simeq 6$ in terms of $\delta_{0.99}/u_\tau$ are then spanwise averaged. While higher-order statistics (e.g. skewness and flatness factors) or statistics involving large-scale structures (e.g. spectra at low wavenumbers) would be slower to converge, it is sufficient for low-order statistics (e.g. mean and fluctuations) of interest in this study. This corresponds to roughly 4 flow through times, after which $\overline{u'w'} \simeq 0$. A comparison with the DNS data available at Re_θ positions of 800, 1000 and 1410 is proposed herefater for a quantitative assessment of the LES.

4.3.2 Comparison to the DNS data of KTH

4.3.2.1 Buoyancy effects

The testing of the TPM on a plane channel flow demonstrated that the local artificial Richardson number Ri_a has to be carefully adjusted for the buoyancy triggering mechanism to be efficient. Although an optimum range of $[0.2 - 0.3]$ has been identified previously, it is interesting to verify this and observe its influence in the case of a TBL.

The integral parameters characteristic of the TBL are computed and the numerical results are compared at corresponding streamwise positions. The mean velocity profiles are represented in Fig. 4.2 a) to c), for three different values of Ri_a corresponding to 0.16, 0.25 and 0.65. As expected, the buoyancy forces introduced by the latter case are too strong. This clearly appears on the shape factor H_{12} plotted in Fig. 4.2 d), especially close to the inlet where the profile is greatly distorted. On the Reynolds stresses shown in Fig. 4.3 at $Re_\theta = 800$; the wall-normal and spanwise components are strongly over-estimated due to excessive fluctuations induced by the TPM. These rapidly dissipate downstream, with turbulence intensities that are of the correct order of magnitude. Despite a similar slope in H_{12} at higher $Re_\theta \geq 1200$, flow distorsions get carried along as indicated by the persisting discrepencies in the shape factor ($\simeq 6\%$).
The results are greatly improved by lowering the strength of buoyancy effects down to similar levels as recommended for the channel. With $Ri_a = 0.25$, the perturbations appear to be within an optimum range that triggers effectively turbulence. Although the wall shear stress is under-predicted, the overall shape of the mean velocity profile is better predicted along the fetch. The transitional region during which H_{12} strongly varies and the turbulent structures reorganize is shortened, while differences reach at most $4\,\%$ at $Re_\theta = 1410$.

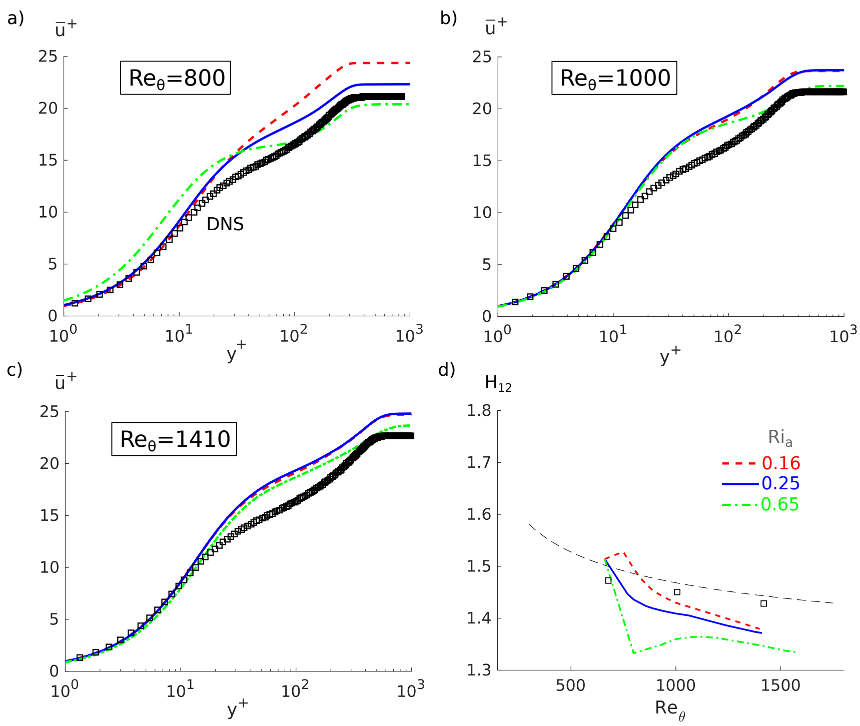

Figure 4.2: *Influence of the artificial Richardson number Ri_a on the mean velocity profiles in a)-c) and on the shape factor H_{12} in d), - - - Monkewitz correlation.*

A partial agreement is obtained for the turbulence intensities and Reynolds shear stress. The inner peak of streamwise Reynolds stress appears at approximately $y^+ \simeq 14$ with a value of 7.25 in the DNS. It is well located by the LES, however its intensity is largely over-estimated (by 35 % at $Re_\theta = 800$). The inner peak, attributed to wall driven shear instabilities, very much dominates the outer peak since the wall is the main source of shear in the case of a ZPG TBL. The outer point of inflection (outer peak) is very well captured. As observed already [10], it also coincides with the slight inflection present in the mean velocity profile, which suggests that a small shear flow instability is causing these fluctuations. No inner or outer peak is evident in the case of the wall-normal and spanwise Reynolds stresses. The profiles are rather dominated by a plateau that spans from $y^+ \simeq 40$ to 100. In general, the location and extent of this region is well captured by the LES, especially at $Re_\theta = 800$, but this is thanks to the inflow technique since, further downstream, the peak value reduces instead of increasing as it should. A realistic behavior is retrieved between the positions $Re_\theta = 1000$ and 1410, but the LES falls below the reference profiles. As for the shear stress, a satisfactory agreement is observed.
Finally, for $Ri_a = 0.16$ the buoyancy effects are not quite sufficient and the

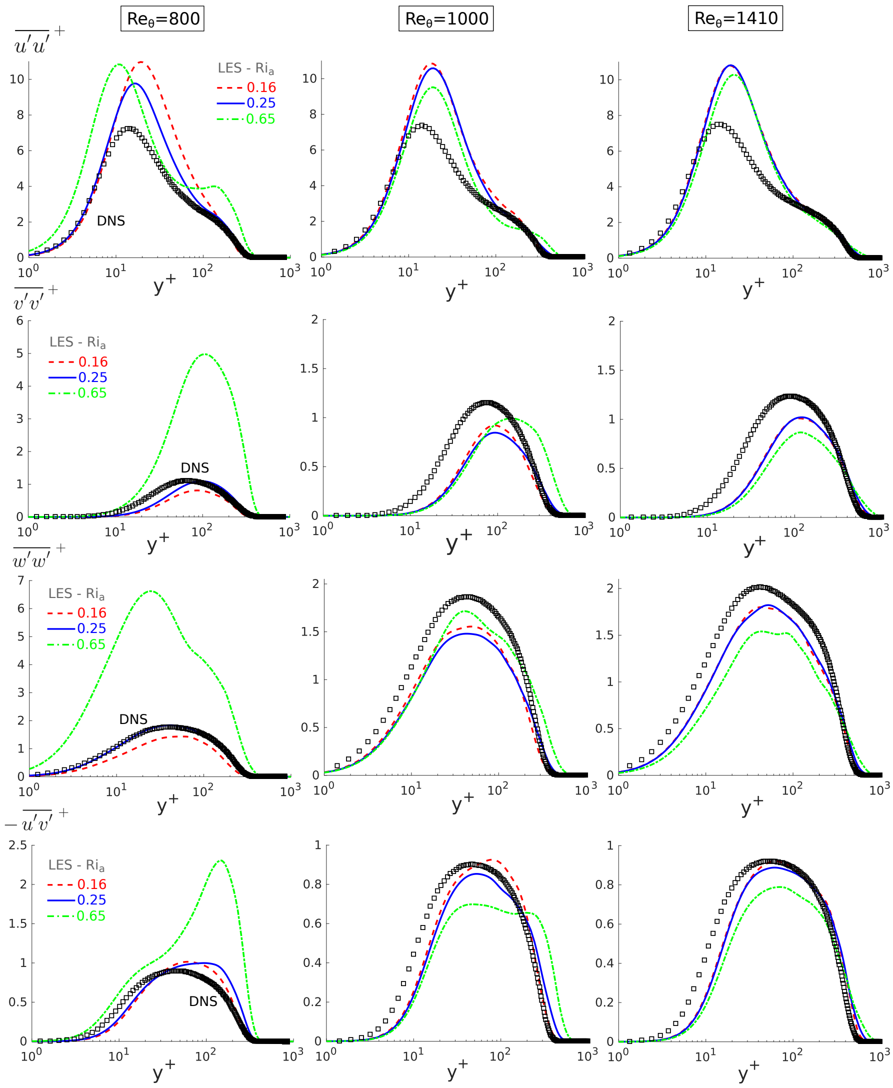

Figure 4.3: *Influence of the artificial Richardson number Ri_a on the Reynolds stresses.*

TPM is less effective. The shape factor H_{12} takes longer to stabilize and the flow solution at the position nearest from the inlet does not agree as well. Further downstream however, the turbulent structures have had enough time to reorganize and the turbulent solution is very similar to the previous case.

This sensitivity study has demonstrated that, similarly to the channel flow, a value of $Ri_a = 0.25$ is found to be most appropriate for a TBL.

4.3.2.2 Influence of the Smagorinsky coefficient

As explained previously, the Smagorinsky coefficient needs to be adjusted to the type of flow. In the case of a channel flow, a value of 0.065 had provided the best agreement with the DNS data at $Re_\tau = 395$.

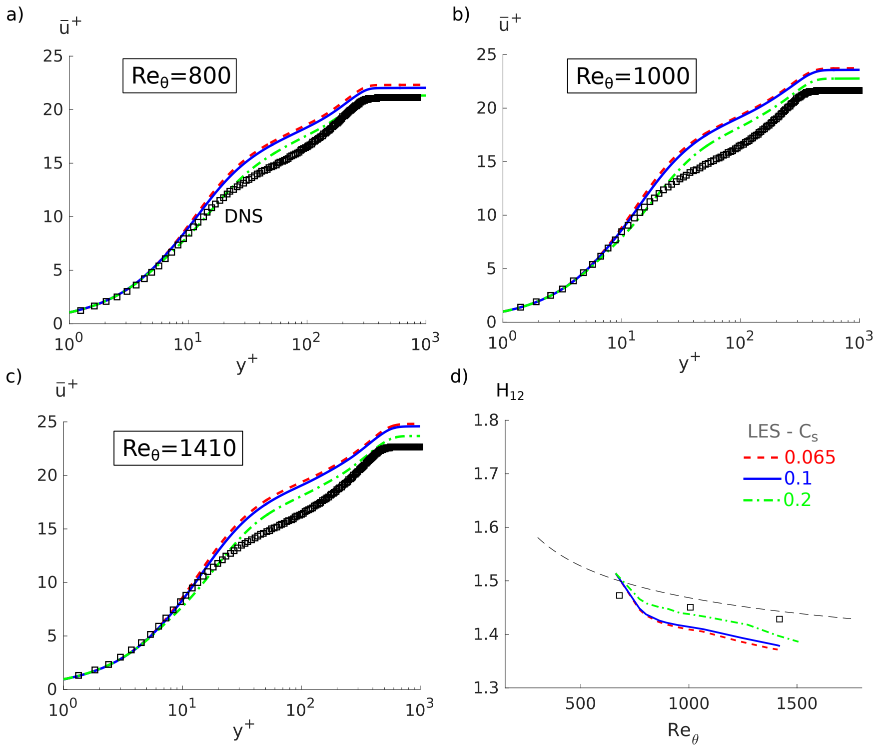

Figure 4.4: *Influence of the Smagorinsky coefficient C_s on the mean velocity profiles in a)-c) and on the shape factor H_{12} in d), - - - Monkewitz correlation.*

Although this value was kept initially, the type of flow has changed from a confined configuration to a spatially developing TBL. It is therefore necessary to reassess whether this value is appropriate for the current test case. For this purpose, two additional LES are run using 0.10 and 0.20. The streamwise variations of the mean velocity profile is represented in Fig. 4.4 a) to c). The best agreement is reached for $C_s = 0.20$, since the overall shape of the profile improves thanks to a better predicted shear stress at the wall. This is directly reflected by the shape factor H_{12} which differs by at most 2 % in Fig. 4.4 d). Concerning the velocity fluctuations in Fig. 4.5, the streamwise turbulence intensity is sensitive to this change, in particular the prediction of the inner peak. Its location shifts slightly from $y^+ \simeq 18$ to 23 for C_s equal to 0.065 and 0.20 respectively, thus moving further away from the DNS located at $y^+ = 14$. However, the peak value reduces; at $Re_\theta = 800$ it is over-estimated by about 5 % whereas the difference increases downstream but stays less than

20 %. This remains a considerable improvement since it was reaching about 35 % previously. The influence of C_s on the other Reynolds stresses is limited, their peaks are also slightly shifted but the effect is less pronounced and the overall shape of the profiles remains very similar. Consequently, the LES of the BFS will be performed using a C_s value of 0.20. The coefficient was not increased beyond 0.20 in order to avoid the peak values in the Reynolds stresses from shifting further away from the reference.

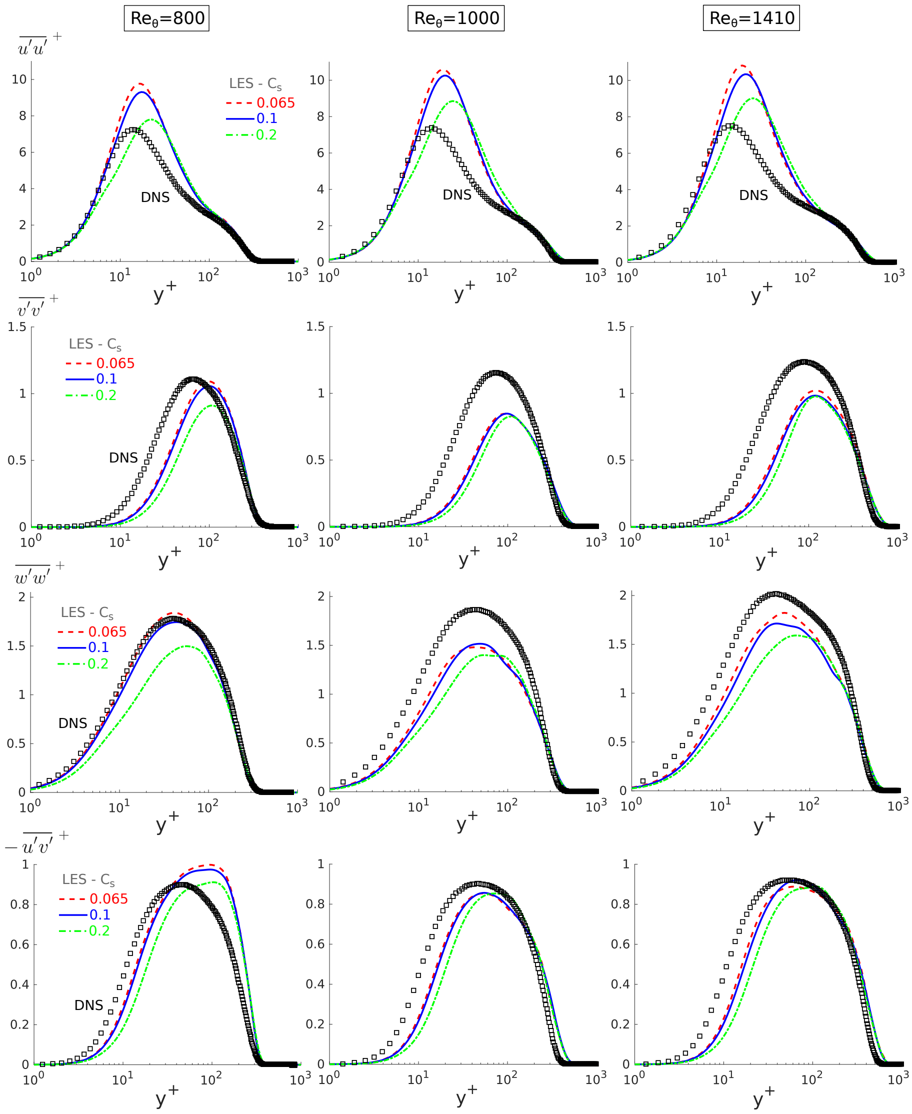

Figure 4.5: *Influence of the Smagorinsky coefficient C_s on the Reynolds stresses.*

4.4 Reproduction of MYRTE upstream conditions

4.4.1 Numerical approach

The focus of this work is to concentrate on the upstream section of the MYRTE experiment and simulate the TBL prior to the step. The objective is to determine at what position along the numerical fetch should the step be in order to have a comparable flow just before the expansion. One recalls, from Chapter 3, that PIV measurements have been made at several positions along the upstream section. Among these, the results obtained at one step height before the step will serve as reference. Therefore, the criteria is firstly to have about the same δ_{step}/h. Moreover, the turbulence intensities should be comparable, as one wants to reach similar inflow conditions between the LES and experiment.

The dimensions of the LES domain are set keeping in mind that this computation will later be part of the LES over a BFS. In particular, the span is set to $6\,h$ since shorter lengths have been reported to be insufficient for the spanwise two-point correlation to drop sufficiently in the separation area [74]. The length of the domain is set to about $30\,\delta_{in}$. PIV measurements presented in Chapter 3 (see Fig. 3.17) had indicated that an upstream height of $5\,h$ would limit the influence of the top boundary.
The numerical set-up is the same as the one used for the preliminary test case of KTH (ref. Section 4.3.1), except that $C_s = 0.20$ according to the sensitivity study performed previously. The boundary conditions are now based on the measurements. The mean velocity profile measured at the entrance of the test section is inserted at the inlet. Along the top boundary, the wall-normal velocity distribution is imposed using a linear fit between the inlet and the step measurements.
To avoid changes in the mesh to alter the results later on in the full computation, the mesh is designed as it would be in the presence of a step. It is progressively refined in the streamwise direction from $\Delta x^+ = 30$ at the inlet to $\Delta x^+ = 5$ at a position located $15\,\delta_{in}$ from the inlet, based on the local friction velocity. This length corresponds to the distance after which realistic turbulence was observed in the case of a channel flow in Chapter 2, in terms of the wall shear stress, the Reynolds stresses and the energy spectrum. It is therefore taken as estimate for the step position. Beyond this position, the mesh is progressively coarsened until the outlet. The mesh resolution in the other two directions is kept the same.

To set-up properly the flow conditions for the LES to match the experiment, several modifications have to be implemented. Firstly, although PIV measurements at different Reynolds numbers showed these effects were minor, the parameter $Re_h (\simeq 8930)$ between the LES and the experiment is kept constant. One important difference though is that no wall effects are reproduced numerically due to spanwise periodicity. Consequently, the free-stream acceleration of 5% measured between the inlet and the step is accounted for by increasing the free -stream velocity at the inlet.

Secondly, to obtain a comparable δ_{step}/h, one must recall from the BL development measurements of Chapter 3 that the boundary thickness at the inlet and at the step were $1.3\,cm$ and $0.85\,cm$ respectively. This corresponds to a shrinking of 35 %, certainly caused by the sand paper strip and very short distance available downstream of this tripping device. In the LES, as for the natural development of a TBL, the opposite trend is observed after the perturbation zone of the TPM. This means that, to reach this objective, the inlet velocity profile needs to be shrinked. To determine by how much, a preliminary LES is run inserting the measured inlet profile without any changes. The evolution of the mean velocity profile is shown in Fig. 4.6 a). Naturally, the TBL grows along the fetch and, between $x = 25\,\delta_{in}$ and $35\,\delta_{in}$, it hardly varies. By that time, the TBL has grown by about 65 % compared to the inlet.

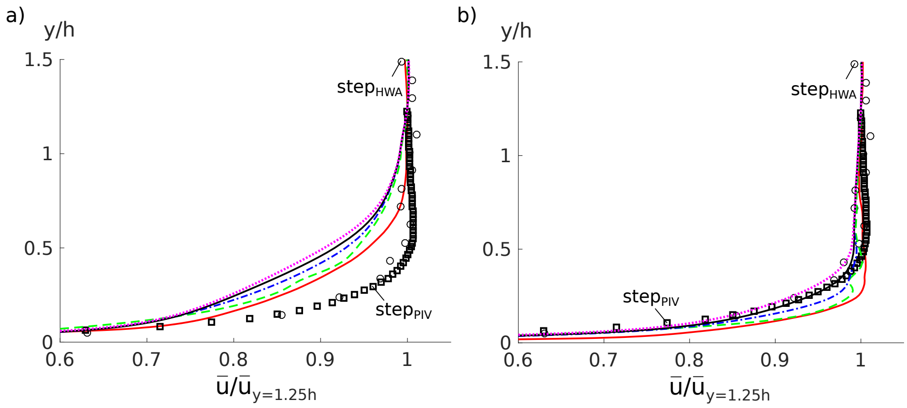

Figure 4.6: *Evolution of the mean velocity profile along the LES domain: —inlet, - - - $5\delta_{in}$, -·-·- $15\delta_{in}$, — $25\delta_{in}$, ······ $35\delta_{in}$ and □ PIV at $x = -1h$ a) original inlet height as measured by PIV b) inlet height shrinked by 35 %.*

Taking this result into account together with the targeted δ_{step}/h, the boundary layer is shrinked at the inlet by a factor of 2.8. This corresponds to $\delta_{in} = 5mm$, which indeed would result in $\delta_{step} = 8.5\,mm$ as measured at $x = -1\,h$. A new LES is run and the results are shown in Fig. 4.6 b). The TBL grows as expected, and one obtains $\delta_{step}/h \simeq 0.41$. This value is considered close enough to the experiment (0.425), and therefore a more detailed comparison of the inflow conditions is proposed hereafter.

4.4.2 Comparison of inflow conditions

The inflow conditions are analyzed by examining the averaged solution, in wall units, in Fig. 4.7. The mean velocity profile is consistently under-estimated, however the shape factor is in excellent agreement. In addition, the starting of the outer flow clearly appears at about the same distance from the wall, which confirms that a comparable δ/h is achieved. As for the Reynolds stresses, there also the comparison is satisfactory. The streamwise component $\overline{u'u'}$ is well predicted by the LES; in particular the inner peak over-predicts the maximum measured point by only 12 %. The outer peak is more pronounced in the PIV, however the differences in this region never exceed 20 %, which remains typical for LES. Finally, the wall-normal component also agrees well. The particular shape, characterized by the presence of an inner and an outer peak, is reproduced by the LES while the turbulence levels remain of the same order.

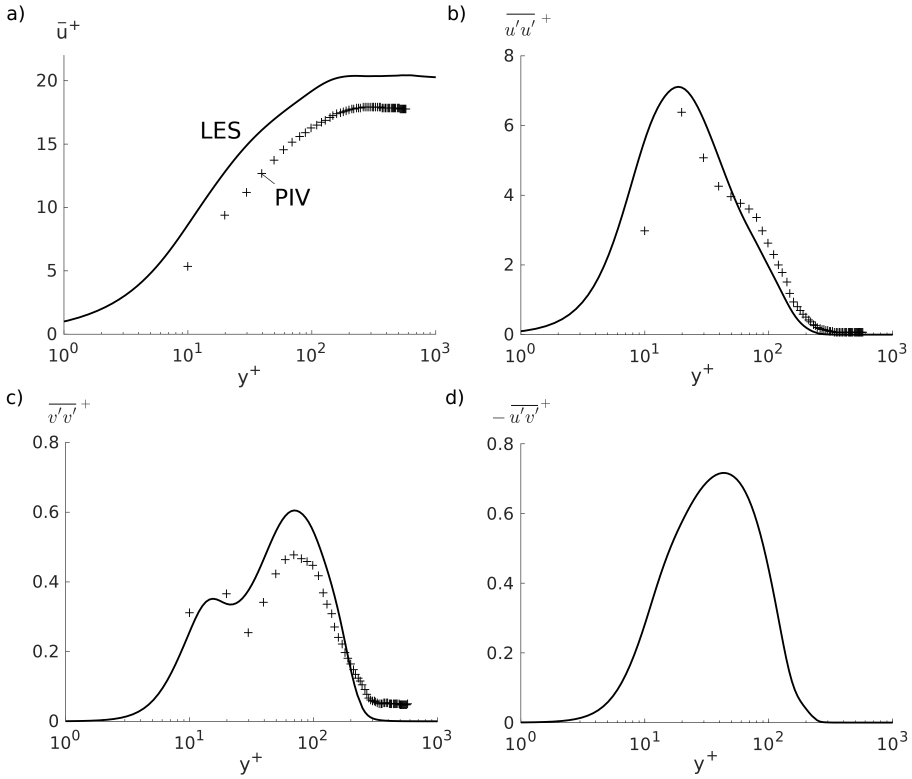

Figure 4.7: *Comparison of the inflow conditions at $x = -1h$ between + PIV and —LES a) mean velocity profile b) streamwise turbulence intensity b) wall-normal turbulence intensity c) Reynolds shear stress (PIV missing for now: loss of data).*

The inflow conditions that are obtained in the LES are considered to be close enough to the experiment, and reproduce a $Re_\theta \simeq 560$ at $x = -1\,h$ before the step. Therefore, the LES over the step is performed in Chapter 5 using the methodology that has been described.

4.5 Conclusions

In conclusion, a first LES of a TBL is run based on the benchmark test case of KTH. It constitutes an opportunity to test the optimized TPM for the first time on a spatially evolving flow. The objective of this preliminary test case

has been to verify that the technique successfully triggers turbulence and provides acceptable results compared to the DNS data. The buoyancy triggering mechanism has proved to effectively generate turbulence at the inflow, provided the strength of these artificial effects falls within the proper range. For $Ri_a = 0.25$, the effect of the artificial inflow is mostly forgotten by the end of the perturbation zone of $10\,\delta_{in}$. Very shortly after is the first reference position ($Re_\theta = 800$), at which, for a suitable Smagorinsky coefficient value of 0.20, the mean flow velocity profile agrees well with the DNS. Concerning the fluctuating velocities, peak values of the three velocity-fluctuation intensities are located slightly further from the wall, and the values are within 20 % compared to reality, which remains typical for LES. Although this is already the case earlier on for the streamwise Reynolds stress, the peak value of all components is increasing from $Re_\theta = 1000$ to 1410 which indicates that the effect of the inflow is no longer felt by the flow. Considering an accomodation length that extends until $Re_\theta = 1000$, this distance corresponds to about 230 initial momentum thicknesses θ_{in}. Distances of at least $300\,\theta_{in}$ are reported in the literature [150] before the artificial inflow is forgotten. As recently survey [63] also confirms that it is difficult to create inflows that have shorter accomodation lengths.
Although a more thorough investigation should be conducted (i.e. streamwise correlations for eddy persistence), the optimized TPM appears to perform as efficiently as competing methods when applied to a TBL; with the advantage once again of only requiring mean velocities at the inlet as input to the method.

The flow along the upstream section of the MYRTE test section has been simulated. This preliminary LES without the step is essential to adapt the set-up so that inflow conditions can be comparable to the experiment. In particular, the free-stream velocity is adjusted to match the Re_h at the level of the step, since side wall effects are not present in the simulation. Also the length of this upstream domain is determined based on the TBL growth rate and the desired δ/h ratio at the step. To approach this criterion, the inlet boundary layer thickness has to be reduced to suit the particularities of the MYRTE experiment in terms of boundary layer development (shrinking). Finally, a satisfactory agreement is reached between the LES and experimental inflow conditions, both in terms of mean and fluctuating properties. This was a necessary achievement before moving on to the BFS simulation, in order to have an LES with conditions just before the step that are comparable to those of the MYRTE experiment.

Chapter 5

Case of a BFS: LES at moderate Prandtl numbers and comparison to experiments

5.1 Introduction

The objective of this Chapter is to compare the LES results with the MYRTE measurements, taking into account the limitations associated to the measurement technique. By treating the LES accordingly, a much more truthfull comparison of the two can be proposed. The aim is then to assess whether the LES is able to predict correctly the turbulent heat transfer. Only then can the data generated in this work be used as reference for turbulent heat transfer modeling of low Prandtl number fluids.

The numerical set-up is firstly described, covering all computational aspects such as domain dimensions, mesh generation and numerical settings. The first comparison between the LES and measurements of the MYRTE experiment concentrates on the results obtained with air. The PIV measurements are taken as reference in terms of mean reattachment length, mean velocity and turbulence intensity. At this point, the LES is also confronted to the mean temperature field measured with a micro-TC in order to complete this assessment of the thermal-hydraulic field.
As introduced previously, an important aspect of this work consists in post-processing the LES for the numerical data to actually be comparable to the experiment. This requires investigating the influence of certain specificities of the HWA-TC probe, related to geometrical constraints or time resolution. Particular attention is brought on the effect of the spacing between the two sensors, as well as the limited frequency response of the micro-TC. The LES is then treated accordingly for comparison with the measurements and investigation of moderate Prandtl number effects. Conclusions can then be drawn concerning the applicability of this measurement technique and the comparison between LES and experimental results within this low frequency range.

5.2 LES over a heated Backward-Facing Step

5.2.1 Computational domain

A schematic view of the three-dimensional single-sided expansion is shown in Fig. 5.1. The streamwise length L_x, includes a downstream length $L_d = 20\,h$

and an upstream length $L_u = 7.25$. The latest is obtained from the work of Chapter 4 that focused on the TBL developing upstream of the step. This length was adjusted to match as closely as possible the measured ratio δ/h, and obtain a satisfactory comparison of the flow field between the LES and the experiment. The height of the domain H was fixed to $6\,h$. Based on the PIV images taken of the test section (ref. Fig. 3.17), the flow at this distance was considered to be sufficiently unaffected by the separation area such that relatively simple boundary conditions could be prescribed with high confidence.

Instead of representing the spanwise width of the test section, a periodic boundary condition is applied to a limited portion. Le [74] reports that a periodic length of $4\,h$ is not enough to guarantee a sufficient drop of the velocity cross-correlations in the free shear layer. Lee et al. [77] succeeded in characterizing these spanwise large-scale vortical structures by performing joint measurements of velocity and multi-point pressure fluctations. Their results highlighted wavelengths of coherent structures up to $2.5\,h$ in the reattachment area. Although further from the region of interest, continuous diffusion of these structures is expected downstream. A spanwise length of $6\,h$ is chosen for this study to limit the influence of these side boundaries.

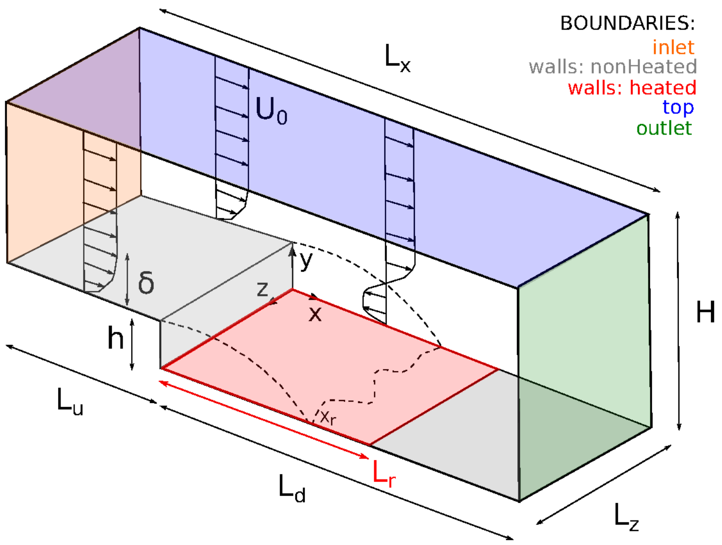

Figure 5.1: *Computational domain over the heated BFS.*

The heated wall downstream of the plate, delimited in red in Fig. 5.1, measures $L_r = 11\,h$. It would be common to adjust this length to roughly correspond to the reattachment length $X_r \simeq 6\,h$, however it is naturally fixed to match the heated plate used in the MYRTE experiment. For the LES performed at $Pr = 0.71$ and 0.2, no noticeable differences are expected compared to a shorter plate. On the contrary, at $Pr = 0.025$ the high thermal diffusivity will allow much more heat diffusion from the wall beyond the reattachment point before this heat is being transported by the flow.

5.2.2 Boundary conditions

The different boundaries that compose the CFD domain are represented in Fig. 5.1 and boundary conditions are summarized in Table 5.1. No-slip conditions are applied on all lower walls. A uniform temperature T_{in} is inserted at the inlet and a constant temperature $T_w > T_{in}$ is applied to the heated wall. This assumption seems realistic given the surface temperature distribution measured by IR Thermography (ref. Section. 3.4.1). Similarly to the experiment, a $\Delta T = T_w - T_{in}$ of $22\,°C$ is imposed in correspondence with the experiment. Indeed, these IR images reported a highly uniform temperature over the plate in the MYRTE experiment. In addition, a satisfactory insulation was observed between the heated plate and the other lower walls, enabling to treat these as adiabatic.
Different boundary conditions were considered for the top boundary (ref. Appendix C), the most promising alternative is the so-called zero vorticity boundary condition, defined as:

$$v = V_{ref}\ , \quad \frac{\partial v}{\partial x} = \frac{\partial u}{\partial y} \ \ and \ \ \frac{\partial v}{\partial z} = \frac{\partial w}{\partial y}\ , \tag{5.1}$$

where V_{ref} is the vertical velocity distribution that controls the pressure gradient. As observed in the PIV contours measured along the test section (ref. Fig. 3.17), at the domain height H the strongest variations are naturally observed above the recirculation area. Thus, the measurements are fitted in this region while, for simplicity, a linear variation is imposed elsewhere to match the first measured point upstream and a value of zero at the outlet.

Boundary	Velocity	Pressure	Temperature
inlet	mean profile	zero gradient	fixed value: $T_{in} = 300\,K$
top	zero vorticity	zero gradient	zero gradient
walls: nonHeated	no slip	zero gradient	zero gradient
walls: heated	no slip	zero gradient	fixed value: $T_w = 322\,K$
outlet	zero gradient	fixed value (0)	zero gradient

Table 5.1: *LES boundary conditions.*

At the inlet, the mean velocity profile measured by PIV at the entrance of the test section is imposed. However, the work carried out in Chapter 4 demonstrated the necessity of shrinking this profile in the wall-normal direction by 65 % to allow for the appropriate TBL growth and matching of δ_{step}/h. The free-stream velocity U_{in} is adjusted to achieve $Re_h = 8930$ at the step.
To generate inflow turbulence, the optimized TPM described in Chapter 2 is applied with appropriate settings required in the case of a TBL. As before, three rows of perturbation cells, each measuring $5\,\Delta x \times 5\,\Delta z \times 5\,\Delta z$, are distributed along the inlet boundary layer height (ref. Fig. 4.1). The local Richardson

number is adjusted to the best suited value $Ri_a = 0.25$ found in Chapter 4. A zero velocity gradient is imposed at the outlet.

5.2.3 Numerical details

The numerical grid must be sufficiently refined to resolve the turbulent structures near the wall and close to the step. A mesh of approximately 19 Millions cells is generated and shown in Fig. 5.2.
The number of grid points upstream of the expansion is $214 \times 140 \times 160$ in the streamwise, wall-normal and spanwise directions. It is progressively refined towards the step such that the streamwise grid resolution reduces from $\Delta x^+ = 32$ at the inlet to $\Delta x^+ = 5$ at the step corner, based on local friction velocity.
The mesh is uniform in the spanwise direction with a resolution of $\Delta z^+ = 16$. For the grid to be fine enough to resolve the turbulent structures in the wall layer, a vertical streching of 1.1 is applied in the wall-normal direction while the first cell center is placed at $y^+_{min} = 0.2$. Within the separated flow area, 80 points are placed along the vertical direction. A double refinement is applied in order to resolve the turbulent scales close to the wall as well as within the mixing layer region downstream of the step corner. 376 streamwise cells are placed dowstream of the expansion, with increasingly high aspect ratios towards the outlet. This resolution is typical of high quality wall-resolved LES [51].

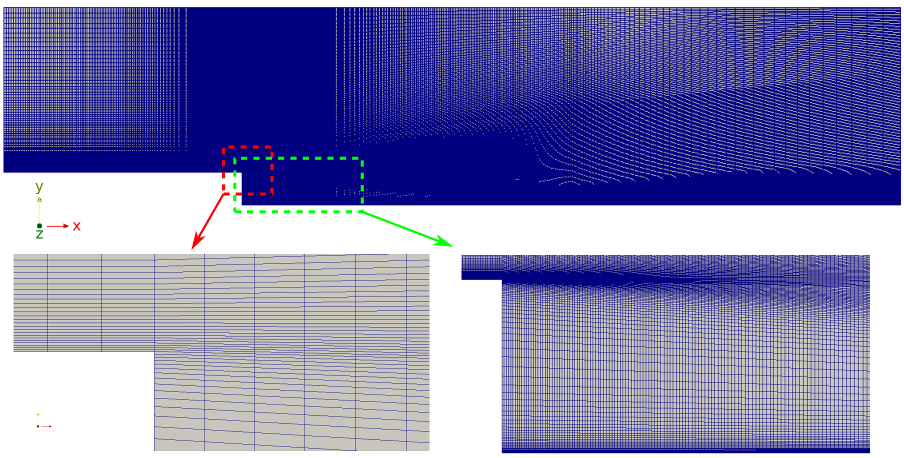

Figure 5.2: *Mesh generated over the BFS in a vertical plane, close-up views of the step corner and the recirculation area.*

As previously, the flow over the BFS is simulated with OpenFOAM v3.0 using the buoyant incompressible solver that has been adapted to accomodate the optimized TPM. The numerical schemes are the same as those used for the LES of a channel flow and TBL (ref. Section. 2.4.1). These preliminary simulations provide the necessary guidelines to set the various numerical parameters.

The Smagorinsky SGS model is applied in the momentum equation, combined with a Piomelli near wall damping. The model coefficient is set to 0.20 since this value provided the most accurate inflow conditions. This model is chosen over more advanced approaches that would employ for instance a dynamic procedure to calculate this constant [46]. The primary task of the SGS model is to impose the appropriate dissipation on the unresolved scales. Although this would not be the case at higher Reynolds number with coarser grids, one may suppose that with a well-resolved grid as employed here, this role is limited. The study of Rodi [124] on LES around bluff bodies agrees with this assumption since no significant improvement was obtained by using advanced SGS models compared to using the Smagorinsky model.

At all Prandtl numbers ($Pr = 0.71, 0.2$ & 0.025), the Reynolds analogy is applied for the modelling of the SGS heat transfer, using a SGS Prandtl number $Pr_{sgs} = 0.6$ as recommended by Moin et al. [88]. It is worth stressing that this parameter is not the turbulent Prandtl number Pr_t, that is used in RANS (and which is typically taken in the range 0.7 to 1. Its influence on the results has been assessed in the case of air by increasing its value to 1 (see Appendix F.1.3), resulting in negligible differences. Although this point is further discussed in Chapter 6, the mesh is sufficiently refined to resolve all the temperature scales at $Pr = 0.025$, which implies that the SGS heat flux model will hardly intervene in this case.

5.3 Thermal-hydraulic comparison with air

5.3.1 Flow topology and reattachment

Streamlines of the time-averaged flow around the vertical mid-plane predicted by LES are shown in Fig. 5.3. These typically illustrate the common features observed in a BFS flow. The sudden expansion causes the flow to abruptly separate at the step corner. A recirculation area appears between the shear layer and the bottom wall, composed of a large primary vortex and a secondary vortex adjacent to the step corner. The shear layer eventually curves downwards and impinges the wall at the reattachment point, resulting in a new attached boundary layer that slowly redevelops further downstream. One recalls that overlined quantities are averaged over time and the homogeneous spanwise direction. The mean skin friction coefficient is computed as:

$$C_f = \frac{\overline{\tau}_w}{\frac{1}{2}\,\rho\, U_{in}^2}\,, \tag{5.2}$$

where $\overline{\tau}_w = \mu\left(\partial\overline{U}/\partial y\right)_w$ is the wall shear stress. Its evolution along the bottom wall is plotted in Fig. 5.4. As observed in previous studies [75], a large negative peak of $C_f \simeq -0.0035$ is obtained which can be attributed to low Reynolds number effects. Moreover, very close to the step, the skin friction coefficient experiences a local maximum, certainly related to the presence of a third recirculation zone [75]. The location of zero wall-shear stress indicates the mean flow reattachment, x_r, found at $5.37\,h$.

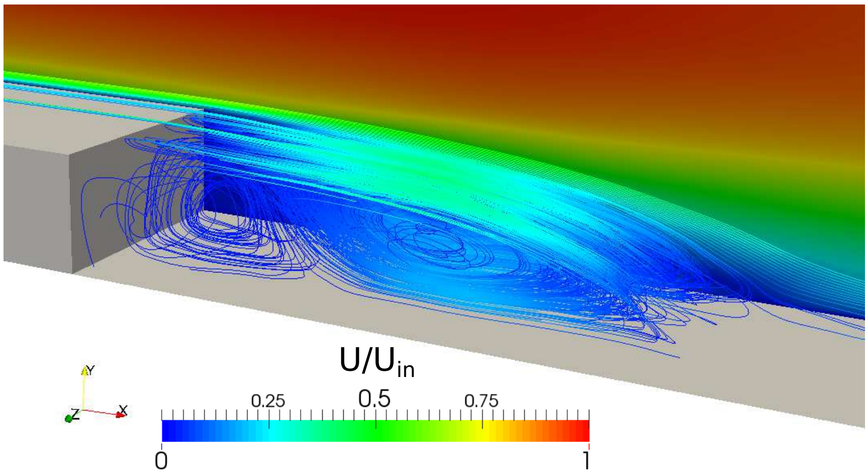

Figure 5.3: *3D flow streamlines colored with velocity and velocity contours in the mid-span vertical plane of the periodic domain.*

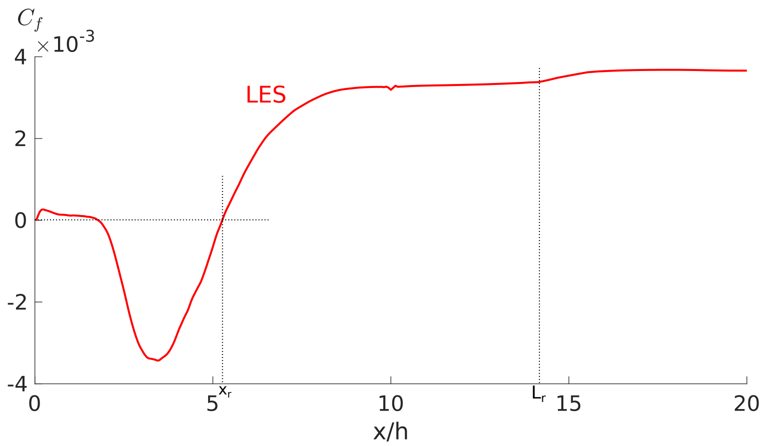

Figure 5.4: *Streamwise variation of the skin friction coefficient obtained by LES at* $Pr = 0.71$.

5.3.2 Velocity field

The mean streamwise and wall-normal velocity profiles obtained by LES and PIV are compared in Fig. 5.5 and 5.6 respectively. The LES shows a very good agreement with the MYRTE measurements. Experimentally, the flow reattachment is located at approximately $5.3\,h$, meaning that the LES only deviates by $+1.3\,\%$. In the streamwise direction, the largest differences are observed within the shear layer. The LES predicts a slightly sharper gradient than found experimentally. However, the discrepencies remain less than $10\,\%$, while a minimum of $2\,\%$ uncertainty should be associated to the PIV results.

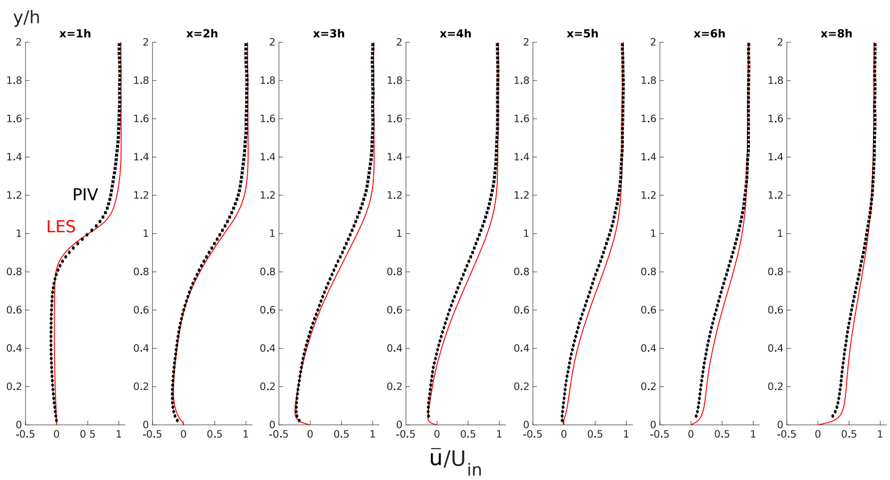

Figure 5.5: *Mean streamwise velocity profiles obtained by LES and PIV in air at several positions downstream of the step.*

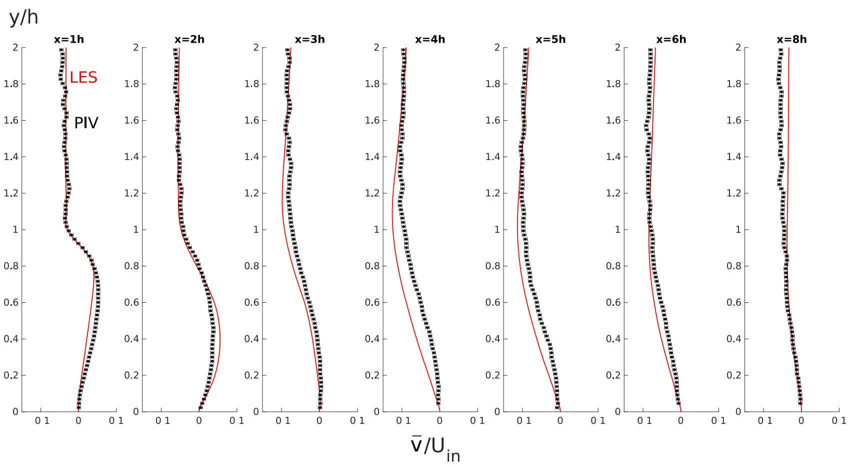

Figure 5.6: *Mean wall-normal velocity profiles obtained by LES and PIV in air at several positions downstream of the step.*

As for the wall-normal component, an excellent agreement is observed throughout the separation area ($< 5\,\%$), which is remarkable if one takes into account the PIV error. Looking at the good match obtained at $y/h = 2$, one may deduce that specifying the measured vertical velocity distribution along the top boundary certainly contributes to this satisfactory comparison.

Finally, the Reynolds stresses are compared in Fig. 5.7, 5.8 and 5.9. In the case of shear stress, the LES profiles represent the total shear stress, thus including the SGS model contribution. The results match relatively well, despite some discrepencies observed in the separated flow area. In particular, the LES over-estimates the maxium value at the first position by nearly 50 %, which diffuses further downstream. Similar trends are observed in comparable studies [7]. A good prediction of the shear layer spreading is observed downstream of the reattachment.

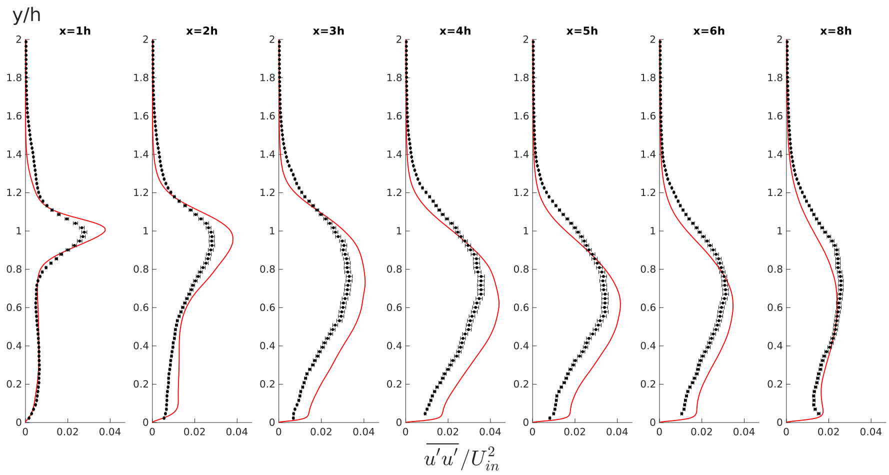

Figure 5.7: *Streamwise Reynolds stress profiles obtained by LES and PIV in air at several positions downstream of the step.*

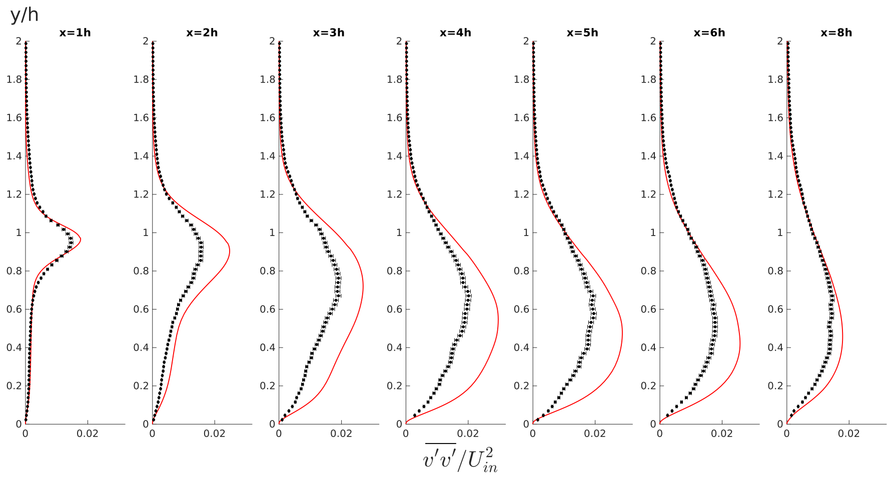

Figure 5.8: *Vertical Reynolds stress profiles obtained by LES and PIV in air at several positions downstream of the step.*

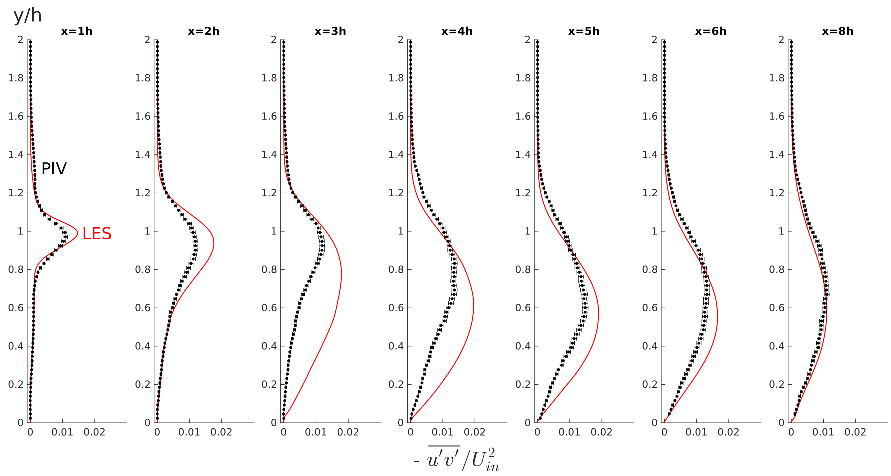

Figure 5.9: *Shear stress profiles obtained by LES and PIV in air at several positions downstream of the step.*

5.3.3 Mean temperature field

Temperature measurements are made using a single micro-TC in order to provide a first assessment of the thermal field predicted by LES at $Pr = 0.71$. Profiles at several streamwise positions after the step are shown in Fig. 5.10.

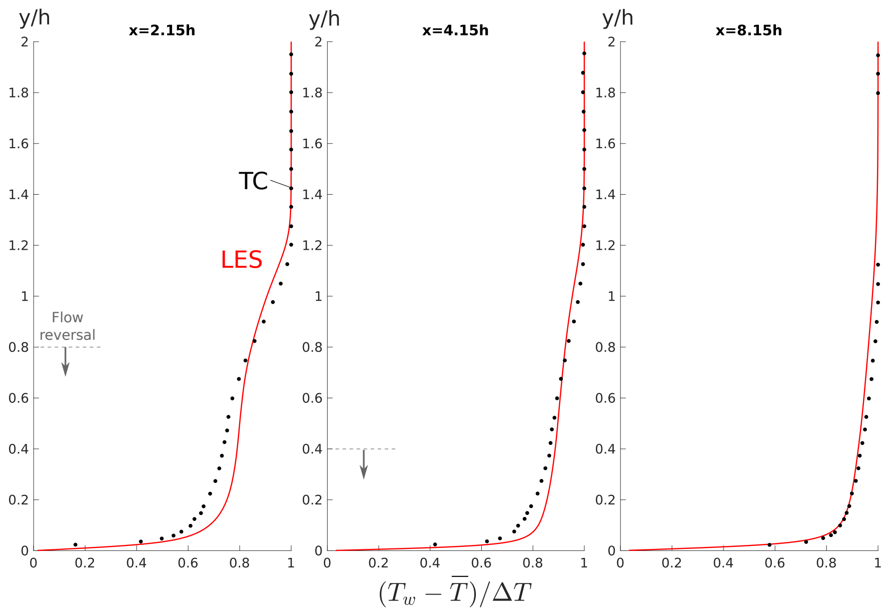

Figure 5.10: *Mean temperature profiles obtained by LES and micro-TC at several positions downstream of the step.*

An acceptable agreement is observed shortly after separation within the shear layer region. The gradient is slightly sharper in the experiment but these differences remain within the uncertainty range of the measurement technique ($\simeq 2\,\%$), calculated in Appendix B.3.
The measurement points below the horizontal dashed line are located within the recirculation region. Although this single probe remains quite small, it is an intrusive measurement technique that certainly disrupts the flow. The discrepencies increase below this limit, which tends to support this argument. Thus, all measurements located within the reversed flow region will be disregarded from this point on. Downstream of the reattachment however, an excellent comparison is observed concerning the re-developing thermal boundary layer.

To conclude, the thermal-hydraulic field obtained by LES on the unconfined BFS compares well with the measurements. The differences observed in the mean velocity and temperature fields are comparable to the uncertainty range of the measurement technique itself, and therefore an excellent agreement has been reached. Discrepencies appear in the shear stress, especially within the shear layer shortly after the expansion. This over-prediction of turbulence by LES dissipates further downstream, and is no longer present shortly after the reattachment.

5.4 LES investigation of HWA-TC probe limitations

The objective in this section is to introduce the different tools that are needed to obtain a representative comparison of the LES and experimental data. This requires processing the LES during run-time in order to sample the data according to the HWA-TC probe specifications. However, we stress that all the LES results without additional treatment can be found in Chapter 6.

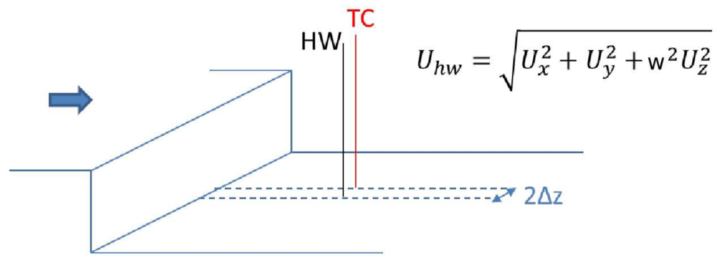

Figure 5.11: *Processing of LES data during run-time according to HWA-TC measurements.*

The variable corresponding to the effective velocity measured by the HWA, U_{hw}, is computed by the solver. Every 10 time steps ($f_{s,\,LES} = 5\,kHz$), this variable is sampled along a vertical line shown in Fig. 5.11, while the temperature is sampled along a line shifted by 1.5 mm in the spanwise direction. One recalls that this shift is equal to the spacing between the two sensors, corresponding to exactly two mesh cells Δz. The data are extracted at the same streamwise positions than during the measurements, every step height downstream of the expansion.

The two main limitations imposed by the HWA-TC probe are investigated hereafter. Firstly, the results obtained with and without probe spacing are compared to determine whether this aspect has a noticeable influence. Secondly, focus is brought on the limited dynamic response of the micro-TC that is studied by filtering the LES data in the frequency domain, based on the probe's frequency response.

5.4.1 Probe spacing

To trully represent the transport of heat due to turbulence, the velocity and temperature should be measured at the same point. However this is not possible given the measurement technique that is used, and a distance of $1.5mm$ remains between the two measured quantities (U_{hw}, T). As introduced previously, the LES is processed accordingly during run-time so that $\overline{u'_{hw}T'}$ with and without a spatial shift is computed while post-processing the data. The influence of this parameter is represented in Fig. 5.12, refering to each set of data as "LES$_S$" and "LES$_{noS}$" respectively.

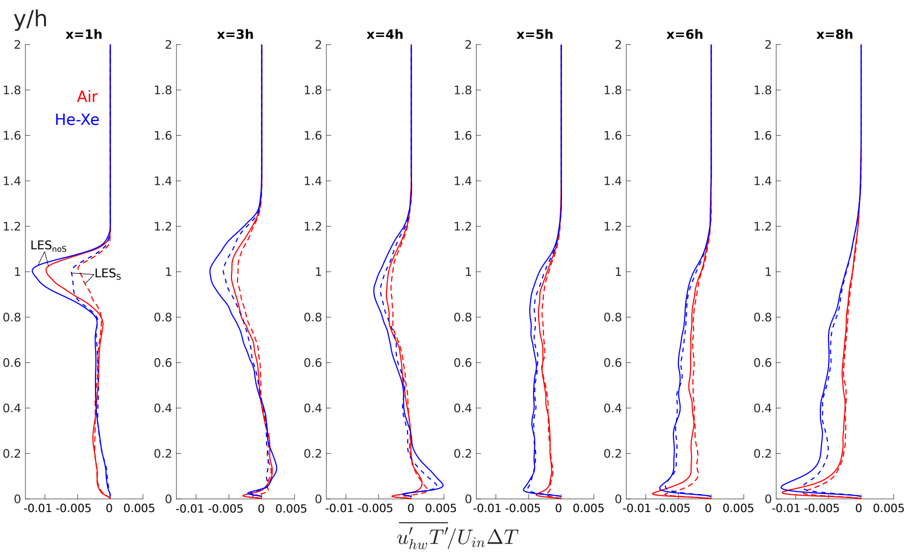

Figure 5.12: *Influence of probe spacing on the measured turbulent heat flux based on the effective velocity measured by a hot-wire.*

Independently on the Prandtl number, the comparison shows that the probe spacing plays a significant role, especially in the shear layer shortly after separation. The correlation between velocity and temperature fluctuations drops substantially at $x = 1\,h$, the maximum value being reduced by a factor of two. These differences slowly decrease as the shear layer expands further downstream. This trend is likely due to the vortex rolling and pairing mechanism that takes place [171], which explains why the two quantities remain correlated along a wider spatial range as the turbulent structures grow in size. Within the recovery region, similar observations can be made close to the wall, with at most a 25 % reduction.

The probe spacing appears to have a strong influence on the measured turbulent heat flux. Due to the spatial distance between the HWA measurement of the effective velocity and the TC probe measurement of the temperature, the quantities are not as correlated. For a direct comparison with the experimental measurement, it is thus also essential to separate the velocity and temperature sampling locations while treating the LES data so that similar quantities are compared later on. We stress that the physically correct turbulent heat fluxes are the ones measured in both directions ($\overline{T'u'}$ and $\overline{T'v'}$), and without spacing between the probes: something that cannot be done in the experiment, but that can be done in the LES (recognizing that the LES is only a model of reality). The two approaches (experiment and LES) are thus very complementary.

5.4.2 Probe frequency response

The micro-TC's frequency response is expected to be well below the frequency range characterizing the smaller thermal turbulent scales present in the flow. To investigate the influence of this early cut-off, the LES is further filtered in the frequency domain based on the probe's frequency response characterized in Section 3.3.4.2. This means that the probe spacing between the two sensors is already taken into account while applying frequency filtering. It is worth stressing once again that the LES data without any spatial or frequency filtering can be found in Chapter 6.

5.4.2.1 Preliminary post-processing of the results

Velocity data

Before investigating the effect of frequency filtering, the velocity signal obtained experimentally and by LES are compared at $x = 5\,h$ and $y = 0.5\,h$. One recalls that the data are sampled at $f_{s,\,Exp} = 7.5kHz$ and $f_{s,\,LES} = 5kHz$ respectively. Regarding statistical convergence, measurement uncertainties can be found in Appendix B. As far as the LES is concerned, the data are sampled during approximately 1.4 s, which means that the statistical errors on the mean and the variance are at most 0.5 % and 2.3 % respectively.
The time series are plotted in Fig. 5.13 a) during the observation time T_{obs} of the LES. The first observation one can make is that the fluctuation levels appear to be comparable. Corresponding spectra are shown in Fig. 5.13 b). The inertial sub-range that contains the most energetic turbulent scales is well represented in both signals by a Kolmogorov's -5/3 power law. On one-hand,

the HWA technique is particularly suited for measuring turbulent flows because of its high frequency response ($f_c \simeq 7.5kHz$) while, on the other-hand, the LES is certainly resolved enough to capture most turbulent scales. A change in slope is observed in the LES spectrum around $1\,kHz$, which can certainly be related to grid resolution. Smaller scales appear to be partly dissipated in this higher frequency range of the spectrum. The amount of implicit filtering will naturally depend on the local grid size.

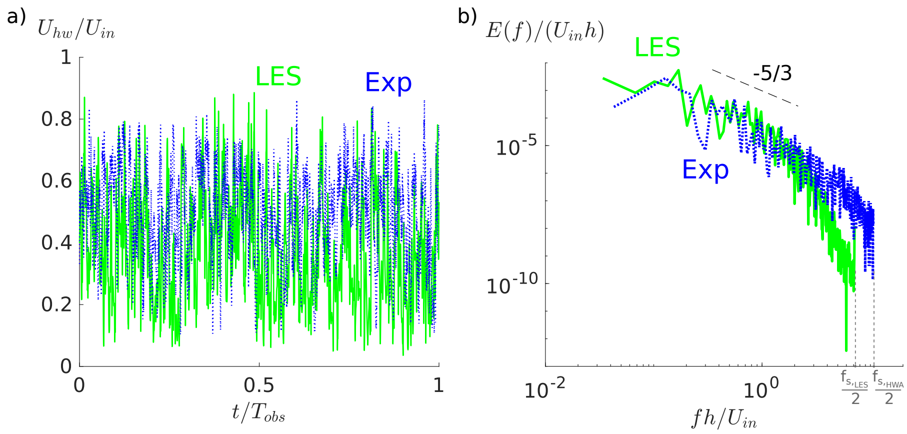

Figure 5.13: *Analysis of the effective velocity signal recorded at $x = 5\,h$ and $y = 0.5\,h$ a) Time variations b) Spectrum.*

The mean effective velocity profiles are compared in Fig. 5.14. As expected, the flow field measured in air and in the gas mixture is practically the same. Indeed, both fluids are ideal gases such that their thermal expansion coefficient is given by $\beta = 1/T$, meaning that buoyancy effects under similar conditions (Re_h, ΔT) will be the same. This is certainly the case in the LES, which is why a single result is shown for both LES performed at $Pr = 0.71$ and 0.2.
In agreement with previous observations made from the LES/PIV comparison, the shear is over-predicted by the LES with sharper gradients of velocity shortly after separation. Up to 15 % differences appear at $x = 1\,h$, while these are progressively attenuated further downstream, yielding a very good agreement from the reattachment onwards.

The turbulence intensity profiles are shown in Fig. 5.15. These are again based on the effective velocity as measured by the hot-wire. The levels are of the same order of magnitude but the turbulence is over-estimated by the LES throughout the separation area with, for instance, a maximum peak of 18 % at $x = 1\,h$ against a measured value of 13 %. This is in agreement with the LES/PIV comparison, and is commonly observed by LES [151].
In addition, the location of this peak differs. At this same streamwise location, the LES predicts it at the step height h, whereas it is measured $0.1\,h$ lower. This tendency is emphasised further downstream, which is in contradiction with the observations made previously between LES and PIV, where despite some

discrepencies, a better correspondance had been observed. This is certainly related to the intrusiveness of the probe measurements, in particular when using the HWA-TC probe that is larger than the micro-TC probe for instance. This is confirmed later on since differences are observed in the temperature measurements acquired with the single and double sensor probe (hot-wire turned off), i.e. Fig. 5.19 and E.1. Nevertheless, the overall agreement remains acceptable, especially downstream of the reattachment.

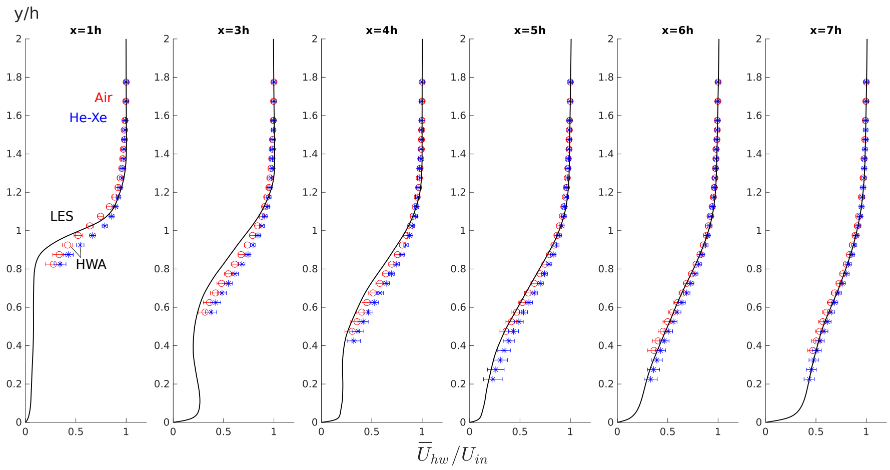

Figure 5.14: *Mean effective velocity profiles obtained by LES and HWA measurements.*

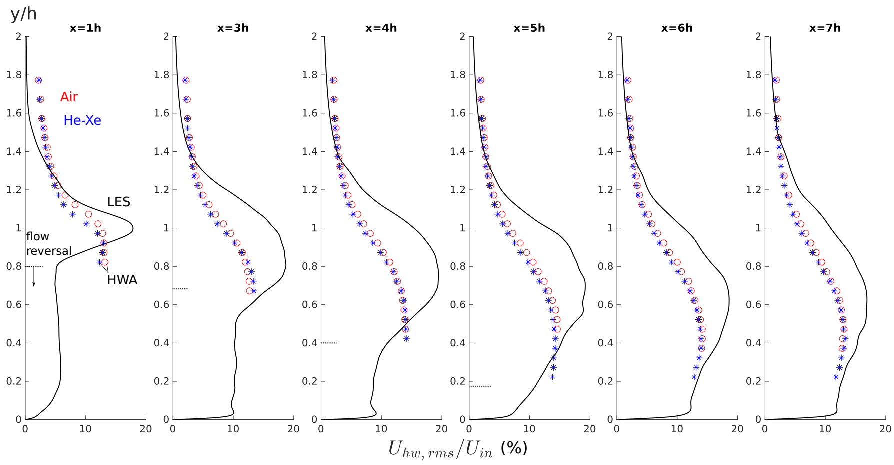

Figure 5.15: *Turbulence intensity profiles obtained by LES and HWA measurements.*

LES frequency filtering applied to temperature

The temperature signals obtained experimentally and by LES are compared at $x = 5\,h$ and $y = 0.5\,h$. Time variations are shown in Fig. 5.16 a), where a clear difference in amplitude is observed between the original LES signal, "LES$_{noF}$", and the micro-TC mesurement, "Exp". This is due to the limited frequency response of the micro-TC sensor, that exhibits a cut-off frequency $f_{c,\,TC}$ of 75 Hz, while the LES can capture much higher frequency fluctuations thanks to a well-resolved mesh. As explained before, the aim is to filter the LES based on the dynamic response of the micro-TC, so that comparable LES and experimental results can be confronted to eachother. Thus, the fitted transfer function given by Eq. (3.5) is applied to the LES. This results in a filtered signal, "LES$_F$", that exhibits much lower fluctuation levels than originally. The corresponding spectra are also represented in Fig. 5.16 b), with an attenuation effect shortly before the sharp cut-off imposed at $f_{c,\,TC}$.

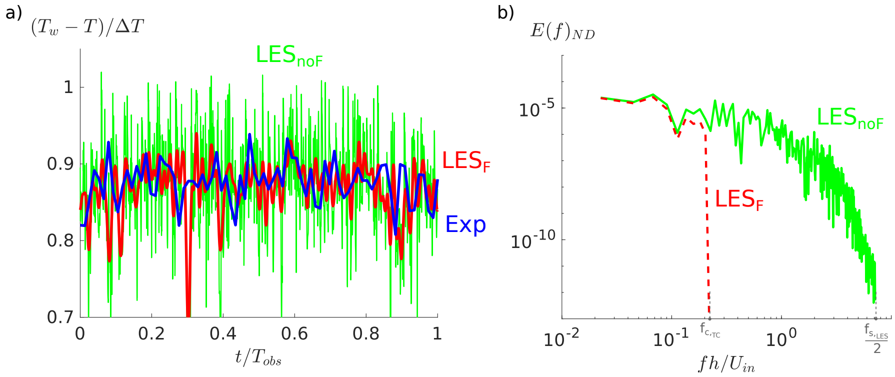

Figure 5.16: *Analysis of the temperature signal recorded at $x = 5\,h$ and $y = 0.5\,h$, effect of LES frequency filtering a) Time variations b) Spectrum.*

The influence of LES frequency filtering on the temperature variance is plotted in Fig. 5.17. Similar effects are observed by applying the low-pass filter in air and He-Xe, with a substantial decrease in the most turbulent regions.
Within the shear-layer region, the temperature fluctuations are strongly affected with close to 40 % reduction in peak values at $x = 1\,h$. This observation implies that a higher frequency energy content, associated to smaller turbulent structures, plays a dominant role in this area. These differences are less pronounced further down as these small scale vortices in the shear layer grow in size. The analysis of hot-wire data [131] illustrates this spatial growth due to vortex pairing. Behind the vertical wall of the step, the velocities are low and the flow is not very turbulent. This is generally true within the recirculation, except near the wall where strong fluctuations of increasing amplitude are observed. The strongest peak appears within the reattachment zone, where fluctuations are much higher due to shear-layer turbulent structures that impinge on the wall. This phenomenon is known as the flapping of the shear layer. It has been observed by a number of researchers [72, 82, 134], who re-

lated this mechanism to a highly energetic low frequency peak in the energy spectrum, associated to a Strouhal number, $St = f\,h/U_{in}$, of the order of 0.02. In the MYRTE experiment, this would correspond to a frequency $f \simeq 10\,Hz$, thus explaining why filtering out higher-frequencies from the LES has a smaller effect ($< 25\,\%$).

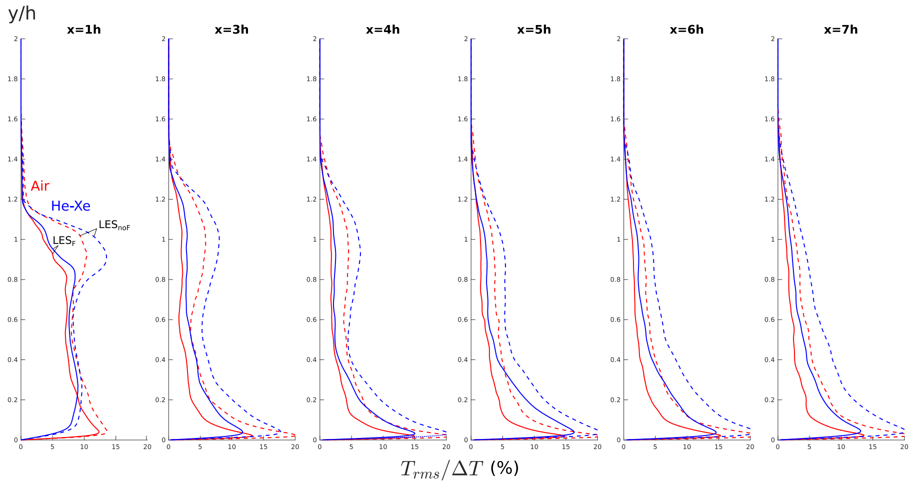

Figure 5.17: *Effect of LES frequency filtering on the rms of temperature fluctuations.*

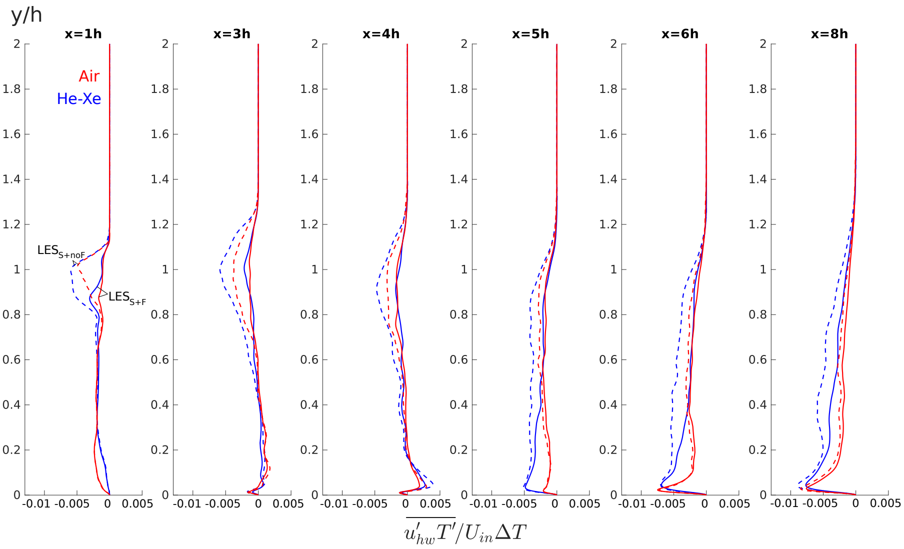

Figure 5.18: *Effect of processed LES (with spatial and frequency filtering) on the turbulent heat flux based on effective velocity*

Finally, retaining the probe spacing introduced previously, the same procedure is applied to the turbulent heat flux $\overline{u'_{hw}T'}$. Fig. 5.18 illustrates that filtering the LES above 75 Hz has a significant impact on the measured turbulent transport of heat. In accordance with previous observations, the strongest effect is found just after separation around step height, thus confirming the role played by the smaller turbulent eddies within the shear layer.

To conclude, it is obvious that both probe limitations related to spatial constraints and time resolution must be taken into account in the processing of the LES data for the results to be fairly comparable with the measurements. This preliminary analysis has highlighted two main aspects:

- The contribution coming from the small turbulent eddies to the transport of heat is minimized, especially in the shear layer shortly after separation.
- The role played by the large impinging vortical structures near the reattachment on the turbulent heat transfer remains important.

Consequently, LES results suggest that, between the experiments in air and He-Xe, Prandtl number effects of stronger amplitude can be expected in the reattachment zone.

5.5 Moderate Prandtl number effects

In this section, the comparison between the LES and the experimental results is presented. The previous study demonstrated that it is fundamental to integrate the probe specificities while processing the simulation results in order to compare them to those of the experiments. Otherwise, very different quantities are confronted to each other. Consequently, the LES is also treated so that velocity and temperature are sampled with a spanwise gap of 1.5 mm, and the frequency content above 75 Hz is filtered out from the temperature. Results obtained both in air and the He-Xe gas mixture are shown hereafter. The untreated LES data are presented in Chapter 6, while investigating Prandtl number effects based on the LES results.

5.5.1 Mean temperature field

One recalls, from the calibration of the HWA-TC probe, that the micro-TC is heated by the HWA at low velocity. In the He-Xe gas mixture, this effect is emphasised due to higher conductivity and starts appearing at already 3 m/s. Given the uncertainty that this behaviour introduces on the mean temperature, measurements presented here are obtained using a single micro-TC. Moreover, the extremity of the probe is twice as small, thus reducing its potential effect on the flow within the shear layer compared to the HWA-TC probe. The profiles are compared in Fig. 5.19. Some discrepencies are observed between the LES and the measurements at the start of the shear layer. Indeed, at $x = 1\,h$, the thermal shear predicted by LES is sharper. Nevertheless, Pr effects start appearing at the same height $y \simeq 1.2\,h$ and are comparable with each other.

Further downstream, these differences between air and He-Xe, reach up to 10 % experimentally, while very similar variations are observed by LES. The agreement is particularly good within the recovery region. As expected, the fluid heated by the step extends further out in He-Xe, and a thicker thermal boundary layer redevelops after the reattachment.

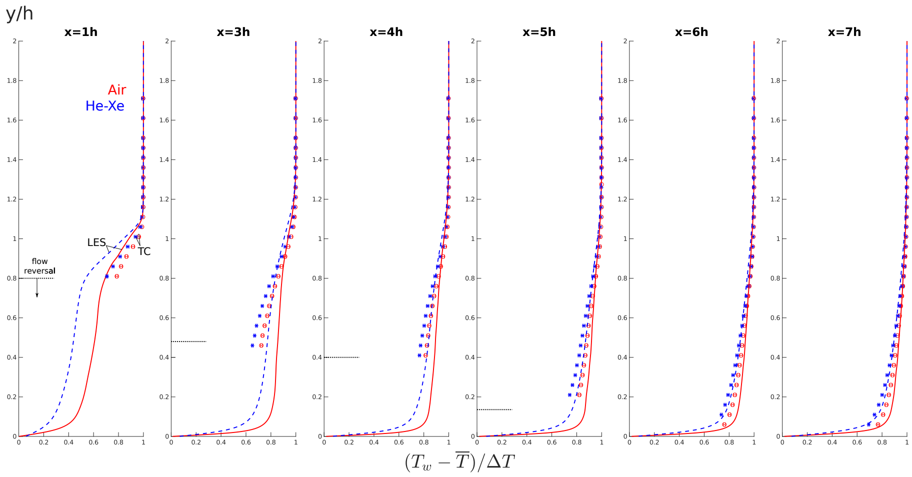

Figure 5.19: *Mean temperature profiles obtained by LES and micro-TC measurements in air and He-Xe.*

One may however notice that in both fluids, the temperature gradient that is measured between the wall and the fluid is consistently less compared to the LES. A better agreement had been observed previously (see Fig. 5.10), while using the micro-TC down to the wall to measure T_w. This procedure was not repeated here in order to limit the risk of breaking the micro-TC. Instead, T_w is measured by several TC placed at the wall ($x = 1\,h$,$3\,h$ and $5\,h$).
These discrepencies may be associated to two main sources of error. Firstly, it is possible that inaccuracies originate from the multiple TC sensors, for which temperature values are deduced from the typical calibration curve provided by the manufacturer. It would have been preferable to re-calibrate these before carrying-out the measurements, to reach a higher precision. Secondly, two different TC are used to measure the temperature at the wall and in the fluid, and an offset is often observed between the two for a given temperature. This shift was taken into account once at the start of the measurements while it may vary in time.

5.5.2 Temperature fluctuations

The experimental profiles of the rms of temperature are shown in Fig. 5.20 and compared to the treated LES profiles. By filtering out the frequency content above 75 Hz, thus mimicking the limited frequency response of the micro-TC, a much more representative comparison between LES and measurements is proposed. As a result, the temperature fluctuations are of the same order of magnitude, whereas the LES levels would have been up to four times larger otherwise. Once again, discrepencies are observed at the start of the shear layer. As seen previously, stronger fluctuations are predicted by LES in both the momentum and thermal fields.

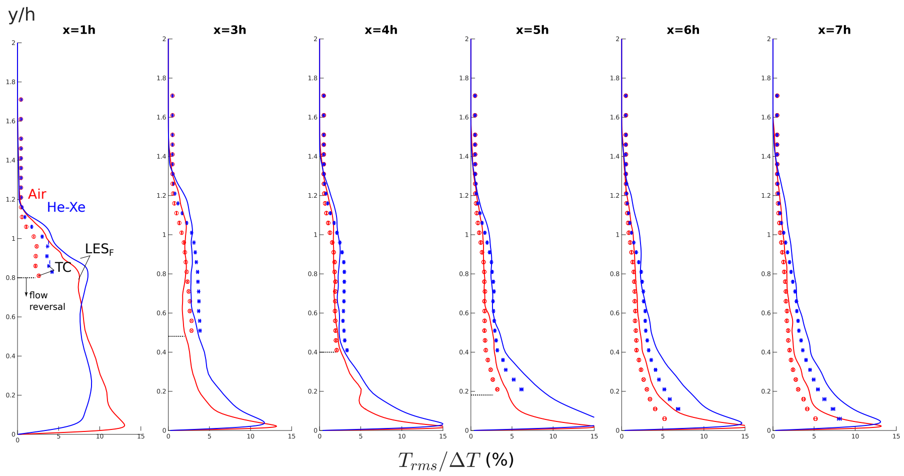

Figure 5.20: *Rms temperature profiles obtained by frequency filtered LES and micro-TC measurements.*

As the shear layer expands further downstream, two main observations can be made; firstly, these temperature fluctuations are caused by the interactions between the colder packets of fluid entrained by the shear layer, and the warmer packets of fluid that are recirculated upstream by the primary bubble. The turbulence levels increase as the eddies pair. A peak is observed near the reattachment ($\simeq 5\,h$) where the strongest heat transfer rates are expected due to an impingement mechanism, in which the large turbulent structures originating from the shear layer impact the wall.
Secondly, Prandtl effects of similar amplitude are predicted between the LES and experiments. The same trend is observed with stronger fluctuations in the gas mixture compared to air. Moreover, the agreement improves also from a quantitative point of view from reattachment on ($x \geq 5\,h$). Within the shear layer, the thermal turbulence levels are very close at both Prandtl numbers. Keeping in mind that the turbulent transport of heat is the main quantity of interest, the good overall agreement that is obtained here on the temperature rms is an essential pre-requirement for predicting properly turbulent heat transfer rates.

5.5.3 Turbulent heat transfer

Profiles of turbulent heat flux obtained by correlating the effective velocity and temperature fields are shown in Fig. 5.21. It is important to note that here the temperature and the effective velocity are measured simultaneously using the HWA-TC probe. Previously, the temperature profiles presented in Section 5.5.1

and 5.5.2 were measured using a single-TC, to reduce probe intrusiveness and avoid the TC to be heated-up by the HWA. For completness, the temperature field measured with the HWA-TC probe can be found in Appendix E. By comparing the two temperature fields measured with the single micro-TC and the HWA-TC probe, it appears that with the latest, Prandtl number effects are limited to the part of the shear layer below step height and progressively gain in strength as the shear layer expands. One may deduce that the HWA-TC probe is more intrusive, and does not capture as well these small Prandtl effects. Nevertheless, below step height, Pr effects become noticeable.

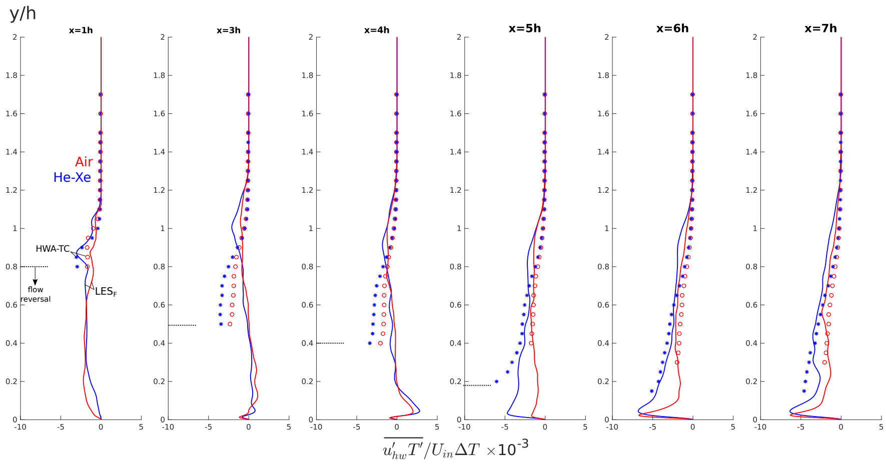

Figure 5.21: *Turbulent heat transfer profiles based on the effective velocity, obtained by processed LES (with spatial and frequency filtering) and HWA-TC probe measurements.*

One recalls that levels of much smaller intensity are produced after taking into account the probe's spacing between the sensors and its frequency response. Nevertheless, the remaining portion of the original flux is sufficient to be measurable, and a difference in behaviour can be distinguished between the two fluids.
At first, the measured Prandtl effects on the turbulent heat flux are negligible in the upper part of the shear layer ($y/h \geq 1$). However, these become stronger as the shear layer expands, which can be attributed to two main aspects: differences in the rms of temperature start to be measurable with the HWA-TC probe and the growing vortical structures transport heat over wider distances. The peak located in the step area is well captured at $x = 1\,h$. Further downstream at $x/h = 3$ and 4, measured levels are too high due to over-predicted velocity fluctuations (see Fig. 5.15) that are potentially caused by the presence of the probe.

Within the recovery region, the correlation between the temperature and the effective velocity increases beyond $x = 5\,h$. The turbulent fluxes penetrate further up into the boundary layer as it redevelops. In addition, two aspects clearly stand out; on one-hand, the turbulent fluxes are sharper near the wall in air because of a thiner boundary layer. On the other-hand, the transport of heat is higher within the shear layer in the He-Xe gas mixture, due to higher temperature fluctuations. This tendancy does not result from the spatial and time filtering imposed by the measurement technique. Further insight into the physical understanding of Prandtl number effects is proposed in the next Chapter. Main conclusions that can be drawn from this comparison between LES and experiments carried out at moderate Prandtl number are presented hereafter.

5.6 Conclusions

To conclude, LES has been used as a predictive tool to study the influence of the measurement technique chosen for the MYRTE experiment. Its ability to resolve an extended range of the turbulent spectrum makes it particularly rich. This large amount of information also provides the opportunity to investigate how the limitations imposed by the probe measurements affect the results. This work has clearly demonstrated the necessity of also incorporating these aspects into the processing of LES data, for a meaningfull comparison with the measurements. Only then, can we conclude wether the LES is sufficiently accurate to predict turbulent heat transfer.

The first step in this validation process, has been to compare the thermal-hydraulic field obtained by LES, with the PIV and micro-TC measurements. An excellent agreement is found on the mean velocity and temperature fields, with only $+1.3\,\%$ on the mean flow reattachment and typically $2\,\%$ deviations on the temperature. The Reynolds stresses within the shear layer are over-predicted but the expansion of the shear layer remains well captured.
To partly quantify the turbulent heat transfer, a HWA-TC probe is used for the measurements. As required, the velocity and temperature are measured simultaneously, but not at the same point since two distinct sensors are used. This spatial contraint is mimicked in the LES by sampling the two quantities at a distance from one another, equal to the probe spacing. Another major constraint imposed by the micro-TC sensor concerns its frequency response. Despite a small TC wire diameter of $12\,\mu m$, the thermal inertia limits the heat transfer rate to the wire junction and imposes a low cut-off frequency of $75\,Hz$. Accordingly, frequency filtering was applied to the LES based on the micro-TC's transfer function.
Each of these parameters have shown to considerably reduce the "measured" turbulent heat transport at the start of the shear layer. The turbulent heat flux based on the effective velocity drops successively by two, yielding less than a quarter of the original peak levels. This drastic reduction results from the spatial and frequency filtering imposed on the smallest turbulent eddies, that dominate in this region, and mainly contribute to the transport of heat in the higher frequency range of the turbulent energy spectrum.
Although to a smaller extent, the reattachment zone is also affected by these

probe limitations. The turbulent contribution remains around 50 % of its original value, this is also where the strongest peak in heat transfer is expected due to larger impinging vortical structures. In this area, the treated LES compares well with the measurements, thus validating the low frequency content of the numerical database. Moreover, very similar Prandtl number effects are observed between air and He-Xe, allowing us to conclude positively on the ability of the LES in providing trustable results that can be used for further validation of turbulent heat transfer models.

Chapter 6

LES Investigation of low Prandtl number effects

6.1 Introduction

The increased performance of low Prandtl number fluids compared to common fluids, in terms of heat tranfer and higher boiling point at atmospheric pressure, make them particularly attractive for use as coolant in fast neutron reactors [41] or heat transfer medium for concentrated solar power technology [83, 114]. Given how challenging it is to investigate liquid metals experimentally [141], numerical simulations have become an essential design tool for predicting turbulent heat transfer and must therefore be accurate at low Prandtl number.

Proposing accurate RANS simulations, on the other-hand, is very challenging since, from a modeling point of view, it is difficult to handle the differences in scale between the momentum and thermal fields. The effective turbulent heat diffusivity can no longer be simply determined using a constant turbulent Prandtl number around unity [37]. Moreover, for low Prandtl number fluids, the molecular heat diffusivity is no longer negligible relatively to the turbulent one, and even dominant in some regions. To represent better its flow dependent behaviour, several Pr_t correlations have been proposed [29, 62, 170]. Although beneficial in simple cases such as channel flows, predictions may be improved in more complex geometries provided the eddy-viscosity is determined accurately by the turbulence model [15]. More advanced models suitable for low Prandtl number fluids and involving additional transport equations [85, 148] need further validation in various flow conditions. For this purpose, highly-resolved simulations are required to get further insight into the physical mechanisms that drive liquid metal turbulent convection.

Despite the rapid progress in high-performance computing, DNS remains out of reach as more realistic flow conditions still require the use of world leading supercomputers. Indeed, a DNS requires a number of mesh points N satisfying $N \sim Re^{9/4}$ [122], which becomes rapidly prohibitive as the Reynolds number increases. LES, on the other-hand, remains an affordable tool that is accurate enough to provide new data at high enough Reynolds number for RANS modeling. Indeed, at low Prandtl number, the advantage is that the smallest scales of the temperature field are much larger than those associated to the velocity field. This implies that if the LES is performed at high enough resolution, although the mesh will not fully resolve the velocity field, the temperature field will be properly captured. Consequently, a SGS model will only be required in the momentum equation whereas no subgrid heat flux model will be required for the energy equation. The spectrum associated to the temperature field decays at low Prandtl number, thus indicating the possibility of fully resolving the temperature field, provided resolution requirements are fulfilled [51]. This approach was first investigated and applied by Schumann et al. [142], and more recently validated by Bricteux et al. [20].

Amongst the most famous reference data at low Prandtl number are DNS carried out by Kawamura et al. [61] and Abe et al. [1] simulating a periodic channel flow for Reynolds numbers up to $Re_\tau = 1020$ and Prandtl numbers down to 0.025. Some studies also include conjugate heat transfer in order to investigate the penetration of the turbulent temperature fluctuations into the heated wall [45, 164, 165]. More recently, the LES/DNS of Bricteux et al. [20] and Duponcheel et al. [37] has served as reference for RANS modelling by providing results at higher Reynolds number ($Re_\tau = 2000$) and lower Prandtl ($Pr = 0.01$). Moreover, best practice guidelines to be used in RANS were formulated, proposing a "law of the wall for temperature" for non-resolved simulations, often the only affordable approach at industrial scale.
However, relatively few numerical results can be found for developing flows with passive scalars. The first DNS of a flat-plate boundary layer under ZPG was performed by Bell and Ferziger [16] up to $Re_\theta = 700$ at $Pr = 0.1$, 0.71 and 2.0. More recently, the DNS of Li et al. [80] reached $Re_\theta = 830$, with one velocity field accomodating several scalars, at $Pr = 0.71$ and 2 but also $Pr = 0.2$.
As far as high fidelity (LES or DNS) simulations of core thermal-hydraulics are concerned, an elaborate review has been performed by Roelofs et al. [130] and recently updated in [125]. Much effort has been put in generating reference data applied to fuel assemblies with wire wraps for the validation of RANS CFD models, e.g. by Pointer et al. [120], Shams et al. [147] and Obabko et al. [103].
Coming back to our case of interest that involves heat transfer in abruptly separated flows, very limited studies can be found at low Prandtl number. Kondoh et al. [71] had simulated in the 1990s a 2D laminar case of a BFS, varying several parameters (ER, Re and Pr) and looking into their influence on the heat transfer in separating and reattaching flows. More recently, this flow configuration has generated an increasing interest and will be implemented into the liquid sodium loop of the KASOLA facility [57], within the frame of the European Horizon 2020 project SESAME [127]. Niemann and Fröhlich [99] simulated a turbulent flow of liquid sodium ($Pr = 0.0088$) over a BFS in forced convection using DNS ($ER = 2$). The study was extended to a mixed convection regime [100], highlighting the strong impact of buoyancy on the thermal field. The Reynolds number was later increased from 4805 to 10000 [101], particularly useful for model development. Schumm et al. [143] investigated the influence of different heat transfer models in forced convection and buoyancy-aided mixed convection [144]. In both flow regimes, Kays correlation [62] showed superior performance compared to two equation heat flux models,

in terms of heat transfer at the wall. On the other-hand, the work of Santis and Shams [132] showed that improved results could be obtained with the AHFM-NRG+ model compared to the Reynolds analogy assumption, thus providing encouraging results for RANS simulations of low Prandtl number fluids.

As pointed out already, the lack of reference data in an unconfined environment, representative of pool flows, strongly motivates this work. A wall-resolved LES is used to solve the flow past a heated unconfined BFS. In addition to simulations in air ($Pr = 0.71$) and the He-Xe gas mixture ($Pr = 0.2$), LES at a low Prandtl number characteristic of LBE ($Pr = 0.025$) is performed. The objectives of these LES are twofold:

- Generate reference data for the assessment and improvement of turbulent heat transfer models suitable for liquid metal flows.
- Provide further insight into low Prandtl number effects on heat transfer in abruptly separated flows, in forced heat convection.

To better understand the heat transfer mechanisms specific to low Prandtl fluids, the LES results obtained at these three Prandtl numbers are compared. Firstly, the needs in terms of mesh resolution for the LES at low Pr are inspected. Different fluid properties are summarized and similarity requirements are discussed, to insure that the same flow regime is simulated in all three cases. The analysis of the results focuses on the Prandtl number effects observed in the thermal field, mean and rms quantities are compared. The heat transfer performance is then assessed by examining the typical heat transfer coefficients. The different mechanisms responsible for the transport of heat are identified by decomposing the heat flux distributions into turbulent and molecular contributions. The inspection of turbulent Prandtl number fields is finally proposed, in order to draw conclusions regarding the applicability of the concept to recirculating and recovering zones.

6.2 Methodology

The numerical set-up described in Section. 5.2 is the same for all simulations at different Pr, that is the computational domain and boundary conditions remain unchanged. In addition, the same mesh is used for all three runs at $Pr = 0.71, 0.2$ and 0.025. At this lowest value, it is naturally much more resolved as far as the temperature field is concerned, due to the large increase in thermal diffusivity. As discussed hereafter, this offers the opportunity to fully resolve all thermal scales, i.e. LES of the velocity field but Q-DNS of the temperature field [69] such that the SGS heat flux model will not play an active role. The fluid properties and similarity parameters are firstly discussed.

During the construction of the MYRTE wind tunnel, a preliminary study [23] was conducted on the test case of Le et al. [75]. This work is summarized in Appendix F and provided the opportunity to set-up the BFS case described previously and carry out a first comparison between the LES run for air, He-Xe and LBE. The results confirmed that noticeable differences should be expected between air and the gas mixture, while significant Prandtl number effects are observed at low Prandtl number.

6.2.1 Fluid properties at different Prandtl numbers

The set of transport properties defining each fluid is given in Table 6.1. Although the physical properties are tabulated, in the LES, the fluid properties are adjusted to insure that the flow regime stays the same, so that changes are solely due to Prandtl number effects.

Fluid	$\beta\ [K^{-1}]$	$\lambda\ [W/m.K]$	$\rho\ [kg/m^3]$	$c_p\ [J/kg.K]$	$\nu\ [m^2/s]$	$\alpha\ [m^2/s]$	Pr
air	0.0034	0.026	1.205	1000	1.57×10^{-5}	2.12×10^{-5}	0.71
He-Xe	0.0034	0.083	1.194	707	2.04×10^{-5}	9.95×10^{-5}	0.2
LBE	0.0013	12.5	10259	144	2.14×10^{-7}	8.44×10^{-6}	0.025

Table 6.1: *Physical fluid properties under atmospheric conditions (1 bar, $20°C$) for air and He-Xe, and MYRRHA operating conditions ($220°C$) for LBE [102].*

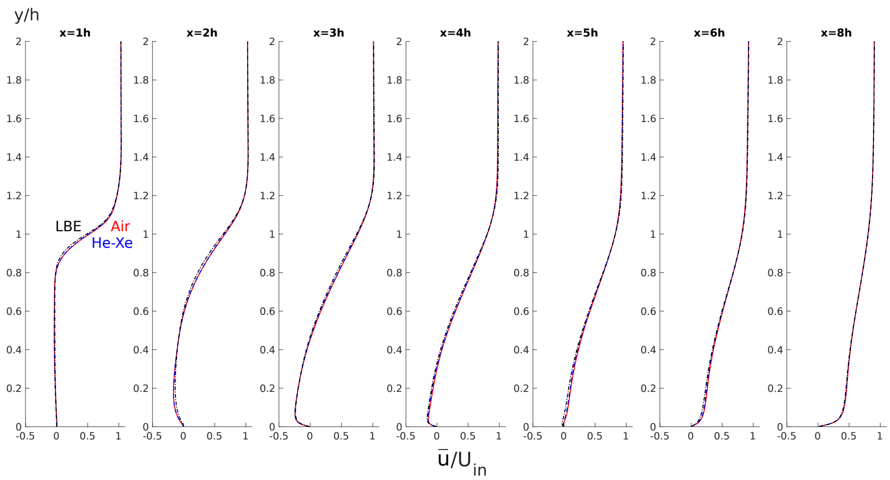

Figure 6.1: *Mean streamwise velocity profiles obtained at different Prandtl numbers.*

This requires to keep the similarity parameters essentially constant. For instance, the Reynolds nmber Re_h, is kept equal to 8930, by keeping the kinematic viscosity constant. The desired Prandtl number is then fixed by adjusting the value of the thermal diffusivity. The last parameter that is read by the OpenFOAM solver, is the thermal expansion coefficient, that influences the natural convection effects. The PIV results of Chapter 3 have shown that the thermal effects have a very weak influence on the velocity field, as indicated by the Richardson number $Ri = \beta\, g\, h\, \Delta T / U_{in}^2$, that is about 3×10^{-4} for air and He-Xe. To maintain the similarity between the LES at moderate ($Pr = 0.71$ and 0.2) and low Prandtl number ($Pr = 0.025$), ΔT is increased from $22\,°C$ to $190\,°C$, to account for the reduced thermal expansion. This temperature difference also corresponds to the gradient in MYRRHA (nominal conditions); T_{in} and T_w are adjusted to $220\,°C$ and $410\,°C$, to match the cold and hot plenum temperatures respectively. The resulting Ri number is approximately 1×10^{-4}. The flow similarity is verified by comparing, in Fig. 6.1, the velocity field obtained at different Pr, which, as expected, is practically identical between the LES.

6.2.2 Numerical approach

As pointed out previously, the advantage of very low Prandtl number flows is that the smallest scales of the temperature field are much larger than the ones associated to the velocity field. This implies that, if the LES is performed at high enough resolution, although the mesh will not fully resolve the velocity field, the temperature field will be properly captured. Consequently, a SGS model is only required in the momentum equation whereas there is no need for any subgrid heat flux model in the energy equation.

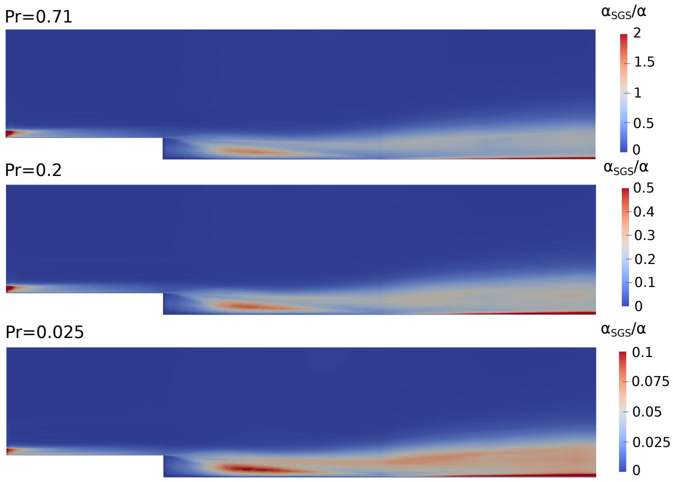

Figure 6.2: *Contours of the ratio α_{sgs}/α in a vertical plane extracted from the LES at Pr=0.71, 0.2 and 0.025.*

This numerical approach has been used previously [37, 50], a pre-requirement though is that the mesh be sufficiently resolved to capture the smallest temperature scales. These are characterized by the Corrsin scale $\eta_T = \eta Pr^{-3/4}$, where $\eta = (\nu^3/\epsilon)^{1/4}$ is the Kolmogorov scale and ϵ is the dissipation. Although, in theory, the mesh size Δ should be smaller than η_T, Grötzbach [51] investigated resolution requirements for heat transfer DNS, and suggested $\Delta/\eta_T < 3.45$ as sufficient at low Pr. The turbulent dissipation rate (ϵ) can be derived from estimating velocity derivatives. This was done experimentally by Kasaga and Matsunaga [60] for instance, using a 3D particle-tracking velocimeter in a BFS at $Re_h = 5540$. The different terms of the turbulent energy budget were found to be in excellent agreement with the corresponding DNS of Le et al. [75]. The focus is here brought on the shear layer, where the highest values are found shortly after separation. To remain conservative, the strongest peak measured at $x/h = 1$ is considered, reaching about 20×10^{-3} (normalized by U_{in}^3/h). At $Pr = 0.025$, this yields a resolution requirement $\Delta/h < 0.16$. Considering $\Delta = (\Delta x\, \Delta y\, \Delta z)^{1/3}$, this condition is respected throughout the computational domain. One may therefore conclude that the mesh at $Pr = 0.025$ should be sufficiently refined to resolve all thermal scales.

The importance of the SGS thermal diffusivity compared to the molecular thermal diffusivity is represented in Fig. 6.3. As expected, the influence of the thermal SGS modelling is progressively reducing as the Pr reduces and has a much smaller influence at Pr=0.025. It is however still acting since independently on the mesh resolution, $\alpha_{sgs} = \nu_{sgs} \cdot Pr_{sgs}$, considering that in all cases the SGS model was kept active. However, it is important to stress that the SGS contribution is found to have a negligible influence compared to the resolved part of the turbulent heat fluxes, with $|\alpha_{sgs}\, \nabla \overline{T}| << |\overline{T'v'}|$. This may be explained by the fact that in abruptly separated flows, the turbulent structures are quite large within the region of interest, which is of course emphasized at low Pr when it comes to the thermal scales.

6.3 Presentation of the results

6.3.1 Turbulent scales

To illustrate further some of the observations made while comparing the results in air and He-Xe (see Chapter 5), the turbulent spectra for the velocity and temperature, at two points within the shear layer, are represented in Fig. 6.3. Signals are sampled every $10\,\Delta t$, over a time window of $800\,\Delta t_p$. All spectra are then spanwise averaged. As expected, the velocity spectrum obtained at different Pr is identical since one remains in forced convection and since the heating effects are adjusted for similarity. The temperature spectrum, on the other-hand, is strongly affected by Prandtl number effects. The comparison of the two illustrates how different the velocity and the temperature scales can be depending on the Prandtl number.
Between air and He-Xe, the temperature fluctuation levels are of the same order but nevertheless, at lower frequency ($f\,h/U_{in} < 1$), the energy content of the gas mixture is slightly higher than for air. This corroborates what had been observed in Section. 5.5.2, where stronger temperature fluctuations appeared in He-Xe within the shear layer. This remains the case whether or not the LES is filtered (ref. Fig. 5.17), which demonstrates that, in this region, most of the energy is found at low frequencies. At low Prandtl number, the amplitude

associated to the temperature spectrum reduces by two orders of magnitude, because of the increased thermal diffusivity. This also implies that the thermal turbulent structures will dissipate faster, as observed on the spectrum, with a dampening that occurs at lower frequencies.

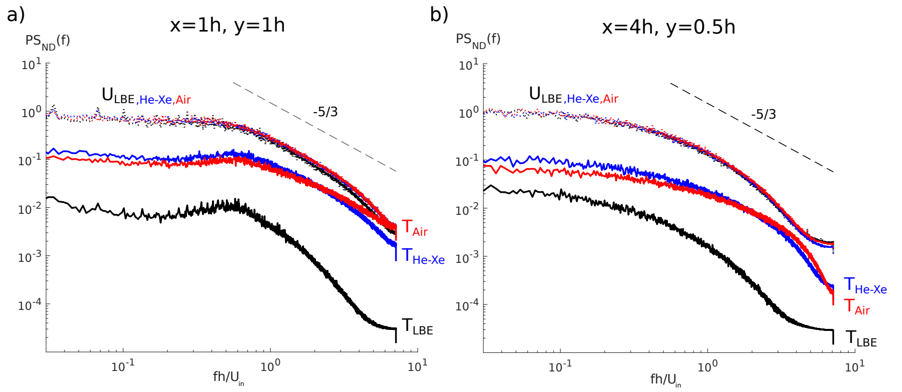

Figure 6.3: *Energy spectra of the velocity and temperature signals extracted from the LES at different locations a) $x = 1\,h$, $y = 1\,h$ b) $x = 4\,h$, $y = 0.5\,h$.*

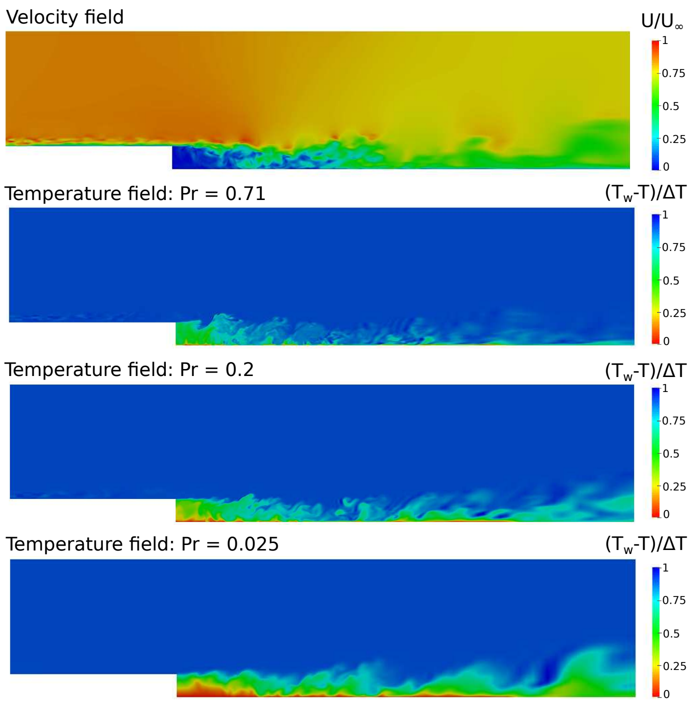

Figure 6.4: *Instantaneous views of the thermal-hydraulic field in a vertical plane.*

These differences appear clearly between instantaneous temperature fields shown in Fig. 6.4. At $Pr = 0.71$, both small and large-scale structures are present in the velocity and temperature fields. On the contrary, for $Pr = 0.025$ only the large-scale thermal structures induced by the velocity field persist. This also confirms that the mesh is able to fully capture these, and that a subgrid heat flux model is not required.

6.3.2 Prandtl number effects on the thermal field

The mean temperature fields are shown in Fig. 6.5, where a strong influence of the Prandtl number is observed. One recalls that all overlined quantities are time and spanwise averaged.

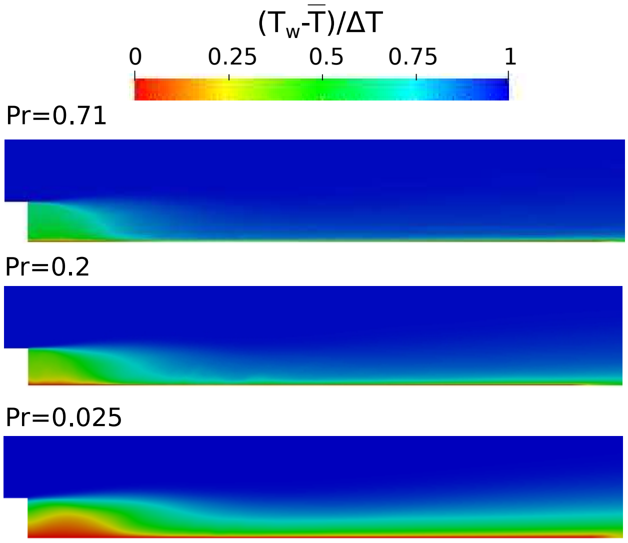

Figure 6.5: *Influence of the Prandtl number on the mean temperature field.*

In the case of air, the thermal behaviour is strongly related to the flow streamlines since both fields are similar. Therefore, the highest differences are concentrated in the step corner, where the secondary recirculation is located. Between $Pr = 0.71$ and 0.2, molecular heat diffusion starts to play a bigger role in the transport of heat. Consequently, heat is conducted slightly further away from the wall. This effect is strongly emphasized at $Pr = 0.025$. The heated area is much larger because of the very important role played by the molecular heat diffusivity. A more quantitative comparison is proposed in Fig. 6.6, where vertical profiles are extracted. Stronger temperature gradients are present across the shear layer. The thermal boundary layer after reattachment becomes thicker as the Prandtl number reduces.
The fields of temperature rms are shown in Fig. E.2, exhibiting high fluctuations in regions of strong turbulence, within the shear layer and in the near-wall region. These naturally result from warm fluid that is transported upwards,

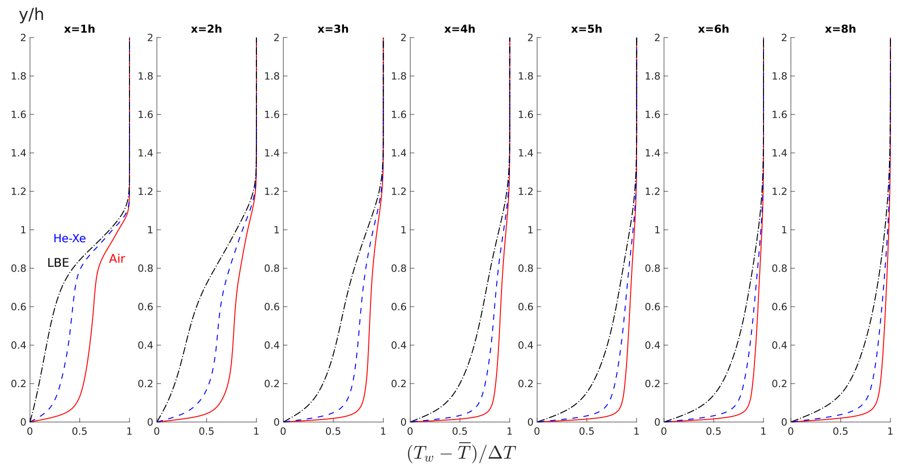

Figure 6.6: *Mean temperature profiles obtained by LES at different Prandtl numbers.*

away from the heated step. Near the wall, the turbulence levels increase with Pr, while in LBE, a much smoother thermal boundary layer is observed. In addition, levels remain high when the thermal diffusion increases, thus the affected region becomes larger as Pr reduces. Consequently, the fluctuations penetrate deeper into the flow, in both streamwise and wall-normal directions.

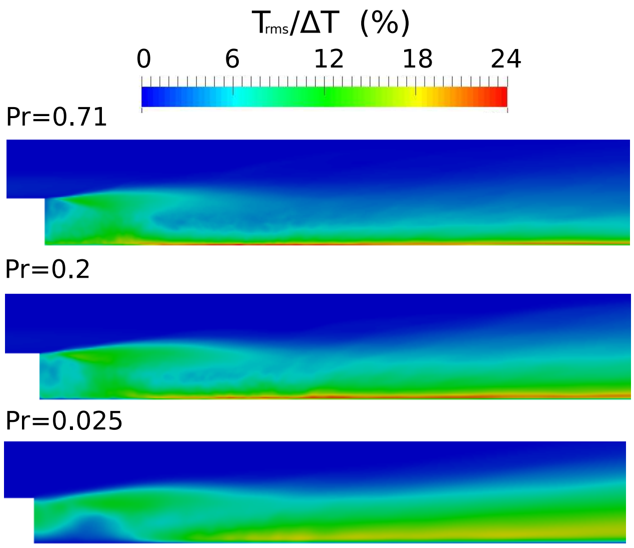

Figure 6.7: *Influence of the Prandtl number on the temperature rms field.*

Moreover, the vertical profiles plotted in Fig. 6.8, show that, along the streamwise direction, levels keep increasing within the recovery region. On the contrary, at higher Prandtl number, the thermal boundary is much thiner and the near-wall peak is confined closer to the wall. Concerning the amplitude of these fluctuations, the differences observed between the fluids very much depend on the mechanism that dominates heat transfer. Further insight on this aspect is proposed hereafter.

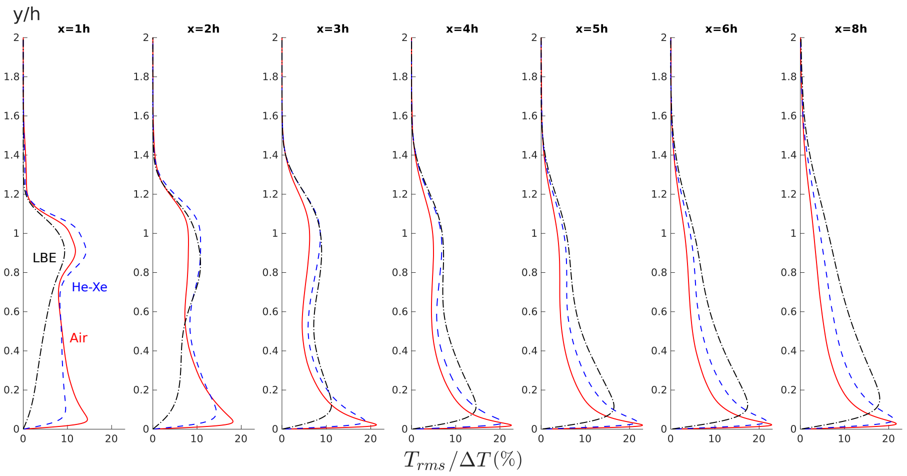

Figure 6.8: *Rms temperature profiles obtained by LES at different Prandtl numbers.*

6.3.3 Heat transfer performance

The Nusselt number, representative of the ratio between the convective and a conductive heat transfer computed using the thermal conductivity and a global temperature difference ΔT and length scale L_r, is defined as:

$$Nu = \frac{\overline{q}_w}{\lambda \, \Delta T / L_r} = \frac{h_c \, \Delta T}{\lambda \, \Delta T / L_r} = \frac{h_c \, L_r}{\lambda} \, , \tag{6.1}$$

where h_c is the convective heat transfer coefficient and λ is the thermal conductivity of the fluid.

The Stanton number, used to characterize heat transfer in forced convection flows, defines the ratio of heat transferred into a fluid to its thermal capacity. It is given by:

$$St = \frac{h_c}{\rho \, U_{in} \, c_p} = \frac{Nu}{Re \, Pr} \, , \quad with \;\; Re = \frac{\rho \, U_{in} \, L_r}{\mu} \, . \tag{6.2}$$

Both of these similarity numbers can be determined locally, by considering the streamwise value of the vertical temperature gradient at the wall. Thus, the heat transfer performance in local portions of the step area are discussed, based on the wall distributions shown in Fig. 6.9.

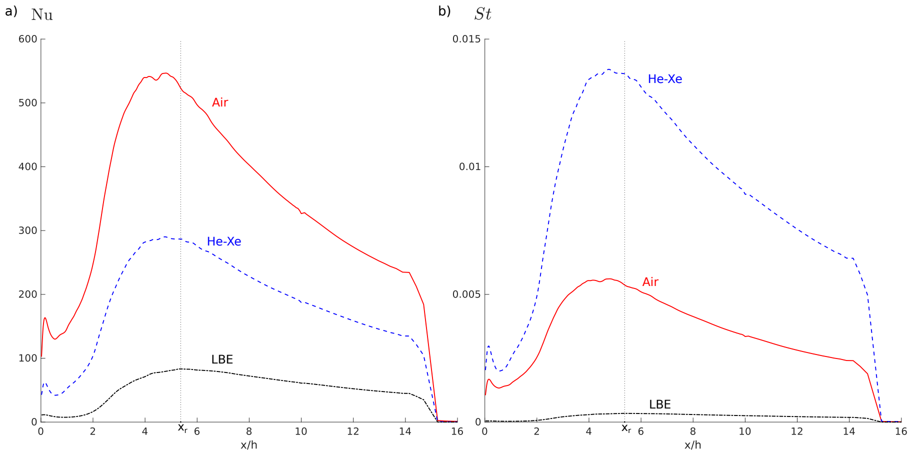

Figure 6.9: *Streamwise variations in the heat transfer coefficients a) Nusselt number b) Stanton number.*

Similar trends are observed between the LES at different Prandtl numbers. The heat transfer increases progressively along the wall, until it reaches a maximum near the reattachment. Indeed, this peak in heat transfer has been correlated [63] to the peak in wall shear stress fluctuations, caused by the impinging eddies that impact the wall. During this "downwash", cold fluid from above the shear layer is brought towards the wall. In general, the heat transfer is enhanced by abrupt flow separation and subsequent reattachment; while it is hindered by the recirculation, it strongly increases near the reattachment.
For the air and the He-Xe gas mixture, the maximum heat transfer is located shortly before the reattachment, in agreement with the experiment of Vogel and Eaton [168] or LES [13, 63]. Here also, it is found approximately $0.1\, x_r$ upstream of mean reattachment. At low Prandtl number, on the other-hand, it moves slightly downstream to the mean reattachment point. In all cases, the heat transfer coefficients attain their minimum value near the step corner ($x/h \simeq 0.5$), as the dominant mode of heat transfer within this "stagnant" zone is through conduction. After reattachment, the thermal boundary layer redevelops and grows progressively, which together with the absence of impinging shear layer eddies, explains the decrease in heat transfer.

Pr	Nu	St
0.71	353	3.6×10^{-3}
0.2	189	8.9×10^{-3}
0.025	55	2.23×10^{-4}

Table 6.2: *Global heat transfer coefficients over the heated length.*

Prandtl number effects on heat transfer coefficients can be clearly distinguished, thus pointing towards the dominant mode of heat transfer. Naturally, conduction becomes more and more important as Pr reduces and eventually takes over the turbulent convection effects at some places [1]. The global heat transfer performance can be determined by integrating the Nusselt number along the heated plate, values resulting from the LES are reported in Table 6.2. At low Prandtl number, the thermal capacity of LBE is such that convection effects are very small compared to inertial effects, which results in very low St values. The gas mixture, on the other-hand, shows the highest St distribution, even compared to the air. This behaviour is associated to a higher thermal diffusivity (see values reported in Table 6.1). Consequently, the highest rate of heat transfer occurs in the gas mixture. This also explains why it exhibits the strongest thermal fluctuations within the shear layer (see Fig. 6.8).

6.3.4 Prandtl number effect on heat flux

The streamwise and vertical turbulent heat fluxes are shown in Fig. 6.10 and Fig. 6.11 respectively. The imprint of the shear layer and of the redeveloping thermal boundary layer is clearly visible on both of these. Unlike the observations made by Vogel and Eaton [168] from their experiment, the streamwise turbulent heat flux is far from negligible. Indeed, levels comparable to the vertical component are obtained, in agreement with previous LES results [13, 63].

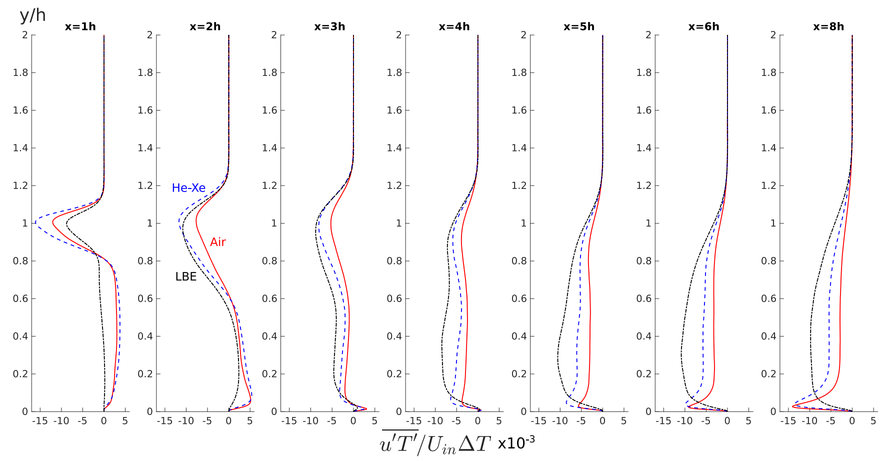

Figure 6.10: *Streamwise turbulent heat transfer obtained by LES at different Prandtl numbers.*

For air and He-Xe, the highest peak in streamwise turbulent heat flux is found at the onset of the shear layer. The peak is not as strong at low Pr, because of strong diffusion effects (see Fig. 6.13). However, this damping reduces further downstream, allowing the correlation between fluctuating velocity and temperature fields to eventually exceed the levels observed at higher Pr. As the flow

[1] In a channel flow, even at $Pr = 0.01$, molecular and turbulent heat flux remain of the same order throughout the flow (see Duponcheel et al. [37]).

redevelops, the streamwise velocity fluctuations increase and therefore similarities with the temperature field pick up near the wall. This peak is naturally further away from the wall in He-Xe than in air as the thermal boundary layer is thicker. In LBE, heat is transported much more smoothly and further away from the wall, showing no distinctive peak.

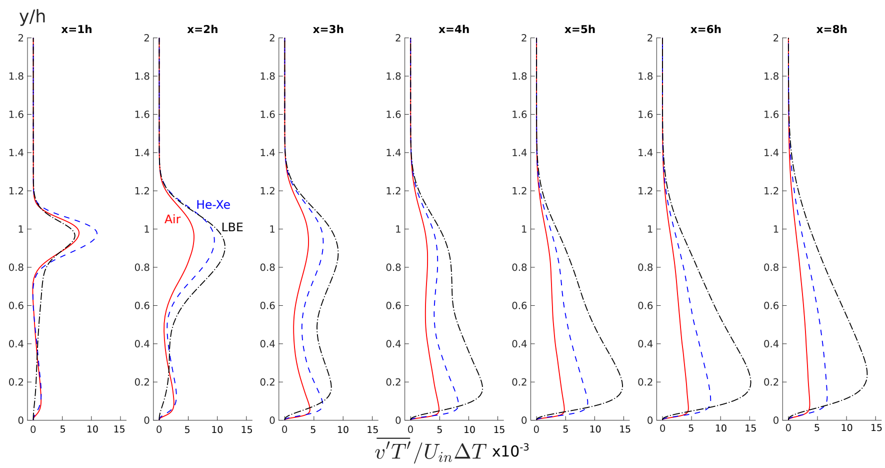

Figure 6.11: *Vertical turbulent heat transfer obtained by LES at different Prandtl numbers.*

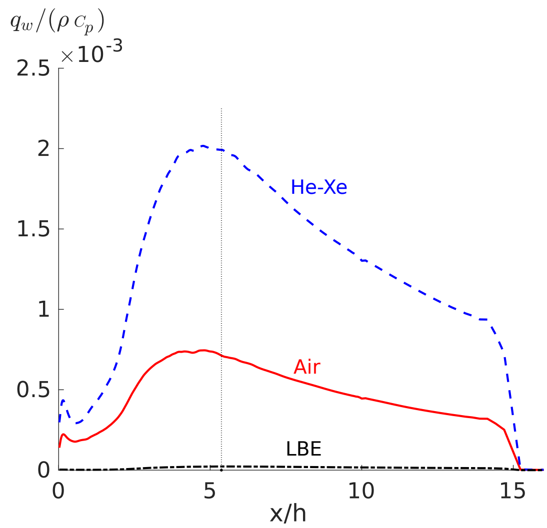

Figure 6.12: *Streamwise variation of* $\frac{q_w}{\rho\, c_p} = \alpha \left.\frac{\partial \overline{T}}{\partial y}\right|_w$ *as a function of the Prandtl number.*

One recalls that a constant temperature is applied to the step wall, resulting in a wall heat flux $q_w = \lambda \left.\frac{\partial \overline{T}}{\partial y}\right|_w$, that varies in the streamwise direction, as shown in Fig. 6.12. Naturally, heat is transported from the heated wall and across the shear layer in the wall-normal direction. A more thorough analysis of wall-normal heat transfer is proposed in Fig. 6.13 by splitting the heat transport into a molecular and a turbulent component. The total vertical heat flux is decomposed as: $\overline{q}^+_{tot,Y} = \overline{q}^+_{m,Y} + \overline{q}^+_{t,Y}$, defined as:

$$\overline{q}^+_{m,Y} = -\alpha \, \frac{\partial \overline{T}}{\partial y} \Big/ \frac{q_w}{\rho \, c_p} \, , \quad \overline{q}^+_{t,Y} = \overline{T'v'} \Big/ \frac{q_w}{\rho \, c_p}, \tag{6.3}$$

At the onset of the shear layer ($x/h = 1$), at high Pr, molecular effects contribute very little compared to turbulence. On the contrary, at $Pr = 0.025$, conduction is the dominant mode of heat transport. Furthermore, instead of dissipating straight away, this peak remains visible even several step heights further downstream.
In the near-wall region, similar observations can be made. Additionally, in LBE, the molecular heat flux extends further out throughout the recirculation as a thicker thermal boundary layer redevelops. Once again, at high Pr, turbulence strongly dominates over diffusion effects, and is mostly responsible for the transport of heat throughout the flow. This is clearly visible in Fig. 6.14, where a direct comparison of molecular and turbulent contributions is proposed.

As pointed out previously, heat transfer along the flow direction is non-negligible. Similarly to Eq. (6.3), one may analyze the heat transfer in the streamwise direction by defining:

$$\overline{q}^+_{m,X} = -\alpha \, \frac{\partial \overline{T}}{\partial x} \Big/ \frac{q_w}{\rho \, c_p} \, , \quad \overline{q}^+_{t,X} = \overline{T'u'} \Big/ \frac{q_w}{\rho \, c_p}, \tag{6.4}$$

By examining the profiles plotted in Fig. 6.15, one observes that the turbulent contribution dominates by far the molecular effects. These become negligible after $x = 2\,h$ at high Pr since the streamwise gradients of temperature are localized within the step corner (secondary recirculation), while at $Pr = 0.025$ they extends sightly further downstream.

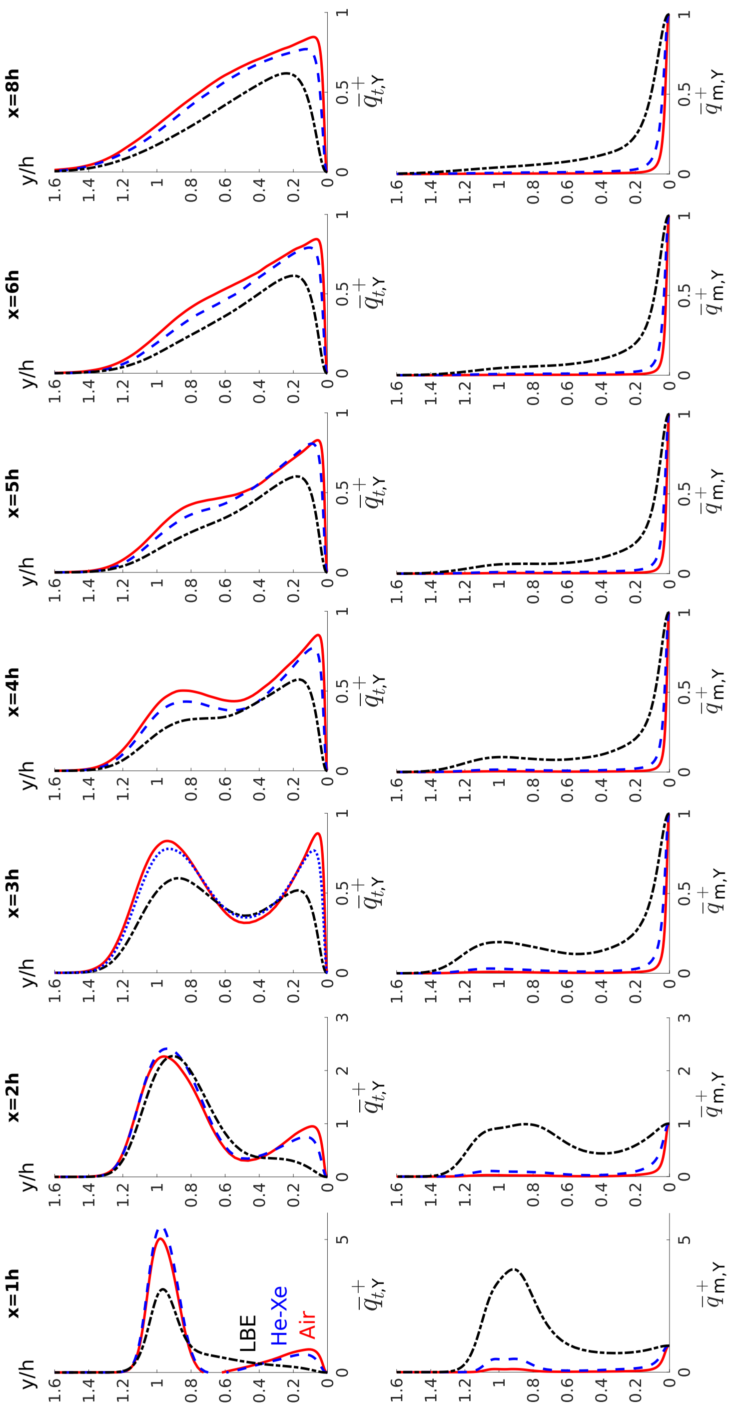

Figure 6.13: *Vertical heat flux decomposition at different Prandtl numbers. Molecular part $\overline{q}^{+}_{m,Y}$ and turbulent part $\overline{q}^{+}_{t,Y}$.*

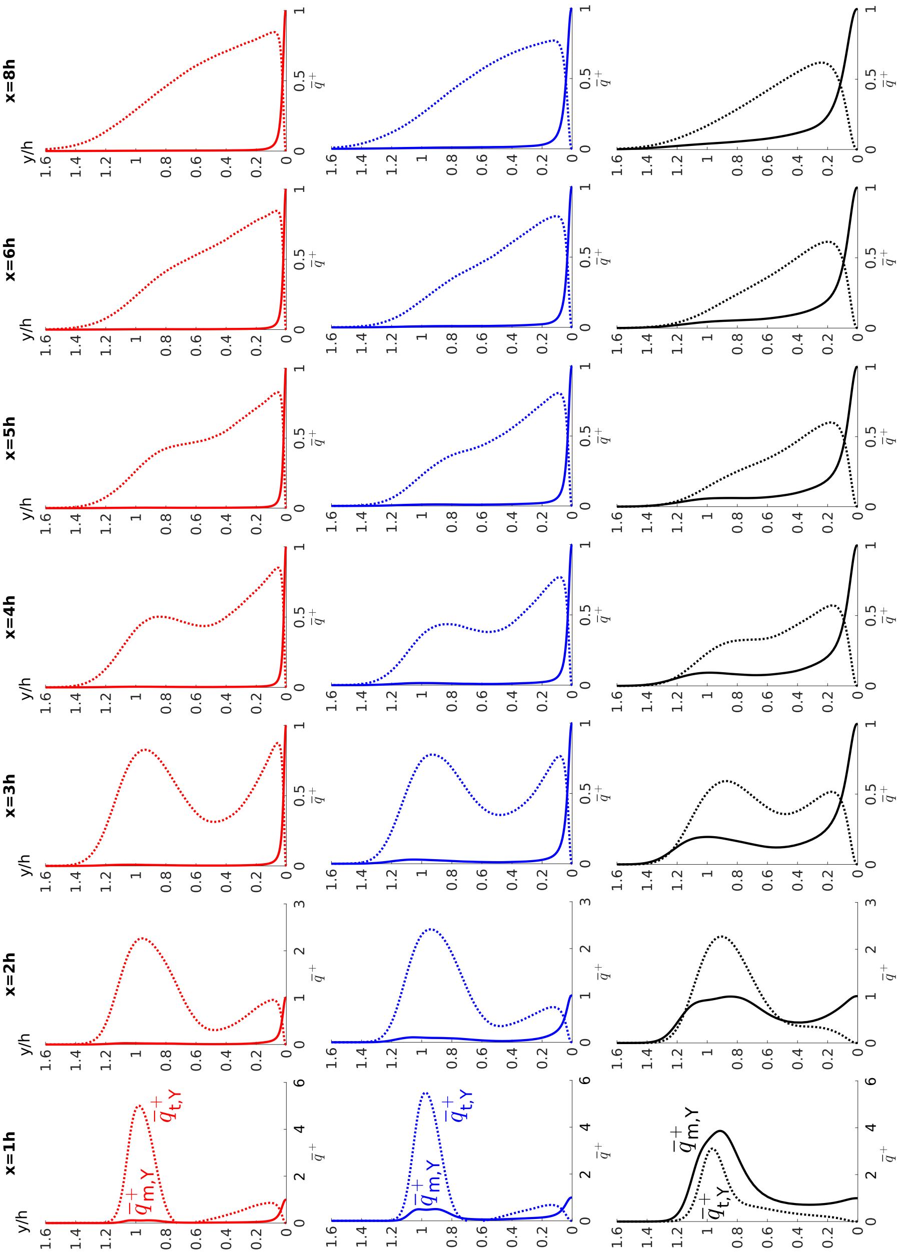

Figure 6.14: *Comparison of molecular and turbulent vertical heat flux at different Prandtl numbers a) $Pr = 0.71$ b) $Pr = 0.2$ c) $Pr = 0.025$.*

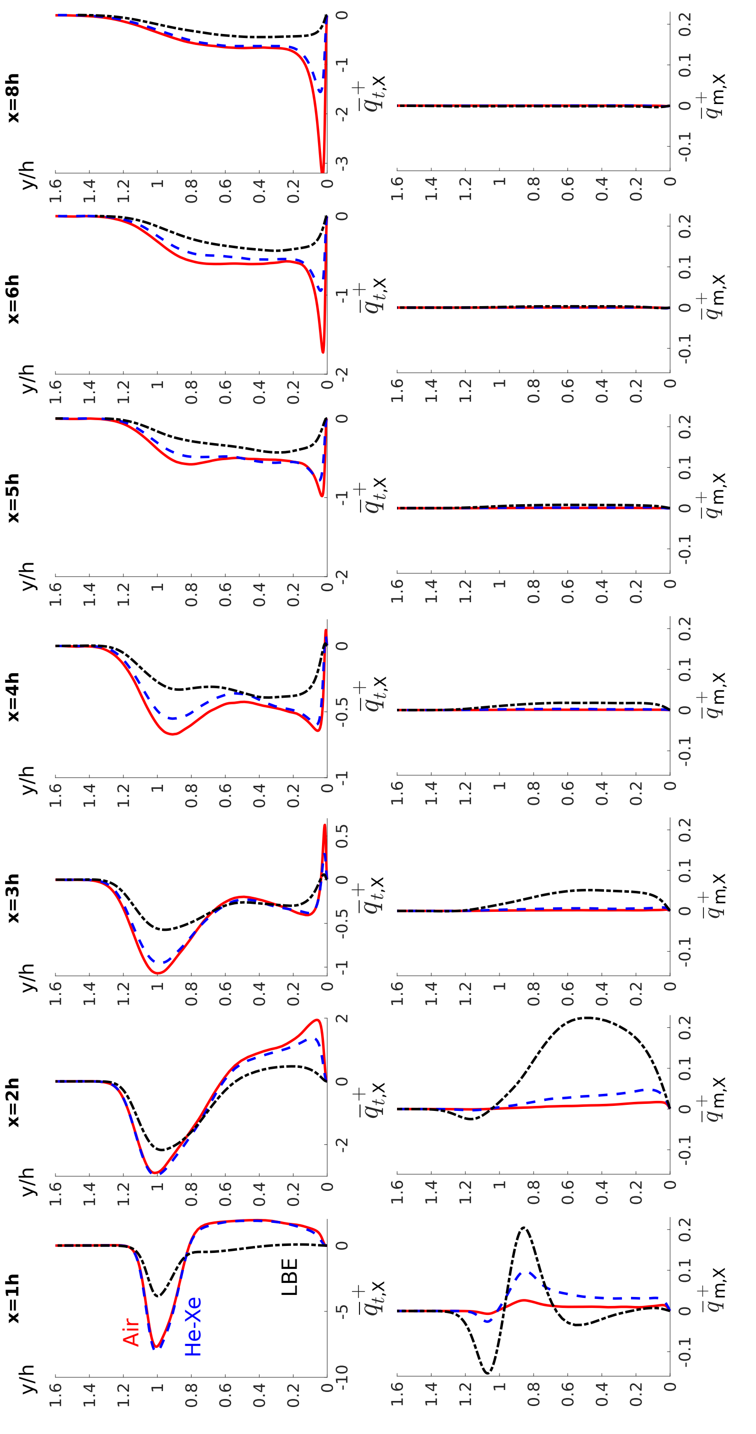

Figure 6.15: *Streamwise heat flux decomposition at different Prandtl numbers. Molecular part* $\overline{q}^+_{m,X}$ *and turbulent part* $\overline{q}^+_{t,X}$.

6.3.5 Turbulent Prandtl number distribution

A gradient assumption is commonly applied by RANS methods to model both the Reynolds stresses and the turbulent heat flux, such that for instance:

$$-\overline{u'v'} = \nu_t \frac{\partial \overline{u}}{\partial y}, \quad -\overline{T'v'} = \alpha_t \frac{\partial \overline{T}}{\partial y}. \tag{6.5}$$

Subsequently, the turbulent Prandtl number concept is used to relate the turbulent diffusivity and the turbulent viscosity, yielding:

$$Pr_t = \frac{(-\overline{u'v'})}{\partial \overline{u}/\partial y} \cdot \frac{\partial \overline{T}/\partial y}{(-\overline{v'T'})}\,. \tag{6.6}$$

In most codes, the Reynolds analogy is the only alternative to model the turbulent heat flux. It is based on the Pr_t concept and assumes similarity between the momentum and thermal turbulence. Thus, Pr_t is simply set to a constant, of order unity. This may be reasonably accurate in the case of fluids characterized by a Prandtl number close to unity, but it is known to fail at low Prandtl number [1, 37].

The objective is to analyze Pr_t variations within exploitable areas, where both ν_t and α_t are well defined, limited to the shear layer and the recovery region. The criteria chosen to delimit the shear layer is represented in Fig. 6.16, where the upper and lower bounds are given by $0.2\,U_\infty$ and $0.8\,U_\infty$ respectively. The shear layer thickness δ_{SL}, is defined as the height between these two limits.

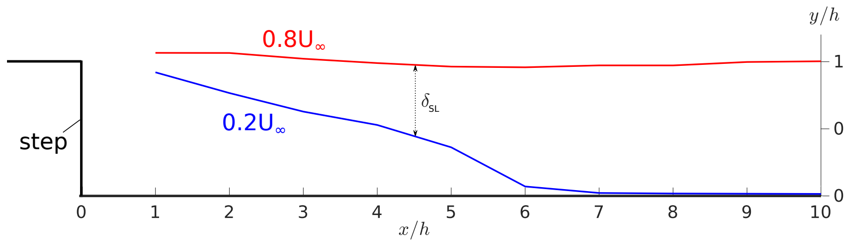

Figure 6.16: *Shear layer development downstream of the step.*

Pr_t vertical profiles along the distance $\pm\delta_{SL}/2$ across the shear layer are plotted in Fig. 6.17. The data are extracted every step height above the recirculation area ($x < x_r$). Just after separation, a bell shape profile is observed at $x/h = 1$ and 2, exhibiting a minimum around the center of the shear layer. At the following two positions $x/h = 3$ and 4, profiles are smoother, while stronger variations reappear closer to reattachment. These trends remain very similar between the three fluids.
On the contrary, predicted values are more significantly affected by the Prandtl number. In air, the average value at positions x/h from 1 to 5 is equal to 0.59, while in the He-Xe gas mixture distributions lie slightly above and correspond to in average 0.62. Prandtl number effects are more significant at low Pr, as the

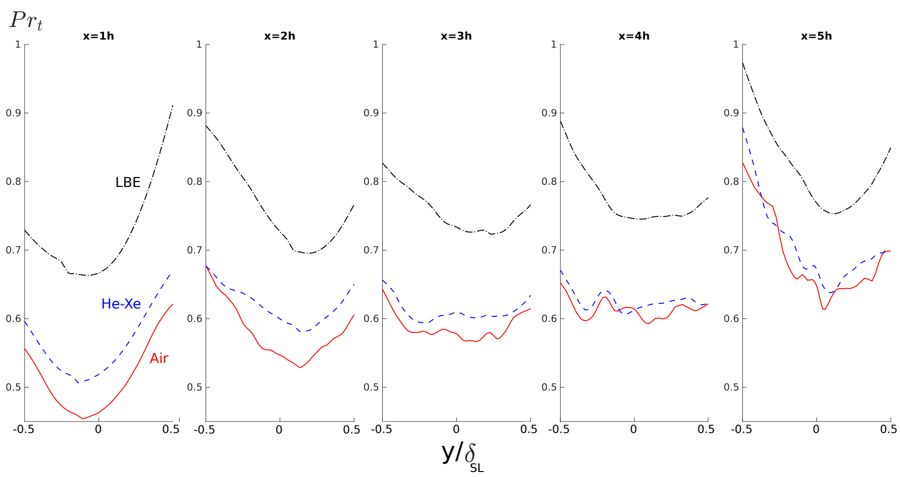

Figure 6.17: *Turbulent Prandtl number variations across the shear layer above the primary recirculation.*

profiles are consistently higher with a mean value of 0.76. The Pr_t distributions rise as Pr reduces because of stronger temperature gradients. The mean values along the streamwise direction are reported every step height in Table 6.3. In all cases, Pr_t keeps increasing as one approaches reattachment. However, values remain lower than standard values used in RANS ($Pr_t \simeq 0.9$).

Pr \ Pr_t	h1	h2	h3	h4	h5	mean
0.71	0.51	0.57	0.59	0.61	0.68	0.59
0.2	0.56	0.62	0.61	0.62	0.70	0.62
0.025	0.72	0.75	0.75	0.77	0.82	0.76

Table 6.3: *Mean turbulent Prandtl number values at different streamwise positions across the shear layer above the primary recirculation.*

Focusing now on the shear layer that expands into the recovering region ($x > x_r$), distributions are plotted in Fig. 6.18. Similarly to the behaviour observed above the recirculation area, Pr_t increases at lower Prandtl number. Nevertheless, the shape of the distribution differs, and remains consistently the same throughout the area. The profiles first increase before decreasing, reaching a maximum located at a given height regardless of the Prandtl number. This behaviour is caused by the dominating momentum shear that persists beyond reattachment [19]. Average Pr_t values are computed along each vertical profile and summarized in Table 6.4. The same trends emerge compared to the previous region. Firstly, the Prandtl number effects are of the same order, with a small increase of 3.6 % between air and He-Xe, and another 21 % for LBE. Secondly, Pr_t keeps increasing along the streamwise flow direction, no matter the Prandtl number value. In air for instance, Pr_t is initially equal to 0.80 at $x/h = 6$ and rises up to 1.2 at $x/h = 14$, which is already closer to the values that are usually used in RANS. In LBE, Pr_t goes from 0.98 to 1.57 respectively, thus lower than values observed in fully developed flows [37].

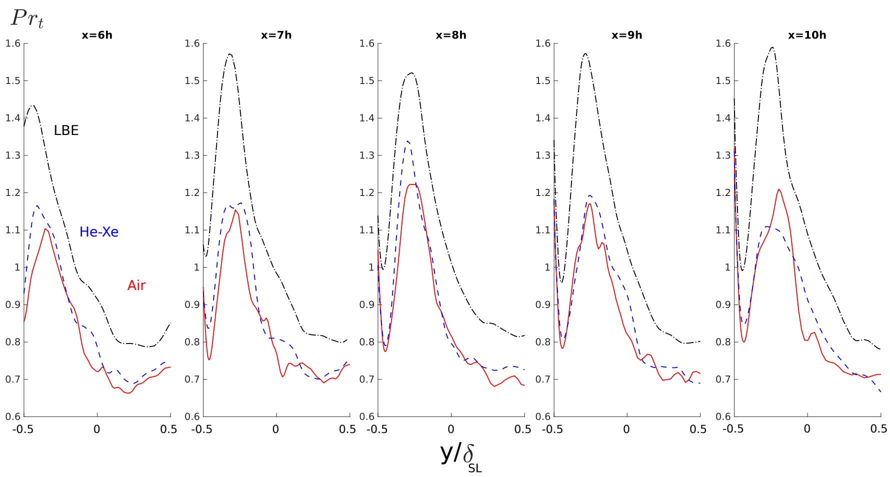

Figure 6.18: *Turbulent Prandtl number variations across the shear layer within the recovering region.*

Pr \ Pr_t	h6	h7	h8	h9	h10	h12	h14	mean
0.71	0.80	0.83	0.90	0.91	0.94	1.1	1.2	0.95
0.2	0.84	0.88	0.92	0.93	0.96	1.14	1.25	0.99
0.025	0.98	1.07	1.11	1.14	1.17	1.39	1.57	1.2

Table 6.4: *Mean turbulent Prandtl numbers at different streamwise positions across the shear layer within the recovering region.*

The main conclusion that can drawn from this study is that, independently on the Pr number, setting a single constant Pr_t value across the entire CFD domain is in contradiction with the flow's physical behaviour. Indeed, this parameter has been shown to vary significantly across the domain. These results suggest that the applicability of the Pr_t concept could be improved by setting different constant values depending on the flow region and the fluid's Pr number. In this particular case for instance, one may consider patching different values within the shear layer region before and after reattachment, i.e. $Pr_t \simeq 0.6$ and $Pr_t \simeq 0.95$ respectively (at $Pr = 0.71$). Moreover, as stated previously, the Pr_t concept remains unapplicable in the areas where ν_t and α_t are not both well defined.

6.3.6 Alignment between the turbulent heat flux and the mean temperature gradient

Finally, one may go a step further by looking into the relevancy of the underlying assumption that is made by the Pr_t concept. Indeed, it is based on the simple gradient diffusion hypothesis (SGDH) since isotropic scalars are used for ν_t and α_t. By convention, this latest parameter is only dependent on the turbulent heat flux and the temperature gradient in the vertical direction:

$$\alpha_t = \frac{-\overline{T'v'}}{\partial \overline{T}/\partial y}. \tag{6.7}$$

An istropic flow would behave uniformly in all directions, and consequently the components of the turbulent heat flux vector $\overline{q}_t$, should be aligned with the corresponding components of the temperature gradient vector, $-\nabla\overline{T}$. The validity of this assumption is investigated hereafter, by computing the angle θ between these two vectors, as:

$$\theta = cos^{-1}\left(\frac{-\overline{q}_t \cdot \nabla\overline{T}}{\|\overline{q}_t\| \cdot \|\nabla\overline{T}\|}\right). \tag{6.8}$$

As proposed previously, this analysis is limited to the areas where Pr_t that is based on the vertical heat flux is well defined: within the shear layer above the primary recirculation in Fig. 6.19 and within the recovery region in Fig. 6.20.

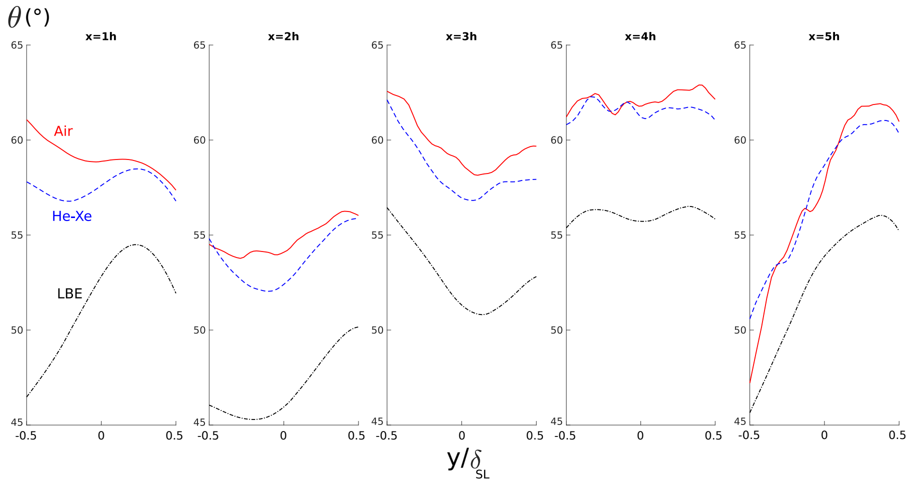

Figure 6.19: *Angle between the turbulent heat flux and the temperature gradient vectors across the shear layer above the primary recirculation.*

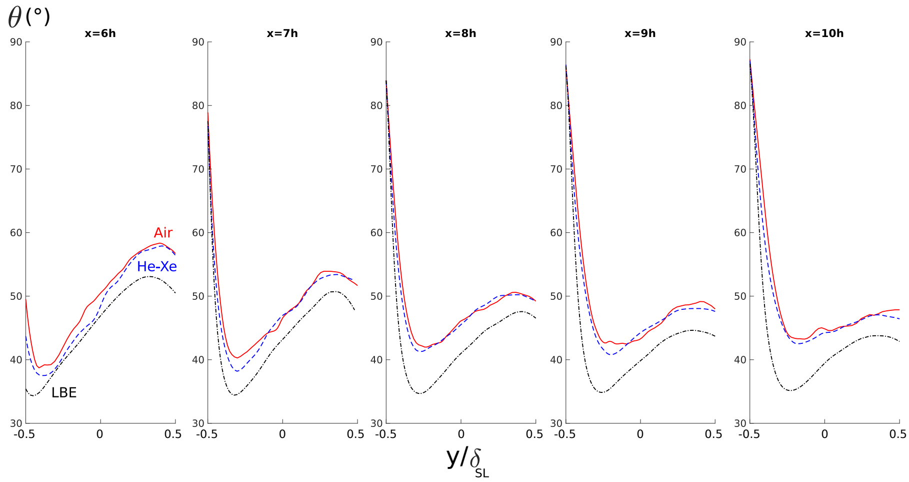

Figure 6.20: *Angle between the turbulent heat flux and the temperature gradient vectors across the shear layer within the recovery region.*

These results indicate that, for all Pr number fluids, an important angle exists between the two vectors. In the shear layer above the recirculation, θ is within $[45-65]^\circ$, while within the recovery region, it is generally contained within $[35-55]^\circ$ but can almost reach orthogonality nearer to the wall. In that sense, the flow is clearly anistropic and one could conclude that the Pr_t concept as defined previously may not be correct.

However, it is crucial to keep in mind what are the quantities that will effectively influence the temperature field. Although it was found that $\overline{T'u'} \approx \overline{T'v'}$, it is the gradient of each turbulent heat flux component in that direction that intervenes in the energy equation, and not the turbulent heat flux itself. Consequently, the net effect on the turbulent diffusion of heat is therefore much less in the streamwise direction, because, in the shear and the boundary layer $\frac{\partial\left(\overline{T'u'}\right)}{\partial x} \ll \frac{\partial\left(\overline{T'v'}\right)}{\partial y}$. This firstly implies that, in regions where $\frac{\partial}{\partial x} \ll \frac{\partial}{\partial y}$, assuming wrongly that the flow is isotropic (scalar α_t), will not actually have a noticeable impact. This also justifies the fact that it is based on a vertical concept, since temperature gradients are predominant in that direction. Nevertheless, in abruptly separated flows, the condition $\frac{\partial}{\partial x} \ll \frac{\partial}{\partial y}$ does not hold in some specific areas, such as the step corner or the flow reattachment zone. As observed in this work, this latest region is also where the strongest peak in heat transfer is expected, of primary interest for designers. More generally, reactor flows are known to be strongly anisotropic. Thus, simple models such as the Pr_t concept would likely fail to represent the temperature field correctly. A more complex modeling approach would certainly be required for the turbulent heat transfer. In the context of liquid metal reactors, one may refer to the extensive review proposed by Shams [146] on this topic.

6.4 Conclusions

This Chapter constitutes the last step of this Thesis and aims to answer the following problematic:

- What are the Prandtl number effects one can expect on the heat transfer in abruptly separated flows ?

Indeed, pool thermal-hydraulics is dominated by shear layers, large recirculations and wall interactions that can be represented in a simplified way by an unconfined BFS. The methodology followed throughout this work has aimed at setting-up the necessary tools to perform an LES of this configuration at different Prandtl numbers: $Pr = 0.71$ for air, $Pr = 0.2$ characterizing the He-Xe gas mixture tested in the MYRTE wind tunnel and $Pr = 0.025$ representing LBE, that is the coolant used in MYRRHA. These implementations concern, in particular adequate boundary conditions, such as the optimized TPM, to generate efficiently turbulence at the inflow, and zero vorticity along the top boundary, to limit the height of the domain without constraining the flow.

After reaching a satisfactory agreement between the LES and experimental results gathered on the MYRTE experiment at $Pr = 0.2$, sufficient confidence has been reached concerning the accuracy of the numerical approach. In addition, resolution requirements to insure that the temperature field is fully resolved at low Pr have been verified. The negligible role of the SGS thermal diffusivity at $Pr = 0.025$ has confirmed the fact that the grid is indeed sufficiently refined. Consequently, the first main conclusion that can be drawn is that valuable results have been produced, which can, as intended, be used with sufficient confidence as reference data for validation of RANS modelling.

As far as Prandtl number effects are concerned, the first observations highlight the difference in scales between the momentum and thermal fields. By respecting flow simarity between the three fluids, the same forced convection regime is reproduced, as illustrated by quasi identical velocity fields.
Differences become evident though when comparing the temperature fields; the smallest thermal eddies present in air dissapear in He-Xe, while only the largest scales remain at low Prandtl number. The conduction effects previously negligible become significant, to the extent in LBE where it becomes a major heat transport mechanism. Consequently, the warmer fluid is transported much further away from the step, and the heated zone is no longer limited to the step corner. The convection effects, that were dominant in air, are taken over by conduction as illustrated by Nusselt number variations. Unlike LBE though, He-Xe still lies in between if one compares this latest heat transfer mode to the fluid's heat capacity. This ratio corresponds to the thermal diffusivity of the fluid, and defines the rate of heat transfer. As it is higher in He-Xe compared to air, stronger thermal fluctuations are observed within the shear layer.
The maximum heat transfer appears near the reattachment, associated to the flapping of the shear layer and the impinging turbulent eddies that impact the wall. These LES have once again illustrated how an abrupt flow separation

may eventually enhance the heat transfer. This phenomenon also explains why the turbulent heat fluxes keep increasing at the reattachment and further down in the recovery region.

Regarding RANS modeling, a critical review of the widely used Reynolds analogy is proposed at various Pr, by extracting the turbulent Prandtl number from the LES. Firstly, Pr_t can only be defined in certain flow areas whereas in practice, it is applied regardless of potential unboundedness. Moreover, the flow is assumed uniform and isotropic, by setting a fixed scalar value throughout the CFD domain. These results have shown that regardless of the fluid's Prandtl number, Pr_t variations are significant, in both the vertical and especially the streamwise direction. This suggests that patching of different constant values in these various flow regions may at least help in improving the predictions. More fundamentally, these results have shown that the basis of this approach, that relies on an isotropic flow assumption, remains questionable. This is particularly true in regions where temperature gradients are not predominantly along the vertical direction, such as the flow reattachment zone for instance. In the frame of abruptly separated flows, for which this flow impingement region gives rise to the strongest heat transfer point, the use of more advanced turbulent heat transfer models is probably required.

Chapter 7

Conclusions

The aim of this thesis was to generate reference data in conditions that are representative of liquid metals in pool type reactors. Indeed, for affordable RANS simulations to become applicable to HLM reactors, such data are needed for further testing, calibration and validation of more-advanced models. To represent simply the flow mechanisms that dominate pool thermal-hydraulics, an unconfined BFS was chosen as benchmark test-case.
These low Prandtl number fluids have the advantage of being characterized by very large thermal scales, which provides the possibility of fully resolving the temperature field having a well-resolved LES of the velocity field. The methodology followed, while setting-up the simulations, was very much driven by the objective of minimizing the computational cost by implementing efficient boundary conditions. In order to verify that high-quality data are produced, an experiment was set-up for comparison. A new sealed wind tunnel was constructed for this purpose, featuring the unique possibility of testing a gas mixture made of Helium and Xenon ($Pr \simeq 0.2$). PIV measurements were performed in air ($Pr = 0.7$) to verify the overall agreement of the velocity field. In addition, simultaneous probe measurements of temperature and velocity allow to assess whether the heat transfer is predicted properly by the LES approach. After gaining sufficient confidence in the numerical results, Prandtl number effects were investigated. The results obtained in air, He-Xe and LBE ($Pr = 0.025$) were compared in order to provide further insight into the heat transfer behaviour of low Prandtl number fluids. The objective of this chapter is to summarize the main contributions of this PhD thesis and discuss further possible investigations.

7.1 Efficient generation of inflow turbulence

Given the computational power available, the computational cost of the simulations had to be minimized in order to be able to carry-out this work. The turbulent inflow condition largely contributes to this aspect, but imposing conditions that are physically "almost correct" remains a considerable challenge in LES. The method had to be efficient, thus limiting the recovery length, and straightforward in terms of the inputs required at the inlet.

The temperature perturbation method of Muñoz-Esparza et al. [95] was selected because of its potential to generate rapidly "realistic" turbulence, without requiring extensive information regarding the turbulent characteristics, that are *a priori* unknown. Moreover, the TPM stood out due to its simplicity; it consists in seeding the flow with random temperature perturbations which, through a buoyancy triggering mechanism, generates turbulent structures, see Fig. 7.1. However, in its original form that relies on natural convection effects, turbulence can only be generated at large scales, characteristic of atmospheric flows for instance. The focus of this work has been to optimize the TPM to make it applicable to a wider variety of wall-bounded flows, that would involve much smaller length scales.

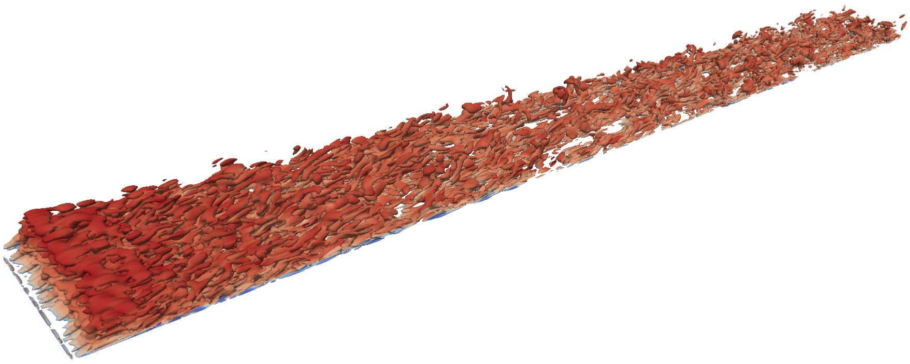

Figure 7.1: *Generation of inflow turbulence with the optimized TPM. LES of a developing TBL showing isosurfaces of Q-criterion.*

The method was adapted to artificially increase buoyancy effects up to strong enough levels, while modulating the local artificial Richardson number in such a way that insures an optimum pre-mixing of the flow. This perturbation function adds a cosine varation to a linear decrease of the artificial local Richardson number. The perturbation time scale was adjusted to avoid contaminating the flow with a distinct footprint characteristic of the perturbation frequency.

The efficient generation of turbulence could be achieved thanks to the optimized TPM. A satisfactory flow recovery is reached shortly after the perturbation zone, in terms of the wall shear stress, the Reynolds stresses and the energy spectrum. For a similar performance (flow recovery after $15\,\delta$ along a channel), its major advantage over existing turbulent inflow methods, is that only the mean velocity profile is required at the inlet. Therefore, in addition to its simplicity, it appears to be very flexible and potentially applicable to a wide variety of flows. It was successfully applied to the MYRTE experiment for the development of the turbulent boundary layer ahead of the BFS, confirming that the set of parameters proposed while validating the technique on the channel flow remains as efficient in the case of spatially developing flows.

7.2 Investigation of probe limitation effects by LES

The objective, while comparing the numerical data with the experiments, was to verify the reliability of the LES approach. However, the work carried out in this Thesis clearly demonstrated that it is fundamental to ensure that similar quantities are confronted to each other. Initially, the aim was to measure, simultaneously and at the same location, the temperature (T') and the velocity fluctuations in both directions (u' and v'), in order to compute the physically correct turbulent heat flux ($\overline{T'u'}$ and $\overline{T'v'}$). However, we were limited by the measurement technique and could only partly quantify the turbulent heat transfer. Nevertheless, these probe limitations were integrated into the processing of the LES data, for a meaningfull comparison.

More specifically, a HWA-TC probe was developed, combining two sensors so that the velocity and temperature could be measured simultaneously. Firstly, the quantity actually measured by the hot-wire had to be considered, that is the effective cooling velocity. In addition, the so-called turbulent heat flux measured by the probe is based on quantities that are measured a certain distance apart, corresponding to the probe spacing between the sensors. It is worth stressing that these aspects must be considered before running the simulations, so that the LES can be processed accordingly during run time. Another major limitation that was incorporated while post-processing the LES data, concerns the TC's frequency response, limited to $75\,Hz$. The probe's transfer function was deduced from a step response, and used to filter the LES data in the frequency domain. This is fundamental if one wants the numerical and experimental fluctuation levels to be comparable.

The influence of the probe's spacing and of its frequency response proved to be considerable. The turbulent heat transport predicted by LES reduced successively by two near the onset of the shear layer This implies that, without taking into account these probe limitations within the processing of the LES results, peak levels up to four times higher would have been confronted with the measurements. As a result of the LES treatment, the overall agreement with the measurements was found to be satisfactory, while very different conclusions could have been drawn otherwise. It is therefore crucial to identify the limitations intrinsic to the experimental or numerical reference, before taking the validity of this database as granted.

7.3 Heat transfer behavior of low Prandtl number fluids in abruptly separated flows

The differences between the LES/DNS results obtained at different Prandtl numbers have helped gain a better understanding of low Prandtl effects. In particular, the analysis of the different heat transport mechanisms has highlighted the importance of the molecular contribution, which is no longer dominated by the turbulent convection effects, as it is the case at high Pr. This observation had been made before in a channel flow or a TBL, but never for an abruptly separated flow.

The particularity of the BFS flow resides in the differences observed between the shear layer that expands above the recirculation region and into the recovery region. The peak in heat transfer moves to the mean reattachment point, whereas it is located slightly upstream at high Pr. Due to strong conductive effects, that extend much further out than for air or He-Xe, strong heat transport is still observed beyond reattachment, as a much ticker thermal boundary layer redevelops.
A critical review of the turbulent Prandtl number concept has been proposed. This parameter is extracted from the LES results, in regions where both the turbulent viscosity and thermal diffusivity are well defined. This exploitable area is limited to the shear layer expansion zone, here a distinction was drawn between the regions before and after reattachment. Unlike what is assumed by the Reynolds analogy commonly applied in RANS, the behavior of Pr_t is far from being uniform across the shear layer, in both vertical and streamwise directions. Above the recirculation, an average value around 0.75 is observed, whereas it is slightly above unity within the recovery region. Interestingly, at higher Pr such as for air, a mean value of about 0.6 is found before reattachment whereas, after that, values are closer to the usual value of 0.9 that is used in most codes. Moreover, the fact of using a scalar value for α_t, implies that the flow should behave the same in all directions. As highlighted by the disalignment between the turbulent heat flux and the temperature gradient vectors, it is clearly anisotropic throughout the shear layer. Despite this fact, the isotropic approximation will not matter much in areas where flow gradients are mostly in the wall-normal direction, since the net effect of other components on the turbulent diffusion of heat will remain negligible. Nevertheless, even in the generic case of a BFS, RANS predictions within some local areas such as the reattachment zone may suffer, especially considering that the peak in heat transfer appears there.

7.4 Recommendations for future work

The new MYRTE wind tunnel is now operational, thus offering the unique possibility of further investigating thermal turbulence in a moderate Prandtl number gas mixture. An interesting direction would be to perform other experiments so that data in various flow regimes can be generated to extend the database available for the validation of RANS models.
The second experiment planned within the frame of MYRTE, also representative of a non-confined flow, is a Forced Plane Jet (FPJ) with heated co-flow. The objective will be to reach a better understanding of the hot jets exiting the core into the hot plenum. There again, similar measurements than performed here will be compared to the LES results of SCK•CEN. In addition, testing of a natural convection boundary layer (NCBL) would constitute a very valuable experiment for the research community. Indeed, in natural convection, avail-

able data at low Pr are limited to Rayleigh-Benard convection [111]. More generally, it is very difficult to find well defined NCBL data even at Prandtl number close to unity.

Concerning the probe measurements, the facility will be further developed thanks to a fully automated 2D traverse system. This will help gain time in these future measurement campaigns, compared to the measurements on the BFS which were often cumbersome. Also, the procedure used to calibrate the hot-wire sensor at different temperatures can be considerably improved. Instead of trying to alter the ambient laboratory conditions, we can use the $3\,kW$ resistances and the heat exchanger that have been added to the FPJ test-section and wind tunnel loop respectively. These will enable to reach a gradient of at least $10\,°C$ but also more stable conditions during the calibration, thus improving the accuracy of the temperature correction that is applied to the measurements. In addition, a new HWA-TC probe will be constructed in order to reduce probe intrusiveness, by resorting to an L-shaped design. This will enable to decrease the local blockage created by the double sensor head, that will be aligned with the flow instead of being inserted perpandicularly as it was the case with the straight probe used during these measurements.
Nevertheless, this work has clearly demonstrated that the HWA-TC probe is unable to accurately measure the turbulent heat flux due to its limited spatial and time resolution. Nevertheless, such measurements can remain exploitable, provided these limitations are taken into account, and still qualify as validation data by insuring that similar quantities are compared. Following the same mindset, it would be interesting to generalize the use of LES in conjunction with experiments. For instance, more truthful comparisons can be proposed by systematically integrating known limitations associated to measurement techniques. Similarly, LES could be used more often as a predictive tool while designing experiments or developing new measurement techniques.
Although not possible experimentally, $\overline{T'u'}$ and $\overline{T'v'}$ can be extracted from the validated LES in order to approach the physically correct turbulent heat fluxes, thus highlighting once again how complementary experiment and LES can be.

The development of a measurement technique able to accurately quantify the turbulent heat transfer would constitute a significant progress towards a better understanding and modeling of turbulent heat transfer. In constant temperature (CTA) mode, the HWA is very sensitive to both temperature and velocity, and benefits from a high frequency response. The sensitivity analysis developed by Morkovin [91], Stainback [158] and Motallebi [93] relates, for small perturbations, the percentage variation of the top bridge voltage to the percentage variation of the quantities of interest ($u^{'}$, $v^{'}$, $w^{'}$ and $T^{'}$), by means of sensitivity coefficients, S, based on these quantities. Introducing the angle sensitivities ($\alpha^{'}$ and $\beta^{'}$) in the two planes perpendicular to the streamwise velocity, the following sensitivity equation is obtained for low speed flows:

$$\frac{E_b^{'}}{\overline{E_b}} = S_u \frac{u^{'}}{\overline{u}} + S_{T_0} \frac{T_0^{'}}{\overline{T_0}} + S_\alpha \frac{\alpha^{'}}{\overline{\alpha}} + S_\beta \frac{\beta^{'}}{\overline{\beta}} \,. \tag{7.1}$$

For such applications, proper velocity and angular calibrations have proved to be sufficient to close the problem and deduce fluctuating velocities and temperature [32]. Although initially developed for high speed flows, Campagna [26] worked in parallel to this Thesis on the application of this principle to low speed flows, deriving the sensitivity relations and setting-up the measurement procedure. Testing of the measurement technique on a heated TBL highlighted the importance of operating the wires at different overheat ratios, in order to introduce larger differences in the sensitivities, thus obtaining a stable solution from the system of equations. This can be achieved by having wires made of different materials and diameters. Further development of this promising measurement technique is ongoing.

In the RANS framework, these results have highlighted the inadequacy of the Reynolds analogy in complex flows, not only at low Pr representative of liquid metals but also at Pr around unity. The constant Pr_t concept could at least be improved by patching different values depending on the flow regions. However, this implies guessing a priori how the flow is going to behave and would require running a preliminary simulation. This does not appear very practical for complex flows and certainly far from the ultimate goal that is to have a model able to provide reasonable results in all flow regimes.
To evaluate the impact of the isotropic assumption in areas where streamwise flow gradients are non-negligible, one recommendation would be to run some RANS simulations at different Pr_t values. It is obvious that in complex flow configurations such as reactor pools, the Pr_t concept would quickly reach its limitations and more complex turbulent heat transfer models would definitely be required. In such cases, interesting directions that are definitely worth investigating are models that are based on an anisotropic eddy diffusivity tensor instead of an isotropic scalar for (ν_t, α_t). Further testing of these various more advanced RANS models is certainly the next step as a continuation of this work.

Appendix A

Periodic channel flow: sensitivity studies

A.1 Effect of the Smagorinsky coefficient

As mentioned in Section 2.4.2, one of the major drawbacks of the Smagorinsky SGS model is that the value of the Smagorinsky coefficient needs to be changed depending on the type of flow.

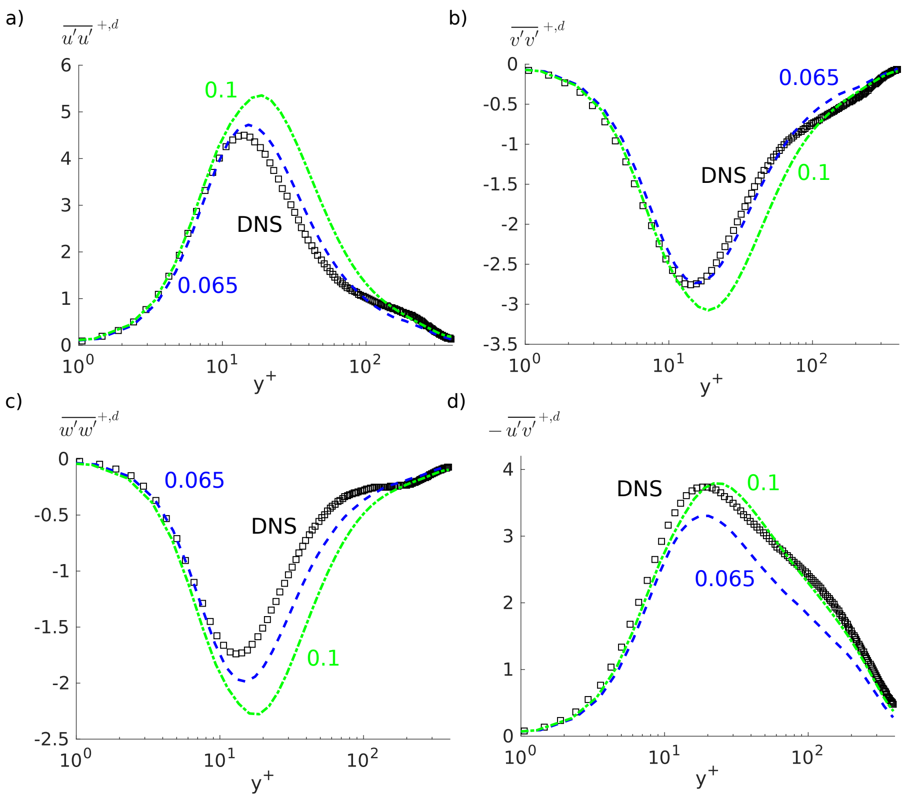

Figure A.1: *Influence of the Smagorinsky coefficient on the Reynolds stresses obtained from a channel flow at $Re_\tau = 395$.*

In this work, focus is brought on a specific flow configuration, the BFS, and on specific flow conditions. Therefore, more ellaborate SGS models such as the dynamic Smagorinsky model [46], which calculates the coefficient value in space

and time, would have a limited added value. Consequently, the simplest SGS modeling approach was chosen but specical care was taken to insure that the near-wall behavior was properly reproduced thanks to the Piomelli near-wall damping function.
It is nevertheless important to estimate the sensitivity of the results with respect to the Smagorinsky coefficient. Initial results have been obtained using the value of 0.065 taken by Moin and Kim [87] for a channel flow at $Re_\tau = 395$. However, a variety of values can be found in the litterature, for instance Deardorff [35] and Piomelli et al. [116] use $C_s = 0.10$ while Sullivan et al. [160] finds an optimum value of $C_s \simeq 0.12$ to 0.13. Considering that the optimum value is case dependent, the influence of this coefficient is evaluated here by considering another value equal to 0.10. Although not shown here, the effect on the mean velocity profile is negligible, which is not the case for the Reynolds stresses as observed in Fig. A.1.
To conclude, the profiles of streamwise, wall normal and spanwise Reynolds stresses for $C_s = 0.065$ show less discrepency than for $C_s = 0.1$ and are in good agreement with the DNS. Concerning the shear stress, although discrepencies almost disappear when $C_s = 0.1$, overall the agreement between the LES and DNS results for $C_s = 0.065$ is superior. Consequently, this value is selected for the remaining simulations.

A.2 Influence of the mesh resolution

In order to properly evaluate the LES resolution, the effective mesh size $\Delta = (\Delta x \Delta y \Delta z)^{1/3}$ should be compared to the Kolmogorov scale $\eta = (\nu^3/\epsilon)^{1/4}$, characteristic of the smallest scales in the velocity field. Considering the initial mesh size corresponding to $\Delta x^+ = 39.5$, $\Delta z^+ = 19.8$ and $\Delta y^+_{max} \simeq 30$, the LES grid is such that $\Delta/\eta < 57$. Although this corresponds to a well-resolved LES, the resolution is not as high as in some highly-resolved LES found in the litterature. The aim in this section is to examine the influence of the mesh on the results, in order to evaluate whether this initial resolution is sufficient.
The first effect that is investigated concerns the wall-normal mesh distribution. Initially, a constant stretching is applied with an expansion ratio of 1.1. In order to limit the maximum mesh size, a stretching law [37] can be defined as:

$$\frac{y}{\delta} = 1 + \frac{tanh(\gamma(\zeta - 1))}{tanh(\gamma)} \; , \tag{A.1}$$

with $\zeta = y/\delta$ ($\zeta = 0$ at the bottom wall and $\zeta = 2$ at the top wall) and $\gamma = \Delta y_{max}/\Delta y_{min}$. This latest parameter is set to 2.4, which results in $\Delta/\eta < 49$. This slight change in vertical mesh distribution has a negligible influence on the results, as shown in Fig. A.2. The influence of the grid resolution is investigated next. Two finer meshes are generated with the following characteristics:

- mesh 1: $\Delta x^+ = 32$, $\Delta z^+ = 16$ and $\Delta y^+_{max} \simeq 20$ ($\Delta/\eta < 37$)
- mesh 2: $\Delta x^+ = 20$, $\Delta z^+ = 16$ and $\Delta y^+_{max} \simeq 20$ ($\Delta/\eta < 32$)

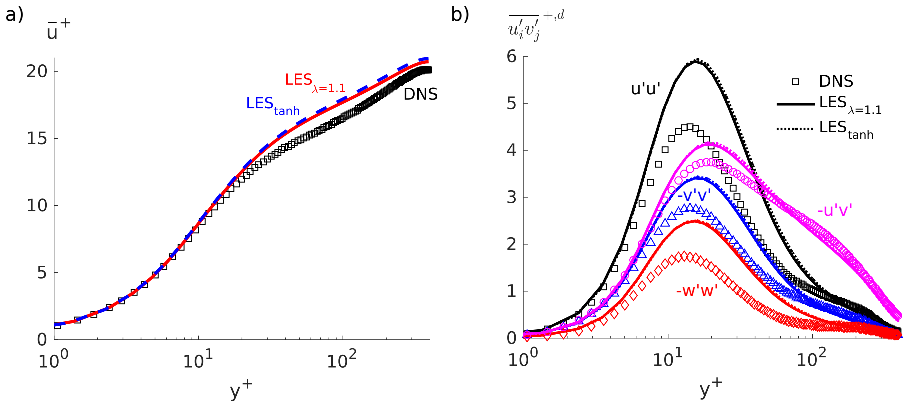

Figure A.2: *Influence of the wall-normal mesh distribution on the LES results obtained for a periodic channel flow at $Re_\tau = 395$. a) Mean velocity profile b) Reynolds stress profiles*

Both of these are equally refined in the wall normal and spanwise directions with respect to the baseline mesh. Compared to the latest, the streamwise resolution is further increased from mesh 1 to 2. The three sets of results are compared in Fig. A.3. Refinement compared to the baseline mesh affects both the mean velocity and Reynolds stress profiles. The over-prediction of velocity in the center of the channel is reduced. The prediction of streamwise and wall normal turbulent stresses actually deteriorates in terms of amplitude but the location of the peak and overall shape of the profiles are better captured. A better estimation of the turbulent shear stress is reached, with a good agreement compared to the DNS with either refined meshes. In general, additional refinement of the mesh streamwise from mesh 1 to 2 does not further improve the results. Considering that a satisfactory agreement is reached with the baseline mesh, it is chosen for the remaining of the study. Most importantly, no matter the mesh resolution, it is fundamental that the optimized TPM is tested in Section 2.5 using the same mesh and set-up as that used while obtaining the reference "PBC" results of Section 2.4.1.

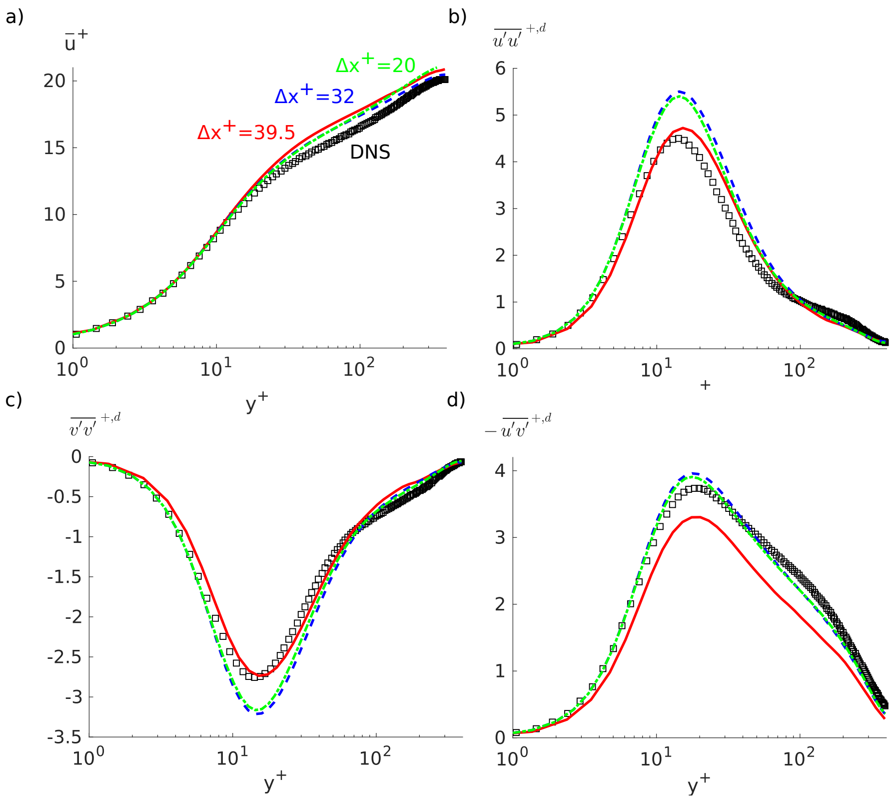

Figure A.3: *Influence of the Smagorinsky constant on the Reynolds stresses obtained from a periodic channel flow at* $Re_\tau = 395$.

Appendix B

Measurement uncertainties

B.1 Error analysis of the PIV technique

It is important to distinguish betwen the systematic error, ϵ_{sys}, and the random error, ϵ_{rand}. The first is made on every measurement and is due to the measurement chain (i.e. calibration devices, acquisition system). The second is related to the variability of the phenomena. The total error is then deduced as follows:

$$\epsilon_{tot} = \sqrt{{\epsilon_{sys}}^2 + {\epsilon_{rand}}^2}. \tag{B.1}$$

The systematic error

Just like for any measurement technique, the systematic error originates from the different steps leading to the determination of the quantity of interest. In the case of PIV, the aim is to measure a velocity:

$$U = \frac{M \times d}{t} \tag{B.2}$$

where d is the displacement of the particle tracers in pixels, t is the separation time between the two frames and M is the magnification factor of the image in $[mm/px]$.

The systematic error on the velocity can be expressed as a chain of errors:

$$\epsilon_{sys} = \frac{\Delta U}{U} = \sqrt{\left(\frac{\Delta M}{M}\right)^2 + \left(\frac{\Delta d}{d}\right)^2 + \left(\frac{\Delta t}{t}\right)^2}. \tag{B.3}$$

In the separation area, the separation time t is in average set to $t = 130\,\mu s$, with a precision of $1\,\mu s$ as specified by the DaVis software. Therefore, the error related to this parameter is $\Delta t/t = 7.69 \times 10^{-3}$.

Although the camera should be perpendicular to the laser sheet, there is always a slight misalignment which introduces a discrepency between the measured value, x, and the actual particle displacement, $d = x/cos\,\theta_1$. As a result, the error on this parameter can be expressed as:

$$\frac{\Delta d}{d} = \sqrt{\left(\frac{\Delta x}{x}\right)^2 + \left(\frac{\Delta L_{\theta_1}}{L_{\theta_1}}\right)^2}. \tag{B.4}$$

A variation of $\pm 2\,^\circ$ is applied, which converted in length yields $\Delta L_{\theta_1} = 1.2 \times 10^{-3}$. The error Δx originates from the processing software itself, and is approximatly 0.1 pixel [133]. The separation time is adjusted so that the typical particle displacement is about 8 pixels. As a result, one obtains $\Delta x/x = 0.0125$ and $\Delta L_{\theta_1}/L_{\theta_1} = 1.2 \times 10^{-3}$.

The magnification factor is function of the angle θ_2 between the calibration plate and the laser plane, the length of the calibration plate in mm, L_{mm}, and the length that is actually measured by the camera in px, L_{px}. This yields:

$$M = \frac{\cos\theta_2 \times L_{mm}}{L_{px}}. \tag{B.5}$$

The error on M related to the angle θ_2 can also be converted to an error in length, such that:

$$\frac{\Delta M}{M} = \sqrt{\left(\frac{\Delta L_{mm}}{L_{mm}}\right)^2 + \left(\frac{\Delta L_{px}}{L_{px}}\right)^2 + \left(\frac{\Delta L_{\theta_2}}{L_{\theta_2}}\right)^2}. \tag{B.6}$$

During calibration, a chessboard is used as calibration plate, allowing for 1 pixel precision while determining the reference length through the camera ($\Delta L_{px} = 1$) and half a millimeter precision while measuring the length of the plate itself ($\Delta L_{mm} = 0.5$). Ideally, the angle θ_2 between the plate and the camera should be $0\,^\circ$, however a usual fluctuation of $\pm 2\,^\circ$ is considered, corresponding to $\Delta L_{\theta_2} = 1.2 \times 10^{-3}$. In the separation area, $L_{mm} = 32\,mm$ and $L_{px} = 753\,px$, which gives $\frac{\Delta M}{M} = 1.838 \times 10^{-1}$.

Taking into account these various contributions, the bias error on the velocity measured by PIV can be approximated as follows:

$$\begin{aligned}
\frac{\Delta U}{U} &= \sqrt{\left(\frac{\Delta t}{t}\right)^2 + \left(\frac{\Delta x}{x}\right)^2 + \left(\frac{\Delta L_{\theta_1}}{L_{\theta_1}}\right)^2 + \left(\frac{\Delta L_{mm}}{L_{mm}}\right)^2} \\
&\quad \overline{+\left(\frac{\Delta L_{px}}{L_{px}}\right)^2 + \left(\frac{\Delta L_{\theta_2}}{L_{\theta_2}}\right)^2} \\
&= \sqrt{(7.69 \times 10^{-3})^2) + (1.25 \times 10^{-2})^2) + (1.2 \times 10^{-3})^2)} \\
&\quad \overline{+(1.562 \times 10^{-2})^2) + (1.328 \times 10^{-3})^2) + (1.2 \times 10^{-3})^2)} \\
&= 0.02154 \simeq 2.15\,\%.
\end{aligned} \tag{B.7}$$

The calculation above is made in the free-stream, where $U_{in} \simeq 7\,m/s$ for $Re_h = 8930$. However, the systematic error will depend on the particle displacement and can therefore be expressed as a function of velocity:

$$\frac{\Delta x}{x} = \frac{\Delta x}{U \times t} M. \tag{B.8}$$

Substituting Eq. (B.8) into Eq. (B.7), the error on the velocity will naturally depend on the local velocity:

$$\frac{\Delta U}{U} = \sqrt{A + \left(\frac{B}{U}\right)^2} \tag{B.9}$$

with a coefficient A that does not contain the error on the displacement but includes all remaining errors ($A = 3.08\times10^{-4}$), and a coefficient $B = (\Delta x \times M/t)$ that depends on the specific settings of the measurement window. While measuring the flow within the separation area, the magnification factor remained constant but the separation time was adjusted to have a typical displacement of 8 pixels (ref. Table B.2).

The random error

Unlike the systematic error that depends on the measurement set-up, the random error is related to the variability of the phenomena. By nature, a turbulent flow varies in time and each PIV image is a snapshot of the flow at a given instant. These flow variations are assumed to follow a Gaussian distribution, and statistical convergence of the data towards an average flow field is obtained by acquiring a large number of images. This statistical error is always defined by a certain error interval and confidence level in %. The random error associated to a mean value is given by:

$$\epsilon_\mu = \frac{z_{\alpha/2}\,\sigma_\mu}{\mu\sqrt{N}} = \frac{z_{\alpha/2}\,TI_\mu}{\sqrt{N}} \tag{B.10}$$

with $z_{\alpha/2}$ dependent on the desired confidence level and given in Table B.1, TI_μ the local turbulence level and N the number of independent samples.

$z_{\alpha/2}$	**Confidence level** [%]
1.65	90
1.96	95
2.33	98
2.57	99

Table B.1: *Parameter $z_{\alpha/2}$ for different confidence intervals*

Samples are independent if the time between them is at least twice the characteristic time of the flow. In the case of a BFS flow, vortex shedding typically occurs at a non-dimensional frequency (St) of 0.07 [76]. The Strouhal number is defined as $St = f\,h/U_{in}$ where f is the characteristic frequency and is around $25\,Hz$ in this application. As the sampling frequency is $4\,Hz$, the acquired sampled are certainly independent.

The error on the mean increases with the local turbulence level, whereas the random error associated to the standard deviation only depends on the number of samples:

$$\epsilon_\sigma = \frac{z_{\alpha/2}}{\sqrt{N}}. \tag{B.11}$$

From the PIV measurements, the turbulence intensity appears not to exceed 20 % within the separated flow area (ref. Fig. 3.20). To remain conservative, this value is taken as reference such that $TI_\mu = 0.2$, while $N = 2000$ for each window. For a 95 % confidence level, the statistical error on the mean is 0.88 % and the error on the variance is 4.4 %.

Total error on the PIV measurements

The total error associated to the PIV results obtained in this work are summarized in Table B.2. These are specified for each measurement window (ref. Figure 3.9) and are based on the free-stream velocity.

PIV window	M $[mm/px]$	t $[ms]$	ϵ_{sys}	$\epsilon_{rand,\mu}$	$\epsilon_{rand,\sigma}$
Inlet	0.1095	0.075	2.73 %	0.88 %	4.4 %
BL (red: 1-3)	0.02081	0.035	1.95 %	0.88 %	4.4 %
Top (blue: 1-3)	2.367	0.15	2.55 %	0.88 %	4.4 %
Separation (w1)	0.04042	0.04	2.27 %	0.88 %	4.4 %
Separation (w2)	0.04042	0.16	1.79 %	0.88 %	4.4 %
Separation (w3)	0.04042	0.16	1.79 %	0.88 %	4.4 %
Separation (w4)	0.04042	0.11	1.83 %	0.88 %	4.4 %
Separation (w5)	0.04042	0.15	1.8 %	0.88 %	4.4 %
Separation (w6)	0.04042	0.16	1.79 %	0.88 %	4.4 %
Separation (w7)	0.04042	0.14	1.80 %	0.88 %	4.4 %
Separation (w8)	0.04042	0.12	1.82 %	0.88 %	4.4 %

Table B.2: *PIV measurement errors, for a confidence level of* 95 %.

As pointed out previously, the total error varies locally as a function of velocity, it is therefore calculated at each measurement point and represented as an error bar. For instance, the evolution of the total error in the first window of the separation area is represented as a function of the local velocity in Figure B.1.

B.2 Error analysis on the Hot-wire anemometry technique

Similarly to the PIV technique, the error related to the HWA measurements is composed of a systematic and a random error. The systematic error is made for each measurement and originates from the measurement chain: calibration instruments, acquisition chain, etc. The random error is rather related to the variability of the phenomena. The total error is then obtained from Eq. (B.1).

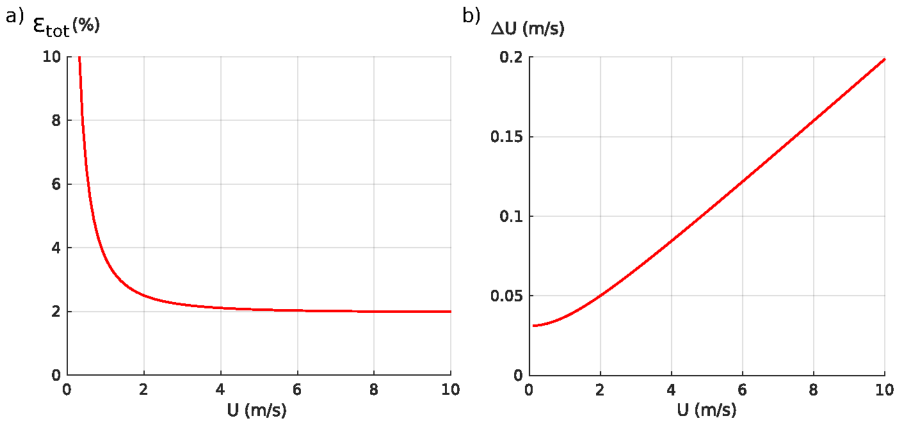

Figure B.1: *Evolution of the total error as a function of the mean velocity measured by PIV (i.e. window 1 of the separation area) a) Relative error b) Absolute error.*

The systematic error

To determine the systematic error associated to every HWA measurement, the calibration procedure is taken into account. The single hot-wire was calibrated inside the MYRTE wind tunnel, using the wind tunnel calibration curve (ref. Figure 3.2) as reference. It is obtained using a pressure transducer that measured the pressure difference, P_{diff}, between the air at ambient pressure, P_{amb} and temperature, T_{amb}, and the stagnation pressure. The velocity is computed from Bernouilli's equation as follows:

$$U_{hw} = \sqrt{\frac{2\,P_{diff}\,R T_a}{P_a}}, \quad P_{diff} = g\,H_{mmH_2O}, \tag{B.12}$$

with R the specific gas constant, g the gravitational acceleration and H_{mmH_2O} the water manometer height in mm.

From this expression, the systematic error on the velocity is determined:

$$\epsilon_{sys} = \frac{\Delta U}{U} = \sqrt{\left(\frac{\partial U}{\partial P_{diff}} \Delta P_{diff}\right)^2 + \left(\frac{\partial U}{\partial T_{amb}} \Delta T_{amb}\right)^2 + \left(\frac{\partial U}{\partial P_{amb}} \Delta P_{amb}\right)^2}. \tag{B.13}$$

Considering that:

$$(\partial P_{diff})^2 = \left(\frac{\partial P_{diff}}{\partial H_{mmH_2O}} \Delta H_{mmH_2O}\right)^2, \tag{B.14}$$

Eq. (B.13) becomes:

$$\frac{\Delta U}{U} = \sqrt{\left(\frac{1}{2}\frac{\Delta H_{mmH_2O}}{H_{mmH_2O}}\right)^2 + \left(\frac{1}{2}\frac{\Delta T_{amb}}{T_{amb}}\right)^2 + \left(\frac{1}{2}\frac{\Delta P_{amb}}{P_{amb}}\right)^2}. \tag{B.15}$$

The ambient conditions are measured by a barometer which has a resolution of 1 hPa on P_{amb} and 1°C on T_{amb}. The uncertainty can be considered as half of the resolution, thus typically $\frac{\Delta P_{amb}}{P_{amb}} = \frac{0.5}{1013}$ and $\frac{\Delta T_{amb}}{T_{amb}} = \frac{0.5}{293}$.

The water manometer used to calibrate the pressure transducer has a resolution of 0.2 mmH_2O which results in an uncertainty $\Delta H_{mmH_2O} = 0.1\ mm$. As the water manometer height changes with velocity, its error is a function of velocity as well:

$$\frac{\Delta H_{mmH_2O}}{H_{mmH_2O}} = \frac{2\,g\,R\,T_{amb}\,\Delta H_{mmH_2O}}{P_{amb}\,U^2}. \tag{B.16}$$

Consequently, Eq. (B.15) yields:

$$\frac{\Delta U}{U} = \sqrt{\left(\frac{1}{2}\frac{1.63}{U^2}\right)^2 + \left(\frac{1}{2}1.7\times10^{-3}\right)^2 + \left(\frac{1}{2}4.93\times10^{-4}\right)^2}. \tag{B.17}$$

In addition, the error associated to fitting the data with a 4^{th} order polynomial is accounted for based on the RMSE (Root Mean Square Error), typically equal to 2.3 %.

The random error

Similarly than for the PIV, the relative errors on the statistical quantities are calculated using Eq. (B.10) and Eq. (B.11). Data is acquired at a high frequency of 7.5 kHz, during an observation time T_{obs}, of 60 s. This results in a large number of samples, but only the *independent* samples are considered while determining statistical errors. These are separated by at least twice the characteristic time of the flow, T_u. Using Taylor's frozen hypothesis, the integral length scale, L_u, is introduced and the number of independent samples can be deduced as:

$$N = \frac{T_{obs}\,U_{in}}{2\,L_u}. \tag{B.18}$$

Lee et al. [77] investigated the three-dimensional large-scale vortical structures that are shed from a BFS. Correlation lengths of typically $4h$ are found, which gives $N = 5250$. For a 95 % confidence level, the statistical error on the mean is 0.54 % ($I_u = 0.2$) and the error on the variance is 2.7 %.

The total error

Thte total error is deduced from Eq. (B.1) that takes into account both the systematic and random errors. As pointed previously, the first is function of the local velocity and is computed accordingly while determining the error bars associated to the measurements. For instance, the total error on the mean effective velocity U_{hw} is represented in Figure B.2.

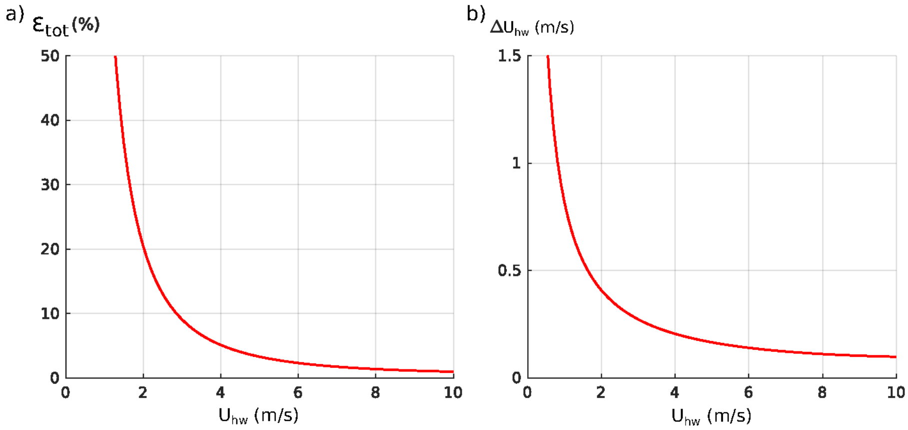

Figure B.2: *Evolution of the total error as a function of the mean velocity measured by HWA a) Relative error b) Absolute error.*

B.3 Thermocouple uncertainty

The systematic error

The error made on each thermocouple measurement depends partly on the following factors:

- the type of thermocouple
- the accuracy of the thermocouple
- the temperature that is measured
- the resistance of the thermocouple wires
- the cold-junction temperature

These will vary depending on the acquisition card used for the measurements. The thermocouple module NI 9213 is chosen as it offers the possibility to operate in high-speed timing mode, with an input bandwidth of up to $78\,Hz$. The temperature measurement accuracy that is provided by the supplier for a type-K thermocouple is $< 0.25\,°C$. This highest limit is taken into account while estimating the absolute systematic error associated to each measurement.

The random error

Once again Eq. (B.10) and Eq. (B.11) are used to determine the relative errors on the statistical quantities. Data is acquired during $60\,s$ at $75\,Hz$ which results in 4500 *independent* samples. Consequently, the statistical error on the mean is $0.58\,\%$ ($TI_u = 0.2$) and the error on the variance is $2.9\,\%$, for a $95\,\%$ confidence level.

The total error

The total error associated to the TC measurements is obtained by taking into account both the systematic and random errors (ref. Eq. (B.1)). The relative error that should be considered on the mean temperature is plotted in Figure B.3.

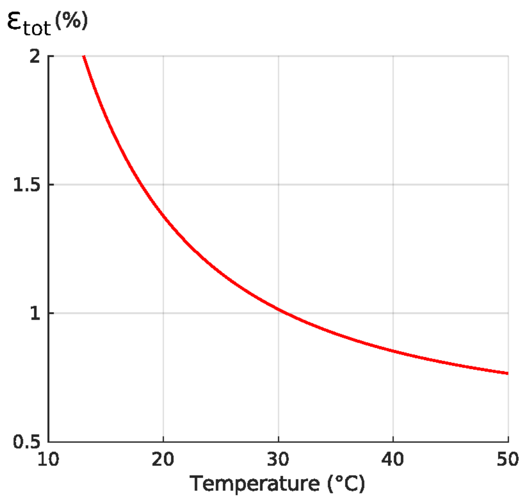

Figure B.3: *Evolution of the total relative error on the mean temperature measured with a TC.*

Appendix C

Influence of top boundary condition

C.1 Free-stream conditions

In the context of ZPG conditions, up to now the flow, has been assumed to extend to an infinite distance from the wall into the free-stream. In practice, the size of the MYRTE wind tunnel is of course finite and is truncated in the direction perpendicular to the wall at a distance y_L. Therefore, an artificial boundary condition needs to be applied along the top boundary, which when properly set, will least disrupt the spatial development of the boundary layer. This requires that the solution to the governing equations in the finite domain best approaches the correct solution (obtained if the domain were infinite).

Similarly to the concept of "fringe region" used to force the flow back to laminar at the outflow [138], a "sponge region" can be set-up in which extra dissipative terms are added to the governing equations to damp disturbances, thus avoiding these to reflect back into the region of interest. However, for the disturbances to be "killed" smoothly, the region must be thick, which becomes computationally costly.

The simplest approach is to impose a Dirichlet condition as

$$u_i\big|_{y=y_L} = \mathcal{U}_i\big|_{y=y_L} . \tag{C.1}$$

where $\mathcal{U}_i(x, y)$ is a base flow, chosen as an approximate solution for ZPG TBL. This is typically prescribed for the streamwise velocity, while free-stress conditions would be applied to the other components.

Another approach is to impose a Neumann condition, i.e.

$$\frac{\partial u_i}{\partial y}\bigg|_{y=y_L} = \frac{\partial \mathcal{U}_i}{\partial y}\bigg|_{y=y_L} . \tag{C.2}$$

As noted by Schlatter et al. [138], this type of free-stream condition combined with incompressibility leads to a constant streamwise velocity along the top, whereas the vertical velocity might be non-zero to account for the boundary-layer growth. However, for the problem to be numerically well posed, this requires prescribing pressure along the top boundary.

In the literature, velocity boundary conditions are mostly used, and the vertical velocity is adjusted to achieve the required pressure gradient. In principle though, a pressure boundary condition can also be applied by setting $P_\infty(x) = f(x)$ and zero-gradient conditions to velocity. This approach has been adopted in the past [44, 113] but only results for a laminar boundary layer were shown. An important advantage is that it should be much easier to reproduce experiments by imposing a measured pressure distribution, since it is no longer necessary to estimate the boundary layer growth.

An alternative that seems to represent well reality, is to impose zero-vorticity along the top. Fasel [43] showed that this condition is indeed reached quite rapidly in the vertical direction since the flow above the boundary layer is indeed quickly irrotational. A possibility is to impose

$$\begin{aligned}
\omega_x &= \frac{\partial w}{\partial y} - \frac{\partial v}{\partial z} = 0 \\
v &= V_{ref}(x) \\
\omega_z &= \frac{\partial v}{\partial x} - \frac{\partial u}{\partial y} = 0,
\end{aligned} \tag{C.3}$$

where a vertical velocity ditribution V_{ref} is imposed along the top. This type of top condition has often been used for a ZPG TBL [84, 150, 173]. The suction-blowing distribution V_{ref} will control the pressure gradient. But the question is how to set this vertical velocity. As derived in Inoue [56], the constant-density continuity equation gives

$$\frac{\partial U_\infty}{\partial x} + \frac{\partial V_\infty}{\partial y} = 0\,. \tag{C.4}$$

Integrating Eq. (C.4) in the vertical direction ($0 \leq y < y_L$), while assuming potential flow down to the wall, yields

$$V_\infty\left(y_L\right) = -y_L \frac{dU_\infty}{dx}\,. \tag{C.5}$$

Considering again continuity but this time in the boundary layer, and averaging spanwise such that $\partial w/\partial z = 0$, one obtains

$$\frac{\partial u}{\partial x} + \frac{\partial v}{\partial y} = 0\,. \tag{C.6}$$

Combining Eq. (C.4) and Eq. (C.6) gives

$$\frac{\partial}{\partial x}\left(U_\infty - u\right) = \frac{\partial}{\partial y}\left(v - V_\infty\right)\,. \tag{C.7}$$

Integrating in the wall-normal direction and inserting δ^*, given by Eq. (4.2), into Eq. (C.7) yields:

$$\frac{d}{dx}\left(U_\infty \delta^*\right) = u(y_L) - V_\infty(y_L)\,. \tag{C.8}$$

The right-hand side term of Eq. (C.8) can be interpreted as a correction to the vertical velocity at L_y, caused by the slope of δ^*. Therefore

$$V_{ref} = v(y_L) = (\delta^* - y_L)\,\frac{dU_\infty}{dx} + U_\infty\,\frac{d\delta^*}{dx}\,. \tag{C.9}$$

In ZPG conditions ($dU_\infty/dx = 0$), thus

$$V_{ref} = U_\infty\,\frac{d\delta^*}{dx}\,. \tag{C.10}$$

In the case of numerical simulations, the vertical velocity distribution along the top boundary can be estimated using Eq. (C.10), based on correlations that are available for δ^*. The vorticity boundary condition is first tested on a laminar boundary layer before applying it to the LES of a TBL in Chapter 4.

C.2 Laminar boundary layer simulation

C.2.1 Blasius solution

To investigate the influence of the top boundary condition, a two-dimensional laminar boundary layer is simulated. Indeed, this test-case is ideal to test the implementation of the zero vorticity boundary condition at a much lower computational cost than for the LES of a TBL. It is also sufficient to determine whether it has an added value compared to simpler boundary conditions.

In the case of a 2D laminar boundary layer flowing over a flat plate with an outer flow at uniform velocity U_∞, the pressure gradient disappears from the boundary layer equations that simplify to

$$\frac{\partial u}{\partial x} + \frac{\partial v}{\partial y} = 0\,. \tag{C.11}$$

$$u\,\frac{\partial u}{\partial x} + v\,\frac{\partial u}{\partial y} = \nu\,\frac{\partial^2 u}{\partial y^2}\,. \tag{C.12}$$

The boundary conditions are $u(x,0) = v(x,0) = 0$ and $u(y=\delta) = U_\infty$. Blasius [18] proposed a similarity solution for this particular case. The following variables are introduced

$$\eta = \frac{y}{\delta(x)},\ \ and\ \ \psi = U_\infty\,\delta(x)\,f(\eta)\,, \tag{C.13}$$

where $\delta(x) = \sqrt{\frac{2\,\nu\,x}{U_\infty}}$ is the boundary layer thickness and ψ is the stream function. This leads directly to the velocity components

$$\begin{aligned} u(x,y) &= \frac{\partial \psi}{\partial y} = U_\infty\,f'(\eta)\,, \\ v(x,y) &= -\frac{\partial \psi}{\partial x} = U_\infty\,\frac{d\delta(x)}{dx}\,[\eta f'(\eta) - f(\eta)] \\ &= U_\infty\sqrt{\frac{\nu}{2\,U_\infty\,x}}\,[\eta\,f'(\eta) - f(\eta)]\,. \end{aligned} \tag{C.14}$$

Derivatives of the velocity field are deduced and substituted into the momentum equation Eq. (C.11), which yields

$$f'''(\eta) + f(\eta)\, f''(\eta) = 0\,. \tag{C.15}$$

This third order non-linear ordinary differential equation is solved numerically via the "shooting method". The boundary conditions are $f(0) = f'(0) = 0$; $f'(\infty) = 1$, corresponding to the no-slip condition, the impermeability of the wall and the free-stream velocity outside of the boundary layer. The Blasius solution is plotted in Fig. C.1 hereafter.

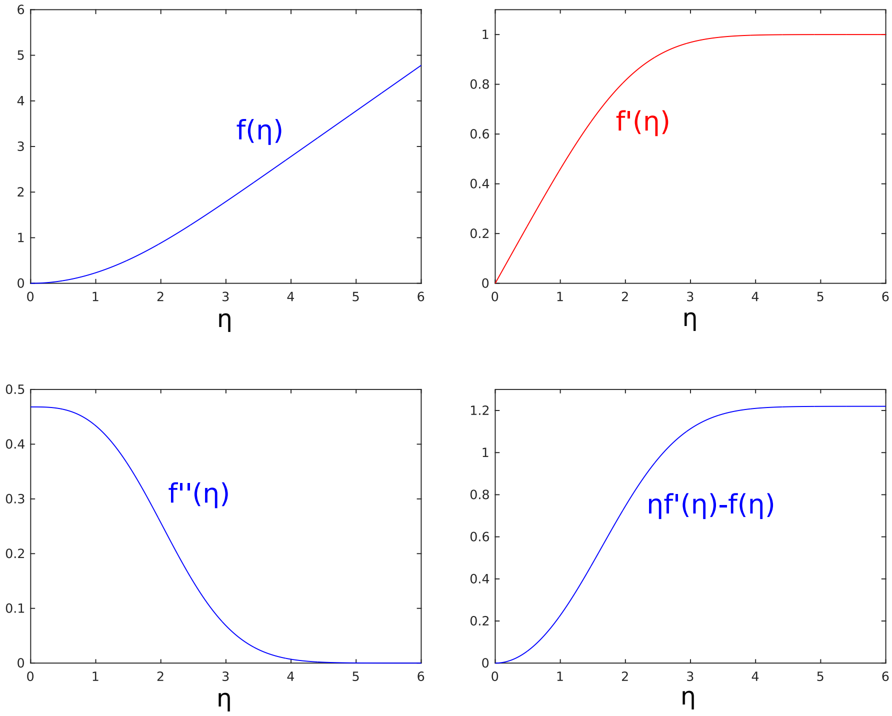

Figure C.1: *Blasius solution for laminar flow over a flat plate: profiles of stream function* $[f(\eta) = \psi/(U_\infty\, \delta)]$, *streamwise velocity* $[f'(\eta) = u/U_\infty]$, *shear stress* $[f''(\eta) = \tau\, \delta/(\mu\, U_\infty)]$ *and vertical velocity* $[\eta\, f'(\eta) - f(\eta) = v/(U_\infty\, \delta'].$

C.2.1.1 Numerical set-up and results

The inlet streamwise coordinate x_1 of the numerical domain is fixed to insure that $d\delta(x)/dx \ll 1$. The boundary layer thickness δ is usually defined as the distance from the wall where 99 % of the free-stream velocity is reached. This corresponds to $\eta_{0.99} = 3.4719$, which yields

$$\frac{\delta_{0.99}}{x} = \frac{\eta_{0.99}}{\left(\frac{U_\infty\, x}{2\,\nu}\right)^{1/2}} = \frac{4.91}{Re_x^{1/2}}\,. \tag{C.16}$$

The boundary layer growth is obtained by deriving the above equation. A value of 0.05 is chosen for limiting the ratio $d\delta(x)/dx$, from which x_1 is deduced. The corresponding boundary thickness is calculated from Eq. (C.16). As described in the previous section, the inlet velocity profiles are determined from the Blasius solution and represented in Fig. C.2.

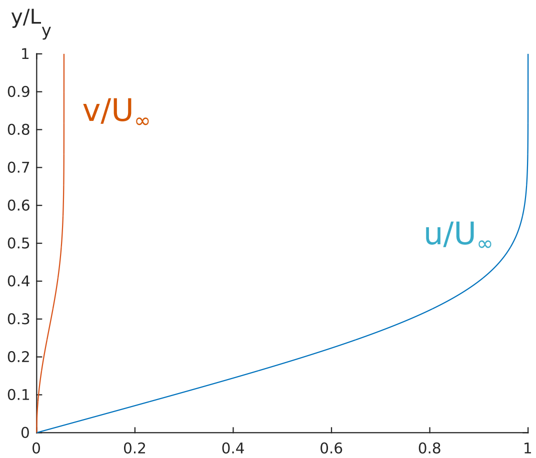

Figure C.2: *Inlet velocity profiles calculated from the Blasius solution.*

The streamwise extent of the domain is set to insure that the boundary layer is still laminar ($Re_{\delta^*} < 400$) by the time it reaches the end of the fetch. The domain height is chosen to be three times higher than the maximum $\delta_{0.99}$. Two different conditions are applied to the top boundary, namely a "slip wall" and a "zero-vorticity" boundary condition.
The first case sets all gradients to zero, which prevents the flow from exiting through the top. To accomodate this condition, the inlet vertical velocity profile is brought back linearly to zero from $\delta_{0.99}$ to the top, as observed in Fig. C.3 c). Naturally, this flow confinement results in free-stream acceleration and prevents the boundary layer from growing properly (ref. Fig. C.5). This overspeed clearly appears on the velocity contours and streamwise velocity profiles shown in Fig. C.3 a) and b) respectively, reaching +7.3 % at the exit. This effect could be reduced by increasing the domain height but this would also increase the computational cost.

Instead, the zero vorticity boundary condition, $\frac{\partial v}{\partial x} = \frac{\partial u}{\partial y}$, is implemented in OpenFOAM and tested. The vertical velocity distribution is set according to Eq. (C.10), based on the fact that, for the laminar ZPG boundary layer,

$$\frac{\delta^*}{x} = \frac{1.721}{Re_x^{1/2}} . \tag{C.17}$$

Observing Fig. C.4, the condition appears to behave well as realistic results are obtained. Firstly, the overspeed remains negligible with less than 0.3 % compared to the inlet free-stream velocity. Secondly, the vertical velocity profiles

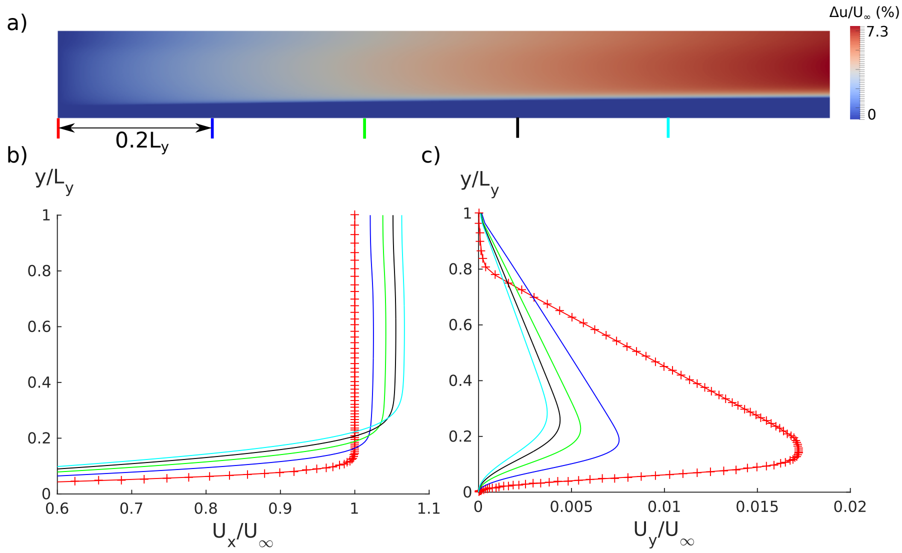

Figure C.3: *Laminar boundary results obtained with a slip wall along the top boundary a) Contours of relative streamwise velocity compared to inlet free-stream velocity. The velocity profile positions are also represented; b) Streamwise velocity profiles; c) Vertical velocity profiles.*

follow very well the distribution set along the top boundary. Similar conclusions can be drawn from Fig. C.5. An intermediate case, "v_{cst} & $0grad$", was first tested. V_{ref} is set to a constant, having applied to the boundary layer growth, while the other velocity components are set to zero gradient. This simple approximation already reduces the overspeed to less than 2 %, further reduced in the zero vorticity case "$0vort$". An excellent comparison with the Blasius solution for boundary growth is obtained with the latest.

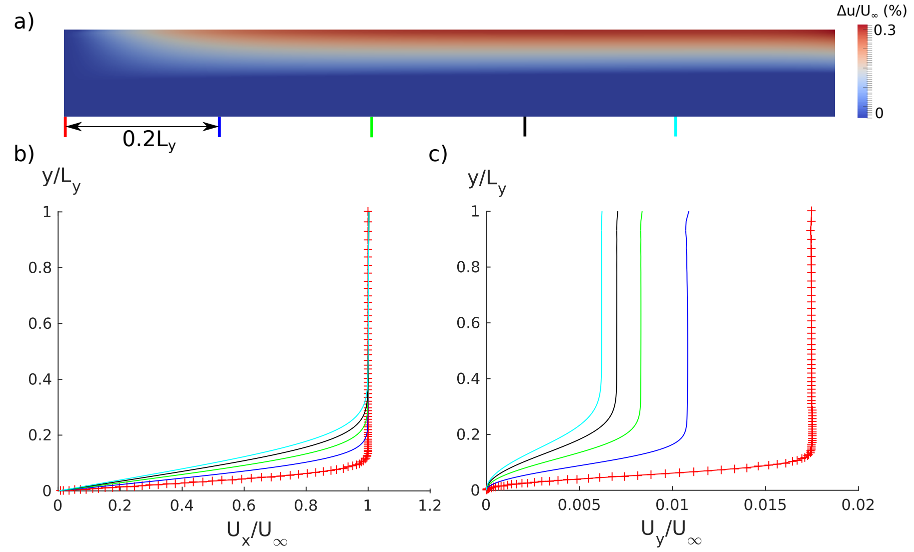

Figure C.4: *Laminar boundary results obtained with a zero vorticity boundary condition along the top a) Contours of relative streamwise velocity compared to inlet free-stream velocity. The velocity profile positions are also represented; b) Streamwise velocity profiles; c) Vertical velocity profiles.*

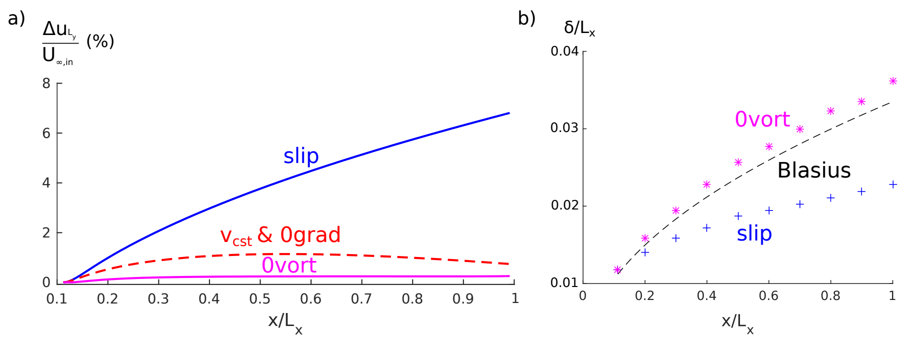

Figure C.5: *Effect of top boundary condition on laminar boundary layer characteristics a) Streamwise evolution of free-stream velocity at y_L b) Boundary layer growth compared to Blasius solution.*

Appendix D

LES of a ZPG turbulent boundary layer

D.1 Influence of the artificial buoyancy effects

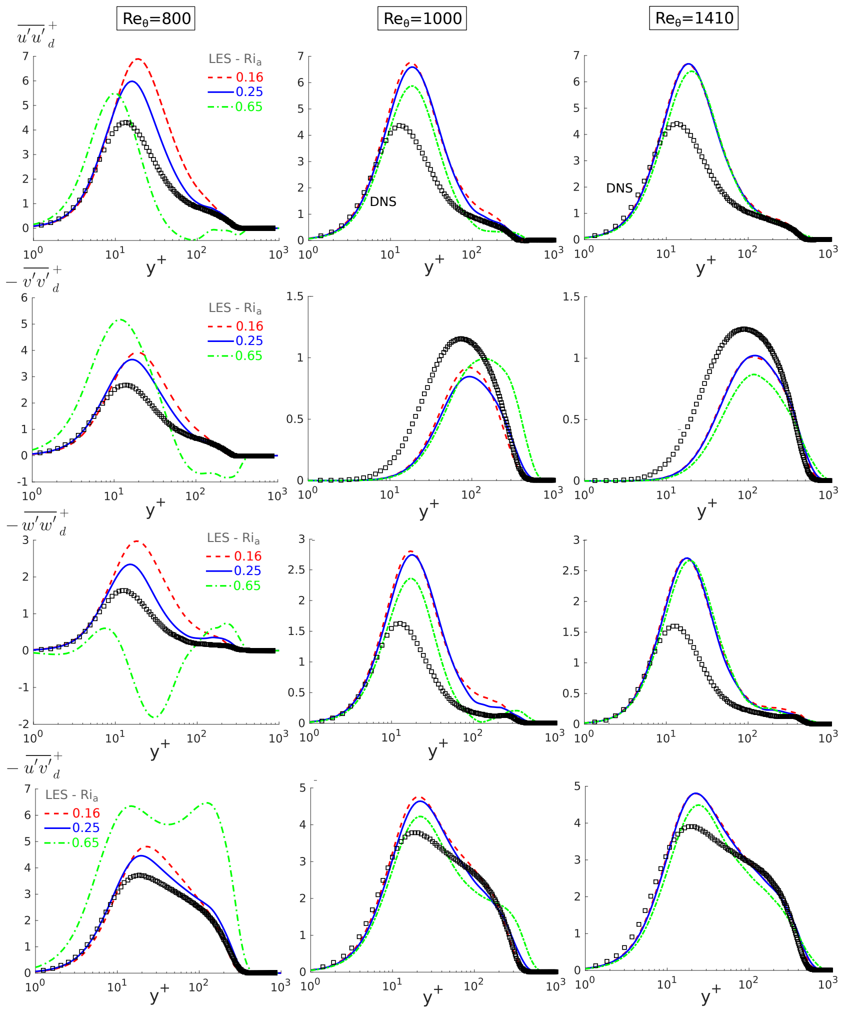

Figure D.1: *Influence of Ri_a on the deviatoric Reynolds stresses*

D.2 Influence of the Smagorinsky coefficient

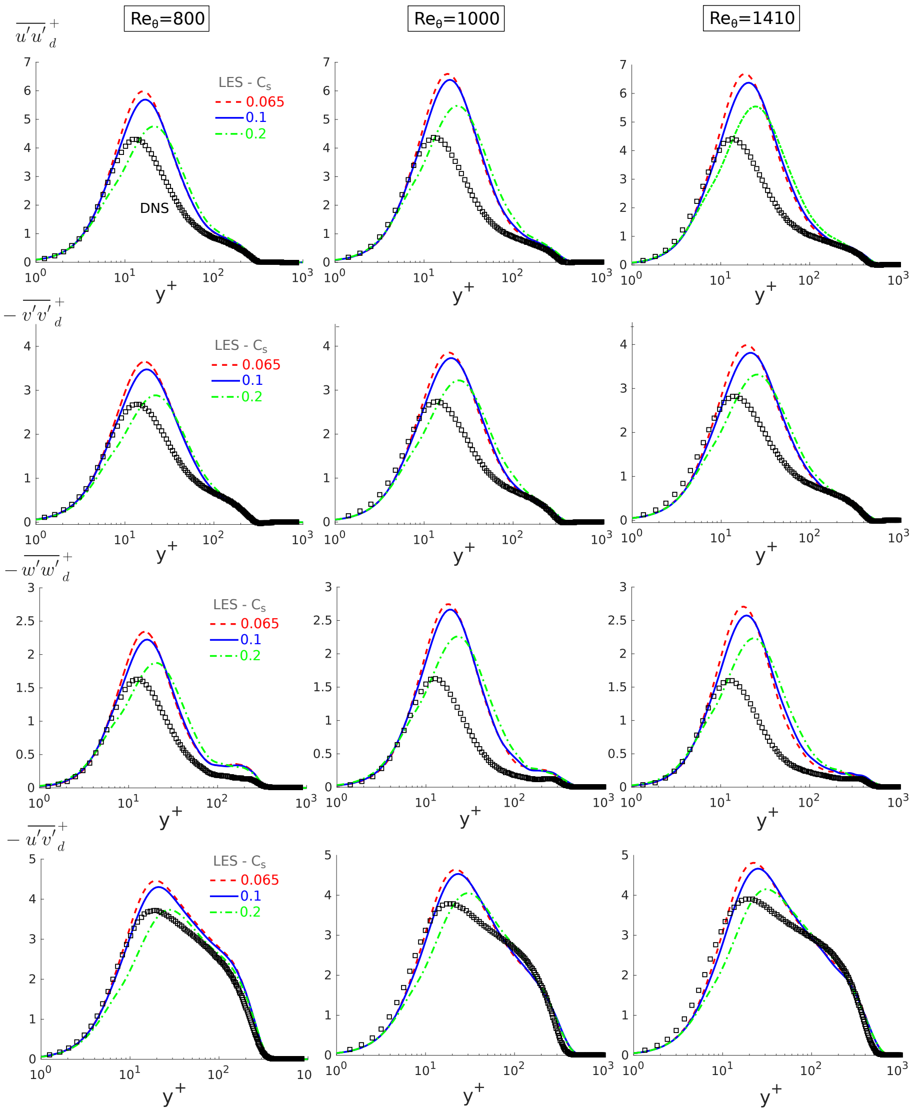

Figure D.2: *Influence of C_s on the deviatoric Reynolds stresses.*

Appendix E

Temperature field measured with the HWA-TC probe

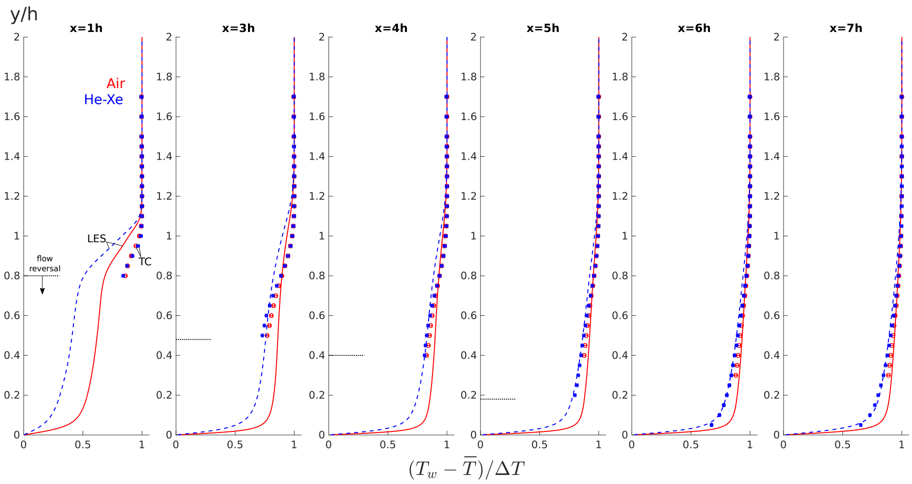

Figure E.1: *Mean temperature profiles obtained by LES and HWA-TC probe.*

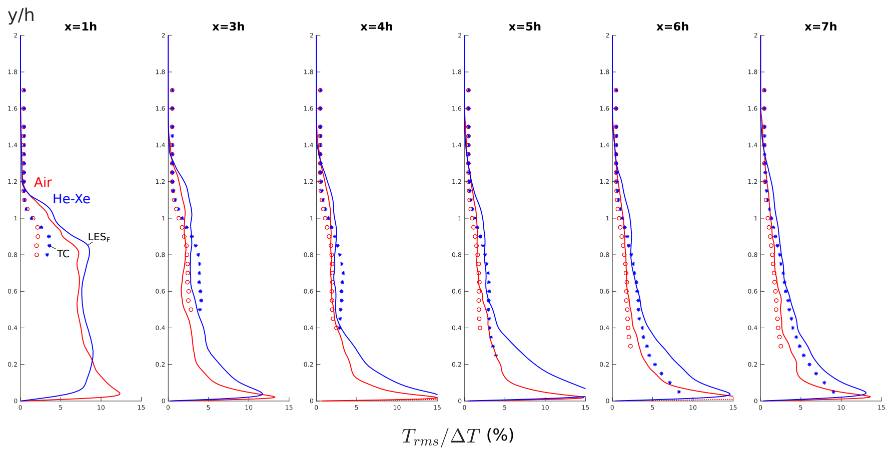

Figure E.2: *Rms temperature profiles obtained by LES and HWA-TC probe.*

Appendix F

Preliminary investigation of Prandtl number effects on heat transfer over a BFS

In preparation to the MYRTE experiment, the objective of this study has been to provide a first insight into low Prandtl number effects in abruptly separated flows. In particular, it is a way of quantifying a *priori* the differences between air and He-Xe, in preparation for the measurement campaign. To do so, LES over a BFS are run at three different Prandtl numbers, i.e. $Pr = 0.71$, $Pr = 0.2$ and $Pr = 0.025$. All of these results can be found in Buckingham et al. [23].

An important parameter in this preliminary investigation, is to identify a test case that reproduces an unconfined flow, so that it respects the main constraint of the targeted application. Consequently, the DNS data generated by Le et al. [75] has been chosen since flow confinement remains limited ($ER = 1.2$).

F.1 Computational details

F.1.1 Domain size

A schematic view of the 3D single-sided expansion can be found in Fig. 5.1. For comparison, the key domain dimensions are taken identical to those used in the benchmark test case of Le et al. [75]. The streamwise length L_x, includes a downstream length $L_d = 20\,h$ and a slightly longer inlet section $L_u = 11\,h$ ($10\,h$ in [75]), in order to better match the reference boundary layer thickness $\delta = 1.2\,h$ at the location $x = -0.3\,h$ upstream of the step.
Although it was found to be a *posteriori* not sufficient to guarantee a sufficient drop of the velocity cross-correlations in the free-shear layer, the spanwise size is fixed to $L_z = 4\,h$ to ensure a full comarison between the LES and DNS results. Finally, the domain height after the step is $H = 6\,h$ such that $ER = 1.2$. The heated wall downstream of the step measures $L_r = 11\,h$, which was initially designed to be the resistance length in the MYRTE experiment, before being increased to $14.7\,h$.

F.1.2 Boundary conditions

No-slip conditions are applied on all the lower walls, the upper boundary of the computational domain is defined as a slip wall, such that velocities are the following:

$$v = 0\,, \quad \frac{\partial u}{\partial y} = \frac{\partial w}{\partial y} = 0. \tag{F.1}$$

A uniform temperature T_{in} is inserted at the inlet and a constant temperature $T_w > T_{in}$ is applied to the heated wall. All other lower walls are treated as adiabatic. Periodic boundary conditions are applied to the side boundaries and a zero velocity gradient is imposed at the outlet.
At the inlet, the mean velocity profile $U(z)$ obtained from the DNS of Schlatter et al. [138] at $Re_\theta = 670$ is imposed. The free-stream velocity U_{in}, is adjusted to match the value of $Re_h = 5100$. The optimized TPM is used to generate inflow turbulence, based on the guidelines formulated in Chapter 2. The local Richardson number is adjusted to the best suited value $Ri_a = 0.25$ found in Chapter 4.

F.1.3 Numerical methodology

All numerical settings are identical to those used in the MYRTE experiment (see Section. 5.2.3). The influence of the SGS Prandtl number Pr_{sgs}, has been investigated in the case of air by changing its value from 0.6 to 1. Results are compared in Fig. F.1 and Fig. F.2, where negligible differences are observed.

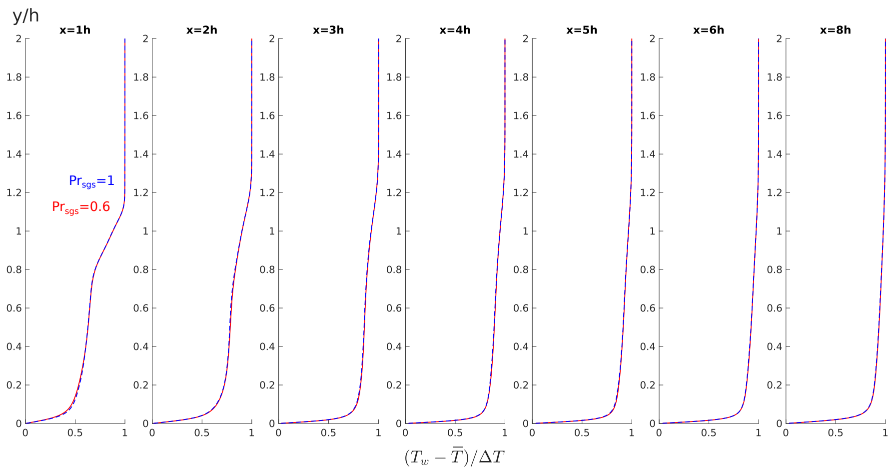

Figure F.1: *Influence of Pr_{sgs} on the mean temperature field at $Pr = 0.71$.*

The mesh also looks very similar and is made of 5.12 Million cells. The number of grid points upstream of the expansion is $190 \times 120 \times 64$ in the streamwise, vertical and spanwise directions and 300 streamwise cells are placed after the expansion. The grid resolution is kept the same.

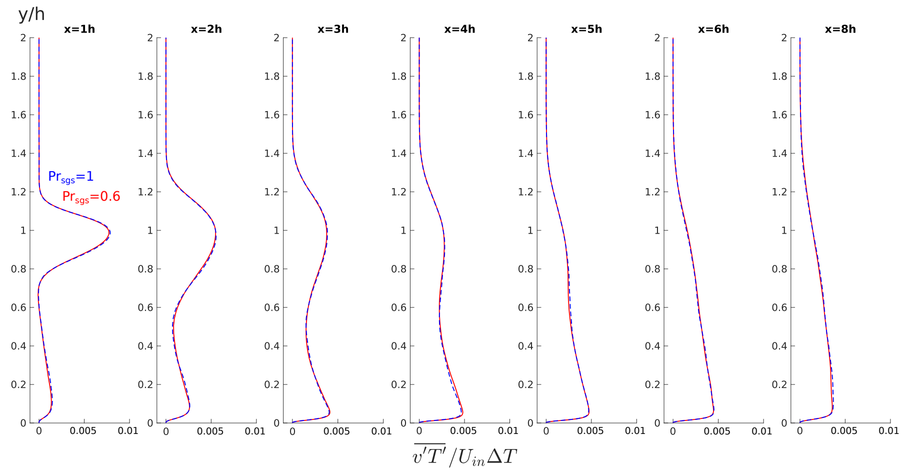

Figure F.2: *Influence of Pr_{sgs} on the vertical turbulent heat flux field at $Pr = 0.71$.*

F.2 Velocity field results

F.2.1 Incoming flow

The inlet TBL profile imposed from the DNS ($Re_\theta = 670$) grows along the upstream section before the step and the boundary layer thickness obtained by LES matches the DNS value of $\delta/h = 1.2$ just upstream of the step, at $x = -0.3\,h$. The resulting boundary layer is compared at $x = -3\,h$ in Fig. F.3.

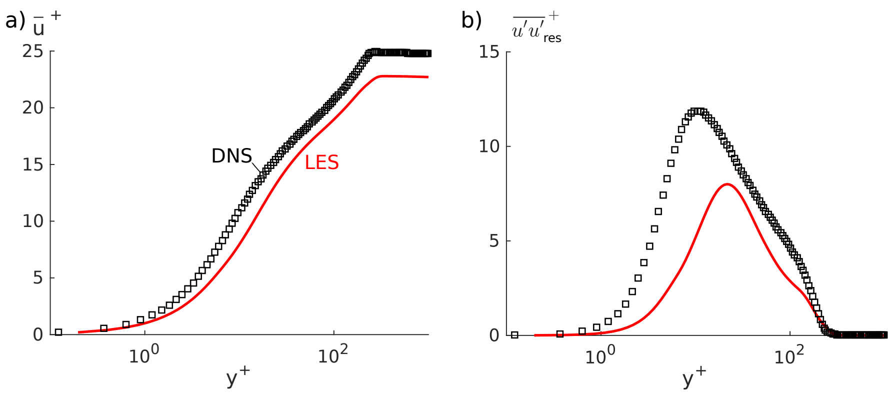

Figure F.3: *Profiles obtained at $x = -3\,h$ a) mean velocity b) streamwise Reynolds stress.*

It is important to note that the subscript (res) refers to the resolved part of the turbulent stresses. As described by Winckelmans et al. [172], the Smagorinsky SGS model is traceless, thus only the deviatoric part of the normal stresses is modeled. In the case of the shear stresses and turbulent heat fluxes, the LES turbulent stresses are composed of a resolved and a SGS part. Therefore, for a true comparison of the turbulent stresses obtained by DNS (fully resolved) and LES (only partially resolved), the trace should be removed from the DNS normal stresses and the SGS contributions should be added to the LES shear stresses and turbulent heat fluxes. This is done in the LES of the MYRTE experiment but not yet in this preliminary test case.

The incoming boundary appears to be in fairly good agreement with the reference DNS. Discrepencies can be associated to an over-prediction in the friction velocity, which leads to a general under-prediction of both the mean velocity and streamwsie Reynolds stress profiles (the velocity outside of the boundary layer is of course correct). Nevertheless, a good match is observed in the overall shape of the profile, which is expected to play a dominant role in the downstream flow development.

F.2.2 Flow reattachment

The evolution of the mean skin friction coefficient along the bottom wall is plotted in Fig. F.4 and compared to the DNS. The predicted reattachment length x_r, is $5.5\,h$ compared to the reference DNS length of $6.28\,h$, corresponding to a slight shift of the negative peak of C_f in the upstream direction. Thus, it is under-predicted by about 12 %, which is not uncommon while trying to match DNS or experimental results with LES [6, 36]. In agreement with Le et al. [75], a very low value of $C_f = -0.0034$ is reached compared to $C_f = -0.0028$ in the DNS, while the flow slowly recovers equilibrium downstream of the reattachment.

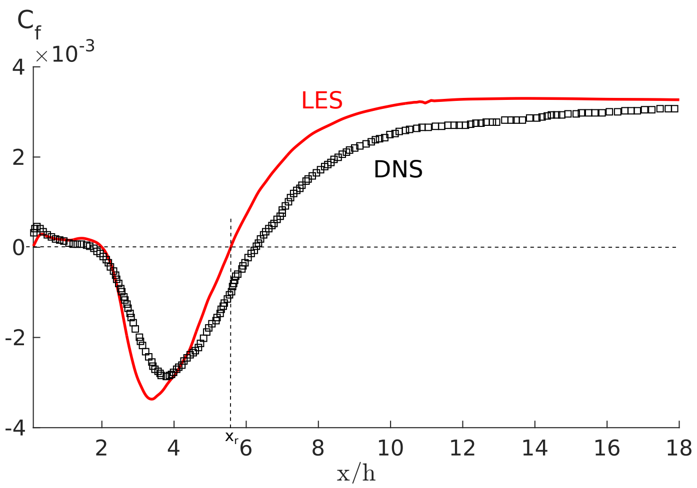

Figure F.4: *Streamwise variation of the skin friction coefficient.*

Mean longitudinal and vertical velocity profiles are plotted in Fig. F.5. All statistical quantities were averaged in time and along the homogeneous spanwise direction. These are non-dimensionalized with the inlet free stream velocity U_{in} and temperature difference $\Delta T = T_w - T_{in}$. Despite the slight under-prediction in the reattachment length, the velocity profiles appear in good agreement with the reference DNS.

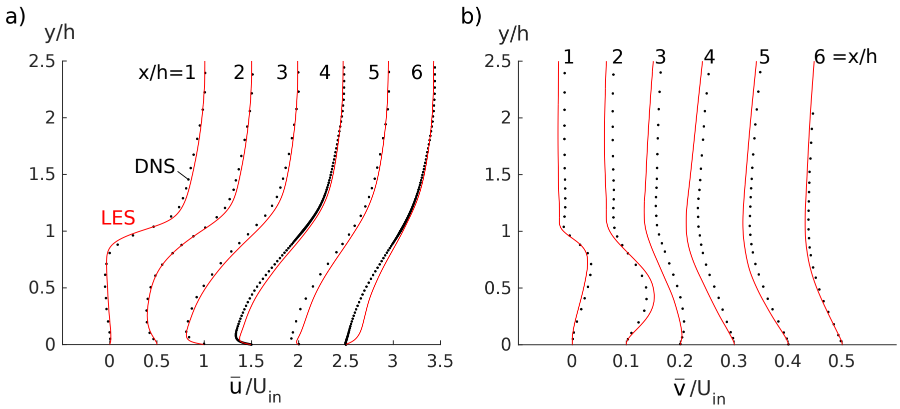

Figure F.5: *Mean velocity profiles a) Streamwise component b) Vertical component.*

The Reynolds stress profiles are shown in Fig. F.6 and F.7, normalized by U_{in}^2. The comparison of the profiles at positions $x/h = 4$ and 6 highlights a slight over-prediction of the turbulence levels.

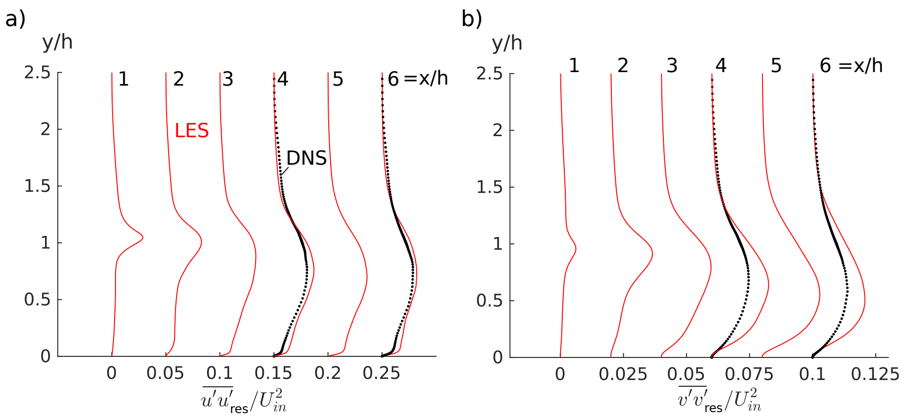

Figure F.6: *Reynolds stress profiles a) Streamwise stress b) Vertical stress.*

Similar discrepencies between LES and DNS can be found in the litterature [151]. Nevertheless, the peak position and growth of the shear layer is well found and the agreement between the LES and DNS remains acceptable. To conclude, comparison of the LES velocity results with those obtained by DNS is satisfactory. We can therefore proceed by analyzing the Prandtl number effect on the thermal flow behavior.

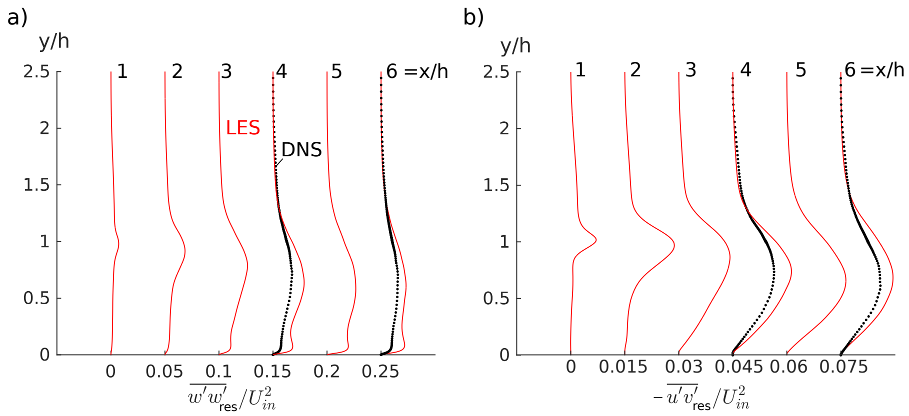

Figure F.7: *Reynolds stress profiles a) Spanwise stress b) Shear stress.*

F.3 Influence of the Prandtl number

F.3.1 Temperature field

Mean temperature fields in the step area are shown in Fig. F.8 for all three fluids at $Pr = 0.71$ (air), 0.2 (He-Xe) and 0.025 (LBE).

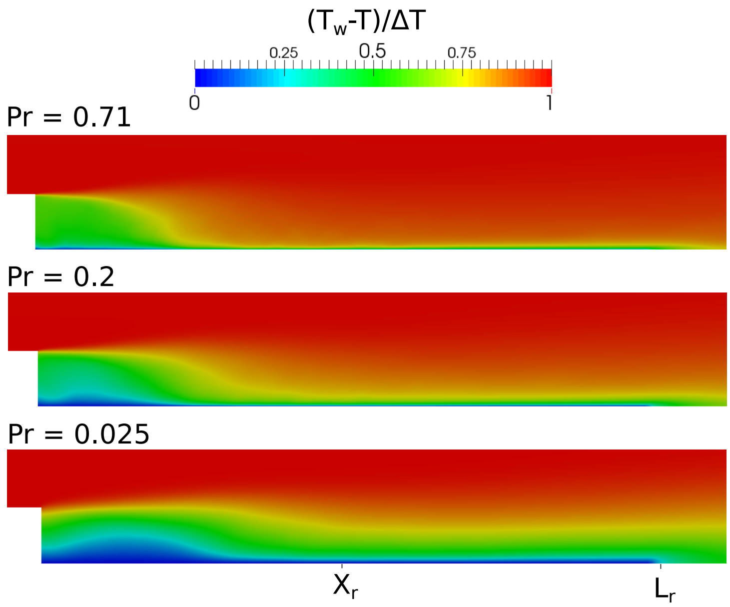

Figure F.8: *Prandtl number effects on the mean temperature field.*

Comparison of these fields indicates strong differences between the evolution of the temperature fields. The Prandtl number effect is already clearly visible between $Pr = 0.71$ and 0.2. As the thermal diffusivity gets higher, heat is conducted further away from the heated wall. In the case of air, the temperature turbulent diffusion is similar to the momentum turbulent diffusion (effective Pr_t is order unity). As a result, the highest differences are concentrated in the step corner where the secondary recirculation is located. In the case of He-Xe, diffusion starts playing a role in the transport mechanism while, with LBE, it becomes the major contributor.

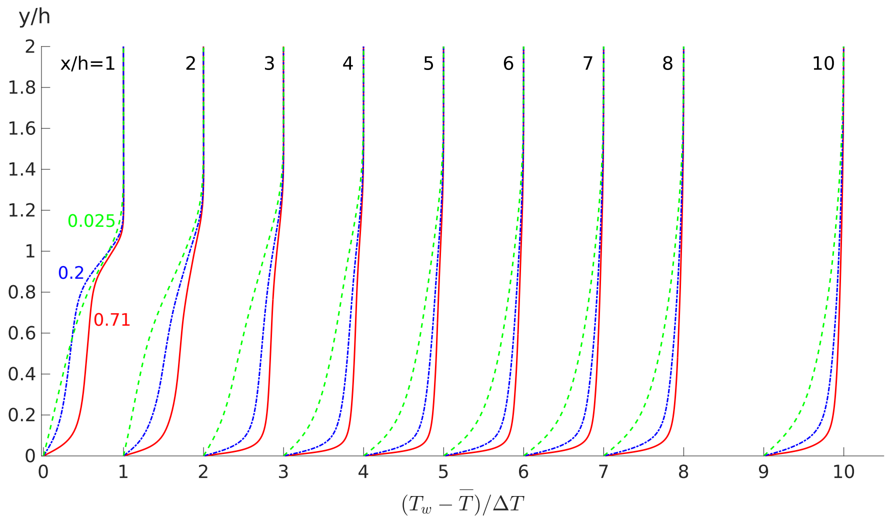

Figure F.9: *Prandtl number effects on the mean temperature profiles.*

The temperature profiles are extracted and shown in Fig. F.8. The Prandtl number influences the characteristics of these profiles, with a shape that is much smoother in the case of LBE, as a thicker thermal boundary layer redevelops. This effect is already visible in the case of He-Xe.

F.3.2 Turbulent heat transfer behaviour

Profiles of streamwise turbulent heat flux are plotted in Fig. F.10. The strongest correlation between temperature and streamwise velocity fluctuations is found within the shear layer region. Once again, it is very localized in case of air to the step corner region while much smoother variations are observed in LBE.

Profiles of vertical turbulent heat flux are examined in Fig. F.11. The turbulent contribution to the transport of heat in the vertical direction strongly varies depending on the streamwise position. For the lowest value of $Pr = 0.025$, it is practically inexistent close to separation and becomes progressively stronger as the flow approaches reattachment. A more thorough investigation is carried out on the MYRTE experiment, by looking at the different modes of heat transfer, not only related to turbulence but also to diffusion.

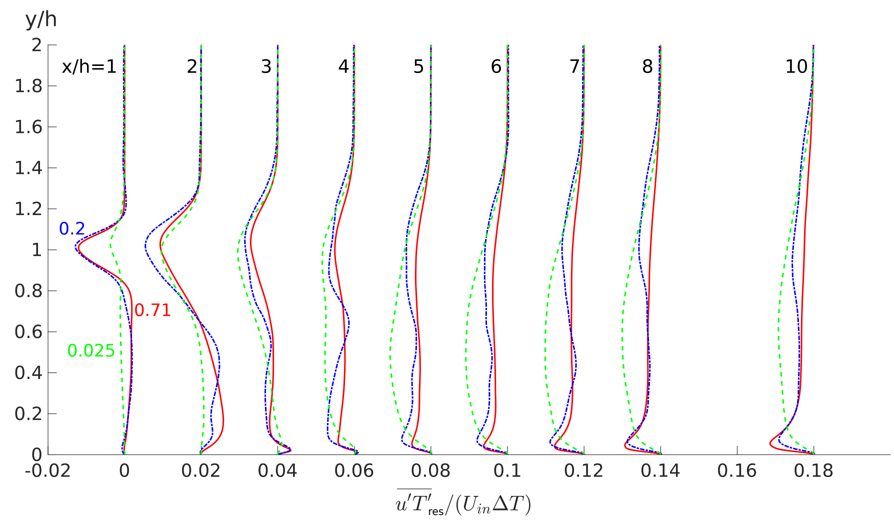

Figure F.10: *Prandtl number effects on the Streamwise turbulent heat flux.*

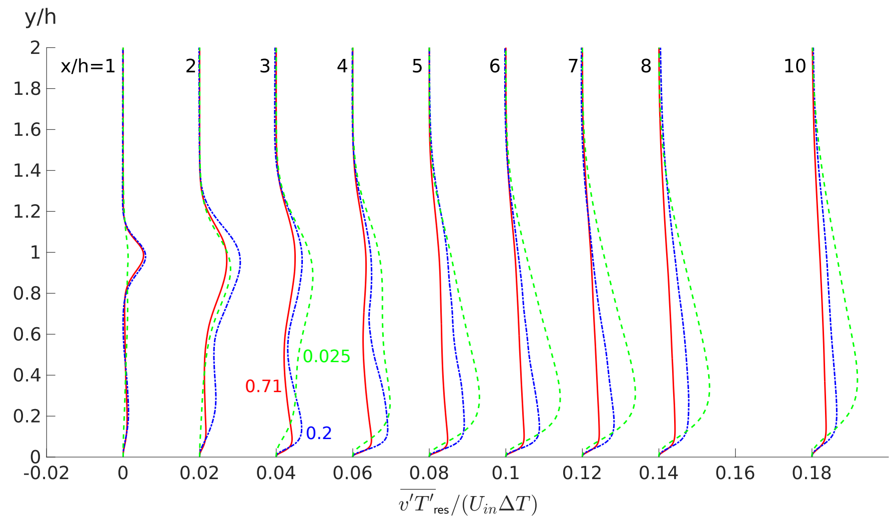

Figure F.11: *Prandtl number effects on the vertical turbulent heat flux.*

F.4 Conclusions

The LES is compared to the DNS test case of Le et al. [75] performed at $Re_h = 5100$ that, similarly to the MYRTE experiment, features an unconfined flow over a BFS. Comparison of the inflow boundary layer satisfies the boundary layer thickness height of $1.2\,h$ just upstream of the step. Despite a slight over-estimation of the friction velocity, the boundary layer shape is very close to the reference. In the separated flow area, a shorter flow reattachment of $5.51\,h$ instead of $6.28\,h$ is predicted. The velocity and Reynolds stress profiles

appear to be in acceptable agreement, despite an over-estimation of the turbulence peak values. Consequently, these LES velocity results provide us with sufficient confidence to proceed and analyze the influence of Pr on the thermal behavior.
The increased conductivity of the He-Xe mixture is sufficient to have a noticeable effect on the temperature field, that is no longer dominated by a purely turbulent convective transport (i.e. effective turbulent diffusion) but also has a significant molecular diffusion contribution. These differences should be sufficiently large to be measurable during the MYRTE test campaign. Profiles of turbulent heat flux indicate that the turbulent contribution is negligible close to separation at low $Pr = 0.025$, while much higher rates are found closer to reattachment.

Bibliography

[1] H. Abe, H. Kawamura, and Y. Matsuo. Surface heat-flux fluctuations in a turbulent channel flow . *Turbulence Heat and Mass Transfer*, 4, 2003.

[2] H. Abe, Y. Matsuo, and H. Kawamura. Reynolds and Prandtl-number effects on turbulence quantities through DNS of turbulent heat transfer in a channel flow up to $Re_\tau = 640$. *Turbulence Heat and Mass Transfer*, 4, 2003.

[3] H. Abu-Mulaweh and B. Armaly. Turbulent mixed convection flow over a backward facing step. *Experimental Heat Transfer*, 12:295–308, 1999.

[4] R. J. Adrian. Particle-imaging techniques for experimental fluid dynamics. *Ann. Rev. Fluid Mech.*, 22:261–304, 1991.

[5] R. J. Adrian. Hairpin vortex organisation in wall turbulence. *Phys. Fluids*, 19:1–16, 2007.

[6] J.L. Aider and A. Danet. Large-eddy simulation study of upstream boundary conditions influence upon a backward-facing step flow. *Comptes Rendus Mécanique*, 334:447–453, 2006.

[7] K. Akselvoll and P. Moin. Large eddy simulation of turbulent flow over a backward facing step. Report No. TF-63, Stanfort University., 1995.

[8] A. Alemberti, L. Mansani, G. Grasso, D. Mattioli, F. Roelofs, and D. De Bruyn. The European Lead Fast reactor strategy and the Roadmap for the Demonstrator ALFRED. FR13, Paris, France, 2013.

[9] *ANSYS FLUENT User's Guide*. ANSYS, 2011. Release 14.0.

[10] G. Araya and L. Castillo. Direct numerical simulations of turbulent thermal boundary layers subjected to adverse streamwise pressure gradients. *Phys. Fluids*, 25, 2013. 095107.

[11] B. F. Armaly, F. Durst, J. C. F. Pereira, and B. Schonung. Experimental and theoretical investigation of backward-facing step flow. *J. Fluid Mech.*, 127:473–496, 1983.

[12] W. Aung. Separated forced convection. ASME/JSME Thermal Engineering Conf. Honolulu, HI, 1983.

[13] R. V.R. Avancha and R.H. Pletcher. Large eddy simulation of the turbulent flow past a backward-facing step with heat transfer and property variations. *Int. J. Heat Fluid Flow*, 23:601–614, 2002.

[14] E. Baglietto. An algebraic heat flux model in STAR-CCM+ for application to innovative reactors. The 14th International Topical Meeting on Nuclear Reactor Thermal Hydraulics (NURETH-14), Toronto, Canada, 2011.

[15] T. Baumann, A. Loges, L. Marocco, T. Schenkel, T. Wetzel, and R. Stieglitz. Modeling the turbulent heat fluxes in low prandtl shear flows. The 14th International Topical Meeting on Nuclear Reactor Thermal Hydraulics (NURETH-14), Toronto, Canada, 2011.

[16] D.M. Bell and J.H. Ferziger. *Turbulent boundary layer dns with passive scalars*. Elsevier, 1993.

[17] B.F. Blackwell and B.F. Armaly. Computational aspects of heat transfer benchmark problems. HTD-ASME Winter Annual Meeting, Toronto, 258, New Orleans, pp. 1-115, 1993.

[18] H. Blasius. Grenzschichten in Flüssigkeiten mit kleiner Reibung. *Z. Angew. Math. Phys.*, 56:1–37, 1908.

[19] P. Bradshaw and F. Y. F. Wong. The reattachment and relaxation of a turbulent shear layer. *J. Fluid Mech.*, 52(1):113–135, 1972.

[20] L. Bricteux, M. Duponcheel, G. Winckelmans, I. Tiselj, and Y. Bartosiewicz. Direct and large eddy simulation of turbulent heat transfer at very low Prandtl number: application to lead-bismuth flows. *Nuclear Engineering and Design*, 246:91–97, 2012.

[21] F. K. Browand. An experimental investigation of the instabilities of an incompressible separate shear layer. *J. Fluid Mech.*, 26(2):281–307, 1966.

[22] D. De Bruyn, H. Ait Abderrahim, P. Baeten, and G. Van den Eynde. The MYRRHA ADS project in Belgium enters the frontend engineering phase. ICAPP14, Charlotte, USA, 2014.

[23] S. Buckingham, L. Koloszar, Y. Bartosiewicz, and G. Winckelmans. Large eddy simulation of turbulent heat transfer at low Prandtl number over a backward-facing step. . The 17th International Topical Meeting on Nuclear Reactor Thermal Hydraulics (NURETH-17), Xian, China, 2017.

[24] S. Buckingham, L. Koloszar, C. Garcia-Sanchez, and G. Winckelmans. Temperature perturbation method to generate turbulent inflow conditions for LES/DNS simulations in OpenFOAM. . Ninth International Conference on Computational Fluid Dynamics (ICCFD9), Istanbul, Turkey, July 11-15, 2016.

[25] S. Buckingham, L. Koloszar, Y. Bartosiewicz, and G. Winckelmans. Optimized temperature perturbation method to generate turbulent inflow conditions for LES/DNS simulations. *Comput. Fluids*, 154:44–59, 2017.

[26] M. Campagna. Instantaneous measurements of fluctuating temperature and velocity. VKI PR 2016-02, von Karman Institut for Fluid Dynamics, 2016.

[27] F.H. Champagne, C.A. Sleigher, and O.H. Wehrmann. Turbulence measurements with inclined hot wires. *J. Fluid Mech.*, 28:153–175, 1967.

[28] M. Chauveau. Instantaneous measurements of fluctuating temperature and velocity. Rapport de stage, Institut Supérieur Industriel de Bruxelles - ISIB-Mca-TFE-15/18, 2017.

[29] X. Cheng and N. Tak. Investigation on turbulent heat transfer to lead-bismuth eutectic flows in circular tubes for nuclear applications. *Nucl. Eng. Des.*, 236:385–393, 2006.

[30] F. H. Clauser. Turbulent boundary layers in adverse pressure gradients. *J. Aerosp. Sci.*, 21:91–108, 1954.

[31] P. Le Coz, J.-F. Sauvage, J.-M. Hamy, V. Jourdain, J.-P. Biaudis, H. Oota, T. Chauveau, P. Audouin, D. Robertson, and R. Gefflot. The ASTRID project: status and future prospects. FR13, Paris, France, 2013.

[32] B. Cukurel, S. Acarer, and T. Arts. A novel perspective to high-speed cross-hot wire calibration methodology. *Exp. Fluids*, 53:1073–1085, 2012.

[33] B. J. Daly and F. H. Harlow. Transport equations in turbulence. *Phys. Fluids*, 18:2634–2649, 1970.

[34] V. de Brederode and P. Bradshaw. Three-dimensional flow in nominally two-dimensional separation bubbles. I. Flow behind a rearward-facing step. Imperial College, Aeronautical Rept., 1972.

[35] JW. Deardorff. A numerical study of three-dimensional turbulent channel flow at large Reynolds numbers. *J. Fluid Mech.*, 41:453–465, 1970.

[36] Y. Dubief and F. Delcayre. On coherent-vortex identification in turbulence. *J. of Turbulence*, 1:1–22, 2000.

[37] M. Duponcheel, L. Bricteux, M. Manconi, G. Winckelmans, and Y. Bartosiewicz. Assessment of RANS and improved near-wall modeling for forced convection at low Prandtl numbers based on LES up to $Re_\tau =$ 2000. *Turbulence Heat and Mass Transfer*, 4, 2003.

[38] J. K. Eaton and J. P. Johnston. A review of research on subsonic turbulent flow reattachment. *AIAA Journal*, 19(9), 1981.

[39] L.P. Erm and P. Joubert. Low-Reynolds-number turbulent boundary layers. *J. Fluid Mech.*, 230:1–44, 1991.

[40] O. Errico and E. Stalio. Direct numerical simulation of low-Prandtl number turbulent convection above a wavy wall. *Nuclear Engineering and Design*, 290:87–98, 2015.

[41] ESNII. ESNII, The European Sustainable Nuclear Industrial Initiative: Concept Paper. SNE-TP, 2010.

[42] Euratom. The Sustainable Nuclear Energy Technology Platform, A Vision Report. European Commission (Directorate General for Research Euratom), Brussels, Belgium, 2007.

[43] H. Fasel. Investigation of the stability of boundary layers by a finite-difference model of the Navier-Stokes equations. *J. Fluid Mech.*, 78(2): 355–383, 1976.

[44] A. Ferrante and S. E. Elghobashi. Reynolds number effect on drag reduction in a microbubblelden spatially developing turbulent boundary layer. *J. Fluid Mech.*, 543:93–106, 2005.

[45] C. Flageul, S. Benhamadouche, E. Lamballais, and D. Laurence. DNS of turbulent channel flow with conjugate heat transfer: effect of thermal boundary conditions on the second moments and budgets. *Int. J. Heat Fluid Flow*, 55:34–44, 2015.

[46] M. Germano, U. Piomelli, P. Moin, and W. H. Cabot. A dynamic subgrid scale eddy viscosity model. *Phys. Fluids*, 3:1760–1765, 1991.

[47] S. Grewal and E. Gluekler. Water simulation of sodium reactors. *Chemical Engineering Community*, 17:343–360, 1982.

[48] G. Grötzbach. Challenges in simulation and modeling of heat transfer in low-Prandtl number fluids. The 14th International Topical Meeting on Nuclear Reactor Thermal Hydraulics (NURETH-14), Toronto, Canada, 2011.

[49] G. Grötzbach. Numerical simulation of turbulent temperature fluctuations in liquid metals. *Int. J. Heat Mass Tran.*, 24:475–490, 1981.

[50] G. Grötzbach. Numerical simulation of turbulent temperature fluctuations in turbulent channels up to $Re_\tau = 590$. *Nuclear Engineering and Design*, 241(11):4379–4390, 2011.

[51] G. Grötzbach. Revisiting the resolution requirements for turbulence simulations in nuclear heat transfer. *Nuclear Engineering and Design*, 241 (11):4379–4390, 2011.

[52] J. Hogg and G. Ahlers. Reynolds-number measurements for low-Prandtl-number turbulnt convection of large-aspect-ratio samples. *J. Fluid. Mech.*, 725:664–680, 2013.

[53] S. Hoyas and J. Jimenez. Scaling of the velocity fluctuations in turbulent channels up to $Re_\tau = 2003$. *Phys. Fluids*, 18, 2006. 011702.

[54] IAEA. Benchmark analyses on the natural circulation test performed during the Phenix end-of-life experiments. IAEA Tecdoc 1703. Vienna, Austria., 2013.

[55] IEA. World Energy Outlook 2017. London, UK, 2017.

[56] M. Inoue. *Large-Eddy Simulation of the flat-plate turbulent boundary layer at high Reynolds numbers.* PhD Thesis, California Institute of Technology, Pasadena, California, United-States, 2012.

[57] W. Jaeger, T. Schumm, M. Niemann, W. Hering, R. Stieglitz, F. Magagnato, B. Frohnapfel, and J. Fröhlich. Thermo-hydraulic flow in sudden expansion. *IOP Conference Series: Materials Science and Engineering. IOP Publishing, Toronto, Canada, 2011.*, page 012001, 2017.

[58] N. Jarrin. *Synthetic inflow boundary conditions for the numerical simulation of turbulence.* PhD Thesis, University of Manchester, Manchester, United-Kingdom, 2008.

[59] S. Jovic and D. M. Driver. Backward-facing step measurements at low Reynolds number, $Re_h = 5000$. NASA Tech. Mem. 108807., 1994.

[60] N. Kasaga and A. Matsunaga. Three-dimensional particle-tracking velocimetry measurement of turbulence statistics and energy budget in a backward-facing step. *Int. J. Heat Fluid Flow*, 16:477–485, 1995.

[61] H. Kawamura, H. Abe, and Y. Matsuo. DNS of turbulent heat transfer in channel flow with respect to Reynolds and Prandtl number effects. *Int. J. Heat Fluid Flow*, 20:196–207, 1999.

[62] W. A. Kays and M. E. Crawford. *Convective Heat and Mass Transfer.* McGraw-Hill, 3rd edition, 1993.

[63] A. Keating, U. Piomelli, and E. Balaras. A priori and a posteriori tests of inflow conditions for large-eddy simulation. *Phys. Fluids*, 16(12):4696–4712, 2004.

[64] S. Kenjeres, S. B. Gunarjo, and K. Hanjalic. Contribution to elliptic relaxation modelling of turbulent natural and mixed convection. *Int. J. Heat Fluid Fl.*, 26:569–586, 2005.

[65] G. Khujadze and M. Oberlack. DNS and scaling laws from new symmetry groups of ZPG turbulent boundary layer flow. *Theor. Comput.Fluid Dyn.*, 18:391–411, 2004.

[66] G. Khujadze and M. Oberlack. New scaling laws in ZPG turbulent boundary layer flows. *Flow Turbul. Combust.*, 68:443–448, 2007.

[67] Y. Kim, I. P. Castro, and Z.-T. Xie. Divergence-free turbulence inflow conditions for large-eddy simulations with incompressible flow solvers. *Computers and Fluids*, 84:56–68, 2013.

[68] T. Koga, T. Murakami, Y. Eguchi, T. Matsuzawa, and O. Watanabe. Water test of natural circulation for decay heat removal in jsfr. The 14th International Topical Meeting on Nuclear Reactor Thermal Hydraulics (NURETH-14), Toronto, Canada, 2011.

[69] E.M.J. Komen, L.H. Camilo, A. Shams, B.J. Geurts, and B. Koren. A quantification method for the numerical dissipation in quasi-dns and under-resolved dns, and effects of numerical dissipation in quasi-dns and under-resolved dns of turbulent channel flows. *J. of Computational Physics*, 345:565–595, 2017.

[70] J. Komminaho and M. Skote. Reynolds stress budgets in couette and boundary layer flows. *Flow Turbul. Combust.*, 68:167–192, 2002.

[71] T. Kondoh, Y. Nagano, and T. Tsuji. Computational study of laminar heat-transfer downstream of a backward-facing step. *Int. J. Heat Mass Tran.*, 36:577–591, 1993.

[72] J. Kostas, J. Soria, and M.S. Chong. Particle image velocimetry measurements of a backward-facing step flow. *Exp. Fluids*, 33:838–853, 2002.

[73] R. H. Kraichnan. Diffusion by a random velocity field. *Phys. Fluids*, 13: 22–31, 1969.

[74] H. Le. *Direct numerical simulation of turbulence flow over a backward-facing step.* PhD Thesis, Stanford University, California, United-States, 1995.

[75] H. Le, P. Moin, and J. Kim. Direct numerical simulation of turbulent flow over a backward-facing step. *J. Fluid Mech.*, 330:349–374, 1997.

[76] I. Lee and H.J. Sung. Characteristics of wall pressure fluctuations in separated and reattaching flows over a backward-facing step: Part i. time-mean statistics and cross-spectral analyses. *Exp. Fluids*, 30:262–272, 2001.

[77] I. Lee, K. Ahn, and H.J. Sung. Three-dimensional coherent structure in a separated and reattaching flow over a backward-facing step. *Exp. Fluids*, 36:373–383, 2004.

[78] I. Lekakis. Calibration and signal interpretation for single and multiple hot-wire/hot-film probes. *Measurement Science of Technology*, 7(10): 1313–1333, 1996.

[79] N. Li, E. Balaras, and U. Piomelli. Inflow conditions for large-eddy simulations of mixing layers. *Phys. Fluids*, 12:935–938, January 2000.

[80] Q. Li, P. Schlatter, L. Brandt, and D. S. Henningson. DNS of a spatially developing turbulent boundary layer with passive scalar transport. *Int. J. Heat Fluid Flow*, 30:916–929, 2009.

[81] J. Liu and G. Ahlers. Rayleigh-Benard convection in binary-gas mixtures: Thermophysical properties and the onset of convection. *Phys. Rev.*, 55 (6):6950–6968, 1997.

[82] Y. Liu, W. Kang, and H.J. Sung. Assessment of the organization of a turbulent separated and reattaching flow by measuring wall pressure fluctuations. *Exp. Fluids*, 38:485–493, 2005.

[83] N. Lorenzin and A. Abanades. A review on the application of liquid metals as heat transfer fluid in Concentrated Solar Power technologies. *Int. J. Hydrogen Energ.*, 41:6990–6995, 2016.

[84] T. S. Lund, X. Wu, and K. D. Squires. Generation of turbulent inflow data for spatially-developing boundary layer simulations. *J. of Computational Physics*, 140:233–258, 1998.

[85] S. Manservisi and F. Menghini. A CFD four parameter heat transfer turbulence model for engineering applications in heavy liquid metals. *Int. J. Heat Mass Tran.*, 69:312–326, 2014.

[86] J. Mirocha, B. Kosovic, and G. Kirkil. Resolved turbulence characteristics in large-eddy simulations nested within mesoscale simulations using the Weather Research and Forecasting model. *Mon. Weather Rev.*, 142:806–831, 2014.

[87] P. Moin and J. Kim. Numerical investigation of turbulent channel flow. *J. Fluid Mech.*, 118:341–377, 1982.

[88] P. Moin, K. Squires, W. Cabot, and S. Lee. A dynamic sub-grid scale model for compressible turbulence and scalar transport. *Phys. Fluids*, 3: 2746–2757, 1991.

[89] P. A. Monkewitz, K. A. Chauhan, and H. M. Nagib. Self-consistent high-Reynolds-number asymptotics for zero-pressure-gradient turbulent boundary layers. *Phys. Fluids*, 19 (115101):1–12, 2007.

[90] N. Mordant, P. Metz, O. Michel, and J.-F. Pinton. Measurement of Lagrangian velocity in fully developed turbulence. *Phys. Rev. Lett.*, 87(21), 2001.

[91] M.V. Morkovin. Fluctuations and Hot Wire Anemometry in Compressible Flows. *AGARDograph*, 24, 1956.

[92] R. D. Moser, J. Kim, and N. N. Mansour. Direct numerical simulation of turbulent channel flow up to $Re_\tau = 590$. *Phys. Fluids*, 11:943–945, 1999.

[93] F. Motallebi. A review of the hot-wire technique in 2-D compressible flows. *Progress in Aerospace Sciences*, 30:267–294, 1994.

[94] D. Muñoz-Esparza. *Multiscale modelling of atmospheric flows: towards improving the representation of boundary layer effects.* PhD Thesis, Université Libre de Bruxelles - von Karman Institute for Fluid Dynamics, Brussels, Belgium, 2013.

[95] D. Muñoz-Esparza, B. Kosovic, J. Mirocha, and J. van Beeck. Bridging the transition from mesoscale to microscale turbulence in numerical weather prediction models. *Boundary Layer Meteorol.*, 153:409–440, 2014.

[96] D. Muñoz-Esparza, B. Kosovic, J. van Beeck, and J. Mirocha. A stochastic perturbation method to generate inflow turbulence in large-eddy simulation models: Application to neutrally stratified atmospheric boundary layers. *Physics of Fluids*, 27(035102), 2015.

[97] B.G. Newman and B.G. Leary. The measurement of Reynolds stresses in a circular pipe as means of testing a hot wire anemometer. Comm. of Australia, Dept. of Supply Aero. Res. Labs, University of Sydney, Report A-72, November 1950., 1950.

[98] F. Nicoud and F. Ducros. Subgrid-scale stress modelling based on the square of the velocity gradient tensor. *Flow Turbulence Combust.*, 62: 183–200, 1999.

[99] M. Niemann and Jochen Fröhlich. Direct numerical simulation of turbulent heat transfer behind a backward-facing step at low Prandtl number. *Proc. Appl. Math. Mech.*, 14:659–660, 2014.

[100] M. Niemann and Jochen Fröhlich. Buoyancy-affected backward-facing step flow with heat transfer at low Prandtl number. *Int. J. Heat Mass Tran.*, 101:1237–1250, 2016.

[101] M. Niemann and Jochen Fröhlich. Turbulence budgets in buoyancy-affected vertical backward-facing step flow at low Prandtl number. *Flow Turbulence Combust.*, 99:705–728, 2017.

[102] *Handbook on Lead-Bismuth Eutectic Allow and Lead Properties, Materials Compatibility, Thermal-hydraulics and Technologies.* Nuclear Energy Agency document, 2015. Second Edition.

[103] A. Obabko, E. Merzari, and P. Fischer. Large-eddy simulations for thermal-hydraulics of deformed wire-wrap fuel assemblies. ANS, vol. 115, Las Vegas, USA, 2016.

[104] S. Ohno, H. Ohshima, A. Sugahara, and H. Ohki. Numerical analysis of sodium experiment for thermal stratification in upper plenum of fast reactor. The 13th International Topical Meeting on Nuclear Reactor Thermal Hydraulics (NURETH-13), Kanazawa City, Japan, 2009.

[105] *OpenFOAM, The Open Source CFD Toolbox, User Guide.* OpenFOAM Foundation Ltd., 2015. Release 3.0.1.

[106] R. Örlü. *Experimental studies in jet flows and zero pressure-gradient turbulent boundary layers.* PhD Thesis, Royal Institute of Technology, Stockholm, Sweden, 2009.

[107] R. Örlü and P. H. Alfredsson. On spatial resolution issues related to time-averaged quantities using hot-wire anemometry. *Exp. Fluids*, 49: 101–110, 2010.

[108] R. Örlü, J. H. M. Fransson, and P. H. Alfredsson. On near wall measurements of wall bounded flows-the necessity of an accurate determination of the wall position. *Prog. Aero. Sci.*, 46:353–387, 2010.

[109] J. M. Österlund. *Experimental studies of zero pressure-gradient turbulent boundary layer flow.* PhD Thesis, Royal Institute of Technology, Stockholm, Sweden, 1999.

[110] J. M. Österlund, A. V. Johansson, H. M. Nagib, and M. H. Hites. A note on the overlap region in turbulent boundary layers. *Physics of Fluids*, 12:1–4, 2000.

[111] I. Otić, G. Grötzbach, and M. Wörner. Analysis and modelling of the temperature variance equation in turbulent natural convection for low-Prandtl-number fluids. *J. Fluid Mech.*, 525:237–261, 2005.

[112] M. V. Ötügen. Expansion ratio effects on the separated shear layer and reattachment downstream of a backward facing step. *Exp. Fluids*, 10: 273–280, 1991.

[113] Simens M. P. *The study and control of wall bounded flows.* PhD Thesis, Universidad Politécnica de Madrid, Madrid, Spain, 2008.

[114] J. Pacio and T. Wetzel. Assessment of liquid metal technology status and research paths for their use as efficient heat transfer fluids in solar central receiver systems. *Solar Energy*, 93:11–22, 2013.

[115] L. Perret, J. Deville, R. Manceau, and J. Bonnet. Generation of turbulent inflow conditions for large eddy simulation from stereoscopic PIV measurements. *Int. J. Heat Fluid Flow*, 27:576–584, 2006.

[116] U. Piomelli, P. Moin, and JE. Ferziger. Model consistency in large eddy simulation of turbulent channel flows. *Physics of Fluids*, 31:1884–1891, 1988.

[117] U. Piomelli, T. A. Zang, C. G. Speziale, and M. Y. Hissaini. On the large eddy simulation of transitional wall-bounded flows. *Physics of Fluids*, 2: 257–265, 1990.

[118] U. Piomelli, E. Ballaras, and A. Pascarelli. Turbulent structures in accelerating boundary layers. *J. Turbul.*, 1:001, 2000.

[119] P. Planquart and K. van Tichelen. Experimental investigation of accidental scenarios using a scale water model of a HLM reactor. The 17th International Topical Meeting on Nuclear Reactor Thermal Hydraulics (NURETH-17), Xian, China, 2017.

[120] W. Pointer, P. Fischer, J. Smith, A. Obabko, and A. Siegel. Simulation of turbulent diffusion in wire-wrapped sodium fast reactor fuel assemblies. FR-09, Kyoto, Japan, 2009.

[121] R. Poletto, A. Revell, T. Craft, and N. Jarrin. Divergence free synthetic eddy method for embedded LES inflow boundary conditions. Seventh int symp turb shear flow phenom (Ottawa), University of Manchester, 2013.

[122] S.B. Pope. *Turbulent Flows.* Cambridge University Press, 2000.

[123] Blackwelder R. and Haritonidis J. Scaling of the bursting frequency in turbulent boundary layers. *J. Fluid Mech.*, 132:87–103, 1983.

[124] W. Rodi. Comparison of LES and RANS calculations of the flow around bluff bodies. *J. of Wind Engineering and Industrial Aerodynamics*, 69: 55–75, 1997.

[125] F. Roelofs. (U)RANS: core thermal hydraulics. In *Thermohydraulics and chemistry of liquid metal cooled reactors*, von Karman Institute for Fluid Dynamics Lecture Series, Rhode-Saint-Genese, Belgium, February 2017.

[126] F. Roelofs, A. Batta, G. Bandini, K. Van Tichelen, A. Gerschenfeld, and X. Cheng. European Liquid Metal Thermal-hydraulics R&D: present and future. . ENC 2014, Marseille, France, 2014.

[127] F. Roelofs, A. Shams, J. Pacio, V. Moreau, P. Planquart, K. van Tichelen, I. Di Piazza, and M. Tarantino. European outlook for lmfr thermal hydraulics. . The 16th International Topical Meeting on Nuclear Reactor Thermal Hydraulics (NURETH-16), Chicago, United States, 2015.

[128] F. Roelofs, K. Van Tichelen, and D. Tenchine. Status and future challenges of liquid metal cooled reactor thermal-hydraulics. . The 15th International Topical Meeting on Nuclear Reactor Thermal Hydraulics (NURETH-15), Pisa, Italy, 2013.

[129] F. Roelofs, K. van Tichelen, and M. Tarantino. European Thermal-Hydraulic Progress for Sodium and Lead Fast Reactors. . The 17th International Topical Meeting on Nuclear Reactor Thermal Hydraulics (NURETH-17), Xian, China, 2017.

[130] F. Roelofs, V.R. Gopala, S. Jayaraju, A. Shams, and E.M.J. Komen. Review of fuel assembly and pool thermal hydraulics for fast reactors. *Nucl. Engng. Design*, 265:1205–1222, 2013.

[131] F.W. Roos and J.T. Kegelman. Control of coherent structures in reattaching laminar and turbulent shear layers. *AIAA Journal*, 24:1956–1963, 1986.

[132] A. De Santis and A. Shams. Application of an algebraic turbulent heat flux model to a backward facing step flow at low Prandtl number. *Annals of Nuclear Energy*, 117:32–44, 2018.

[133] F. Scarano. *Particle Image Velocimetry - Development and application.* PhD Thesis, von Karman Institute for Fluid Dynamics, Brussels, Belgium, 2000.

[134] F. Scarano and M. Riethmuller. Iterative multigrid approach in PIV image processing with discrete window offset. *Exp. Fluids*, 26:513–523, 1999.

[135] P. Schlatter. Boundary Layer LES/DNS Data. `https://www.mech.kth.se/~pschlatt/DATA/`. Simulations performed by the Royal Institute of Technology, Stockholm, Sweden.

[136] P. Schlatter and R. Örlü. Assessment of direct numerical simulation data of turbulent boundary layers. *J. Fluid Mech.*, 659:116–126, 2010.

[137] P. Schlatter and R. Örlü. Turbulent boundary layers at moderate Reynolds numbers. Part I: Inflow length and tripping effects. *J. Fluid Mech.*, 710:5–34, 2011.

[138] P. Schlatter, R. Örlü, Q. Li, G. Brethouwer, J. H. M. Fransson, A. V. Johansson, P. H. Alfredsson, and D. S. Henningson. Turbulent boundary layers up to $Re_\theta = 2500$ studied through simulation and experiment. *Phys. Fluids*, 21, 2009.

[139] P. Schlatter, Q. Li, G. Brethouwer, J. H. M. Fransson, A. V. Johansson, P. H. Alfredsson, and D. S. Henningson. Simulations of spatially evolving turbulent boundary layers up to $Re_\theta = 4300$. *Intl J. Heat Fluid Flow*, 31:251–261, 2010.

[140] H. Schlichting. *Boundary Layer Theory.* McGraw-Hill, 7th edition, 1987.

[141] T. Schulenberg and R. Stieglitz. Flow measurement techniques in heavy liquid metals. *Nucl. Engng. Design*, 240:2077–2087, 2010.

[142] U. Schumann, G. Grötzbach, and L. Kleiser. *Direct numerical simulation of turbulence.* In W. Kollman, 1980.

[143] T. Schumm, B. Frohnapfel, and L. Marocco. Numerical simulation of the turbulent convective buoyant flow of sodium over a backward-facing step. Journal of Physics: Conference Series 745, 021051, 2016.

[144] T. Schumm, B. Frohnapfel, and L. Marocco. Investigation of a turbulent convective buoyant flow of sodium over a backward-facing step. *Heat Mass Trans.*, pages 1–11, 2017.

[145] A. Scotti, C. Meneveau, and DK. Lilly. Generalized smagorinsky model for anistropic grids. *Phys. Fluids*, 5:2306–2308, 1993.

[146] A. Shams. (U)RANS: turbulence modelling. In *Thermohydraulics and chemistry of liquid metal cooled reactors*, von Karman Institute for Fluid Dynamics Lecture Series, Rhode-Saint-Genese, Belgium, February 2017.

[147] A. Shams, F. Roelofs, and E. Komen. High-fidelity numerical simulation of the flow through an infinite wire-wrapped fuel assembly. The 16th International Topical Meeting on Nuclear Reactor Thermal Hydraulics (NURETH-16), Chicago, United States, 2015.

[148] A. Shams, F. Roelofs, E. Baglietto, S. Lardeau, and S. Kenjeres. Assessment and Calibration of an Algebraic Turbulent Heat Flux Model for Low-Prandtl Fluids. *Int. J. Heat Mass Tran.*, 79:589–601, 2014.

[149] A. Shams, F. Roelofs, E. Baglietto, and E.M.J. Komen. High fidelity numerical simulations of an infinite wire-wrapped fuel assembly. *Nucl. Engng. Design*, 335:441–459, 2018.

[150] M. P. Simens, J. Jimenez, S. Hoyas, and Y. Mizuno. A high-resolution code for turbulent boundary layers. *J. Comput. Phys.*, pages 4218–4231, 2009.

[151] E. Simons, M. Manna, and C. Benocci. *Parallel multi-domain large-eddy simulation of the flow over a backward-facing step at Re=5100.* Kluwer Academic Publishers, R. Friedrich and W. Rodi (eds.) edition, 2002.

[152] W. Skamarock, J. Klemp, J. Dudhia, D. Gill, D. Barker, M. Duda, X. Huang, W. Wang, and J. Powers. A description of the advanced research WRF version 3. NCAR Tech. Note NCAR/TN-475+STR, National Center for Atmospheric Research, 2008.

[153] A. Smirnov, S. Shi, and I. Celik. Random flow generation technique for large eddy simulations and particle dynamics modeling. *J. Fluids Eng*, 71:123–359, 2001.

[154] K. Snyers. Etude de conception d'une soufflerie tanche pour coulement d'un mlange hlium-xnon. Travail de fin d'tudes, Institut Suprieur Industriel de Bruxelles - ISIB-Mca-TFE-15/18, 2015.

[155] C. Spaccapaniccia, P. Planquart, J. M. Buchlin, M. Greco, F. Mirelli, and K. van Tichelen. Experimental results from a water scale model for the thermal-hydraulic analysis of a HLM reactor. The 16th International Topical Meeting on Nuclear Reactor Thermal Hydraulics (NURETH-16), Chicago, United States, 2015.

[156] P. R. Spalart. Direct simulation of a turbulent boundary layer up to Re=1410. *J. Fluid Mech.*, 187:61–98, 1988.

[157] A. Spille-Kohoff and H.-J. Kaltenbach. Generation of turbulent inflow data with a prescribed shear-stress profile. In *Third AFOSR International Conference on DNS/LES*, Arlington, Texas, USA, 2001. In DNS/LES Progress and Challenges, edited by C. Liu, L. Sakell, and T. Beutner.

[158] P. Stainback and K. Nagabushana. Review of hot-wire anemometry and the range of their applicability. Third International Symposium on Thermal Anemometry, A.F.E. Division, ed., vol. 167, pp. 93-134, 1993.

[159] R. Stieglitz and T. Schulenberg. Flow measurement techniques in heavy liquid metals. *Nuclear Engineering and Design*, 240:2077–2087, 2010.

[160] PP. Sullivan, JC. McWilliams, and C. Moeng. A subgrid-scale model for large-eddy simulation of planetary boundary-layer flows. *Boundary-Layer Meteorology*, 71:247–276, 1994.

[161] M.F. Taylor, K.E. Bauer, and D.M. McEligot. Internal forced convection to low-Prandtl-number gas mixtures. *Int. J. Heat Mass Transfer*, 31(1): 13–25, 1988.

[162] D. Tenchine. Some thermal hydraulic challenges in sodium cooled fast reactors. *Nucl. Engng. Design*, 240:1195–1217, 2010.

[163] K. Van Tichelen, F. Mirelli, M. Greco, and G. Viviani. E-SCAPE: A scale facility for liquid-metal, pool-type reactor thermal hydraulic investigations. *Nuclear Engineering and Design*, 290:65–77, 2015.

[164] I. Tiselj, R. Bergant, B. Mavko, I. Bajsic, and G. Hetsroni. DNS of turbulent heat transfer in channel flow with heat conduction in the solid wall. *J. Heat Trans. - Tran. ASME*, 123:849–857, 2001.

[165] I. Tiselj, J. Oder, and L. Cizelj. Double-sided cooling of heated slab: Conjugate heat transfer DNS. *Int. J. Heat Mass Tran.*, 66:781–790, 2013.

[166] E. R. van Driest. On turbulent flow near a wall. *AIAA*, 23:1007–1011, 1956.

[167] K. Velusamy, P. Chellapandi, S. Chetal, and B. Raj. Overview of pool hydraulic design of Indian prototype fast breeder reactor. *Sadhana*, 35: 97–128, 2010.

[168] J.C. Vogel and J.K. Eaton. Combined heat transfer and fluid dynamic measurements downstream of a backward facing step. *J. Heat Transfer*, 107:922–929, 1985.

[169] T. von Kármán. Mechanische Ähnlichkeit und Turulenz. In *Proceedings of the 3rd international congress on applied mechanics*, Stockholm, Sweden, 1930.

[170] B. Weigand, J. Ferguson, and M. Crawford. An extended Kays and Crawford turbulent Prandtl number model. *Int. J. Heat Mass Transfer*, 40:4191–4196, 1997.

[171] C.D. Winant and F.K. Browand. Vortex pairing: the mechanism of turbulent mixing-layer growth at moderate reynolds number. *J. Fluid Mech.*, 63:237–255, 1974.

[172] G. S. Winckelmans, H. Jeanmart, and D. Carati. On the comparison of turbulence intensities from large-eddy simulation with those from experiment or direct numerical simulation. *Brief Comm. in Phys. Fluids*, 14 (5):1809–1811, 2002.

[173] X. Wu and P. Moin. Dirtect numerical simulation of turbulence in a nominally zero-pressure-gradient flat-plate boundary layer. *J. Fluid Mech.*, 630:5–41, 2009.

[174] Z-T. Xie and I. P. Castro. Efficient generation of inflow conditions for large eddy simulation of street-scale flows. *Flow Turbulence and Combustion*, 81(3):449–470, 2008.

[175] E-S. Zanoun, F. Durst, and HM. Nagib. Evaluating the law of the wall in two-dimensional fully developed turbulent channel flows. *Phys. Fluids*, 15:3079–89, 2003.